

Universiteit
Leiden
The Netherlands

Exploring the sarcoma immune landscape

Oost, S. van

Citation
Oost, S. van. (2026, July 7). *Exploring the sarcoma immune landscape*. Retrieved from https://hdl.handle.net/1887/4307808

Version:	Publisher's Version
License:	Licence agreement concerning inclusion of doctoral thesis in the Institutional Repository of the University of Leiden
Downloaded from:	https://hdl.handle.net/1887/4307808

Note: To cite this publication please use the final published version (if applicable).

Exploring the sarcoma immune landscape

Siddh van Oost

Exploring the sarcoma immune landscape

ISBN: 978-94-6537-590-8

Cover design: Arina van Londen and Siddh van Oost

Layout: Arina van Londen | www.ridderprint.nl

Print: www.ridderprint.nl

Financial support for the printing of this thesis was kindly provided by the Department of Pathology, Leiden University Medical Center.

© 2026, Siddh van Oost, the Netherlands

All rights reserved. No part of this thesis may be reproduced, stored, or transmitted without prior permission of the author.

Exploring the sarcoma immune landscape

Proefschrift

ter verkrijging van
de graad van doctor aan de Universiteit Leiden,
op gezag van rector magnificus prof.dr. S. de Rijcke,
volgens besluit van het college voor promoties
te verdedigen op dinsdag 7 juli 2026
klokke 13:00 uur

door

Siddh van Oost
geboren te Rotterdam
in 1995

Promotores

Prof.dr. J.V.M.G. Bovée

Prof.dr. N.F.C.C. de Miranda

Leden promotiecommissie

Prof.dr. S.H. van der Burg

Prof.dr. S. Fröhling (Duits Kankeronderzoekscentrum (DKFZ), Heidelberg)

Prof.dr. W.T.A. van der Graaf (Nederlands Kanker Instituut)

Dr. N. Ogrinc

TABLE OF CONTENTS

Chapter 1	General introduction	7
Chapter 2	Linking immunity with genomics in sarcomas: is genomic complexity an immunogenic trigger?	25
Chapter 3	Divergent therapeutic and prognostic impacts of immunogenic features in undifferentiated pleomorphic sarcoma and myxofibrosarcoma	57
Chapter 4	Multimodal profiling of chordoma immunity reveals distinct immune contextures	95
Chapter 5	Immune infiltration is associated with distinct transcriptional states and metabolic profiles in chordomas	147
Chapter 6	General discussion & future perspectives	187
Appendices	PhD Portfolio	202
	Nederlandse samenvatting	208
	Curriculum Vitae	212
	List of publications	213
	Dankwoord	214



1

General introduction

Sarcomas are mesenchymal tumors of uncertain cell-of-origin that can arise anywhere in the body. They are very rare and account for only 1% of all adult cancers (1). According to the World Health Organization, there are currently more than 75 malignant sarcoma subtypes, which originate in soft tissues, such as fat, muscle or blood vessels, or in bone and cartilage. Among these subtypes, some are relatively more common (e.g. chondrosarcoma), while others are considered ultra-rare (e.g. adamantinoma), with incidence rates ≤ 1 per 1.000.000 per year (2). For research purposes, sarcomas are commonly classified into two categories according to their genomic architecture: sarcomas with simple genomes or sarcomas with complex genomes. Sarcomas with simple genomes are driven by specific, recurrent genetic alterations, typically involving single gene fusions or mutations. Examples include myxoid liposarcoma with the *FUS::DDIT3* fusion (3) and alveolar soft part sarcoma (ASPS) with the *ASPSCR1::TFE3* fusion (4). Conversely, sarcomas with complex genomes are characterized by genomic instability, involving large-scale genetic alterations such as gene amplifications, deletions and chromosomal rearrangements. This genomic complexity can vary substantially, even within the same histological subtype. Such variability contributes to differences in tumor behavior and treatment response, thereby complicating the clinical management of these subtypes (5). Examples of sarcomas with complex genomes include undifferentiated pleomorphic sarcoma (UPS), myxofibrosarcoma (MFS), and osteosarcoma. The treatment of sarcomas depends on the specific subtype, but typically involves surgery, chemotherapy, or radiotherapy. Depending on the tumor's anatomical location and aggressiveness, a combination of these modalities may also be used (6, 7). Nevertheless, despite continued refinement of multidisciplinary treatment strategies, only modest improvements in clinical outcomes have been achieved over the last decade, as disease recurrence remains common and many sarcomas exhibit intrinsic or acquired resistance to conventional systemic therapies. These challenges underscore the urgent need for more effective and innovative therapeutic approaches.

The link between the immune system and cancer has long been recognized, however, only in the past two decades has the molecular basis of anti-tumor immunity been elucidated in detail. The immune system can detect and target cancer cells by identifying molecules that distinguish malignant from healthy cells. Two major classes of such molecules, collectively referred to as antigens, can elicit anti-tumor immune responses: tumor-specific antigens and tumor-associated antigens (8, 9). Tumor-specific antigens, also known as neoantigens, arise from somatic mutations that generate novel peptide sequences. As these antigens are not present in normal tissues, they are recognized by the

immune system as “non-self” and are therefore often highly immunogenic. In contrast, tumor-associated antigens are derived from normal-self proteins that are aberrantly expressed, overexpressed, or expressed in inappropriate contexts within tumor cells. Examples include oncofetal proteins such as carcinoembryonic antigen and cancer-testis antigens such as NY-ESO-1, which are normally expressed only during embryonic development or in germline tissues such as the testis. Because these tissues lack human leukocyte antigen (HLA) expression and are not surveyed by the immune system, lymphocytes recognizing these self-antigens are not eliminated during immune maturation. Consequently, when these antigens are re-expressed in tumors, they tend to induce relatively weak immune responses due to central immune tolerance.

Tumor cells present antigens on HLA class I molecules, enabling recognition and elimination by cytotoxic $CD8^+$ T cells (**Figure 1A**) (10). In addition, tumor antigens released during cell death can be taken up by dendritic cells, which process and cross-present them via HLA class I to activate cytotoxic T cells (11), or present them via HLA class II molecules to $CD4^+$ helper T cells, which in turn promote cytotoxic T cell activation through cytokine secretion (**Figure 1A**) (12). However, many tumors evade immune recognition by downregulating components of the antigen presentation machinery (**Figure 1B**) (13), recruiting immunosuppressive cell types (14), or upregulating inhibitory immune checkpoints like programmed death-ligand 1 (PD-L1) (15). These mechanisms collectively suppress T cell activation and effector function, allowing tumors to escape immune-mediated elimination and providing the rationale for immune checkpoint blockade, which aims to restore and enhance anti-tumor immunity by releasing inhibitory constraints on T cell function.

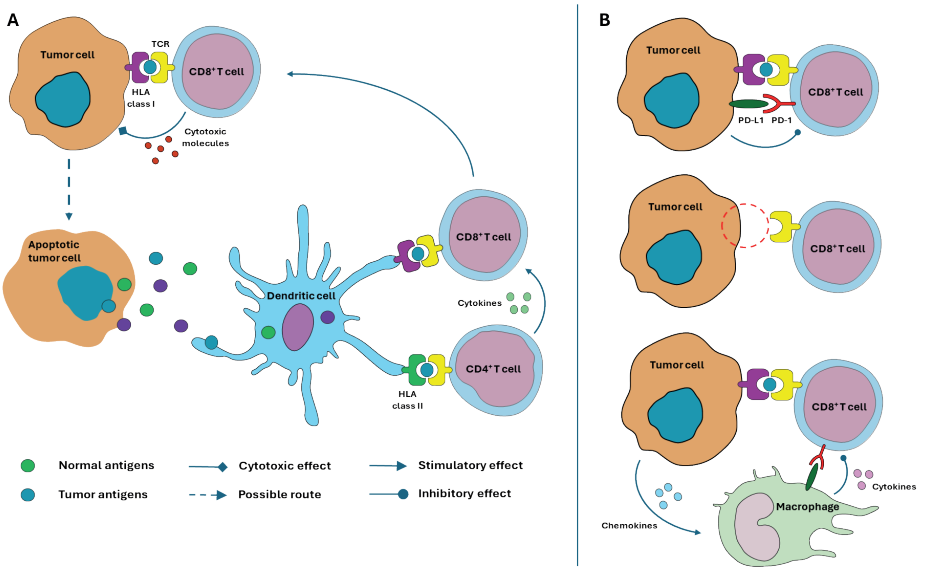


Figure 1. Schematic representation of T cell-mediated tumor recognition and mechanisms of tumor immune evasion. A) $CD8^+$ T cells recognize tumor cells through their T cell receptor (TCR) binding to neoantigens presented on HLA class I molecules. This interaction activates cytotoxic effector functions, leading to tumor cell killing. Following cell death, either via T cell-mediated killing or other mechanisms, tumor-derived antigens are released and captured by dendritic cells, which can (cross-)present them to T cells. When these antigens are tumor-associated, T cells are activated, which either triggers or enhances the anti-tumor immune response. **B**) Tumor cells have various mechanisms to evade T cell-mediated killing. They can upregulate inhibitory ligands such as PD-L1, which binds PD-1 on activated T cells and suppresses effector functions. Alternatively, tumor cells can downregulate antigen presentation machinery to escape immune recognition. In addition, tumor cells secrete chemokines that recruit immunosuppressive (myeloid) cells, which further inhibit T cell activity through immunosuppressive cytokines or inhibitory ligands.

THE CANCER IMMUNOTHERAPY REVOLUTION

Over the last decade, immune checkpoint inhibitors targeting inhibitory molecules like programmed cell death protein 1 (PD-1), PD-L1, and cytotoxic T-lymphocyte associated protein 4 (CTLA-4), have transformed the treatment landscape of several cancers, producing durable responses in melanoma (16) and non–small cell lung cancer (17). The remarkable efficacy of mono- or dual-checkpoint blockade in these tumors is largely attributed to their high mutational burden (18, 19), which enhances tumor antigenicity, and to their robust pre-existing anti-tumor immune response (20, 21). However, these features vary considerably between cancer types and even among patients

with the same tumor type, limiting the overall effectiveness of checkpoint blockade (22, 23).

In contrast, sarcomas have generally been considered poorly immunogenic, owing to their relatively low mutational burden (24) and lack of other predictive biomarkers such as PD-L1 expression or mismatch repair deficiency (25, 26). Consequently, the initial wave of immunotherapy trials yielded limited efficacy across most sarcoma subtypes. Nevertheless, objective responses have been observed in certain histologies. Notably, ASPS has emerged as the striking exception, becoming the first sarcoma subtype for which an immune checkpoint inhibitor, atezolizumab, has received FDA approval (27-29). Intriguingly, the mechanisms underlying the pronounced sensitivity of ASPS to checkpoint blockade remain poorly understood. Additional evidence of sensitivity has been observed in chordoma (30, 31), UPS (32-34), MFS (33, 35-37), and dedifferentiated liposarcoma (DDLPS) (32, 34, 38) (**Table 1**). However, the strength of evidence varies substantially among subtypes, with data for MFS, in particular, being largely limited to case reports or clinical trials enrolling fewer than 5 patients.

Table 1. Overview of clinical trials with checkpoint blockade, either as monotherapy or as a combination therapy. Only trials with ≥ 5 patients for that subtype are presented. ORR = objective response rate (as measured by RECIST); ASPS = alveolar soft part sarcoma; DDLPS = dedifferentiated liposarcoma; UPS = undifferentiated pleomorphic sarcoma; CT = chemotherapy; RT = radiotherapy; TLS = tertiary lymphoid structure.

Subtype	ORR	Drugs	Clinical trial	Reference
ASPS	37%	Atezolizumab	NCT03141684	(28)
	54%	Pembrolizumab + axitinib	NCT02636725	(27)
	82%	TQB2450 + anlotinib	CTR20190938	(29)
Chordoma	12%	Pembrolizumab	NCT03012620	(31)
	20%	Durvalumab + tremelimumab	NCT02815995	(30)
DDLPS	10%	Pembrolizumab	NCT02301039	(32) – after expansion
	42%	Pembrolizumab + CT	NCT02406781	(38) – TLS-positive
	12%	Nivolumab + RT	NCT03307616	(34) – neoadjuvant
	0%	Nivolumab + ipilimumab + RT	“”	“”
UPS	23%	Pembrolizumab	NCT02301039	(32) – after expansion
	33%	Nivolumab + ipilimumab	NCT02500797	(33)
	17%	Nivolumab + RT	NCT03307616	(34) – neoadjuvant
	25%	Nivolumab + ipilimumab + RT	“”	“”

While monotherapy shows rather limited efficacy in unselected sarcoma populations, combining checkpoint blockade with radiotherapy, chemotherapy, or antiangiogenic agents seem to enhance anti-tumor immunity and thereby improve clinical responses (**Table 1**). More recently, neoadjuvant or perioperative checkpoint blockade has produced remarkable clinical

outcomes in colorectal, gastric and gastroesophageal junction cancers (39, 40), underscoring the potential of optimizing immunotherapeutic strategies in traditionally less immunogenic cancers. Encouragingly, this concept has begun to translate into sarcoma, with the first trials combining neoadjuvant/perioperative checkpoint blockade and radiotherapy reporting promising early results in UPS (34, 41). Many clinical trials are currently underway and may soon clarify whether immunotherapy could become a mainstay in sarcoma treatment. Immunotherapeutic strategies such as tumor vaccines or chimeric antigen receptor-T cell therapy are further discussed in **Chapter 2**.

UNRAVELING THE SARCOMA IMMUNE MICROENVIRONMENT

Although the precise mechanisms underlying sarcoma sensitivity to checkpoint blockade remain elusive, the tumor immune microenvironment clearly plays a key role. In recent years, advances in molecular profiling, ranging from bulk sequencing to single-cell and spatially resolved approaches, have dramatically improved our insight into sarcoma immunity. Early studies using immunohistochemistry described the immune infiltration in various sarcoma subtypes (42-45), enabling the classification of tumors into inflamed/immune "hot", immune-excluded, or immune desert/immune "cold" phenotypes, a framework first established in carcinomas according to T cell infiltration patterns (46). In sarcoma, tumors often fall into the immune-excluded category, especially bone sarcomas due to their dense extracellular matrix, or the immune desert group with minimal T cell infiltration. Only a small subset shows an inflamed phenotype. **Chapter 2** dives further into this framework in sarcomas and how it associates with their genomic architecture.

Bulk RNA sequencing studies further refined these phenotypes by using computational deconvolution to estimate the relative composition of the immune microenvironment. A pivotal study classified soft tissue sarcomas (STS) into five immune classes (SIC A-E), representing a spectrum from poorly to highly immunogenic (47). The highly immunogenic group (SIC E) was enriched for B cells and tertiary lymphoid structures (TLS), which are clearly defined clusters of T cells, B cells, and myeloid cells, often associated with anti-tumor immunity (48). Intriguingly, SIC E was retrospectively associated with checkpoint blockade response in the SARC028 trial, and validated in the PEMBROSARC trial, where selecting TLS-positive patients increased response rates and established TLS as a predictive biomarker in sarcoma (**Table 1**) (38).

Although the presence of TLS enhances sensitivity to checkpoint blockade, they remain uncommon across sarcoma subtypes (present in 12% of the overall STS population in the Petitprez study (47); up to 75% in well-differentiated/DDLPS, and around 22% in UPS in the PEMBROSARC trial (38)). Moreover, the presence of TLS alone does not fully explain the variability in checkpoint blockade response, as roughly 40% of TLS-positive patients achieved improved 6-month progression-free survival (38). This suggests that additional immunological processes underlying effective anti-tumor immunity may complement TLS as predictive markers. In this context, the Immunologic Constant of Rejection (ICR) signature, a 20 gene signature reflecting type 1 T (Th1) cell signaling, offers an additional framework for assessing immune activation across tumor types (49). The ICR signature has been shown to stratify tumors into immune-active and immune-silent phenotypes (50, 51), including in STS cohorts, and to correlate with clinical response to checkpoint blockade (52). Although bulk transcriptomic profiling is powerful for analyzing large cohorts, it provides limited insights into immune and stromal cell composition or cellular heterogeneity. Technologies like single-cell and single-nucleus RNA sequencing overcome these limitations and have provided high-resolution profiling of the tumor microenvironment across diverse sarcoma subtypes, including chordoma (53), osteosarcoma (54), Ewing sarcoma (55), synovial sarcoma (56), UPS (57), and rhabdomyosarcoma (58). These studies have revealed subtype-specific patterns of immune infiltration, stromal composition, and mechanisms of immune evasion.

While single-cell transcriptomic analyses offer invaluable molecular insights, they lack spatial information, which limits our understanding of how cells interact and organize within tissues. Spatially resolved transcriptomic approaches address this gap by preserving tissue context and enabling detailed mapping of cellular neighborhoods, immune niches, and stromal organization. GeoMx digital spatial profiling enables compartmentalized transcriptomic profiling across regions of interest, whereas Visium provides high-resolution mapping across entire tissue sections. Using these approaches, spatially distinct patterns of inflammation have been identified in angiosarcoma (59, 60) and osteosarcoma (61). Complementary proteomic technologies such as imaging mass cytometry (IMC) and high-dimensional multiplex immunofluorescence enable subcellular-resolution quantification of approximately 40 and 60 proteins, respectively, providing detailed insights into cellular phenotypes, interactions, and spatial organization within the tumor microenvironment. For example, spatial mapping of primary osteosarcomas revealed that immunosuppressive macrophage niches correlate with metastasis-free survival (62), whereas in lung metastatic lesions, the spatial distance between effector

immune and immunosuppressive cells was associated with overall survival (63). Similarly, mass spectrometry imaging provides spatially resolved lipid and metabolite profiles and has, for instance, revealed tumor-promoting metabolic features in macrophages in malignant peripheral nerve sheath tumors (64).

Building on these insights, single-cell spatial transcriptomic platforms such as CosMx and Xenium in situ now allow gene expression to be mapped at true single-cell resolution directly onto tissue sections. By combining in-depth cellular behavior with precise spatial localization, these technologies can reveal cellular neighborhoods, immune-stromal interactions, and the spatial distribution specific cellular states, bridging the gap between single-cell transcriptional states and tissue architecture. Although still very new, the first application of this technology in sarcomas has already been reported, identifying distinct mechanisms of resistance to checkpoint blockade in Ewing sarcoma using samples from the SARC028 trial (65).

Together, these approaches have generated key insights into sarcoma immunobiology. The research presented in this thesis builds on this foundation, applying state-of-the-art bulk, single-cell, and spatial technologies to explore the immune landscape of sarcomas known to respond, albeit variably, to checkpoint blockade.

UNDIFFERENTIATED PLEOMORPHIC SARCOMA AND MYXOFIBROSARCOMA

UPS and MFS are two subtypes of STS that predominantly arise in the extremities and trunk (1). Both are defined by extensive chromosomal alterations, few recurrent mutations (66, 67), and a lack of lineage-specific differentiation markers. Despite these shared features, they present with distinct clinical and histological characteristics (**Figure 2A+B**). MFS is a spectrum of disease, ranging from low- to high-grade tumors, and can develop either superficially or deeper-seated (1). Low-grade tumors are hypocellular with abundant myxoid matrix, whereas high-grade lesions display increased cellularity, nuclear pleomorphism, and reduced myxoid stroma. In contrast, UPS presents almost exclusively as deep-seated, intermediate- to high-grade tumors. Histologically, UPS is characterized by a dense mesh of highly pleomorphic spindle and giant cells.

The current standard-of-care for UPS and high-grade MFS consists of surgery accompanied with neoadjuvant radiotherapy (7). And although this is effective for local disease control, a substantial proportion of patients still develop

metastases (68), underscoring the necessity for more effective systemic therapies. From an immunological perspective, UPS has emerged as one of the more responsive sarcoma subtypes to T cell checkpoint blockade, while responses in MFS have also been observed, though evidence remains more limited. Because of their shared genomic complexity and lack of differentiation, UPS and MFS are often grouped together in translational research and clinical trials. However, whether they truly share the same immunogenic landscape, or instead harbor meaningful differences that shape therapeutic response, remains unresolved. Exploring these similarities and divergences is therefore a critical step toward optimizing immunotherapeutic strategies in these aggressive sarcomas.

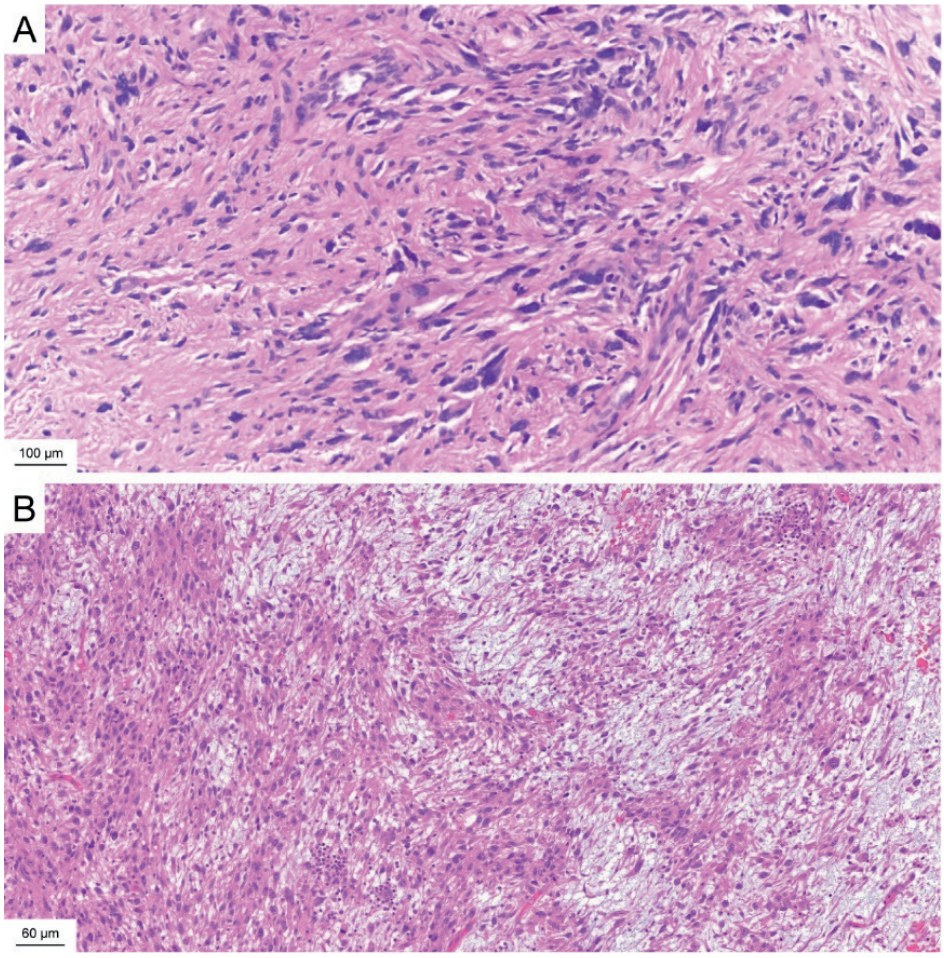


Figure 2. Histological images of UPS and MFS. A) UPS showing pleomorphism. **B**) High-grade MFS showing areas with myxoid matrix.

CHORDOMA

Chordomas are ultra-rare bone sarcomas showing notochordal differentiation that predominantly arise in the axial skeleton, including the skull base, mobile spine, and sacrococcygeal region (1). They express the notochordal transcription factor brachyury, encoded by the *TBXT* gene, which drives their distinctive biology and confers both epithelial and mesenchymal characteristics (69). Genetically, chordomas are relatively stable and exhibit a low mutational burden, though chromosomal alterations can occur, with *CDKN2A/B* loss being the most frequent (70, 71). Histologically, chordomas are typically organized in lobules separated by fibrous septa (1), often containing a myxoid or chondroid matrix (**Figure 3A**), and the tumor cells stain positive for brachyury (**Figure 3B**). The hallmark physaliphorous cells have large vacuolated cytoplasm giving them a "bubbly" appearance (**Figure 3C**). Nuclear pleomorphism is generally uncommon, observed only in a subset of tumors. Conventional chordomas may also present with a chondroid pattern, characterized by a hyaline-cartilage like matrix resembling that of chondrosarcomas, a feature seen more frequently at the skull base. Rare, more aggressive subtypes include poorly differentiated chordoma, marked by *SMARCB1* (INI1) loss with retention of brachyury expression, and dedifferentiated chordoma, which contains high-grade sarcomatous areas lacking brachyury expression, typically adjacent to conventional chordoma areas.

Standard-of-care treatment aims for *en bloc* surgical resection whenever feasible, often complemented by (proton beam) radiotherapy (72). However, complete resection is often difficult due to the tumor's proximity to critical neurovascular structures, contributing to high rates of local recurrence (73). In addition, conventional chemotherapy has minimal efficacy because of the indolent nature of chordomas (74), highlighting the urgent need for improved therapeutic strategies. Intriguingly, chordomas have demonstrated responsiveness to T cell checkpoint blockade despite their low mutational burden and abundant extracellular matrix. This underscores the importance of characterizing their immune microenvironment to uncover mechanisms that may explain their sensitivity to immunotherapy.

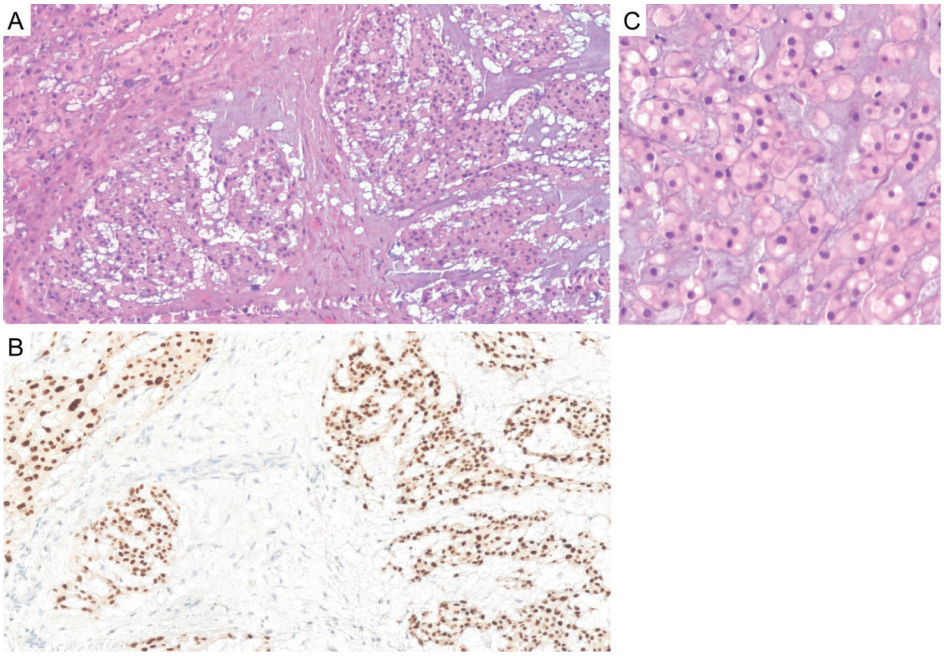


Figure 3. Histological images of chordoma. A) H&E image of a chordoma, rich in myxoid matrix, with some fibrous septations. **B**) Immunohistochemistry for brachyury, the diagnostic marker for chordoma (*TBXT*). **C**) H&E image of physaliphorous cells in a myxoid matrix.

OUTLINE OF THIS THESIS

The work presented in this thesis aims to gain insight into the sarcoma immune landscape across subtypes with reported, yet heterogeneous, sensitivity to checkpoint blockade, with the goal of informing patient stratification for rational immunotherapeutic combination strategies.

Building on recent advances in cancer immunotherapy, **Chapter 2** provides a conceptual overview of genomic complexity and its association with sarcoma immunogenicity. It explores how features of the immune microenvironment relate to genomic architecture and responsiveness to checkpoint blockade, thereby establishing a framework for the marked heterogeneity of immunotherapy responses across sarcoma subtypes.

Chapter 3 investigates two genomically complex STS subtypes — UPS and MFS — characterizing the immune microenvironment of pre-treatment samples using a combination of bulk RNA sequencing and IMC. T cells and macrophages are further analyzed in an extended cohort and associated with clinical outcome. Additionally, the impact of neoadjuvant radiotherapy on the

tumor microenvironment is assessed by comparing pre-treatment biopsies with post-treatment resections through IMC.

In contrast, chordoma — an intriguing sarcoma subtype — exhibits responses to checkpoint blockade despite its relatively low genomic complexity. **Chapter 4** provides the first large-scale characterization of the chordoma immune microenvironment, integrating bulk RNA sequencing, bulk T cell receptor sequencing, IMC and multiplex immunofluorescence to define distinct immune contextures. **Chapter 5** builds directly on these findings by applying spatial transcriptomics alongside lipidomic and metabolomic profiling to the same tumors; analyses of sequential tissue sections enable integration of tumor- and stroma-specific transcriptional profiles with spatially resolved lipid and metabolite data.

Finally, **Chapter 6** synthesizes the overall findings, discusses their biological and clinical implications, and outlines perspectives for future research and potential therapeutic strategies.

REFERENCES

1. WHO Classification of Tumours Editorial Board. Soft Tissue and Bone Tumours. WHO Classification of Tumours. 5 ed. Lyon, France: IARC Publications; 2020.
2. Stacchiotti S, Frezza AM, Blay JY, Baldini EH, Bonvalot S, Bovee J, et al. Ultra-rare sarcomas: A consensus paper from the Connective Tissue Oncology Society community of experts on the incidence threshold and the list of entities. Cancer. 2021;127(16):2934-42.
3. Crozat A, Aman P, Mandahl N, Ron D. Fusion of CHOP to a novel RNA-binding protein in human myxoid liposarcoma. Nature. 1993;363(6430):640-4.
4. Ladanyi M, Lui MY, Antonescu CR, Krause-Boehm A, Meindl A, Argani P, et al. The der(17)t(X;17)(p11;q25) of human alveolar soft part sarcoma fuses the TFE3 transcription factor gene to ASPL, a novel gene at 17q25. Oncogene. 2001;20(1):48-57.
5. Soupir A, Ospina OE, Hampton O, Churchman M, Radmacher M, Hedges D, et al. Genomic, transcriptomic, and immunogenomic landscape of over 1300 sarcomas of diverse histology subtypes. Nat Commun. 2025;16(1):4206.
6. Strauss SJ, Frezza AM, Abecassis N, Bajpai J, Bauer S, Biagini R, et al. Bone sarcomas: ESMO-EURACAN-GENTURIS-ERN PaedCan Clinical Practice Guideline for diagnosis, treatment and follow-up. Ann Oncol. 2021;32(12):1520-36.
7. Gronchi A, Miah AB, Dei Tos AP, Abecassis N, Bajpai J, Bauer S, et al. Soft tissue and visceral sarcomas: ESMO-EURACAN-GENTURIS Clinical Practice Guidelines for diagnosis, treatment and follow-up. Ann Oncol. 2021;32(11):1348-65.
8. Peri A, Salomon N, Wolf Y, Kreiter S, Diken M, Samuels Y. The landscape of T cell antigens for cancer immunotherapy. Nat Cancer. 2023;4(7):937-54.
9. Shah S, Al-Omari A, Cook KW, Paston SJ, Durrant LG, Brentville VA. What do cancer-specific T cells 'see'? Discov Immunol. 2023;2(1):kyac011.
10. Yewdell JW, Reits E, Neefjes J. Making sense of mass destruction: quantitating MHC class I antigen presentation. Nat Rev Immunol. 2003;3(12):952-61.
11. Joffre OP, Segura E, Savina A, Amigorena S. Cross-presentation by dendritic cells. Nat Rev Immunol. 2012;12(8):557-69.
12. den Haan JM, Arens R, van Zelm MC. The activation of the adaptive immune system: cross-talk between antigen-presenting cells, T cells and B cells. Immunol Lett. 2014;162(2 Pt B):103-12.
13. Jhunjhunwala S, Hammer C, Delamarre L. Antigen presentation in cancer: insights into tumour immunogenicity and immune evasion. Nat Rev Cancer. 2021;21(5):298-312.
14. Lasser SA, Ozbay Kurt FG, Arkhypov I, Utikal J, Umansky V. Myeloid-derived suppressor cells in cancer and cancer therapy. Nat Rev Clin Oncol. 2024;21(2):147-64.
15. Lin X, Kang K, Chen P, Zeng Z, Li G, Xiong W, et al. Regulatory mechanisms of PD-1/PD-L1 in cancers. Mol Cancer. 2024;23(1):108.
16. Wolchok JD, Chiarion-Sileni V, Rutkowski P, Cowey CL, Schadendorf D, Wagstaff J, et al. Final, 10-Year Outcomes with Nivolumab plus Ipilimumab in Advanced Melanoma. N Engl J Med. 2025;392(1):11-22.

17. Borghaei H, Gettinger S, Vokes EE, Chow LQM, Burgio MA, de Castro Carpeno J, et al. Five-Year Outcomes From the Randomized, Phase III Trials CheckMate 017 and 057: Nivolumab Versus Docetaxel in Previously Treated Non-Small-Cell Lung Cancer. J Clin Oncol. 2021;39(7):723-33.

18. Rizvi NA, Hellmann MD, Snyder A, Kvistborg P, Makarov V, Havel JJ, et al. Cancer immunology. Mutational landscape determines sensitivity to PD-1 blockade in non-small cell lung cancer. Science. 2015;348(6230):124-8.

19. Snyder A, Makarov V, Merghoub T, Yuan J, Zaretsky JM, Desrichard A, et al. Genetic basis for clinical response to CTLA-4 blockade in melanoma. N Engl J Med. 2014;371(23):2189-99.

20. Tumeh PC, Harview CL, Yearley JH, Shintaku IP, Taylor EJ, Robert L, et al. PD-1 blockade induces responses by inhibiting adaptive immune resistance. Nature. 2014;515(7528):568-71.

21. Shien K, Papadimitrakopoulou VA, Wistuba, II. Predictive biomarkers of response to PD-1/PD-L1 immune checkpoint inhibitors in non-small cell lung cancer. Lung Cancer. 2016;99:79-87.

22. Lee M, Samstein RM, Valero C, Chan TA, Morris LGT. Tumor mutational burden as a predictive biomarker for checkpoint inhibitor immunotherapy. Hum Vaccin Immunother. 2020;16(1):112-5.

23. Roelands J, Kuppen PJK, Ahmed EI, Mall R, Masoodi T, Singh P, et al. An integrated tumor, immune and microbiome atlas of colon cancer. Nat Med. 2023;29(5):1273-86.

24. Chalmers ZR, Connelly CF, Fabrizio D, Gay L, Ali SM, Ennis R, et al. Analysis of 100,000 human cancer genomes reveals the landscape of tumor mutational burden. Genome Med. 2017;9(1):34.

25. Lam SW, Kostine M, de Miranda N, Schoffski P, Lee CJ, Morreau H, et al. Mismatch repair deficiency is rare in bone and soft tissue tumors. Histopathology. 2021.

26. D'Angelo SP, Shoushtari AN, Agaram NP, Kuk D, Qin LX, Carvajal RD, et al. Prevalence of tumor-infiltrating lymphocytes and PD-L1 expression in the soft tissue sarcoma microenvironment. Hum Pathol. 2015;46(3):357-65.

27. Wilky BA, Trucco MM, Subhawong TK, Florou V, Park W, Kwon D, et al. Axitinib plus pembrolizumab in patients with advanced sarcomas including alveolar soft-part sarcoma: a single-centre, single-arm, phase 2 trial. Lancet Oncol. 2019;20(6):837-48.

28. Chen AP, Sharon E, O'Sullivan-Coyne G, Moore N, Foster JC, Hu JS, et al. Atezolizumab for Advanced Alveolar Soft Part Sarcoma. N Engl J Med. 2023;389(10):911-21.

29. Tan Z, Wu Y, Fan Z, Gao T, Guo W, Bai C, et al. Anlotinib plus TQB2450, a PD-L1 Antibody, in Patients with Advanced Alveolar Soft Part Sarcoma: A Single-Arm, Phase II Trial. Clin Cancer Res. 2024;30(24):5577-83.

30. Somaiah N, Conley AP, Parra ER, Lin H, Amini B, Solis Soto L, et al. Durvalumab plus tremelimumab in advanced or metastatic soft tissue and bone sarcomas: a single-centre phase 2 trial. Lancet Oncol. 2022;23(9):1156-66.

31. Blay JY, Chevret S, Le Cesne A, Brahmi M, Penel N, Cousin S, et al. Pembrolizumab in patients with rare and ultra-rare sarcomas (AcSe Pembrolizumab): analysis of a subgroup from a non-randomised, open-label, phase 2, basket trial. Lancet Oncol. 2023.

32. Tawbi HA, Burgess M, Bolejack V, Van Tine BA, Schuetze SM, Hu J, et al. Pembrolizumab in advanced soft-tissue sarcoma and bone sarcoma (SARC028): a multicentre, two-cohort, single-arm, open-label, phase 2 trial. Lancet Oncol. 2017;18(11):1493-501.

33. D'Angelo SP, Mahoney MR, Van Tine BA, Atkins J, Milhem MM, Jahagirdar BN, et al. Nivolumab with or without ipilimumab treatment for metastatic sarcoma (Alliance A091401): two open-label, non-comparative, randomised, phase 2 trials. Lancet Oncol. 2018;19(3):416-26.

34. Roland CL, Nassif Haddad EF, Keung EZ, Wang WL, Lazar AJ, Lin H, et al. A randomized, non-comparative phase 2 study of neoadjuvant immune-checkpoint blockade in retroperitoneal dedifferentiated liposarcoma and extremity/truncal undifferentiated pleomorphic sarcoma. Nat Cancer. 2024.

35. Kelly CM, Antonescu CR, Bowler T, Munhoz R, Chi P, Dickson MA, et al. Objective Response Rate Among Patients With Locally Advanced or Metastatic Sarcoma Treated With Talimogene Laherparepvec in Combination With Pembrolizumab: A Phase 2 Clinical Trial. JAMA Oncol. 2020;6(3):402-8.

36. Zhou M, Bui N, Lohman M, van de Rjin M, Hwang G, Ganjoo K. Long-Term Remission with Ipilimumab/Nivolumab in Two Patients with Different Soft Tissue Sarcoma Subtypes and No PD-L1 Expression. Case Rep Oncol. 2021;14(1):459-65.

37. Kalofonou F, Napolitano A, Benson C, Miah A, Zaidi S, Lindsay D, et al. The efficacy of combination immunotherapy with ipilimumab plus nivolumab in metastatic myxofibrosarcoma. Rare Tumors. 2024;16:20363613241290788.

38. Italiano A, Bessede A, Pulido M, Bompas E, Piperno-Neumann S, Chevreau C, et al. Pembrolizumab in soft-tissue sarcomas with tertiary lymphoid structures: a phase 2 PEMBROSARC trial cohort. Nat Med. 2022;28(6):1199-206.

39. Chalabi M, Fanchi LF, Dijkstra KK, Van den Berg JG, Aalbers AG, Sikorska K, et al. Neoadjuvant immunotherapy leads to pathological responses in MMR-proficient and MMR-deficient early-stage colon cancers. Nat Med. 2020;26(4):566-76.

40. Verschoor YL, van de Haar J, van den Berg JG, van Sandick JW, Kodach LL, van Dieren JM, et al. Neoadjuvant atezolizumab plus chemotherapy in gastric and gastroesophageal junction adenocarcinoma: the phase 2 PANDA trial. Nat Med. 2024;30(2):519-30.

41. Mowery YM, Ballman KV, Hong AM, Schuetze SM, Wagner AJ, Monga V, et al. Safety and efficacy of pembrolizumab, radiation therapy, and surgery versus radiation therapy and surgery for stage III soft tissue sarcoma of the extremity (SU2C-SARC032): an open-label, randomised clinical trial. Lancet. 2024;404(10467):2053-64.

42. Ogose A, Kawashima H, Hotta T, Ariizumi T, Yamagishi T, Oike N, et al. Frequent expression of human leukocyte antigen class I and the status of intratumoral immune cells in alveolar soft part sarcoma. Oncol Lett. 2017;13(4):2169-76.

43. Pollack SM, He Q, Yearley JH, Emerson R, Vignali M, Zhang Y, et al. T-cell infiltration and clonality correlate with programmed cell death protein 1 and programmed death-ligand 1 expression in patients with soft tissue sarcomas. Cancer. 2017;123(17):3291-304.

44. Dancsok AR, Gao D, Lee AF, Steigen SE, Blay JY, Thomas DM, et al. Tumor-associated macrophages and macrophage-related immune checkpoint expression in sarcomas. Oncoimmunology. 2020;9(1):1747340.

45. Zou MX, Pan Y, Huang W, Zhang TL, Escobar D, Wang XB, et al. A four-factor immune risk score signature predicts the clinical outcome of patients with spinal chordoma. Clin Transl Med. 2020;10(1):224-37.

46. Galon J, Bruni D. Approaches to treat immune hot, altered and cold tumours with combination immunotherapies. Nat Rev Drug Discov. 2019;18(3):197-218.

47. Petitprez F, de Reynies A, Keung EZ, Chen TW, Sun CM, Calderaro J, et al. B cells are associated with survival and immunotherapy response in sarcoma. Nature. 2020;577(7791):556-60.

48. Fridman WH, Meylan M, Petitprez F, Sun CM, Italiano A, Sautes-Fridman C. B cells and tertiary lymphoid structures as determinants of tumour immune contexture and clinical outcome. Nat Rev Clin Oncol. 2022;19(7):441-57.

49. Bertucci F, Finetti P, Simeone I, Hendrickx W, Wang E, Marincola FM, et al. The immunologic constant of rejection classification refines the prognostic value of conventional prognostic signatures in breast cancer. Br J Cancer. 2018;119(11):1383-91.

50. Roelands J, Hendrickx W, Zoppoli G, Mall R, Saad M, Halliwill K, et al. Oncogenic states dictate the prognostic and predictive connotations of intratumoral immune response. J Immunother Cancer. 2020;8(1).

51. Bertucci F, Niziers V, de Nonneville A, Finetti P, Mescam L, Mir O, et al. Immunologic constant of rejection signature is prognostic in soft-tissue sarcoma and refines the CINSARC signature. J Immunother Cancer. 2022;10(1).

52. Mogenet A, Finetti P, Denicolai E, Greillier L, Boudou-Rouquette P, Goldwasser F, et al. Immunologic constant of rejection as a predictive biomarker of immune checkpoint inhibitors efficacy in non-small cell lung cancer. J Transl Med. 2023;21(1):637.

53. Duan W, Zhang B, Li X, Chen W, Jia S, Xin Z, et al. Single-cell transcriptome profiling reveals intra-tumoral heterogeneity in human chordomas. Cancer Immunol Immunother. 2022;71(9):2185-95.

54. Zhou Y, Yang D, Yang Q, Lv X, Huang W, Zhou Z, et al. Single-cell RNA landscape of intratumoral heterogeneity and immunosuppressive microenvironment in advanced osteosarcoma. Nat Commun. 2020;11(1):6322.

55. Visser LL, Bleijs M, Margaritis T, van de Wetering M, Holstege FCP, Clevers H. Ewing Sarcoma Single-cell Transcriptome Analysis Reveals Functionally Impaired Antigen-presenting Cells. Cancer Res Commun. 2023;3(10):2158-69.

56. Jerby-Arnon L, Neftel C, Shore ME, Weisman HR, Mathewson ND, McBride MJ, et al. Opposing immune and genetic mechanisms shape oncogenic programs in synovial sarcoma. Nat Med. 2021;27(2):289-300.

57. Luthria K, Shah P, Caldwell B, Melms JC, Abuzaid S, Jakubikova V, et al. Single-Cell Profiling of Sarcomas from Archival Tissue Reveals Programs Associated with Resistance to Immune Checkpoint Blockade. Clin Cancer Res. 2024;30(19):4530-41.

58. DeMartino J, Meister MT, Visser LL, Brok M, Groot Koerkamp MJA, Wezenaar AKL, et al. Single-cell transcriptomics reveals immune suppression and cell states predictive of patient outcomes in rhabdomyosarcoma. Nat Commun. 2023;14(1):3074.

59. Loh JW, Lee JY, Lim AH, Guan P, Lim BY, Kannan B, et al. Spatial transcriptomics reveal topological immune landscapes of Asian head and neck angiosarcoma. Commun Biol. 2023;6(1):461.

60. Ko TK, Guo Z, Kannan B, Lim BY, Lee JY, Li Z, et al. Multiomics characterization of breast angiosarcoma from an Asian cohort reveals enrichment for angiogenesis signaling pathway and tumor-infiltrating macrophages. Front Immunol. 2024;15:1515935.

61. Zheng X, Liu X, Zhang X, Zhao Z, Wu W, Yu S. A single-cell and spatially resolved atlas of human osteosarcomas. J Hematol Oncol. 2024;17(1):71.

62. Gyau BB, Wang J, Wu W, Scull B, Major AM, Jin W, et al. Multiplex Imaging Mass Cytometry Reveals Prognostic Immunosuppressive Subpopulations and Macrophage-Driven Metastasis in Osteosarcoma. Cancers (Basel). 2025;17(17).

63. Lacinski RA, Dziadowicz SA, Melemai VK, Fitzpatrick B, Pisquiy JJ, Heim T, et al. Spatial multiplexed immunofluorescence analysis reveals coordinated cellular networks associated with overall survival in metastatic osteosarcoma. Bone Res. 2024;12(1):55.

64. Ursem R, Groen JL, Malessy MJA, Briaire-de Bruijn I, McDonnell LA, Heijs B, et al. Spatial Lipidomics Reveals Myelin Defects and Protumor Macrophage Infiltration in Malignant Peripheral Nerve Sheath Tumor Adjacent Nerves. Lab Invest. 2025;105(1):102186.

65. Daley JD, Mukherjee E, Ferraro D, Bhaskar S, Green A, Meyer EM, et al. SARC028 samples reveal an interplay between TGFbeta, interferon signaling and low HLA class I expression as contributors to Ewing sarcoma checkpoint blockade resistance. Clin Cancer Res. 2025.

66. Cancer Genome Atlas Research Network. Comprehensive and Integrated Genomic Characterization of Adult Soft Tissue Sarcomas. Cell. 2017;171(4):950-65 e28.

67. Mitra S, Farswan A, Piccinelli P, Sydow S, Hesla A, Tsagkozis P, et al. Transcriptomic profiles of myxofibrosarcoma and undifferentiated pleomorphic sarcoma correlate with clinical and genomic features. J Pathol. 2024;264(3):293-304.

68. Yoshimoto M, Yamada Y, Ishihara S, Kohashi K, Toda Y, Ito Y, et al. Comparative Study of Myxofibrosarcoma With Undifferentiated Pleomorphic Sarcoma: Histopathologic and Clinicopathologic Review. Am J Surg Pathol. 2020;44(1):87-97.

69. Nelson AC, Pillay N, Henderson S, Presneau N, Tirabosco R, Halai D, et al. An integrated functional genomics approach identifies the regulatory network directed by brachyury (T) in chordoma. J Pathol. 2012;228(3):274-85.

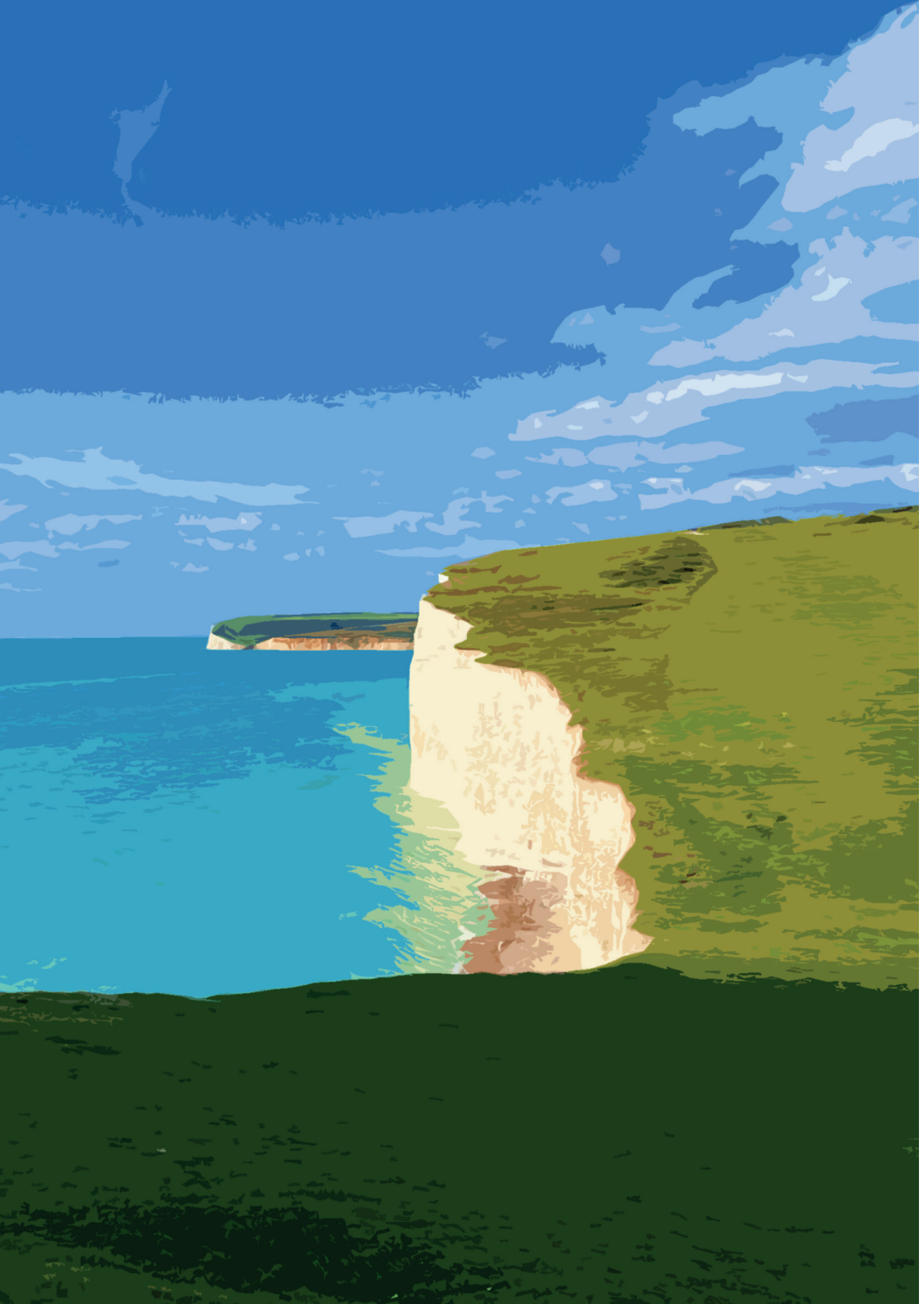
70. Tarpey PS, Behjati S, Young MD, Martincorena I, Alexandrov LB, Farndon SJ, et al. The driver landscape of sporadic chordoma. Nature Communications. 2017;8.

71. Bai J, Shi J, Li C, Wang S, Zhang T, Hua X, et al. Whole genome sequencing of skull-base chordoma reveals genomic alterations associated with recurrence and chordoma-specific survival. Nat Commun. 2021;12(1):757.

72. Stacchiotti S, Gronchi A, Fossati P, Akiyama T, Alapetite C, Baumann M, et al. Best practices for the management of local-regional recurrent chordoma: a position paper by the Chordoma Global Consensus Group. Ann Oncol. 2017;28(6):1230-42.

73. Walcott BP, Nahed BV, Mohyeldin A, Coumans JV, Kahle KT, Ferreira MJ. Chordoma: current concepts, management, and future directions. Lancet Oncol. 2012;13(2):e69-76.

74. Colia V, Stacchiotti S. Medical treatment of advanced chordomas. Eur J Cancer. 2017;83:220-8.



2

Linking immunity with genomics in sarcomas: is genomic complexity an immunogenic trigger?

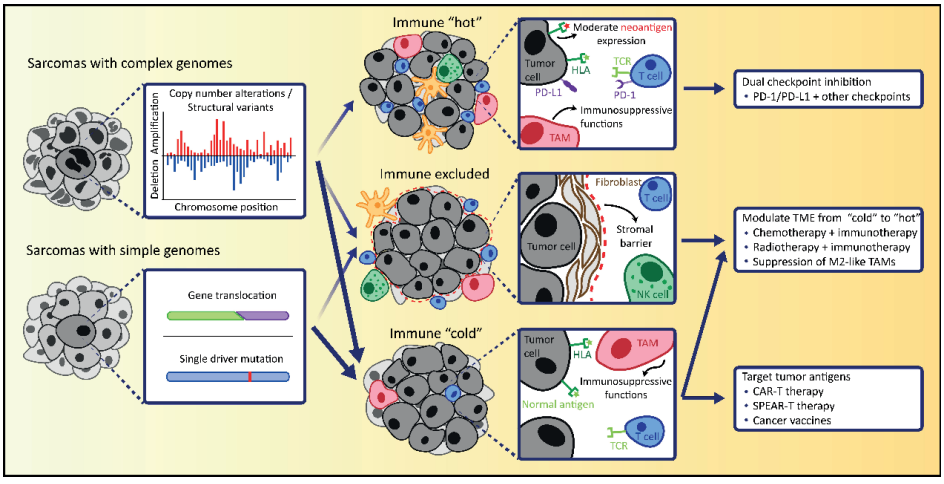
Siddh van Oost, Debora M. Meijer, Marieke L. Kuijjer, Judith V.M.G. Bovée, and Noel F.C.C. de Miranda

Biomedicines ***2021, 9(8), 1048***

ABSTRACT

Sarcomas comprise a collection of highly heterogeneous malignancies that can be grossly grouped in the categories of sarcomas with simple or complex genomes. Since the outcome for most sarcoma patients has barely improved in the last decades, there is an urgent need for improved therapies. Immunotherapy, and especially T cell checkpoint blockade, has recently been a game-changer in cancer therapy as it produced significant and durable treatment responses in several cancer types. Currently, only a small fraction of sarcoma patients benefit from immunotherapy, supposedly due to a general lack of somatically mutated antigens (neoantigens) and spontaneous T cell immunity in most cancers. However, genomic events resulting from chromosomal instability are frequent in sarcomas with complex genomes and could drive immunity in those tumors. Improving our understanding of the mechanisms that shape the immune landscape of sarcomas will be crucial to overcoming the current challenges of sarcoma immunotherapy. This review focuses on what is currently known about the tumor microenvironment in sarcomas and how this relates to their genomic features. Moreover, we discuss novel therapeutic strategies that leverage the tumor microenvironment to increase the clinical efficacy of immunotherapy, and which could provide new avenues for the treatment of sarcomas.

Graphical abstract



INTRODUCTION

Sarcomas are a heterogeneous group of tumors arising in the bone and soft tissue. Currently, the World Health Organization recognizes over 70 distinct sarcoma subtypes, which illustrates the biological complexity of these tumors (1). This complexity also implies considerable challenges regarding their diagnosis and treatment. Conventional treatments, such as surgical resection, chemotherapy, and radiotherapy, are the mainstay of treatment, but the survival of patients has barely improved over the last decades. Therefore, there is an urgent need for effective treatment options. In recent years, immunotherapy, mainly through the advent of T cell checkpoint blockade therapies, has revolutionized the treatment of a number of solid cancers, particularly ones with immunogenic features. In sarcomas, however, it currently has limited use as only a small group of patients benefits from these therapies. Nevertheless, recent studies have highlighted immunogenic features in some sarcomas that may support immunotherapeutic approaches for their treatment.

At the genomic level, a simplified distinction can be made between sarcomas with simple or complex genomes. Sarcomas with simple genomes often harbor a recurrent driver genomic event (e.g., translocation, mutation, or amplification), while other extensive alterations throughout the genome are not observed (**Figure 1A**). For instance, Ewing sarcoma contains a gene fusion between *EWSR1* (or *FUS*) and a member of the ETS family of transcription factors (e.g., *EWSR1-FLI1*) (2). Next to a few secondary mutations in *TP53* and *STAG2*, Ewing sarcomas generally lack other genetic alterations. In addition, well-differentiated liposarcoma and dedifferentiated liposarcoma are associated with amplifications in a specific region on chromosome 12 (12q13-15) that encompasses genes such as *MDM2* and *CDK4* (3). Other well-known examples of sarcomas with simple genomes include alveolar soft-part sarcoma and synovial sarcoma. In contrast, sarcoma subtypes with complex genomes present extensive, non-recurrent genetic alterations, including single nucleotide variants (SNVs) and structural variants (**Figure 1B**) (4). Mutational patterns reminiscent of catastrophic genomic events, such as *chromothripsis* and *kataegis,* are commonly observed in tumors with complex genomes, such as osteosarcomas (5). Since these genomic alterations are so extensive and largely non-recurrent, sarcomas with complex genomes are highly heterogeneous entities, both intratumorally as well as across patients. This has complicated the understanding of the mechanisms underlying tumorigenesis in these cancers (6). Other sarcomas with complex genomes include myxofibrosarcoma, undifferentiated soft tissue sarcoma,

and leiomyosarcoma. Of note, sarcomas with simple genomes may progress towards complex genomes through the acquisition of secondary mutations and chromosomal instability, as seen in low-grade chondrosarcomas carrying an *IDH1* or *IDH2* mutation in a simple genomic background that develop into high-grade chondrosarcomas with complex genomes (7).

Genetic alterations can be perceived by the immune system via various mechanisms. Mutations in the coding genome that impact protein sequences can trigger T cell immunity when neoepitopes undergo antigen presentation in the context of the Human Leukocyte Antigen (HLA) system (8). In addition, DNA sensing pathways can be activated by the presence of cytosolic DNA as a result, for instance, of faulty mitotic events (9). In response, signaling cascades that lead to the production of pro-inflammatory cytokines are triggered, thereby attracting immune cells to the tumor microenvironment. The link between antigen presentation and response to T cell checkpoint blockade immunotherapies is well-established, as demonstrated by the exceptional responses to this type of immunotherapy in cancers with high mutation burden, such as non-small cell lung cancer and melanoma, as well as mismatch repair deficient (MMRd) cancers (10). In sarcomas with complex genomes, such as osteosarcoma, the tumor mutation burden is generally low (~1.15 mutations per Mb) (11). Chromosomal instability, on the other hand, is frequently observed in complex sarcomas and could promote immune responses via sensing of cytosolic DNA by the cyclic GMP-AMP synthase-Stimulator of Interferon Genes (cGAS-STING) pathway or through upregulation of ligands that can activate effector immune cells, such as NK cells (12, 13). Hence, it is hypothesized that sarcomas with complex genomes would have an increased probability of benefiting from immunotherapy as compared to sarcomas with simple genomes. Conversely, chromosomal aberrations can also promote immune evasion and reduced response to immunotherapy (14). Although infrequent, responses to immunotherapy have been reported in sarcoma patients, which advocates further elucidation of their biology, including the role of genetics and the tumor microenvironment (TME) in underlying responses to immunotherapy (15).

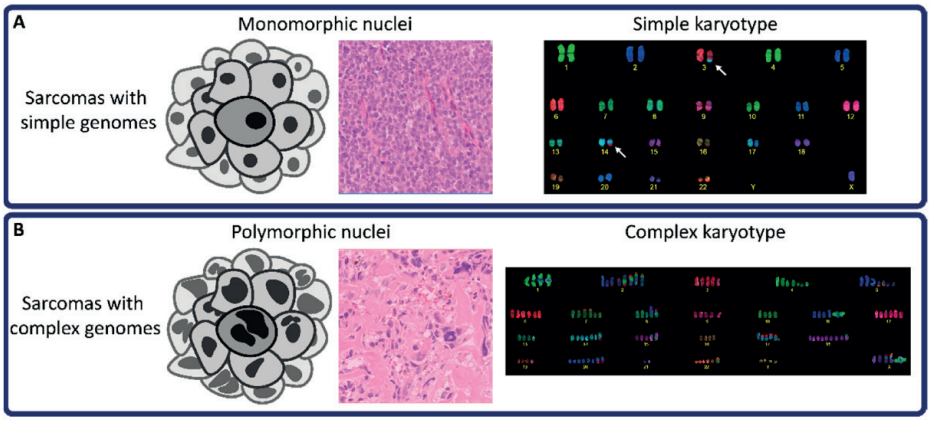


Figure 1. Morphological and karyotypic differences between sarcomas with simple and complex genomes. A) schematic figure and HE staining demonstrating monomorphic nuclei. White arrows in simple karyotype image indicate a translocation (3:14), typically observed in translocation-driven sarcomas. **B**) schematic figure and HE staining demonstrating polymorphic nuclei. The complex karyotype image displays extensive chromosomal aberrations, including chromosomal gains and translocations.

THE TUMOR MICROENVIRONMENT IN THE CONTEXT OF GENOMIC COMPLEXITY

The composition and functional orientation of the cells that compose the TME, including immune cells, stromal cells, mesenchymal stem cells, endothelial cells, and pericytes, play a fundamental role in determining cancer progression and response to (immuno-)therapy. In particular, the TME can exhibit features that are indicative of ongoing antitumor immunity, as indicated by the presence of cytotoxic T cells and pro-inflammatory signals, or display hallmarks of immune suppression, such as the ones related to the activity of immune inhibitory pathways (e.g., IL-10, TGF-β) (16, 17). A TME enriched with lymphocytic infiltration, and pro-inflammatory signals are often referred to as immunologically "hot". However, cancers often present with immune-suppressed TMEs that can either be classified as immune-excluded or immunologically "cold" (18). In tumors with an immune-excluded phenotype, cytotoxic T lymphocytes (CTLs) are confined to the periphery of tumors, barred from infiltrating the tumor core by immune suppressive signals or physical barriers provided by cancer, immune, and stromal cells as well as by an aberrant extracellular matrix. Immunologically "cold" tumors are generally defined by the overall absence of CTLs either due to a lack of immunogenic features in cancer

cells or as a result of various immunosuppressive mechanisms. Importantly, non-cancer cells encompassed in the TME can also aid in immune evasion through various mechanisms of immunosuppression that, for instance, include the expression of immune suppressive molecules (19, 20). Impairment of the antigen-presenting machinery in tumor cells, for instance, through defective HLA class I expression, is another prominent means of immune escape (21, 22).

While sarcomas generally present with an immunologically "cold" TME (23), immunogenic features can be encountered in a relevant proportion of cases (24). The fact that predominantly sarcomas with complex genomes present immunogenic features indicate an association between genome complexity and immune response in these tumors. An overview of the TME compositions for several example sarcoma types is given in **Table 1** to illustrate the diversity in terms of genomics and TME.

THE TUMOR MICROENVIRONMENT OF SARCOMAS WITH SIMPLE GENOMES

Sarcomas with simple genomes, such as Ewing sarcomas, synovial sarcomas, and alveolar soft-part sarcomas, harbor isolated genomic alterations and present with a low mutation burden. Accordingly, they are, in general, poorly infiltrated by immune cells. In addition to having a low tumor mutation burden, Ewing sarcomas are, in many cases, noted to have a low expression of Human Leukocyte Antigen (HLA) class I and to have acquired expression of the immunosuppressive HLA-G molecule at the surface of tumor cells. Both observations have previously been associated with decreased levels of CD8+ T cell infiltration (25, 26). Even though lymphocytes are usually absent in Ewing sarcomas, most cases do contain tumor-associated macrophages (TAMs) with anti-inflammatory properties as well as immunosuppressive monocytes (27, 28). The presence of these cells might be an important contribution to the lack of lymphocytic infiltration in Ewing sarcomas. Nevertheless, some exceptional cases show moderate levels of infiltration by T cells, which has been associated with interferon-γ signaling (29). Similar observations have been made in synovial sarcomas and alveolar soft-part sarcomas, as these malignancies often encompass myeloid cells with immunosuppressive traits and, only occasionally, display moderate levels of lymphocytes co-occurring with HLA class I expression in tumor cells (30-33).

Regarding immunotherapeutic targets, most sarcomas with simple genomes show little to no expression of PD-L1 or infiltration of T cells expressing PD-1

or cytotoxic T lymphocyte antigen 4 (CTLA-4) (**Table 1**) (34-38). Surprisingly, PD-L1 expression has been observed in alveolar soft-part sarcoma patients of which the majority had received either chemo-, molecular targeted-, or immuno-therapy, or multiple lines of treatment prior to this particular study (39). This group of tumors was infiltrated with T lymphocytes as well, which raises the question of whether T cell infiltration and PD-L1 expression had been induced by previous treatments.

Although well-differentiated liposarcomas are rarely infiltrated by T cells, roughly 50% of cases feature tertiary lymphoid structures (TLSs) in their TME (40). TLSs are newly formed lymphoid structures that develop at sites of chronic inflammation, such as in a pro-inflammatory TME. They are comprised of T cells, B cells, and dendritic cells, resembling a germinal center structure in a lymph node (41). Moreover, TLSs displaying PD-L1 expression are found in both fusion-driven alveolar rhabdomyosarcoma and non-fusion-driven embryonal rhabdomyosarcoma (42). What triggers the formation of these TLSs in well-differentiated liposarcomas, and rhabdomyosarcomas is still unknown but warrants further elucidation as these structures have been associated with good response to immunotherapy in sarcomas. In addition, CD8+ T cells infiltrated into well-differentiated liposarcomas can express PD-1, suggesting those could be harnessed by therapies targeting the PD-1/PD-L1 axis (40).

Sarcomas with simple genomes are often driven by translocations, many of which involve transcription factors. The fusion product can profoundly reshape the transcriptional profiles of these cancers, potentially leading to the de novo expression of immunomodulatory molecules in the TME. Indeed, this has been suggested to occur in alveolar soft-part sarcoma, since TFE3, the transcription factor translocated and overexpressed in these tumors, is involved in the regulation of expression of transforming growth factor-beta (TGF-β), a well-known mediator of immune suppression, as well as the receptor tyrosine kinase MET, which can affect PD-L1 expression through activation of the PI3K pathway (43, 44).

THE TUMOR MICROENVIRONMENT IN SARCOMAS WITH COMPLEX GENOMES

The observation that, in general, sarcomas with complex genomes are more often infiltrated by effector immune cells suggests a connection between chromosomal instability and immunogenicity. A pan-cancer analysis showed that CTL infiltration is independent of the number of expressed neoantigens

in cancer types that are characterized by copy number alterations, including sarcomas (45). Furthermore, using multi-omics analyses, the authors of that study found an association between CTL infiltration in cancers with chromosomal instability and phosphorylation of the Ataxia Telangiectasia Mutated (ATM) protein, a DNA double-strand break damage response protein. They showed that ATM phosphorylation levels were positively correlated with the expression of CCL5, CXCL10, and IL-16. These chemokines and cytokines are known T cell attractants, indicating that chromosomal instability may modulate CTL infiltration via ATM signaling. Interestingly, *ATM* is frequently mutated or affected by copy number alterations in sarcomas with complex genomes, including myxofibrosarcoma and leiomyosarcoma, which could possibly affect the extent of immune cell infiltration in those (46, 47). As discussed, chromosomal instability can also lead to the release of genomic DNA into the cytosol of cells and to the subsequent activation of DNA-sensing pathways, such as the cGAS-STING pathway, which, in turn, can evoke an antitumor immune response. While the cGAS-STING mechanism has been extensively studied in other tumors (48), not much is known about its activity in sarcomas. Of note, the activity of this pathway can be silenced during tumorigenesis, as demonstrated in melanomas, where epigenetic silencing of STING pathway genes can occur (49). Altogether, in sarcomas, it is likely that chromosomal instability contributes to a more immunogenic TME, but additional research will be necessary to underpin a mechanistic link.

Even though genetically complex sarcomas harbor many genomic alterations, most subtypes are considered to be immunologically "cold" (e.g., osteosarcoma, chondrosarcoma, and leiomyosarcoma) (**Table 1**). Interestingly, in osteosarcoma, an association has been reported between genomic instability and immunogenicity. Wang et al. (2019) showed a higher occurrence of chromosomal instability and putative neoantigens in metastatic osteosarcoma compared to matched primary tumors (50). In parallel, they also demonstrated that metastatic osteosarcomas more frequently contained higher numbers of tumor cells expressing PD-L1 and were infiltrated by more T cells. Comparable results were also found by another study that reported significantly higher numbers of TILs and of PD-L1 expression in osteosarcoma metastases compared to primary tumors (51). However, contradictory results were found by Wu et al. (2020), where no significant differences were found between primary, recurrent, and metastatic osteosarcoma in the number of somatic alterations and potential neoantigens (52). Of note, the extent of immune infiltration could also be related to the location of the metastatic lesion. For example, osteosarcoma commonly metastasizes to lung tissue,

which has different tissue characteristics compared to the primary tumors originating from bone. This possibly affects the accessibility of immune cells to the tumor tissue.

In recent years, several studies have identified soft tissue sarcomas with an immunologically "hot" TME, including subsets of dedifferentiated liposarcomas, undifferentiated soft tissue sarcomas, and myxofibrosarcomas (**Table 1**). By integrating publicly available sarcoma datasets, Petitprez et al. (2020) identified five sarcoma immune classes, two of which being immunologically "hot" and encompassing a total of 33.3% of the cases (24). One of these immune "hot" subsets, comprising 17.8% of all cases, was found to be not only enriched with T lymphocytes, myeloid cells, and immune checkpoint expression but also with B cells and TLSs. Concurrently, the authors observed a relatively low mutational burden across all sarcoma immune classes, which suggests that other mechanisms are driving the immunologically "hot" microenvironment in both classes. Indeed, another study that utilized the same dataset highlighted a role for chemotaxis, interferon-γ signaling, and antigen presentation in the shaping of the pro-inflammatory TME phenotype in these sarcomas (53). Nevertheless, soft tissue sarcomas with a high mutational burden have been observed, including angiosarcomas and undifferentiated soft tissue sarcomas (54-56). Interestingly, these tumors were superficially located and contained UV-related mutational signatures similar to melanomas. In concordance with their high mutational load (~21–68 mutations per Mb), UV-exposed angiosarcomas and undifferentiated soft tissue sarcomas were found to be enriched with pro-inflammatory and immune-related (transcriptional) signatures (55-57).

While several sarcoma types with complex genomes are often considered "cold", the TME composition within specific sarcoma types can be quite diverse, resulting in subsets displaying a "hot" phenotype (**Table 1**). This may be linked to the stochastic and heterogeneous nature of the genomic alterations that occur in these tumors. For example, the mutational landscape of uterine leiomyosarcomas shows highly heterogeneous patterns of chromosomal alterations (58, 59). A study into the adaptive and innate immune cell landscape of uterine leiomyosarcomas showed that half of the cases were classified as immune cold. However, infiltrate represented by TAMs, T cells, and NK cells was seen in the other half of the cases (60). Unfortunately, studies correlating somatic chromosomal alterations to the amount of immune infiltrate and immune composition in uterine leiomyosarcomas are lacking. The investigation of a potential association between the extent of genomic alterations and immune infiltrates in leiomyosarcoma would be of great interest.

Table 1. An overview illustrating TME characteristics of a selection of simple and complex genome sarcoma types.

Sarcoma type	DNA alterations	Immune infiltration 1	PD-L1 expression 2	Genomic/TME	General TME composition
Simple genome					
Alveolar soft-part sarcoma	*TFE3-ASPCR1*	-	29.7–100%	−/−	CD8 T cells; TAMs (30, 39, 61)
Chondrosarcoma (low-grade)	*IDH, COL2A1*		0%	/±	CD4 and CD8 T cells; TAMs (34, 62, 63)
Well-differentiated liposarcoma	*MDM2, CDK4, CNA*	−/±	0–50%	−/−	CD4 Th and CD8 T cells; B cells, DCs; TAMs (35, 40, 64, 65)
Ewing sarcoma	*EWSR1-ETS*	-	0%	−/−	M2-like TAMs; CD4 and CD8 T cells (27, 65-67)
Synovial sarcoma	*SS18-SSX*	-	0%	−/±	TAMs; CD4 FOXP3 Tregs and CD8 T cells (31, 65, 66)
Complex genome					
Chondrosarcoma (dedifferentiated)	*IDH, COL2A1, CNA*	±	41–52%	+/±	CD4 and CD8 T cells; TAMs (34, 63)
Chordoma	*CDKN2A, PBRM1, SMARCB1, CNA*	+	0–68.5%	±/±	CD4 FOXP3 Tregs and CD8 T cells; M1-like and M2-like TAMs (28, 68-70)
Dedifferentiated liposarcoma	*MDM2, CDK4, CNA*	+	10–67%	+/+	CD4 Th and CD8 T cells; B cells, DCs; TAMs (24, 35, 40, 64, 65)
Myxofibrosarcoma	*CIN*	+	16–20%	+/+	CD4 Th, CD4 Treg and CD8 T cells; B cells; DCs; M1-like and M2-like TAMs (28, 36, 65, 71, 72)
Osteosarcoma	*CIN*	±	0–25%	+/+	CD4 and CD8 T cells; M1-like and M2-like TAMs, NK cells; DCs (27, 73-75)
Soft tissue leiomyosarcoma	*CNA*	±	34–59%	+/+	M2-like TAMs, CD4 T cells (28, 35, 71, 76)
Undifferentiated soft tissue sarcoma	*CIN, SNV*	+	0–33%	+/+	CD4 Th, CD4 Treg and CD8 T cells; B cells; DCs; M2-like TAMs (24, 28, 65, 71, 72, 77, 78)
Uterine leiomyosarcoma	*CNA*	±	0–70%	+/+	M2-like TAMs; CD4 T cells; NK cells (28, 60, 71, 76, 79)

[1] Amount of immune infiltration, genomic heterogeneity, and TME heterogeneity: −, low; ±, moderate; +, high. [2] Percentage of tumors expressing PD-L1 in tumor cells. Abbreviations: CIN, chromosomal instability; CNA, copy number alteration; DCs, dendritic cells; MDSCs, myeloid-derived suppressor cells; PD-L1, programmed death-ligand 1; SNV, single nucleotide variant; TAMs, tumor-associated macrophages; Th, T helper cells; TME, tumor microenvironment; Tregs, regulatory T cells.

Chordomas—a rare subtype of sarcoma of notochordal origin, which arise either in the skull base, the spine, or in the sacrum (80)—are, potentially the most immunologically "hot" sarcoma type. This is exemplified by their frequent infiltration with considerable amounts of CD4+ and CD8+ T cells, as well as with M1-like and M2-like TAMs (28, 68-70). In addition, at the protein level, PD-L1 is frequently expressed on tumor cells, whereas HLA class I is often expressed at varying degrees within a lesion (81). These findings further support an immunogenic character of chordomas. It is remarkable that conventional chordomas are so highly infiltrated as their mutational burden is relatively low. Genetic features of chordomas include chromosomal copy number loss of the tumor suppressor gene *CDKN2A* as well as structural variants in genes that encode members of the chromatin-remodeling complex, including *PBRM1* and *SMARCB1* (82, 83). Of note, loss-of-function mutations in these two genes were found to be poor prognostic factors in chordomas, indicating a pivotal role for epigenetic deregulation in progression of chordomas. Interestingly, mutations affecting these chromatin-remodeling genes have also been associated with immunogenic features of several solid cancers. For instance, mutations in *PBRM1* associate with increased CTL infiltration and PD-L1 expression, as well as with decreased infiltration by regulatory T cells in clear cell renal cell carcinoma (84, 85). In addition, mutations in *PBRM1* were also found predictive for worse clinical outcomes after PD-L1 blockade in various cancers, including clear cell renal cell carcinoma and lung adenocarcinoma, highlighting the ambiguous role of *PBRM1* in immunity (86). In chordomas, however, these findings suggest that alterations in the chromatin-remodeling complex, in part, could explain the extensive infiltration. As epigenetic deregulation through genetic alterations frequently appears in chordomas, it would be interesting to study its role in relation to immunogenicity further.

CLINICAL RESPONSES TO IMMUNOTHERAPY IN RELATION TO THE IMMUNOGENOMICS OF SARCOMAS

Response to T cell checkpoint blockade

Over the years, immunotherapy with T cell checkpoint blockade antibodies has proven to be an excellent strategy to treat a subset of cancer patients (87). In particular, this approach has been effective in immunogenic cancers that present an immunologically "hot" microenvironment (18). On the other hand, cancers that do not elicit robust, spontaneous antitumor immune responses are, in general, poor candidates to benefit from checkpoint blockade therapies.

Currently, several biomarkers exploiting features related to immunogenicity are being applied to guide patient selection for immune checkpoint inhibition, including tumor mutation burden, mismatch repair-deficiency, and PD-L1 expression. These features have been predictive for response to checkpoint blockade in cancers such as melanoma, non-small cell lung cancer, or colon cancer (10). Thus, many clinical trials with T cell checkpoint blockade have enrolled sarcoma patients using these markers for selection, of which an all-encompassing overview is presented in the recent review article by Chew and colleagues (88). In general, sarcomas have a relatively low mutational burden, infrequently express PD-L1, and less than 2% display defects in the DNA mismatch repair system (89-91). Despite the absence of these predictive biomarkers, a considerable fraction of sarcoma patients respond to checkpoint blockade which supports the pursue of immunotherapy in sarcoma. However, this observation also highlights that good predictive biomarkers for response to immune checkpoint inhibition are still lacking, particularly in sarcoma, emphasizing the need to improve our understanding of the underlying biology of this disease.

Alveolar soft-part sarcomas are an exceptional sarcoma subtype in relation to checkpoint blockade, as approximately half of all patients with this disease are responsive to this immunotherapy although the mechanisms of response are still elusive. Given their immunologically "cold" microenvironment, lymphocytic infiltration is often absent. PD-L1 expression has been reported in 50–100% of alveolar soft-part sarcoma but did not correlate with clinical response to PD-1 blockade (39, 92). Moreover, alveolar soft-part sarcomas do not harbor many mutations aside from their characteristic *TFE3-ASPCR1* fusion. Interestingly, it was suggested that few cases of alveolar-soft part sarcomas that responded well to checkpoint blockade exhibited MMRd (92, 93), although the alleged prevalence of MMRd in alveolar soft-part sarcomas could not be confirmed in a larger cohort (91). As opposed to tumors with well-known immunogenic features, such as a high mutation burden, it is speculated that the specific fusion found in alveolar soft-part sarcomas influences immune-related pathways underlying response to anti-PD-1 treatment. Apart from alveolar soft-part sarcomas, no remarkable responses to checkpoint blockade have been observed in the remaining sarcomas with a simple genome.

Even though sarcomas with complex genomes contain higher numbers of immune cells, in general, they also respond poorly to immunotherapeutic agents. Treatment with pembrolizumab, which targets PD-1, led to a partial response in only 1 out of 22 osteosarcoma cases, and no responses were observed in a total of 10 leiomyosarcomas (94). Nevertheless, some responses

to PD-1 blockade have been observed in undifferentiated soft tissue sarcomas, dedifferentiated liposarcomas, myxofibrosarcomas, and chordomas. In the SARC028 trial, for instance, 40% of undifferentiated soft tissue sarcoma and 20% of dedifferentiated liposarcoma patients responded to pembrolizumab. Interestingly, only half of the responsive cases of undifferentiated soft tissue sarcomas expressed PD-L1 (94). Similarly, a case study involving a metastatic chordoma observed clinical benefit from pembrolizumab treatment. This particular chordoma did not express PD-L1 before treatment but did contain a loss-of-function mutation in *PBRM1*, which again hints at a role for the chromatin-remodeling complex in response to PD-1 blockade in chordomas (95). The fact that PD-L1 expression is not associated with response to PD-1 blockade highlights its inaptness as a predictive marker in sarcomas. In line with these findings, half of the sporadic cases of sarcomas with MMRd lack PD-L1 expression. However, MMRd sarcomas are still considered eligible for immune checkpoint inhibition as they often harbor a high mutational burden (91, 96). Some interesting and illustrative examples of the importance of TMB for response to checkpoint blockade are UV-induced angiosarcomas and occasional cases of myxofibrosarcomas and (UV-induced) undifferentiated soft tissue sarcomas (6, 55, 56, 97-99). All of these highly mutated tumors responded exceptionally well to anti-PD-1 therapy. In addition, B cells and TLSs could be other predictive markers for response to PD-1 blockade in soft tissue sarcomas (24). In their innovative study, Petitprez and colleagues categorized the pre-treatment tumors from the SARC028 trial into sarcoma immune classes and found that half of the responsive cases (5 out of 10 patients) had similar gene expression signatures as the immunologically “hot” class enriched with B cells and TLSs. The other responsive cases were observed in the second immunologically “hot” class and in the “vascularized” immune class, comprising mostly endothelial cell expression signatures. This observed association between the TME and response to immunotherapy again underlines the importance of characterizing the immune microenvironment of sarcomas.

Monotherapy with anti-PD-1 antibodies often falls short in sarcomas, but targeting the immune system remains a promising approach. Therefore, clinical trials have been set up with complementary checkpoint inhibitors, and with success. As an example, ipilimumab, which targets CTLA-4 on T cells, showed beneficial responses when combined with nivolumab, an anti-PD-1 antibody, compared to nivolumab mono treatment in various soft tissue sarcomas, including leiomyosarcomas, myxofibrosarcomas, undifferentiated soft tissue sarcomas, and angiosarcomas (100). Since dual blockade of CTLA-4 and PD-1 induced responses similar to chemotherapy in these soft tissue sarcomas,

combinatory immunotherapy is being further explored in the clinic (**https://clinicaltrials.gov/** Identifiers: NCT04741438; NCT04480502; NCT02500797. Accessed on 17 August 2021).

Response to other immunotherapeutic agents

In addition to T cell checkpoint blockade, other immunotherapeutic strategies have been explored in sarcoma, although to a lesser extent. These include, for instance, T cell receptor (TCR) gene therapy and cancer vaccines. TCR gene therapy involves the exploitation of a TCR that recognizes a specific HLA/peptide complex and which is transduced into a patient's own T cells (101). Once administered, these modified T cells should elicit a robust antitumor immune response when the target antigen is expressed by cancer cells. TCR gene therapies can be particularly useful when a group of tumors expresses a well-defined cancer-associated antigen. Therefore, this strategy is highly interesting for simple genome sarcomas that, in general, lack neoantigens derived from somatic mutations. A well-known example is the targeting of the tumor-associated antigen New York Esophageal Squamous cell carcinoma 1 (NY-ESO-1) in synovial sarcomas, which has been explored in multiple trials (102). NY-ESO-1 is found to be expressed in 49.3–82% of synovial sarcomas (103). One trial using TCR gene therapy against a total of 42 NY-ESO-1 expressing synovial sarcomas showed partial responses in 14 patients and a complete response in one patient (104). In addition to NY-ESO-1, tumor-associated antigen Preferentially Expressed Antigen in Melanoma (PRAME) is highly expressed in synovial sarcomas and was suggested to be a suitable target for TCR gene therapy as well (105). However, a downside of TCR gene therapy is that T cells can only recognize antigens in complex with HLA class I molecules. The fact that synovial sarcomas, like other less immunogenic tumors, often lack expression of HLA class I might complicate their targeting. Nevertheless, combining lympho-depleting agents with TCR gene therapy has proven successful in overcoming this obstacle and in maintaining antitumor immune responses in synovial sarcomas (104). Since synovial sarcomas are not the only subtype expressing such tumor-associated antigens, applying TCR gene therapy in immunologically "cold" sarcomas can prove beneficial in the clinical management of these malignancies.

Another path to the generation of antitumor immunity is the exploitation of cancer antigens through vaccination. These can consist of tumor-associated antigens but also neoantigens in a personalized setting (106, 107). Compared to other cancer types, only a handful of vaccines are currently being tested in sarcomas. One vaccine targeting NY-ESO-1 makes use of a lentiviral vector

which is preferentially taken up by dendritic cells and subsequently elicits an antitumor T cell response (108). A phase I trial including 24 sarcoma patients only showed partial response in 1 patient and stable disease in 13 patients (109). In line with these findings, a sequential phase II trial that explored the combination of this NY-ESO-1 vaccine with anti-PD-L1 treatment in 45 sarcoma patients observed a partial response and stable disease in one and 23 patients, respectively (110). To further improve T cell activation upon antigen presentation by dendritic cells, combination therapy of TCR gene therapy and vaccination is currently being explored in the clinic (**https://clinicaltrials.gov/** Identifier: NCT03450122. Accessed on 17 August 2021). In so-called pulsed dendritic cell vaccines, autologous dendritic cells are pulsed, i.e., loaded, with tumor lysate. Subsequently, the dendritic cell can present the tumor antigens and thereby trigger an immune response. A phase I/II trial using this method has been performed in bone and soft tissue sarcomas. While significantly increased levels of interferon-γ and IL-12 were observed, indicating an increased immune response, only one patient out of 35 showed a partial response to the vaccine (111). A vaccine against advanced chordoma, in which the tumor-associated antigen brachyury is targeted, has recently finished a phase II trial (112). Unfortunately, no significant differences were found in the overall response between the treated and control group.

CUES FROM THE TUMOR MICROENVIRONMENT FOR THE DEVELOPMENT OF NOVEL (IMMUNO)THERAPEUTIC APPROACHES

Modulating the tumor microenvironment of sarcomas towards immunologically "hot"

So far, T cell checkpoint blockade has not delivered sufficient clinical benefit in the majority of sarcomas, largely due to their immunologically "cold" TME. As immune "hot" sarcomas are more likely to respond to checkpoint blockade, modulating the TME of immune "cold" sarcomas towards a pro-inflammatory phenotype could prove advantageous in enhancing the efficacy of checkpoint blockade in sarcomas (**Figure 2A**). One attractive path towards sensitizing sarcomas to checkpoint blockade immunotherapies is the combination of the latter with traditional chemo- or radiotherapy treatments. For instance, the immune status of the TME of osteosarcomas was shown to be effectively altered by making use of conventional chemotherapy (113). After neoadjuvant chemotherapy, resected osteosarcomas displayed an increased density of TILs and an increased expression of PD-L1, thus converting to an immunologically "hot" microenvironment. In line with this, a combination treatment of

cyclophosphamide and pembrolizumab has been explored in soft tissue sarcomas (114). However, effective responses were limited to 6% of the cohort. Furthermore, elevated levels of TAM infiltrate together with an upregulation of the inhibitory enzyme indoleamine-2,3-dioxygenase (IDO) were observed, indicating the onset of an immunosuppressive TME (114, 115).

In addition, radiotherapy complementary to PD-1 blockade is currently being investigated. As an example, chordomas are generally treated with radiotherapy but often recur. Since these tumors are considered immunogenic, and no clinical trials with mono checkpoint inhibition have yet been finished, anti-PD-1 immunotherapy is being explored in combination with radiotherapy (**https://clinicaltrials.gov/** Identifier: NCT02989636. Accessed on 17 August 2021). This is also an interesting combination for those types of soft tissue sarcomas that are often treated with radiotherapy, as radiotherapy was found to affect the TME by inducing the cGAS-STING pathway as a result of the accumulation of cytosolic DNA (116). This accumulation results in interferon-γ signaling and upregulation of HLA class I and could, therefore, enhance both lymphocytic infiltration and recognition of neoantigens by T cells (48, 117). Stimulating HLA class I expression by adding interferon-γ to immune checkpoint inhibition has been investigated in synovial sarcomas (118). The interferon-γ treatment did not only modulate the TME towards a more immunogenic phenotype by induction of HLA class I expression and T cell infiltration but also induced PD-L1 expression. Given the immunologically “cold” TME in sarcomas in general, the opportunity to alter the TME towards an immune “hot” state through conventional therapies could provide clinical benefits as an addition to checkpoint blockade.

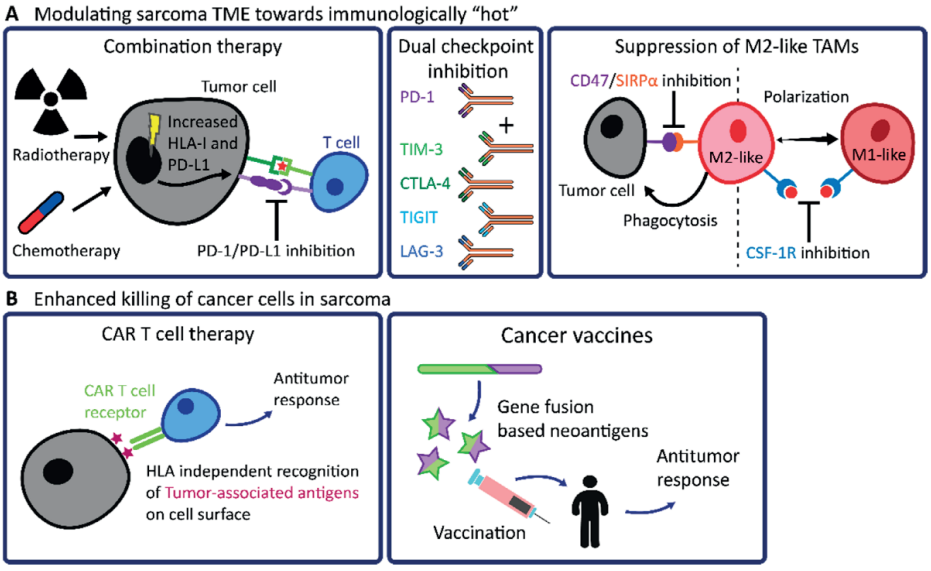


Figure 2. Overview of high-potential future therapeutic approaches for sarcomas with simple genomes or sarcomas with immunologically "cold" or excluded TME.

Besides modulation with conventional therapies, the immune microenvironment of sarcomas may also be directly targeted. More immune checkpoints have been identified in recent years, offering possibilities for dual therapy with anti-PD-1 or anti-PD-L1 antibodies, of which a comprehensive overview is provided in the recent review article by Zhu and colleagues (119). Such therapeutic targets in sarcomas include T cell Immunoglobulin and Mucin-domain containing-3 (TIM-3), Leukocyte Activation Gene-3 (LAG-3), and T cell Immunoreceptor with Ig and ITIM domains (TIGIT). Both TIM-3 and LAG-3 are expressed on immune cells and are co-expressed with PD-1 within the TME of immunologically "hot" soft tissue sarcomas, whereas T cells and NK cells highly express TIGIT in several osteosarcomas (24, 120, 121). Interestingly, most of these "next-generation" immune checkpoints are co-expressed with PD-1, which means that dual therapy with PD-1 blockade is a promising therapeutic option. Indeed, a phase I/IIa trial utilizing co-inhibition of LAG-3 and PD-1 has already shown improved efficacy in melanomas compared to anti-PD-1 monotherapy, and this will soon be investigated in sarcomas as well (**https://clinicaltrials.gov/** Identifier: NCT04095208. Accessed on 17 August 2021) (122).

Since the TME of sarcomas often contains large numbers of immunosuppressive TAMs, it makes sense to investigate these immune cells further and find ways to polarize their pro-tumoral anti-inflammatory (M2-like) properties towards

antitumoral pro-inflammatory (M1-like) activities. Similar to the aforementioned immune checkpoints, macrophages also have several receptors involved in their regulatory functions, which can be pursued for treatment, such as signal-regulatory protein alpha (SIRPα) and colony-stimulating factor 1 receptor (CSF-1R). SIRPα inhibits the phagocytic activity of macrophages when interacting with its ligand CD47 which can be expressed on tumor cells (123). In many sarcomas, including chordomas, dedifferentiated liposarcomas, and osteosarcomas, CD47 was observed to be highly expressed on tumor cells along with SIRPα expression on macrophages, suggesting a means of immune evasion in these tumors through this inhibitory axis (28). Furthermore, macrophages polarize towards an M2-like phenotype upon stimulation of CSF-1R by its ligand CSF-1 (124). In leiomyosarcomas and osteosarcomas, CSF-1R was found to be highly expressed by TAMs, and, in leiomyosarcomas, expression of CSF-1 and related proteins have also been associated with worse clinical outcomes (125, 126). Interestingly, CSF-1R expression has been found to be associated with good prognosis in osteosarcomas (127), which is in line with the reported protective function of TAMs in osteosarcomas (128). Since CSF-1R can be expressed by both M1-like and M2-like TAMs, it is still unclear what specific roles these macrophages have in sarcoma genesis. By inhibiting the CD47/SIRPα or the CSF-1/CSF-1R axis, macrophages can be stimulated to exert their phagocytotic function or can be guided towards more pro-inflammatory phenotypes, respectively (129, 130). This can potentially aid in mounting efficient antitumor immune responses as it might sensitize sarcomas for checkpoint blockade. In the coming years, several trials will be held that apply macrophage-targeting therapeutics (**https://clinicaltrials.gov/** Identifiers: NCT04751383; NCT04242238. Accessed on 17 August 2021).

Future prospects in engineered T cell therapy and cancer vaccines in sarcomas

Over the years, other methods next to TCR gene therapy which genetically modifies T cells, have gained interest as clinical applications in sarcomas. For instance, chimeric antigen receptor (CAR) T cell therapy is an approach where patient's T cells are collected from their peripheral blood and genetically modified ex vivo through the introduction of a CAR (131). The CAR is composed of a variable fragment of an antibody and a T cell signaling domain. Afterward, the CAR-expressing T cells can recognize tumor-associated antigens that are expressed at the surface of tumor cells, in an HLA-independent context, and mount an immune response against the tumor (**Figure 2B**) (132). Ongoing clinical trials involving CAR T cell therapy are directed at a multitude of tumor-associated antigens regularly found in sarcomas, but predominantly in

osteosarcomas and Ewing sarcomas. These antigens, or proteins, in this case, include the epidermal growth factor receptor 2 (HER2), disialoganglioside (GD2), and B7 homolog 3 (B7-H3). They have all been found overexpressed in tumor tissue but not in normal tissue (133-135). Although CAR T cells promisingly mediate anti-or immunity in vitro, overcoming the barrier formed by the TME remains difficult in vivo. Especially since the TME of sarcomas generally encompasses immune suppressive cells, finding a way to circumvent these will be necessary to improve the therapeutic efficacy of CAR T cells. Furthermore, it is known that infiltration of CAR T cells into solid tumors is challenging due to physical barriers, e.g., vascular endothelium, and the lack of chemo attractants, thereby limiting the therapy responses (136). Nonetheless, similar to T cell checkpoint blockade, lymphodepletion (cyclophosphamide or all-trans retinoic acid) or adjuvant cytokine treatment (IL-2, IL-12, or IL-15) can aid in improving CAR T cell-induced immune responses in sarcomas (137, 138).

In the context of cancer vaccines, targeting neoantigens originating from gene fusions has become an interesting strategy for translocation-driven sarcomas (**Figure 2B**). In theory, antigens derived from gene fusions can be more immunogenic than most point mutations due to the joining of two open reading frames. Although not compared to SNVs, it has recently been shown that gene fusion-based neoantigens can indeed stimulate T cell responses (139). In an older study, the antigenicity of fusion proteins of several sarcoma subtypes has been assessed by the binding ability of peptides from the fusion breakpoints to HLA class I (140). Two peptides derived from the *SS18-SSX* gene fusion in synovial sarcoma showed specific binding to HLA-A24 molecules. Later, the *SS18-SSX* gene fusion in synovial sarcoma was targeted with vaccines (141, 142). One pilot clinical trial showed increased CTL frequencies after vaccination in nine out of 21 patients. However, shrinkage of the tumor was only observed in one patient. Although the majority of synovial sarcomas do not seem to profit from cancer vaccines targeting the *SS18-SSX* gene fusion, many other neoantigens derived from gene fusions that drive the oncogenesis in sarcoma types have not yet been included in clinical trials. Furthermore, novel gene fusions are still being discovered in sarcomas, indicating a potential for the future (143-145).

CONCLUSIONS

The composition of the TME in sarcomas is highly influenced by their genome. Since genetically complex sarcomas are consistently infiltrated by larger quantities of immune cells than sarcomas with simple genomes, it can be postulated that genomic complexity plays an influential role in conferring an immunogenic character to sarcomas. The accumulation of chromosomal alterations, such as copy number alterations and structural variants, generates extensive genetic heterogeneity in complex sarcomas. Consequently, immune-related pathways become deregulated, thereby provoking either pro-inflammatory or immunosuppressive signals which all contribute to diverging compositions and immune statuses of the TME. Because of these heterogeneous features of many sarcomas, understanding the mechanisms that shape their TME remains intricate. However, state-of-the-art tools, such as single-cell approaches, spatial transcriptomics, and proteomics, have enhanced our ability to study the immunophenotypes of the sarcoma TME in detail and could help to overcome these challenges.

So far, immunotherapeutic options for sarcomas have not yet booked great successes. An encouraging strategy for sarcomas with a "cold" is the modulation of their TME towards an inflammatory state. This can be established, for instance, by employing chemo- or radiotherapy or "next-generation" checkpoint inhibitors, thereby increasing the efficacy of established immunotherapies. Furthermore, T cell engineering therapies and cancer vaccines are highly promising in sarcomas as specific neoantigens, or tumor-associated antigens can be targeted directly. In the coming years, utilizing high-resolution spatial technologies will help identify immune cells in the TME of sarcomas associated with clinical responses, which will aid in making sarcoma patients better amenable to immunotherapy.

Even though most sarcomas are generally considered immune "cold," there is sufficient evidence of immune infiltration and antitumor immune responses in their microenvironment. Deepening our understanding of the TME can aid in discovering suitable biomarkers and novel targets for immunotherapy and therefore improve clinical management of sarcomas.

AUTHOR CONTRIBUTIONS

Conceptualization S.v.O. and D.M.M.; writing-original draft preparation S.v.O. and D.M.M.; review and editing S.v.O., D.M.M., M.L.K., J.V.M.G.B. and N.F.C.C.d.M.; visualization, D.M.M.; supervision, M.L.K., J.V.M.G.B. and N.F.C.C.d.M. All authors have read and agreed to the published version of the manuscript.

FUNDING

N.F.C.C.d.M. is funded by the European Research Council (ERC) under the European Union's Horizon 2020 Research and Innovation Programme (grant agreement no. 852832).

ACKNOWLEDGMENTS

We thank K. Szuhai of the Cell and Chemical Biology department of the LUMC for providing the karyotype images.

CONFLICTS OF INTEREST

The authors declare no conflict of interest.

REFERENCES

1. WHO Classification of Tumours Editorial Board. WHO Classification of Tumours of Soft Tissue and Bone, 5th ed.: IARC Press: Lyon, France; 2020.
2. Grunewald TGP, Cidre-Aranaz F, Surdez D, Tomazou EM, de Alava E, Kovar H, et al. Ewing sarcoma. Nat Rev Dis Primers. 2018;4(1):5.
3. Pedeutour F, Forus A, Coindre JM, Berner JM, Nicolo G, Michiels JF, et al. Structure of the supernumerary ring and giant rod chromosomes in adipose tissue tumors. Genes Chromosomes Cancer. 1999;24(1):30-41.
4. Lam SW, van IJzendoorn DGP, Cleton-Jansen AM, Szuhai K, Bovee J. Molecular Pathology of Bone Tumors. J Mol Diagn. 2019;21(2):171-82.
5. Cortes-Ciriano I, Lee JJ, Xi R, Jain D, Jung YL, Yang L, et al. Comprehensive analysis of chromothripsis in 2,658 human cancers using whole-genome sequencing. Nat Genet. 2020;52(3):331-41.
6. Chibon F, Lagarde P, Salas S, Perot G, Brouste V, Tirode F, et al. Validated prediction of clinical outcome in sarcomas and multiple types of cancer on the basis of a gene expression signature related to genome complexity. Nat Med. 2010;16(7):781-7.
7. Nicolle R, Ayadi M, Gomez-Brouchet A, Armenoult L, Banneau G, Elarouci N, et al. Integrated molecular characterization of chondrosarcoma reveals critical determinants of disease progression. Nat Commun. 2019;10(1):4622.
8. Jhunjhunwala S, Hammer C, Delamarre L. Antigen presentation in cancer: insights into tumour immunogenicity and immune evasion. Nat Rev Cancer. 2021;21(5):298-312.
9. Bakhoum SF, Cantley LC. The Multifaceted Role of Chromosomal Instability in Cancer and Its Microenvironment. Cell. 2018;174(6):1347-60.
10. Samstein RM, Lee CH, Shoushtari AN, Hellmann MD, Shen R, Janjigian YY, et al. Tumor mutational load predicts survival after immunotherapy across multiple cancer types. Nat Genet. 2019;51(2):202-6.
11. Alexandrov LB, Kim J, Haradhvala NJ, Huang MN, Tian Ng AW, Wu Y, et al. The repertoire of mutational signatures in human cancer. Nature. 2020;578(7793):94-101.
12. Santaguida S, Richardson A, Iyer DR, M'Saad O, Zasadil L, Knouse KA, et al. Chromosome Mis-segregation Generates Cell-Cycle-Arrested Cells with Complex Karyotypes that Are Eliminated by the Immune System. Dev Cell. 2017;41(6):638-51.
13. Kwon J, Bakhoum SF. The Cytosolic DNA-Sensing cGAS-STING Pathway in Cancer. Cancer Discov. 2020;10(1):26-39.
14. Davoli T, Uno H, Wooten EC, Elledge SJ. Tumor aneuploidy correlates with markers of immune evasion and with reduced response to immunotherapy. Science. 2017;355(6322).
15. Siozopoulou V, Domen A, Zwaenepoel K, Van Beeck A, Smits E, Pauwels P, et al. Immune Checkpoint Inhibitory Therapy in Sarcomas: Is There Light at the End of the Tunnel? Cancers (Basel). 2021;13(2).
16. van den Bulk J, de Miranda N, Ten Dijke P. Therapeutic targeting of TGF-beta in cancer: hacking a master switch of immune suppression. Clin Sci (Lond). 2021;135(1):35-52.
17. Fridman WH, Zitvogel L, Sautes-Fridman C, Kroemer G. The immune contexture in cancer prognosis and treatment. Nat Rev Clin Oncol. 2017;14(12):717-34.

18. Galon J, Bruni D. Approaches to treat immune hot, altered and cold tumours with combination immunotherapies. Nat Rev Drug Discov. 2019;18(3):197-218.

19. Kumar V, Patel S, Tcyganov E, Gabrilovich DI. The Nature of Myeloid-Derived Suppressor Cells in the Tumor Microenvironment. Trends Immunol. 2016;37(3):208-20.

20. Whiteside TL, Demaria S, Rodriguez-Ruiz ME, Zarour HM, Melero I. Emerging Opportunities and Challenges in Cancer Immunotherapy. Clin Cancer Res. 2016;22(8):1845-55.

21. Montesion M, Murugesan K, Jin DX, Sharaf R, Sanchez N, Guria A, et al. Somatic HLA Class I Loss Is a Widespread Mechanism of Immune Evasion Which Refines the Use of Tumor Mutational Burden as a Biomarker of Checkpoint Inibitor Response. Cancer Discovery. 2021;11(2):282-92.

22. Ijsselsteijn ME, Petitprez F, Lacroix L, Ruano D, van der Breggen R, Julie C, et al. Revisiting immune escape in colorectal cancer in the era of immunotherapy. Br J Cancer. 2019;120(8):815-8.

23. Koumarianou A, Duran-Moreno J. The Sarcoma Immune Landscape: Emerging Challenges, Prognostic Significance and Prospective Impact for Immunotherapy Approaches. Cancers (Basel). 2021;13(3).

24. Petitprez F, de Reynies A, Keung EZ, Chen TW, Sun CM, Calderaro J, et al. B cells are associated with survival and immunotherapy response in sarcoma. Nature. 2020;577(7791):556-60.

25. Yabe H, Tsukahara T, Kawaguchi S, Wada T, Torigoe T, Sato N, et al. Prognostic significance of HLA class I expression in Ewing's sarcoma family of tumors. J Surg Oncol. 2011;103(5):380-5.

26. Spurny C, Kailayangiri S, Altvater B, Jamitzky S, Hartmann W, Wardelmann E, et al., editors. T cell infiltration into Ewing sarcomas is associated with local expression of immune-inhibitory HLA-G2018.

27. Hingorani P, Maas ML, Gustafson MP, Dickman P, Adams RH, Watanabe M, et al. Increased CTLA-4(+) T cells and an increased ratio of monocytes with loss of class II (CD14(+) HLA-DR(lo/neg)) found in aggressive pediatric sarcoma patients. J Immunother Cancer. 2015;3:35.

28. Dancsok AR, Gao D, Lee AF, Steigen SE, Blay JY, Thomas DM, et al. Tumor-associated macrophages and macrophage-related immune checkpoint expression in sarcomas. Oncoimmunology. 2020;9(1):1747340.

29. Berghuis D, Santos SJ, Baelde HJ, Taminiau AH, Egeler RM, Schilham MW, et al. Pro-inflammatory chemokine-chemokine receptor interactions within the Ewing sarcoma microenvironment determine CD8(+) T-lymphocyte infiltration and affect tumour progression. J Pathol. 2011;223(3):347-57.

30. Ogose A, Kawashima H, Hotta T, Ariizumi T, Yamagishi T, Oike N, et al. Frequent expression of human leukocyte antigen class I and the status of intratumoral immune cells in alveolar soft part sarcoma. Oncol Lett. 2017;13(4):2169-76.

31. Oike N, Kawashima H, Ogose A, Hotta T, Hatano H, Ariizumi T, et al. Prognostic impact of the tumor immune microenvironment in synovial sarcoma. Cancer Sci. 2018;109(10):3043-54.

32. Boxberg M, Steiger K, Lenze U, Rechl H, von Eisenhart-Rothe R, Wortler K, et al. PD-L1 and PD-1 and characterization of tumor-infiltrating lymphocytes in high grade sarcomas of soft tissue - prognostic implications and rationale for immunotherapy. Oncoimmunology. 2018;7(3):e1389366.

33. He M, Abro B, Kaushal M, Chen L, Chen T, Gondim M, et al. Tumor mutation burden and checkpoint immunotherapy markers in primary and metastatic synovial sarcoma. Hum Pathol. 2020;100:15-23.

34. Kostine M, Cleven AH, de Miranda NF, Italiano A, Cleton-Jansen AM, Bovee JV. Analysis of PD-L1, T-cell infiltrate and HLA expression in chondrosarcoma indicates potential for response to immunotherapy specifically in the dedifferentiated subtype. Mod Pathol. 2016;29(9):1028-37.

35. Pollack SM, He Q, Yearley JH, Emerson R, Vignali M, Zhang Y, et al. T-cell infiltration and clonality correlate with programmed cell death protein 1 and programmed death-ligand 1 expression in patients with soft tissue sarcomas. Cancer. 2017;123(17):3291-304.

36. Dancsok AR, Setsu N, Gao D, Blay JY, Thomas D, Maki RG, et al. Expression of lymphocyte immunoregulatory biomarkers in bone and soft-tissue sarcomas. Mod Pathol. 2019;32(12):1772-85.

37. Nowicki TS, Akiyama R, Huang RR, Shintaku IP, Wang X, Tumeh PC, et al. Infiltration of CD8 T Cells and Expression of PD-1 and PD-L1 in Synovial Sarcoma. Cancer Immunol Res. 2017;5(2):118-26.

38. Machado I, Lopez-Guerrero JA, Scotlandi K, Picci P, Llombart-Bosch A. Immunohistochemical analysis and prognostic significance of PD-L1, PD-1, and CD8+ tumor-infiltrating lymphocytes in Ewing's sarcoma family of tumors (ESFT). Virchows Arch. 2018;472(5):815-24.

39. Wilky BA, Trucco MM, Subhawong TK, Florou V, Park W, Kwon D, et al. Axitinib plus pembrolizumab in patients with advanced sarcomas including alveolar soft-part sarcoma: a single-centre, single-arm, phase 2 trial. Lancet Oncol. 2019;20(6):837-48.

40. Tseng WW, Malu S, Zhang M, Chen J, Sim GC, Wei W, et al. Analysis of the Intratumoral Adaptive Immune Response in Well Differentiated and Dedifferentiated Retroperitoneal Liposarcoma2015.

41. Tertiary lymphoid structures in the era of cancer immunotherapy, (2019).

42. Chen L, Oke T, Siegel N, Cojocaru G, Tam AJ, Blosser RL, et al. The Immunosuppressive Niche of Soft-Tissue Sarcomas is Sustained by Tumor-Associated Macrophages and Characterized by Intratumoral Tertiary Lymphoid Structures. Clin Cancer Res. 2020;26(15):4018-30.

43. Lazar AJ, Das P, Tuvin D, Korchin B, Zhu Q, Jin Z, et al. Angiogenesis-promoting gene patterns in alveolar soft part sarcoma. Clin Cancer Res. 2007;13(24):7314-21.

44. Balan M, Teran EMY, Waaga-Gasser AM, Gasser M, Choueiri TK, Freeman G, et al. Novel Roles of c-Met in the Survival of Renal Cancer Cells through the Regulation of HO-1 and PD-L1 Expression. J Biol Chem. 2015;290(13):8110-20.

45. McGrail DJ, Federico L, Li Y, Dai H, Lu Y, Mills GB, et al. Multi-omics analysis reveals neoantigen-independent immune cell infiltration in copy-number driven cancers. Nat Commun. 2018;9(1):1317.

46. Chudasama P, Mughal SS, Sanders MA, Hubschmann D, Chung I, Deeg KI, et al. Integrative genomic and transcriptomic analysis of leiomyosarcoma. Nat Commun. 2018;9(1):144.

47. Lewin J, Garg S, Lau BY, Dickson BC, Traub F, Gokgoz N, et al. Identifying actionable variants using next generation sequencing in patients with a historical diagnosis of undifferentiated pleomorphic sarcoma. Int J Cancer. 2018;142(1):57-65.

48. Ng KW, Marshall EA, Bell JC, Lam WL. cGAS-STING and Cancer: Dichotomous Roles in Tumor Immunity and Development. Trends Immunol. 2018;39(1):44-54.

49. Xia TL, Konno H, Barber GN. Recurrent Loss of STING Signaling in Melanoma Correlates with Susceptibility to Viral Oncolysis. Cancer Research. 2016;76(22):6747-59.

50. Wang D, Niu X, Wang Z, Song CL, Huang Z, Chen KN, et al. Multiregion Sequencing Reveals the Genetic Heterogeneity and Evolutionary History of Osteosarcoma and Matched Pulmonary Metastases. Cancer Res. 2019;79(1):7-20.

51. Sundara YT, Kostine M, Cleven AH, Bovee JV, Schilham MW, Cleton-Jansen AM. Increased PD-L1 and T-cell infiltration in the presence of HLA class I expression in metastatic high-grade osteosarcoma: a rationale for T-cell-based immunotherapy. Cancer Immunol Immunother. 2017;66(1):119-28.

52. Wu CC, Beird HC, Andrew Livingston J, Advani S, Mitra A, Cao S, et al. Immuno-genomic landscape of osteosarcoma. Nat Commun. 2020;11(1):1008.

53. Chen HM, Song YJ, Deng CZ, Xu YY, Xu HY, Zhu XJ, et al. Comprehensive analysis of immune infiltration and gene expression for predicting survival in patients with sarcomas. Aging-Us. 2021;13(2):2168-83.

54. Campbell BB, Light N, Fabrizio D, Zatzman M, Fuligni F, de Borja R, et al. Comprehensive Analysis of Hypermutation in Human Cancer. Cell. 2017;171(5):1042-56 e10.

55. The Angiosarcoma Project: enabling genomic and clinical discoveries in a rare cancer through patient-partnered research, (2020).

56. Cheung LS, Chen LL, Oke TF, Schaffer TB, Boudadi K, Ngo JT, et al. Anti-PD-1 elicits regression of undifferentiated pleomorphic sarcomas with UV-mutation signatures. Journal for Immunotherapy of Cancer. 2021;9(6).

57. Chan JY, Lim JQ, Yeong J, Ravi V, Guan P, Boot A, et al. Multiomic analysis and immunoprofiling reveal distinct subtypes of human angiosarcoma. J Clin Invest. 2020;130(11):5833-46.

58. Choi J, Manzano A, Dong WL, Bellone S, Bonazzoli E, Zammataro L, et al. Integrated mutational landscape analysis of uterine leiomyosarcomas. P Natl Acad Sci USA. 2021;118(15).

59. Yatsenko SA, Mittal P, Wood-Trageser MA, Jones MW, Surti U, Edwards RP, et al. Highly heterogeneous genomic landscape of uterine leiomyomas by whole exome sequencing and genome-wide arrays. Fertil Steril. 2017;107(2):457-+.

60. Manzoni M, Bolognesi MM, Antoranz A, Mancari R, Carinelli S, Faretta M, et al. The Adaptive and Innate Immune Cell Landscape of Uterine Leiomyosarcomas. Sci Rep. 2020;10(1):702.

61. Shi Y, Cai Q, Jiang Y, Huang G, Bi M, Wang B, et al. Activity and Safety of Geptanolimab (GB226) for Patients with Unresectable, Recurrent, or Metastatic Alveolar Soft Part Sarcoma: A Phase II, Single-arm Study. Clin Cancer Res. 2020;26(24):6445-52.

62. Simard FA, Richert I, Vandermoeten A, Decouvelaere AV, Michot JP, Caux C, et al. Description of the immune microenvironment of chondrosarcoma and contribution to progression. Oncoimmunology. 2017;6(2):e1265716.

63. Iseulys R, Anne GB, Corinne B, Gonzague DBP, Marie K, Jean-Yves B, et al. The immune landscape of chondrosarcoma reveals an immunosuppressive environment in the dedifferentiated subtypes and exposes CSFR1+ macrophages as a promising therapeutic target. J Bone Oncol. 2020;20:100271.

64. Kim JR, Moon YJ, Kwon KS, Bae JS, Wagle S, Kim KM, et al. Tumor infiltrating PD1-positive lymphocytes and the expression of PD-L1 predict poor prognosis of soft tissue sarcomas. PLoS One. 2013;8(12):e82870.

65. Vargas AC, Maclean FM, Sioson L, Tran D, Bonar F, Mahar A, et al. Prevalence of PD-L1 expression in matched recurrent and/or metastatic sarcoma samples and in a range of selected sarcomas subtypes. PLoS One. 2020;15(4):e0222551.

66. van Erp AEM, Versleijen-Jonkers YMH, Hillebrandt-Roeffen MHS, van Houdt L, Gorris MAJ, van Dam LS, et al. Expression and clinical association of programmed cell death-1, programmed death-ligand-1 and CD8(+) lymphocytes in primary sarcomas is subtype dependent. Oncotarget. 2017;8(41):71371-84.

67. Handl M, Hermanova M, Hotarkova S, Jarkovsky J, Mudry P, Shatokhina T, et al. Clinicopathological correlation of tumor-associated macrophages in Ewing sarcoma. Biomed Pap Med Fac Univ Palacky Olomouc Czech Repub. 2018;162(1):54-60.

68. Dridi M, Krebs-Drouot L, Meyronet D, Dumollard JM, Vassal F, Jouanneau E, et al. The Immune Microenvironment of Chordomas: An Immunohistochemical Analysis. Cancers (Basel). 2021;13(13).

69. Zou MX, Lv GH, Wang XB, Huang W, Li J, Jiang Y, et al. Clinical Impact of the Immune Microenvironment in Spinal Chordoma: Immunoscore as an Independent Favorable Prognostic Factor. Neurosurgery. 2019;84(6):E318-E33.

70. Zou MX, Pan Y, Huang W, Zhang TL, Escobar D, Wang XB, et al. A four-factor immune risk score signature predicts the clinical outcome of patients with spinal chordoma. Clin Transl Med. 2020;10(1):224-37.

71. Smolle MA, Herbsthofer L, Goda M, Granegger B, Brcic I, Bergovec M, et al. Influence of tumor-infiltrating immune cells on local control rate, distant metastasis, and survival in patients with soft tissue sarcoma. Oncoimmunology. 2021;10(1):1896658.

72. Wunder JS, Lee MJ, Nam J, Lau BY, Dickson BC, Pinnaduwage D, et al. Osteosarcoma and soft-tissue sarcomas with an immune infiltrate express PD-L1: relation to clinical outcome and Th1 pathway activation. Oncoimmunology. 2020;9(1):1737385.

73. Koirala P, Roth ME, Gill J, Piperdi S, Chinai JM, Geller DS, et al. Immune infiltration and PD-L1 expression in the tumor microenvironment are prognostic in osteosarcoma. Sci Rep. 2016;6:30093.

74. Palmerini E, Agostinelli C, Picci P, Pileri S, Marafioti T, Lollini PL, et al. Tumoral immune-infiltrate (IF), PD-L1 expression and role of CD8/TIA-1 lymphocytes in localized osteosarcoma patients treated within protocol ISG-OS1. Oncotarget. 2017;8(67):111836-46.

75. Zheng B, Ren T, Huang Y, Guo W. Apatinib inhibits migration and invasion as well as PD-L1 expression in osteosarcoma by targeting STAT3. Biochem Biophys Res Commun. 2018;495(2):1695-701.

76. Kostine M, Briaire-de Bruijn IH, Cleven AHG, Vervat C, Corver WE, Schilham MW, et al. Increased infiltration of M2-macrophages, T-cells and PD-L1 expression in high grade leiomyosarcomas supports immunotherapeutic strategies. Oncoimmunology. 2018;7(2):e1386828.

77. Keung EZ, Tsai JW, Ali AM, Cormier JN, Bishop AJ, Guadagnolo BA, et al. Analysis of the immune infiltrate in undifferentiated pleomorphic sarcoma of the extremity and trunk in response to radiotherapy: Rationale for combination neoadjuvant immune checkpoint inhibition and radiotherapy. Oncoimmunology. 2018;7(2):e1385689.

78. Toulmonde M, Lucchesi C, Verbeke S, Crombe A, Adam J, Geneste D, et al. High throughput profiling of undifferentiated pleomorphic sarcomas identifies two main subgroups with distinct immune profile, clinical outcome and sensitivity to targeted therapies. EBioMedicine. 2020;62:103131.

79. Shanes ED, Friedman LA, Mills AM. PD-L1 Expression and Tumor-infiltrating Lymphocytes in Uterine Smooth Muscle Tumors: Implications for Immunotherapy. Am J Surg Pathol. 2019;43(6):792-801.

80. Karpathiou G, Dumollard JM, Dridi M, Dal Col P, Barral FG, Boutonnat J, et al. Chordomas: A review with emphasis on their pathophysiology, pathology, molecular biology, and genetics. Pathol Res Pract. 2020;216(9).

81. Patel SS, Nota SP, Sabbatino F, Nielsen GP, Deshpande V, Wang X, et al. Defective HLA Class I Expression and Patterns of Lymphocyte Infiltration in Chordoma Tumors. Clin Orthop Relat Res. 2021;479(6):1373-82.

82. Bai J, Shi J, Li C, Wang S, Zhang T, Hua X, et al. Whole genome sequencing of skull-base chordoma reveals genomic alterations associated with recurrence and chordoma-specific survival. Nat Commun. 2021;12(1):757.

83. Tarpey PS, Behjati S, Young MD, Martincorena I, Alexandrov LB, Farndon SJ, et al. The driver landscape of sporadic chordoma. Nat Commun. 2017;8(1):890.

84. Chakiryan NH, Hajiran A, Kim Y, Aydin AM, Zemp L, Katende E, et al. Correlating Immune Cell Infiltration Patterns with Recurrent Somatic Mutations in Advanced Clear Cell Renal Cell Carcinoma br. Eur Urol Focus. 2022;8(3):784-93.

85. Miao D, Margolis CA, Gao W, Voss MH, Li W, Martini DJ, et al. Genomic correlates of response to immune checkpoint therapies in clear cell renal cell carcinoma. Science. 2018;359(6377):801-6.

86. Yang QA, Shen R, Xu HL, Shi XL, Xu LL, Zhang L, et al. Comprehensive analyses of PBRM1 in multiple cancer types and its association with clinical response to immunotherapy and immune infiltrates. Ann Transl Med. 2021;9(6).

87. van den Bulk J, Verdegaal EME, de Miranda NFCC. Cancer immunotherapy: broadening the scope of targetable tumours. Open Biol. 2018;8(6).

88. Chew HY, Chan V, Simpson F, Dolcetti R. Will Next-Generation Immunotherapy Overcome the Intrinsic Diversity and Low Immunogenicity of Sarcomas to Improve Clinical Benefit? Cancers. 2020;12(11).

89. Chalmers ZR, Connelly CF, Fabrizio D, Gay L, Ali SM, Ennis R, et al. Analysis of 100,000 human cancer genomes reveals the landscape of tumor mutational burden. Genome Medicine. 2017;9.

90. D'Angelo SP, Shoushtari AN, Agaram NP, Kuk D, Qin LX, Carvajal RD, et al. Prevalence of tumor-infiltrating lymphocytes and PD-L1 expression in the soft tissue sarcoma microenvironment. Human Pathology. 2015;46(3):357-65.

91. Lam SW, Kostine M, de Miranda N, Schoffski P, Lee CJ, Morreau H, et al. Mismatch repair deficiency is rare in bone and soft tissue tumors. Histopathology. 2021.

92. Lewin J, Davidson S, Anderson ND, Lau BY, Kelly J, Tabori U, et al. Response to Immune Checkpoint Inhibition in Two Patients with Alveolar Soft-Part Sarcoma. Cancer Immunol Res. 2018;6(9):1001-7.

93. Modi MB, Patel PN, Modi VM, Mehta SP, Nilkanthe RG, Patel PH, et al. First reported case of alveolar soft part sarcoma in constitutional mismatch repair deficiency syndrome tumor spectrum - diagnosed in one of the siblings with constitutional mismatch repair deficiency. South Asian J Cancer. 2017;6(1):41-3.

94. Tawbi HA, Burgess M, Bolejack V, Van Tine BA, Schuetze SM, Hu J, et al. Pembrolizumab in advanced soft-tissue sarcoma and bone sarcoma (SARC028): a multicentre, two-cohort, single-arm, open-label, phase 2 trial. Lancet Oncol. 2017;18(11):1493-501.

95. Wu XL, Lin XW, Chen Y, Kong WC, Xu JH, Yu ZY. Response of Metastatic Chordoma to the Immune Checkpoint Inhibitor Pembrolizumab: A Case Report. Frontiers in Oncology. 2020;10.

96. Doyle LA, Nowak JA, Nathenson MJ, Thornton K, Wagner AJ, Johnson JM, et al. Characteristics of mismatch repair deficiency in sarcomas. Mod Pathol. 2019;32(7):977-87.

97. Boichard A, Wagner MJ, Kurzrock R. Angiosarcoma heterogeneity and potential therapeutic vulnerability to immune checkpoint blockade: insights from genomic sequencing. Genome Med. 2020;12(1):61.

98. Luo Y, Li M, Zhou Y, Tang F, Lu MX, Xie HM, et al. Remarkable response to anti-PD1 immunotherapy in refractory metastatic high-grade myxofibrosarcoma patient A case report. Medicine. 2021;100(12).

99. Lazar AJ, McLellan MD, Bailey MH, Miller CA, Appelbaum EL, Cordes MG, et al. Comprehensive and Integrated Genomic Characterization of Adult Soft Tissue Sarcomas. Cell. 2017;171(4):950-+.

100. D'Angelo SP, Mahoney MR, Van Tine BA, Atkins J, Milhem MM, Jahagirdar BN, et al. Nivolumab with or without ipilimumab treatment for metastatic sarcoma (Alliance A091401): two open-label, non-comparative, randomised, phase 2 trials. Lancet Oncol. 2018;19(3):416-26.

101. Tsimberidou AM, Van Morris K, Vo HH, Eck S, Lin YF, Rivas JM, et al. T-cell receptor-based therapy: an innovative therapeutic approach for solid tumors. J Hematol Oncol. 2021;14(1).

102. Dallos M, Tap WD, D'Angelo SP. Current status of engineered T-cell therapy for synovial sarcoma. Immunotherapy. 2016;8(9):1073-80.

103. Endo M, de Graaff MA, Ingram DR, Lim S, Lev DC, Briaire-de Bruijn IH, et al. NY-ESO-1 (CTAG1B) expression in mesenchymal tumors. Mod Pathol. 2015;28(4):587-95.

104. Ramachandran I, Lowther DE, Dryer-Minnerly R, Wang R, Fayngerts S, Nunez D, et al. Systemic and local immunity following adoptive transfer of NY-ESO-1 SPEAR T cells in synovial sarcoma. J Immunother Cancer. 2019;7(1):276.

105. Luk SJ, van der Steen DM, Hagedoorn RS, Jordanova ES, Schilham MW, Bovee JV, et al. PRAME and HLA Class I expression patterns make synovial sarcoma a suitable target for PRAME specific T-cell receptor gene therapy. Oncoimmunology. 2018;7(12):e1507600.

106. Melief CJM, van Hall T, Arens R, Ossendorp F, van der Burg SH. Therapeutic cancer vaccines. Journal of Clinical Investigation. 2015;125(9):3401-12.

107. Sahin U, Türeci Ö. Personalized vaccines for cancer immunotherapy. Science. 2018;359(6382):1355-60.

108. Albershardt TC, Campbell DJ, Parsons AJ, Slough MM, ter Meulen J, Berglund P. LV305, a dendritic cell-targeting integration-deficient ZVex™-based lentiviral vector encoding NY-ESO-1, induces potent anti-tumor immune response. Mol Ther-Oncolytics. 2016;3.

109. Pollack SM. The potential of the CMB305 vaccine regimen to target NY-ESO-1 and improve outcomes for synovial sarcoma and myxoid/round cell liposarcoma patients. Expert Rev Vaccines. 2018;17(2):107-14.

110. Chawla SP, Van Tine BA, Pollack SM, Ganjoo KN, Elias AD, Riedel RF, et al. Phase II Randomized Study of CMB305 and Atezolizumab Compared With Atezolizumab Alone in Soft-Tissue Sarcomas Expressing NY-ESO-1. J Clin Oncol. 2022;40(12):1291-+.

111. Miwa S, Nishida H, Tanzawa Y, Takeuchi A, Hayashi K, Yamamoto N, et al. Phase 1/2 study of immunotherapy with dendritic cells pulsed with autologous tumor lysate in patients with refractory bone and soft tissue sarcoma. Cancer. 2017;123(9):1576-84.

112. DeMaria PJ, Bilusic M, Park DM, Heery CR, Donahue RN, Madan RA, et al. Randomized, Double-Blind, Placebo-Controlled Phase II Study of Yeast-Brachyury Vaccine (GI-6301) in Combination with Standard-of-Care Radiotherapy in Locally Advanced, Unresectable Chordoma. Oncologist. 2021;26(5):e847-e58.

113. Deng C, Xu Y, Fu J, Zhu X, Chen H, Xu H, et al. Reprograming the tumor immunologic microenvironment using neoadjuvant chemotherapy in osteosarcoma. Cancer Sci. 2020;111(6):1899-909.

114. Toulmonde M, Penel N, Adam J, Chevreau C, Blay JY, Le Cesne A, et al. Use of PD-1 Targeting, Macrophage Infiltration, and IDO Pathway Activation in Sarcomas: A Phase 2 Clinical Trial. JAMA Oncol. 2018;4(1):93-7.

115. Prendergast GC, Malachowski WJ, Mondal A, Scherle P, Muller AJ. Indoleamine 2,3-Dioxygenase and Its Therapeutic Inhibition in Cancer. Int Rev Cel Mol Bio. 2018;336:175-203.

116. Yum S, Li MH, Chen ZJJ. Old dogs, new trick: classic cancer therapies activate cGAS. Cell Res. 2020;30(8):639-48.

117. Lhuillier C, Rudqvist NP, Elemento O, Formenti SC, Demaria S. Radiation therapy and anti-tumor immunity: exposing immunogenic mutations to the immune system. Genome Med. 2019;11(1):40.

118. Zhang S, Kohli K, Black RG, Yao L, Spadinger SM, He Q, et al. Systemic Interferon-gamma Increases MHC Class I Expression and T-cell Infiltration in Cold Tumors: Results of a Phase 0 Clinical Trial. Cancer Immunol Res. 2019;7(8):1237-43.

119. Sarcomas: Immune biomarker expression and checkpoint inhibitor trials, (2020).

120. Klaver Y, Rijnders M, Oostvogels A, Wijers R, Smid M, Grunhagen D, et al. Differential quantities of immune checkpoint-expressing CD8 T cells in soft tissue sarcoma subtypes. J Immunother Cancer. 2020;8(2):271.

121. Zhou Y, Yang D, Yang Q, Lv X, Huang W, Zhou Z, et al. Single-cell RNA landscape of intratumoral heterogeneity and immunosuppressive microenvironment in advanced osteosarcoma. Nat Commun. 2020;11(1):6322.

122. Ascierto PA, Bono P, Bhatia S, Melero I, Nyakas MS, Svane IM, et al. Efficacy of BMS-986016, a monoclonal antibody that targets lymphocyte activation gene-3 (LAG-3), in combination with nivolumab in pts with melanoma who progressed during prior anti-PD-1/PD-L1 therapy (mel prior IO) in all-comer and biomarker-enriched populations. Annals of Oncology. 2017;28.

123. Logtenberg MEW, Scheeren FA, Schumacher TN. The CD47-SIRPα Immune Checkpoint. Immunity. 2020;52(5):742-52.

124. Stanley ER, Chitu V. CSF-1 Receptor Signaling in Myeloid Cells. Csh Perspect Biol. 2014;6(6).

125. Gomez-Brouchet A, Gilhodes J, Acker NV, Brion R, Bouvier C, Assemat P, et al. Characterization of Macrophages and Osteoclasts in the Osteosarcoma Tumor Microenvironment at Diagnosis: New Perspective for Osteosarcoma Treatment? Cancers (Basel). 2021;13(3):1-19.

126. Espinosa I, Beck AH, Lee CH, Zhu S, Montgomery KD, Marinelli RJ, et al. Coordinate Expression of Colony-Stimulating Factor-1 and Colony-Stimulating Factor-1-Related Proteins Is Associated with Poor Prognosis in Gynecological and Nongynecological Leiomyosarcoma. Am J Pathol. 2009;174(6):2347-56.

127. Song YJ, Xu Y, Zhu X, Fu J, Deng C, Chen H, et al. Immune Landscape of the Tumor Microenvironment Identifies Prognostic Gene Signature CD4/CD68/CSF1R in Osteosarcoma. Front Oncol. 2020;10:1198.

128. Buddingh EP, Kuijjer ML, Duim RAJ, Bürger H, Agelopoulos K, Myklebost O, et al. Tumor-Infiltrating Macrophages Are Associated with Metastasis Suppression in High-Grade Osteosarcoma: A Rationale for Treatment with Macrophage Activating Agents. Clinical Cancer Research. 2011;17(8):2110-9.

129. Fujiwara T, Yakoub MA, Chandler A, Christ AB, Yang GL, Ouerfelli O, et al. CSF1/CSF1R Signaling Inhibitor Pexidartinib (PLX3397) Reprograms Tumor-Associated Macrophages and Stimulates T-cell Infiltration in the Sarcoma Microenvironment. Mol Cancer Ther. 2021;20(8):1388-99.

130. Querfeld C, Thompson JA, Taylor M, Pillai R, Johnson LDS, Catalano T, et al. Intralesional Injection of the CD47-blocking immune checkpoint inhibitor TTI-621 (SIRPaFc) induces antitumor activity in patients with relapsed/refractory mycosis fungoides and Sezary syndrome: Interim results of a multicenter Phase 1 trial. Eur J Cancer. 2018;101:S34-S.

131. Chimeric antigen receptor T (CAR-T) cell immunotherapy for sarcomas: From mechanisms to potential clinical applications, (2020).

132. June CH, O'Connor RS, Kawalekar OU, Ghassemi S, Milone MC. CAR T cell immunotherapy for human cancer. Science. 2018;359(6382):1361-5.

133. Chulanetra M, Morchang A, Sayour E, Eldjerou L, Milner R, Lagmay J, et al. GD2 chimeric antigen receptor modified T cells in synergy with sub-toxic level of doxorubicin targeting osteosarcomas. Am J Cancer Res. 2020;10(2):674-+.

134. Majzner RG, Theruvath JL, Nellan A, Heitzeneder S, Cui Y, Mount CW, et al. CAR T Cells Targeting B7-H3, a Pan-Cancer Antigen, Demonstrate Potent Preclinical Activity Against Pediatric Solid Tumors and Brain Tumors. Clin Cancer Res. 2019;25(8):2560-74.

135. Hegde M, DeRenzo CC, Zhang HM, Mata M, Gerken C, Shree A, et al. Expansion of HER2-CAR T cells after lymphodepletion and clinical responses in patients with advanced sarcoma. J Clin Oncol. 2017;35:10508-.

136. Marofi F, Motavalli R, Safonov VA, Thangavelu L, Yumashev AV, Alexander M, et al. CAR T cells in solid tumors: challenges and opportunities. Stem Cell Res Ther. 2021;12(1).

137. Long AH, Highfill SL, Cui Y, Smith JP, Walker AJ, Ramakrishna S, et al. Reduction of MDSCs with All-trans Retinoic Acid Improves CAR Therapy Efficacy for Sarcomas. Cancer Immunol Res. 2016;4(10):869-80.

138. Li S, Siriwon N, Zhang X, Yang S, Jin T, He F, et al. Enhanced Cancer Immunotherapy by Chimeric Antigen Receptor-Modified T Cells Engineered to Secrete Checkpoint Inhibitors. Clin Cancer Res. 2017;23(22):6982-92.

139. Yang W, Lee KW, Srivastava RM, Kuo FS, Krishna C, Chowell D, et al. Immunogenic neoantigens derived from gene fusions stimulate T cell responses. Nat Med. 2019;25(5):767-+.

140. Worley BS, van den Broeke LT, Goletz TJ, Pendleton CD, Daschbach EM, Thomas EK, et al. Antigenicity of fusion proteins from sarcoma-associated chromosomal translocations. Cancer Research. 2001;61(18):6868-75.

141. Kawaguchi S, Wada T, Ida K, Sato Y, Nagoya S, Tsukahara T, et al. Phase I vaccination trial of SYT-SSX junction peptide in patients with disseminated synovial sarcoma. J Transl Med. 2005;3(1):1.

142. Kawaguchi S, Tsukahara T, Ida K, Kimura S, Murase M, Kano M, et al. SYT-SSX breakpoint peptide vaccines in patients with synovial sarcoma: a study from the Japanese Musculoskeletal Oncology Group. Cancer Sci. 2012;103(9):1625-30.

143. Suehara Y, Kohsaka S, Hayashi T, Akaike K, Kurisaki-Arakawa A, Sato S, et al. Identification of a Novel MAN1A1-ROS1 Fusion Gene Through mRNA-based Screening for Tyrosine Kinase Gene Aberrations in a Patient with Leiomyosarcoma. Clin Orthop Relat Res. 2021;479(4):838-52.

144. Hirose K, Usami Y, Kohara M, Sato S, Iwamoto Y, Murakami S, et al. Clear Cell Carcinoma of Palatal Minor Salivary Gland Harboring a Novel EWSR1-ATF1 Fusion Gene: Report of a Case and Review of the Literature. Head Neck Pathol. 2021;15(2):676-81.

145. Lin DI, Hemmerich A, Edgerly C, Duncan D, Severson EA, Huang RSP, et al. Genomic profiling of BCOR-rearranged uterine sarcomas reveals novel gene fusion partners, frequent CDK4 amplification and CDKN2A loss. Gynecol Oncol. 2020;157(2):357-66.



3

Divergent therapeutic and prognostic impacts of immunogenic features in undifferentiated pleomorphic sarcoma and myxofibrosarcoma

Siddh van Oost, Debora M. Meijer, Zeynep B. Erdem, Marieke E. IJsselsteijn, Jessica Roelands, Suk Wai Lam, Melissa S. Boejharat, Brendy E.W.M. van den Akker, Ruud van der Breggen, Inge H. Briaire-de Bruijn, Lukas J.A.C. Hawinkels, Anouk A. Kruiswijk, Manon van der Ploeg, Pauline M. Wijers-Koster, Rick L. Haas, Michiel A.J. van den Sande, Noel F.C.C. de Miranda, and Judith V.M.G. Bovée

Cancer Immunology, Immunotherapy **2025, 74(8): 258**

ABSTRACT

Undifferentiated pleomorphic sarcoma (UPS) and myxofibrosarcoma (MFS) are genetically complex soft tissue sarcomas with distinct morphological features. Treatment typically involves surgery, often combined with neoadjuvant chemo- or radiotherapy. To better understand the immunobiology of these sarcomas and its associations with treatment response and prognosis, we performed transcriptomic and immunophenotypic profiling.

RNA sequencing was performed on 13 UPS and 10 MFS and immunological profiles were compared with soft tissue sarcoma data from The Cancer Genome Atlas (*n* = 206 including 44 UPS and 17 MFS). Immune contextures were further evaluated in 14 UPS and 15 MFS using imaging mass cytometry. Characterization of T cell and macrophage infiltration in tumors was further assessed in 23 UPS and 22 MFS through multispectral immunofluorescence and immunohistochemical analysis.

UPS and MFS demonstrated immunogenic features compared to other soft tissue sarcomas, with subsets of UPS and MFS demonstrating high T cell infiltration while UPS demonstrated a higher infiltration by myeloid cells as compared to MFS. Prognostically, T cells and $CD68^{+}CD163^{+}$ macrophages were associated with metastasis-free survival in UPS but not in MFS. Notably, in UPS, neoadjuvant radiotherapy appeared to induce cytotoxic T cell infiltration and depletion of myeloid cells, whereas these effects were not observed in MFS.

These findings highlight important differences in the immunobiology of UPS and MFS with therapeutic and prognostic implications. These differences should be taken into account given the growing availability of immunotherapeutic options for treating patients with soft tissue sarcomas.

INTRODUCTION

Soft tissue sarcomas (STS) are a rare and diverse group of malignant mesenchymal neoplasms that predominantly arise in the extremities or trunk. Undifferentiated pleomorphic sarcoma (UPS) and myxofibrosarcoma (MFS) are two subtypes distinguished by their morphological features and lack of specific line of differentiation. UPS (also known as undifferentiated soft tissue sarcoma) present exclusively as intermediate- or high-grade deep-seated tumors, while MFS encompass a spectrum of low- to high-grade tumors and can occur either superficially or deep-seated (1). Localized disease is typically treated with surgery, often complemented by (neo-)adjuvant radiotherapy depending on tumor size, grade, and anatomical location (2). However, clinical outcomes remain poor, with approximately 15-45% of patients experiencing local recurrence or distant metastases (3-5). As options for systemic therapy in recurrent disease are limited, improving clinical management through the development of novel therapeutic approaches is crucial.

Genomically, UPS and MFS present complex and heterogeneous profiles characterized by extensive chromosomal alterations and few recurrent mutation targets (e.g., *TP53*, *RB1, CDKN2A, ATRX*) (6, 7). Additionally, these tumors display similar transcriptional and epigenetic profiles when compared to other STS (6-9). Despite these overlaps, their clinical behavior differs considerably: UPS is more prone to metastasize, with distinct responses to neoadjuvant therapy, whereas MFS show a higher propensity for local recurrence, suggesting underlying biological differences (3, 10). The contribution of the immune microenvironment to these differing outcomes remains unclear.

To address this, we characterized the immune microenvironment of UPS and MFS using transcriptomic and immunophenotypic profiling. Immune-related transcriptional profiles were compared with STS from The Cancer Genome Atlas (TCGA) and immune cell populations were associated with metastasis-free and disease-specific survival. Moreover, the effect of radiotherapy on the immune microenvironment was explored. Our study underscores distinct immunobiological features between UPS and MFS, with potential implications for developing tailored therapeutic strategies

METHODS

Patient samples

Formalin-fixed paraffin embedded (FFPE) and snap-frozen material was collected for 16 UPS and 17 MFS patients diagnosed between 2008 and 2021. This discovery cohort comprised high- and low-grade MFS, with patients receiving surgery alone, post-operative radiotherapy or pre-operative radiotherapy. Subsequently, the cohort was expanded to include FFPE biopsy samples from an additional 14 UPS and 16 MFS patients diagnosed between 2011 and 2023. These cases were exclusively high-grade tumors that underwent neoadjuvant radiotherapy.

For imaging mass cytometry (IMC), regions representative of the tumor's immune microenvironment were identified on hematoxylin and eosin (H&E)-stained sections of FFPE tissue by a soft tissue tumor pathologist (JVMGB). Tissue microarrays (TMAs) were then constructed using a TMA Master (3DHISTECH). Each resection contributed four cores (1.6 mm in diameter), with two central and two peripheral cores, while biopsies provided two cores. For immunohistochemistry (IHC)/immunofluorescence (IF), FFPE blocks of biopsies with sufficient tumor tissue were selected for whole slide imaging. Pathological response to radiotherapy was assessed by two soft tissue tumor pathologists (JVMGB & SWL), who defined the modified EORTC response score including percentage of necrosis, hyalinization/fibrosis and viable tumor adding up to 100% of tumor volume (11, 12).

RNA sequencing

RNA sample processing and sequencing were performed as previously described on treatment-naïve tumors from 13 UPS and 10 MFS (13). In short, RNA was extracted from snap-frozen tissues using TRIzol and isopropanol/ethanol, followed by purification with the RNeasy kit, including DNase treatment. Paired-end 150 base pair (bp) reads were generated on a NovaSeq6000 Illumina at GenomeScan (Leiden, The Netherlands). Sequencing data were processed with the RNA-seq BioWDL pipeline from the Sequencing Analysis Support Core (**https://biowdl.github.io/**, LUMC, The Netherlands). Reads were aligned to the hg38 reference genome using STAR and gene expression was quantified using HTSeq-count (14). The processed data were stored as a matrix containing gene counts per sample.

Integration with TCGA-STS dataset

RNA sequencing (RNAseq) data from 206 revised cases of primary STS from TCGA (6) were downloaded and processed using TCGA Assembler (R, v.2.0.3). This dataset included UPS (*n* = 44), MFS (*n* = 17; including 3 low-grade), dedifferentiated liposarcomas (*n* = 50), soft tissue leiomyosarcomas (*n* = 53; including 11 low-grade), uterine leiomyosarcomas (*n* = 27; including 1 low-grade), malignant peripheral nerve sheath tumors (*n* = 5), and synovial sarcomas (*n* = 10). Gene symbols were converted to HGNC gene symbols and Entrez Gene identifiers using biomaRt (R, v.2.60). The dataset was filtered for overlapping genes with our own RNAseq dataset, referred to as the Leiden Center for Computational Oncology (LCCO) dataset, using Entrez Gene identifiers. Since TCGA data was in transcripts per million (TPM), the processed RNAseq counts from the LCCO cohort were converted to TPM with IOBR (R, v.0.99.8), which also removed genes without HGNC symbols. The LCCO and TCGA datasets were then merged based on HGNC symbols. Normalization was performed within lanes and between lanes by using EDASeq (R, v.2.38), after which the data was quantile normalized with preprocessCore (v.1.66.0) and log2 transformed.

Gene expression analysis

Batch correction was performed with limma (R, v.3.60.0) to compare immune-related gene expression between our dataset and TCGA dataset. As described previously, the immunologic constant of rejection (ICR) gene signature was utilized to characterize the Th1-like inflammatory state of the STS microenvironment (15, 16). Additionally, immunological composition was evaluated with MCPcounter (R, v.1.2.0), which clusters samples into previously established Sarcoma Immune Classes (SIC) by using TCGA-STS data (17). Z-scores were calculated per gene/cell population to visualize the immune-related transcriptional signatures using ComplexHeatmap (R, v.2.20.0). The attributed clusters were visualized per subtype, per dataset in bar plots with ggplot2 (R, v.3.5.1).

Imaging mass cytometry

The conjugation of BSA-free antibodies and immunodetection using a 40-marker panel that provides an overall description of the immune cell composition (**Supplementary Table 1**) were carried out as previously described (13, 18). Briefly, four-µm sections of the generated TMAs were deparaffinized, rehydrated and subjected to heat-induced antigen retrieval in a low pH antigen retrieval solution (pH 6, Thermo Fisher Scientific). The first set

of primary antibodies was incubated overnight at 4 °C. Following washes with PBS supplemented with 1% BSA and 0.05% Tween, sections were incubated with conjugated anti-mouse (Abcam, ab6708) and anti-rabbit (Abcam, ab6701) antibodies for one hour at room temperature. Next, the second batch of primary antibodies was applied for five hours at room temperature, followed by an overnight incubation at 4 °C with the final antibody batch. Finally, DNA was stained using 1.25 µM Cell-ID™ Intercalator-Ir (Standard BioTools) for five minutes. ROIs of 1000 x 1000 µm were ablated with a Hyperion mass cytometry imaging system (Standard BioTools) at the Flow Core Facility (LUMC, Leiden). Imaging data was acquired with CyTOF Software (v.7.0) and exported using MCD Viewer (v.1.0.5).

Imaging mass cytometry analysis

Analysis of the IMC data was performed as described previously (13, 19). In short, images were normalized in Matlab (v.R2021a) and binarized in Ilastik (v.1.3.3). Probability masks were generated in Ilastik and used for cell segmentation in CellProfiler (v.2.2.0). Single cell-FCS files were generated in ImaCyte (20) and utilized for phenotyping in CytoSplore (v.2.3.1). Mean cell density per mm^2 was calculated for every sample. Lineage markers used for phenotyping are shown in **Supplementary Table 2**. The relative abundance of phenotypes was calculated using the total number of cells per sample and visualized using ComplexHeatmap (R, v.2.20.0).

Multispectral immunofluorescent imaging

A T cell Opal panel comprising four markers was developed for IF imaging of pre-treatment biopsies using a Vectra system (Akoya Biosciences) as described previously (13, 21). The panel included anti-PD-1 (D4W2J, 1:250, Cell Signaling Technology, #86163), anti-CD8α (D8A8Y, 1:500, Cell Signaling Technology, #85336), anti-CD3ε (EP449E, 1:1000, Abcam, ab52959) and anti-CD4 (EPR6855, 1:2000, Abcam, ab133616) antibodies. Each antibody was paired with a specific Opal fluorophore in an optimized staining sequence to maximize intensity and specificity: CD8-Opal 690 (1:100), CD4-Opal 570 (1:400), PD-1-Opal 620 (1:100), and CD3-Opal 520 (1:400). Endogenous peroxidase was blocked with 0.3% hydrogen peroxide in methanol, antigen retrieval was performed with citrate buffer (pH 6.0) and tissue was blocked with SuperBlock™ Blocking Buffer (ThermoFisher Scientific). Slides were incubated with a primary antibody for one hour at room temperature, washed with PBS-Tween (0.05%,) and incubated with BrightVision DPVO-HRP (Immunologic) for 10 minutes. After washing, the first Opal reagent (Akoya Bioscience), diluted in Opal amplification diluent,

was applied for 10 minutes. Slides were then heated in citrate buffer (pH 6.0) for 15 minutes at a reduced wattage and washed with PBS-Tween. This process was repeated for the remaining antibodies. Finally, slides were incubated with DAPI (1:1000) for five minutes and mounted with ProLong™ Gold Antifade Mountant (ThermoFisher Scientific). Up to five ROIs per slide were selected based on consecutive hematoxylin and eosin-stained slides and imaged at 20x magnification. Image processing was performed using inForm (v.2.4) and analyzed with QuPath (v.0.3.1). Due to nonspecific staining, CD4 was excluded from the analysis. T cells ($CD3^+$) were classified as $CD8^+$ or $CD8^-$, and further categorized based on PD-1 expression ($PD\text{-}1^+$ or $PD\text{-}1^-$). Cell counts per image (1.5 mm x 2 mm) were normalized per patient as counts per mm^2 tissue.

Double immunohistochemical detection

Double IHC was performed to identify macrophages in pre-treatment biopsies using the ImmPRESS Duet Double Staining Polymer Kit (HRP Anti-Mouse IgG-brown, AP Anti-Rabbit IgG-magenta, Vector Laboratories, MP-7724-15). Anti-CD163 (10D6, Mouse, 1:400, MONOSAN, MONX10445) and anti-CD68 (D4B9C, Rabbit, 1:3200, Cell Signaling Technology, #76437) antibodies were applied on the same slide following the manufacturer's protocol. Slides were scanned using a Pannoramic™ 480 (3D HISTECH) slide scanner and analyzed with QuPath. Macrophages were identified using the optical density sum for cell detection, thereby excluding most $CD68^+$ and/or $CD163^+$ tumor cells. The same ROIs were selected as for the T cell imaging, and macrophage counts per ROI were normalized to counts per mm^2 tissue. A detailed description of the used workflow in QuPath is presented as **Supplementary Methods**.

Statistical analyses

To associate the immune microenvironment with clinical outcome in the validation cohort, patients were stratified as T cell high or T cell low based on the median total T cell count per sarcoma subtype. The same was done based on the $CD68^+CD163^-$ macrophage density and $CD68^+CD163^+$ macrophage density. To correlate T cell infiltration with $CD68^+CD163^+$ macrophage infiltration, a heatmap was generated using the mean cell densities per mm^2 from the IF and double IHC analyses. Furthermore, the T cell to macrophage ratio was calculated by dividing the total T cell density by the $CD68^+CD163^+$ macrophage density per sample, as identified by IF and double IHC, respectively. For survival analysis, patients were stratified as high or low based on the median T cell-to-macrophage ratio.

Kaplan-Meier survival curves were generated using the survminer (R, v.0.4.9) and survival (R, v3.6-4) packages in R. Disease-specific survival was defined as the time until death due to the disease. Given the high number of censored cases in the cohort, statistical significance was assessed using the log-rank *P* value. Univariate and multivariate Cox proportional hazards analyses were conducted in R, with only variables found significant in the univariate analysis included in the multivariate model.

RESULTS

Clinicopathological characteristics are prognostic in MFS, but not in UPS

In this study, a total of 63 patients were enrolled, including 30 individuals diagnosed with UPS and 33 with MFS. Initially, we performed RNAseq and/or IMC on treatment-naïve samples from 16 UPS (all pre-surgical biopsies) and 17 MFS (comprising 9 pre-surgical biopsies and 8 resections) to characterize the immunological landscape of these tumors. Findings were validated using IF and IHC in an extended cohort of treatment-naïve cases, consisting of 23 UPS and 22 high-grade MFS (all pre-surgical biopsies), which partly overlapped with the discovery cohort (9 UPS and 6 MFS), and was also used to investigate associations with clinical outcomes. In addition, to assess the impact of neoadjuvant radiotherapy, we analyzed surgical resection specimens from 13 UPS and 8 MFS cases that underwent treatment, matched to their respective biopsies from the discovery cohort, using IMC. Clinicopathological data for both cohorts are summarized in **Table 1**.

To investigate associations between clinicopathological characteristics and prognosis, we focused on a subset of 54 patients with high-grade tumors who received standard-of-care treatment, including neoadjuvant radiotherapy. In UPS, no clinical parameters, including pathologic response after neoadjuvant treatment (<5% vital tumor), were found to associate with metastasis-free or disease-specific survival (**Supplementary Table 3**). In contrast, tumor size and tumor depth were identified as prognostic factors for both metastasis-free and disease-specific survival in MFS (**Supplementary Table 4**). Interestingly, a good pathological response to radiotherapy in MFS was negatively associated with metastasis-free and disease-specific survival.

Table 1. Clinicopathological characteristics of the studied cohorts of UPS and MFS. Tumor grades were assessed according to the Fédération Nationale des Centres de Lutte Contre le Cancer (FNCLCC) grading system. IQR = interquartile range, RT = radiotherapy.

	Discovery cohort		Validation cohort	
Variable	**MFS**	**UPS**	**MFS**	**UPS**
Total patients, *n*	17	16	22	23
Gender, *n* (%)				
Female	6 (35.3)	8 (50)	9 (40.9)	10 (43.5)
Male	12 (70.6)	8 (50)	13 (59.1)	13 (56.5)
Age (years), *median* (range)	65 (24-77)	74 (40-80)	70 (24-81)	67 (40-87)
Follow-up (months), *median* (range)	42 (6-150)	50 (12-92)	24 (4-63)	41 (15-104)
Grade, *n* (%)				
Low (1)	5 (29.4)	-	-	-
High (2, 3)	12 (70.6)	16 (100)	22 (100)	23 (100)
Anatomical location, *n* (%)				
Head & Neck	1 (5.9)	-	-	1 (4.3)
Upper extremities	3 (17.6)	1 (6.3)	3 (13.6)	4 (17.3)
Trunk	4 (23.5)	1 (6.3)	3 (13.6)	-
Lower extremities	9 (52.9)	14 (87.5)	16 (72.7)	18 (78.3)
Max tumor size (cm), *median* (IQR)[a]	7.2 (7.9)	8.9 (3.88)	10 (7.45)	8.9 (7.45)
Treatment, *n* (%)[b]				
Adjuvant radiotherapy	2 (11.8)	-	-	-
Neoadjuvant radiotherapy[c]	9 (52.9)	16 (100)	22 (100)	23 (100)
Surgery alone[d]	6 (35.3)	-	-	-
Histological response to neoadjuvant RT (%), *median* (IQR)				
Vital tumor	60 (12.5)	15 (34.3)	49.5 (45)	10 (30.5)
Hyalinization / fibrosis	20 (17.5)	40 (43.3)	15 (15)	55 (40)
Necrosis	12.5 (21.3)	20 (37.5)	25 (54.6)	20 (25)
Pathological response to neoadjuvant RT, *n* (%)[e]				
Good	-	6 (37.5)	5 (22.7)	9 (39.1)
Poor	8 (100)	10 (62.5)	17 (77.3)	14 (60.9)
Tumor depth, *n* (%)				
Deep	9 (52.9)	16 (100)	14 (63.6)	23 (100)
Superficial	8 (47.1)	-	8 (36.64)	-
Patients with recurrent disease, *n* (%)				
Local recurrence	3 (17.6)	2 (12.5)	2 (9.1)	1 (4.3)
Metastasis	3 (17.6)	8 (50)	10 (45.5)	13 (56.5)

a: size was missing for one UPS from the head & neck area
b: treatment for primary tumors
c: one high-grade MFS patient received neoadjuvant RT + pazopanib
d: one high-grade MFS patient had an amputation
e: pathologic response was defined as <5% vital tumor after neoadjuvant radiotherapy

Pathological responses to radiotherapy differed between the two sarcoma types. While UPS primarily exhibited hyalinization and fibrosis, MFS predominantly displayed necrosis (**Supplementary Fig. 1a**). Furthermore, histological responses in MFS were observed exclusively in large, deep-seated tumors, suggesting an association between tumor depth, tumor size, and necrosis (**Supplementary Fig. 1b**). Multivariate analysis did not identify any of these clinical parameters as independent prognostic factors in MFS (**Supplementary Table 4**).

Heterogeneity in immune-enriched microenvironments of UPS and MFS

To evaluate the "natural" immune microenvironment of UPS and MFS, we analyzed treatment-naïve samples, including pre-treatment biopsies or surgical resections, from patients who had not received neoadjuvant radiotherapy. RNAseq was performed on 23 samples from 13 UPS and 10 MFS patients, while IMC analysis was conducted on 29 samples from 14 UPS and 15 MFS patients. Of these, 20 samples (from 11 UPS and 9 MFS patients) were included in both analyses.

To confirm that our cohort was representative of previously described immune profiles in UPS and MFS, transcriptional profiles were compared to publicly available datasets comprising 206 primary STS from TCGA (6, 22). Immune-related transcriptional signatures were evaluated using SIC classification system (17) (**Supplementary Fig. 2a**) and the ICR signature (16) (**Supplementary Fig. 2b**).

Based on the ICR signature, samples were clustered into three categories: ICR-high, ICR-medium and ICR-low (23) (**Supplementary Fig. 2b**). The distribution of samples across ICR and SIC categories in the LCCO cohort closely mirrored that of TCGA cohort (**Fig. 1a, b**), underscoring the representativeness of the LCCO cohort. UPS and high-grade MFS frequently exhibited a Th1-related immune signature compared to other STS (**Fig. 1a**). Up to 33% of UPS and 43% of high-grade MFS were classified as ICR-high, compared to only 0–27% in other STS (**Fig. 1a**). Moreover, only 2% of UPS and 9% of high-grade MFS presented as ICR-low, compared to as much as 14-90% in other STS. The SIC classification further corroborated these findings, showing an enrichment of SIC D and E classifications (immune-high) in UPS and high-grade MFS, alongside DDLPS (**Fig. 1b**). These classifications were much more frequent in these tumors compared to other STS (44% in UPS, 43% in high-grade MFS, 43% in DDLPS while only 0-26% in other STS).

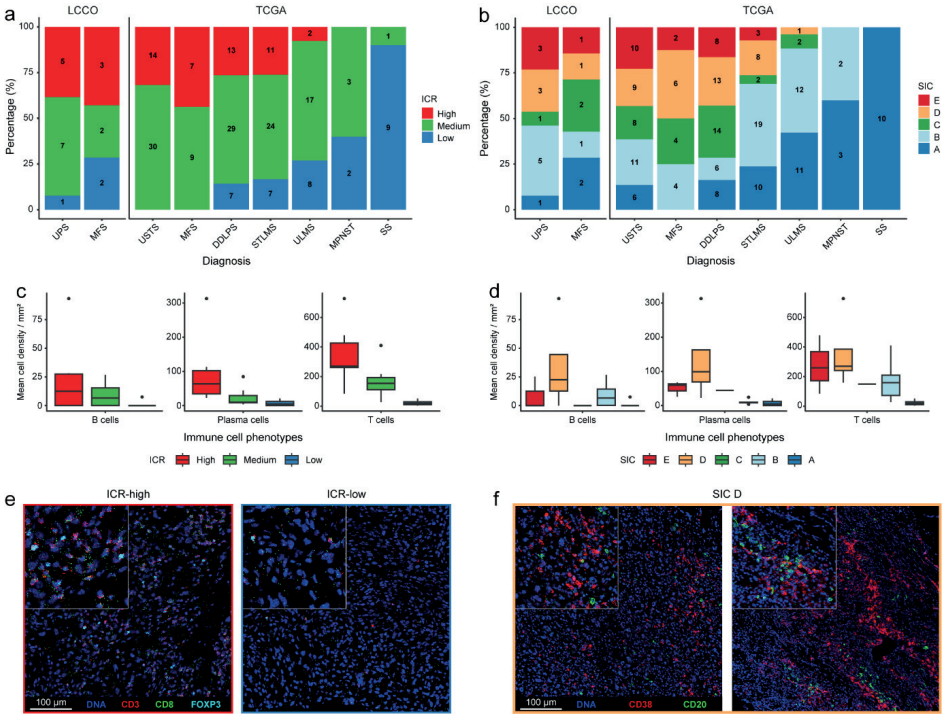


Fig. 1 Overview of immune profiles in UPS and MFS. a-b) Bar plots illustrating the percentage of samples across **a)** ICR categories and **b)** SIC phenotypes for each STS subtype across the LCCO and TCGA datasets, excluding low-grade tumors. The number of samples in each cluster is indicated within the bars. **c-d)** Boxplots presenting the IMC-based mean cell densities per mm^2 for B cells, plasma cells and T cells per **c)** ICR category and **d)** SIC phenotype. **e)** Representative IMC images of an ICR-high and ICR-low UPS, highlighting T cells (CD3 in red, CD8 in green, FOXP3 in cyan). **f)** IMC images of UPS and MFS enriched for B cell populations (SIC D), highlighting B cells (CD20 in green) and plasma cell/plasmablasts (CD38 in red). Abbreviations: DDLPS = dedifferentiated liposarcoma; MPNST = malignant peripheral nerve sheath tumor; SS = synovial sarcoma; STLMS = soft tissue leiomyosarcoma; ULMS = uterine leiomyosarcoma

MFS included more tumors classified as highly vascularized (SIC C) compared to UPS (26% vs 14%; **Fig. 1b**). However, both subtypes exhibited some heterogeneity. Up to 42% of UPS and 30% of MFS were classified as SIC A (immune-desert) or SIC B (immune-low), emphasizing that, while these tumors are relatively immune-enriched, variability exists within these subtypes. In contrast, low-grade MFS (*n* = 3), which exhibit lower genomic complexity (24), displayed an immune "cold" profile overall, similar to other STS like synovial sarcoma. All three cases were classified as immune desert (SIC A) and ICR-low (**Supplementary Fig. 2a, b**). These findings support the hypothesis that

immunogenicity in sarcomas correlates with increasing genomic complexity (25).

Since the ICR signature reflects a Th1-related immune response and that SIC D and E phenotypes are enriched in B cell lineage signatures, we used IMC to examine the association of B cells, plasma cells, and T cells with ICR categories and SIC phenotypes (**Fig. 1c, d**). This analysis demonstrated a clear enrichment of these immune cell populations in ICR-high and SIC D/E phenotypes (**Fig. 1e, f**).

Extended immunophenotyping of UPS and MFS using IMC resulted in the identification of 32 distinct cell populations, including overlapping tumor and stromal clusters due to the absence of tumor-specific markers in these sarcomas (**Supplementary Table 2**). The immune cell infiltrate predominantly consisted of myeloid cells, such as macrophages and monocytes, alongside lymphoid cells, including various T cell and innate lymphoid cell populations (**Supplementary Fig. 3a**). Since UPS and MFS cancer cells are known to express myeloid markers like CD68 and CD163, we reviewed the imaging data to ensure that the observed myeloid cell counts were not confounded by tumor cells expressing these markers. Consistent with the immune-related transcriptional profiles, low-grade MFS exhibited the lowest immune cell densities (**Supplementary Fig. 3a, b**). Among high-grade tumors, UPS demonstrated higher immune cell densities compared to MFS (**Supplementary Fig. 3a**), which may reflect the lower overall cellularity in MFS due to their myxoid extracellular matrix.

To correct for this difference in extracellular matrix, we calculated the relative immune cell abundance for all treatment-naïve samples of high-grade tumors (**Fig. 2**). Unsupervised clustering revealed a relative enrichment of T cells in a subset of both MFS and UPS (**Fig. 2**; **Supplementary Fig. 3c**), while myeloid cells, including monocytes and macrophages, were more prevalent in UPS compared to MFS (**Fig. 2**).

T cell and $CD68^{+}CD163^{+}$ macrophage infiltration is associated with an improved prognosis in UPS but not in MFS

To validate the IMC findings and investigate the clinical impact of T and myeloid cell populations, we composed a cohort of 45 patients (23 UPS and 22 high-grade MFS) that underwent the current standard-of-care treatment of neoadjuvant radiotherapy followed by surgery. T cell infiltration was assessed in pre-treatment biopsies using a multispectral IF panel, including anti-CD3, anti-CD8 and anti-PD-1 antibodies, while macrophages were evaluated with anti-

CD68 and anti-CD163 antibodies by two-color IHC. Based on the IMC findings, CD163 was included to identify most macrophages and the dual staining with CD68 supported the distinction between macrophages and tumor cells.

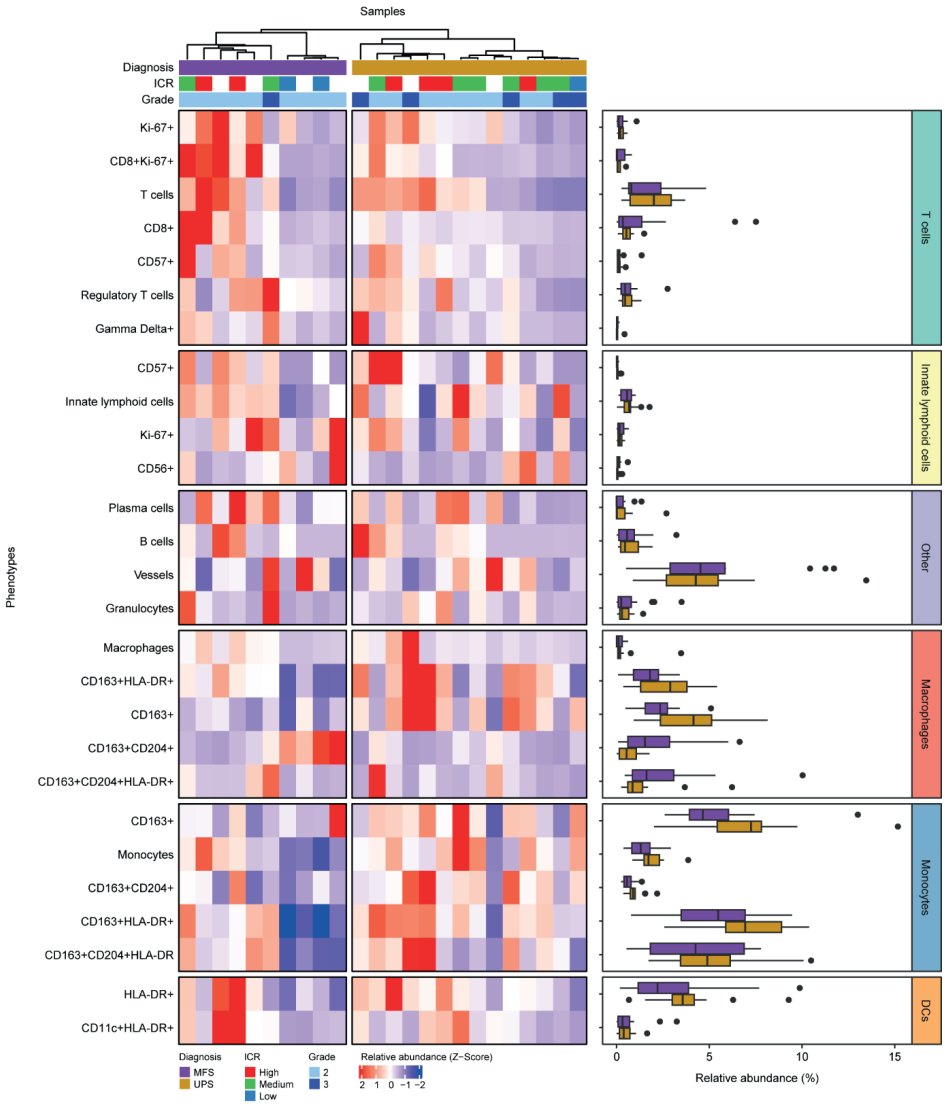


Fig. 2 IMC-based immunophenotypic analysis of UPS and high-grade MFS. The heatmap displays the relative abundance z-scores of all identified immune cell populations within the tumor microenvironments. Samples are annotated with diagnosis, the ICR classification, and tumor grade. Missing ICR data due to unavailable RNAseq results are indicated in white. Accompanying boxplots display the relative abundance of each phenotype by tumor type. Abbreviations: DCs = dendritic cells

Consistent with the IMC results, T cell infiltration showed high variability in both UPS and MFS (**Fig. 3a**). A strong correlation was observed between T cell infiltration levels determined by IMC and those detected using multispectral IF (**Supplementary Fig. 4a**). A significantly larger proportion of $CD8^+$ T cells exhibited PD-1 positivity (min: 0%, median: ~17%, max: ~87%) compared to $CD8^-$ T cells (supposedly $CD4^+$ T cells; min: 0%, median: ~2%, max: ~49%; *P* = 4.1e-6), with similar levels in UPS and MFS (**Fig. 3a**). For survival analysis, the cohort was grouped into T cell high and T cell low based on the median total T cell density per mm^2 within each subtype (**Fig. 3a, b**). Higher T cell infiltration was associated with improved metastasis-free survival in UPS but not in MFS (**Fig. 3c**). The same association was observed for disease-specific survival, but was not found statistically significant due to the low number of events (**Supplementary Fig. 4b**).

For the macrophages both UPS and MFS exhibited comparable densities of $CD68^+CD163^+$ macrophages, while MFS displayed higher levels of $CD68^+CD163^-$ macrophages, though this difference was not statistically significant (**Fig. 3a**). As with T cells, samples were categorized as macrophage high or low based on the median macrophage density per mm^2, which was assessed separately for $CD68^+CD163^-$ and $CD68^+CD163^+$ subsets. $CD68^+CD163^+$ macrophages associated with better metastasis-free survival in UPS but not in MFS (**Fig. 3d**). Again, the same association was observed for disease-specific survival and not found statistically significant due to the low number of events (**Supplementary Fig. 4b**). Interestingly, high T cell infiltration was linked to high $CD68^+CD163^+$ macrophage infiltration in both subtypes (**Fig. 3e**), suggesting a coordinated role of these immune cells within the tumor microenvironment. This was further strengthened by the observation that patients with high infiltration of both T cell and $CD68^+CD163^+$ macrophages had the longest metastasis-free survival whereas patients with low infiltration of both immune phenotypes had the shortest metastasis-free survival in UPS (**Supplementary Fig. 4c**). $CD68^+CD163^-$ macrophages were not associated with survival in either subtype (**Supplementary Fig. 4d**). Additionally, the ratio of T cells to $CD68^+CD163^+$ macrophages was assessed for both UPS and MFS and analyzed in relation to metastasis-free survival (**Supplementary Fig. 4e, f**). Although not statistically significant, an opposite association between the T cell-to-macrophage ratio and metastasis-free survival was observed for UPS and MFS, further underscoring the diverging roles of the immune microenvironment in these sarcoma subtypes.

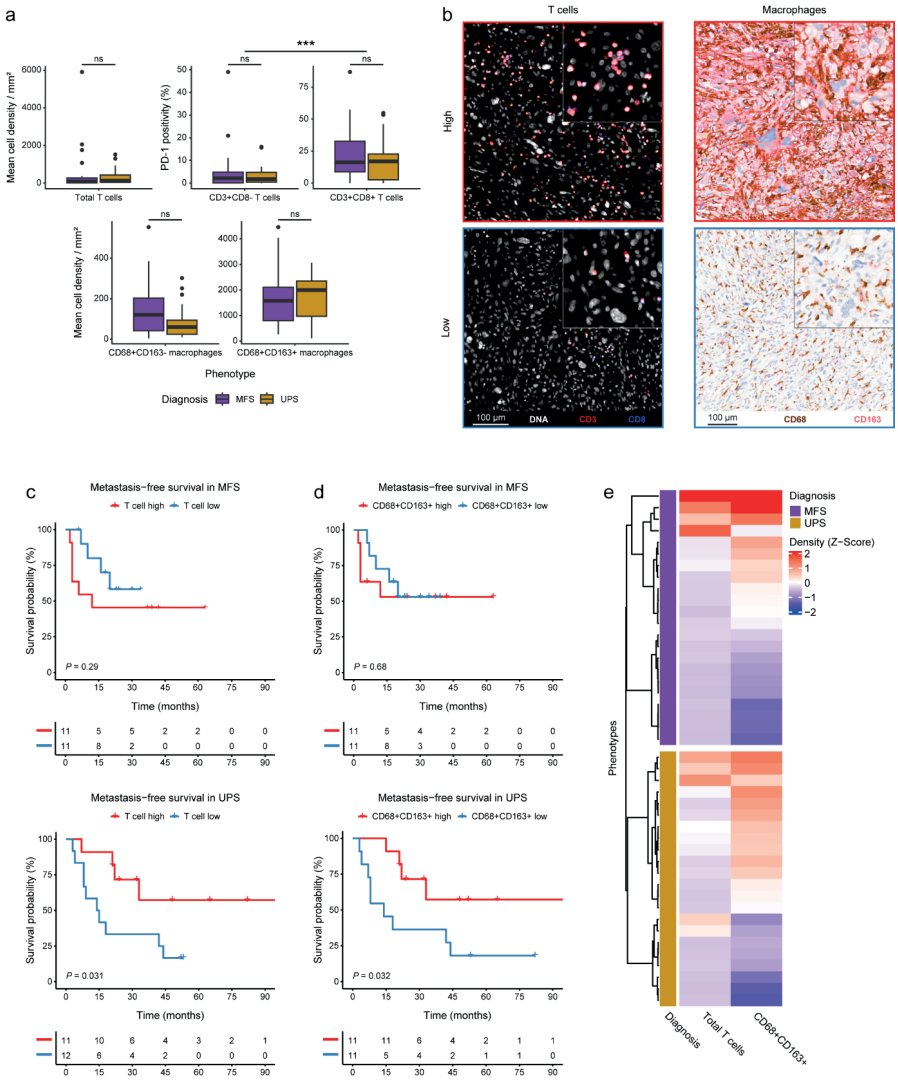


Fig. 3 T cells and CD68+CD163+ macrophages are prognostic in UPS, but not in MFS. a) Boxplots presenting the mean cell densities per mm^2 of T cells and macrophages, as well as the percentage of PD-1$^+$ T cells (CD8$^-$ and CD8$^+$) in the validation cohort. The significance level was evaluated with a student's t-test and is indicated per phenotype. ns = not significant, *** = P < 0.001. **b)** Representative IF images of a T cell high and a T cell low UPS (CD3 in red, CD8 in blue) and double IHC images of a CD68$^+$CD163$^+$ high and a CD68$^+$CD163$^+$ low MFS (CD68 in brown, CD163 in magenta). **c-d)** Survival curves for metastasis-free survival in both MFS and UPS, **c)** grouped based on the median T cell infiltration and **d)** grouped based on the median CD68$^+$CD163$^+$ macrophage infiltration. The association between macrophages and metastasis-free survival could not be assessed for one UPS patient due to insufficient biopsy material for macrophage detection. Significance is presented per Kaplan-Meier curve by the log-rank P value. **e)** Heatmap showing the z-score of the mean cell densities per mm^2 of T cells and CD68$^+$CD163$^+$ macrophages in UPS and MFS, as identified by IF and IHC respectively. The samples are annotated according to their diagnosis

Neoadjuvant radiation affects UPS and MFS differently

Since T cells and macrophages were assessed in pre-treatment samples for their prognostic value—and that neoadjuvant radiotherapy is part of the standard-of-care for both UPS and MFS—we investigated whether these immune cell populations respond differently to radiotherapy in the two subtypes. IMC data was used to compare matched pre- and post-treatment samples of 21 patients (13 UPS and 8 MFS). In post-treatment samples, only vital tumor areas were assessed, including both central and peripheral regions to account for intratumoral heterogeneity. In UPS (n = 13) various myeloid cell populations decreased following radiotherapy (**Fig. 4**), including both monocytes ($CD14^+CD68^-$) and macrophages ($CD68^+$). Among T cells, $CD57^+$ T cells and $CD8^+$ T cells increased after radiotherapy ($P < 0.01$ and $P < 0.05$, respectively). Additional phenotypes affected by the radiotherapy in UPS included tumor/stromal cell populations and vessels, which also decreased (**Supplementary Fig. 5a**). These alterations were all independent from pathological response. In contrast, no significant alterations in the immune microenvironment were observed in MFS following neoadjuvant radiotherapy (n = 8; **Supplementary Fig. 5a, b**). These findings suggest that radiotherapy may exert an immunogenic effect specifically in UPS.

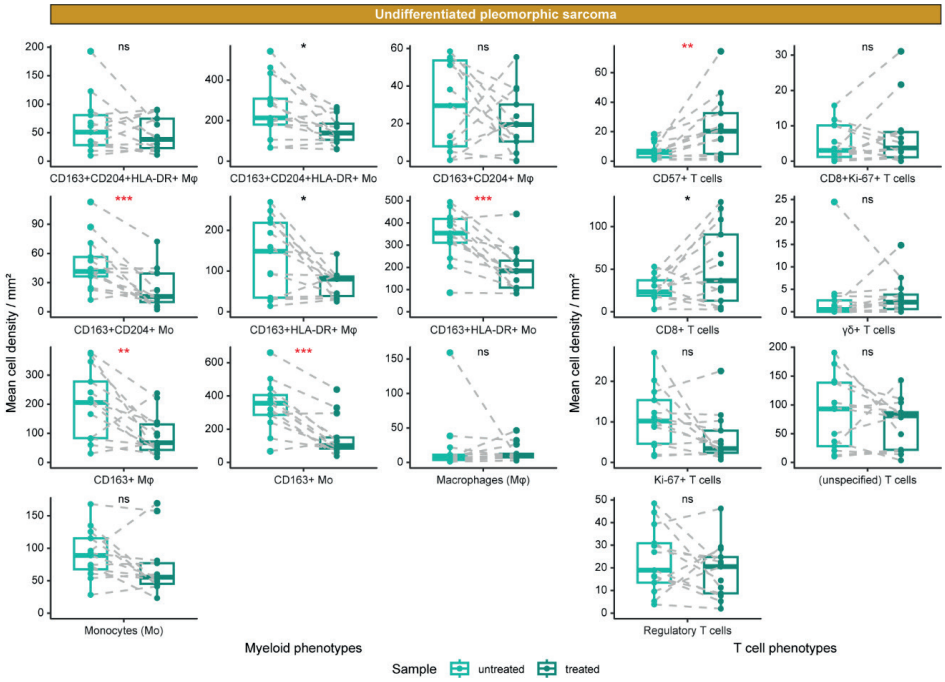


Fig. 4 The effect of radiotherapy on UPS. IMC-based comparison of pre- vs post-treatment UPS, presented in paired boxplots. Immune cell phenotypes are grouped into myeloid and T cell phenotypes. Myeloid phenotypes include monocytes (Mo; $CD14^{+}CD68^{-}$) and macrophages (Mφ; $CD68^{+}$). The significance level was evaluated with a student's t-test followed by a Benjamini-Hochberg false discovery rate (FDR) correction. The significance is indicated per phenotype and FDR-significant phenotypes are indicated in red. ns = not significant, * = P < 0.05, ** = P < 0.01, *** = P < 0.001

DISCUSSION

Although both UPS and MFS demonstrate more hallmarks of anti-tumor immunity than other STS, this study reveals considerable differences between the two subtypes. While both subtypes include T cell-enriched tumors, UPS demonstrated relatively higher myeloid cell infiltration compared to MFS. In UPS, T cells and $CD68^{+}CD163^{+}$ macrophages were positively associated with improved metastasis-free survival. Interestingly, radiotherapy altered the UPS microenvironment, reducing myeloid cell populations and increasing cytotoxic T cell phenotypes. In contrast, in MFS, neither T cells nor macrophages were associated with survival, and the immune microenvironment remained largely unchanged following radiotherapy. These findings highlight fundamental biological differences between the two subtypes, with UPS being more responsive to immune modulation by radiotherapy.

There is a growing interest in the immune microenvironment of STS, particularly UPS, due to its responsiveness to T cell checkpoint blockade (26-28). While pathological response to neoadjuvant radiotherapy was not prognostic in UPS, consistent with the findings from Danieli *et al.* (29), a pre-existing immune response appeared to reduce the metastatic potential of tumors. Furthermore, we show that radiotherapy may promote a more favorable context for anti-tumor immunity in UPS, potentially enhancing T cell-mediated responses and modulating myeloid cell interactions. These observations appear to align with findings by Keung *et al.* (30), who observed a trend for increased T cell infiltration following radiotherapy in UPS. Interestingly, our findings contrast with the ones by Goff *et al.,* who reported an increase in myeloid cells after radiotherapy in UPS (31). This discrepancy may arise from differences in data presentation; Goff *et al*. reported cell percentages relative to total cells, whereas we analyzed cell densities per tissue area to enable accurate pre- and post-treatment comparisons. Despite these differences, our results underscore the potential of radiotherapy to enhance anti-tumor immunity in UPS.

The association between $CD68^{+}CD163^{+}$ macrophages and metastasis-free survival highlights the complexity of macrophage biology given that $CD163^{+}$ macrophages have traditionally been associated with worse outcomes in many solid tumors (32), including various sarcoma subtypes (33-35). However, several studies on sarcomas, including UPS, have reported positive associations with clinical outcomes (36-39), emphasizing the context-dependent nature of macrophage function. Moreover, we observed a marked decrease in their abundance following neoadjuvant radiotherapy, further complicating the interpretation of their role. Given the well-established functional heterogeneity

of tumor-associated macrophages (40), further research will be needed to define the specific roles and functional states of these populations in UPS. Although the current study highlights the prognostic effect of immunity in the context of neoadjuvant radiotherapy, it is important to note that this effect may be independent of radiotherapy altogether, as studies by Toulmonde *et al.* and Guegan *et al.* found $CD8^+$ T cells to be prognostic in both untreated and chemotherapy-treated UPS, respectively (36, 41).

Similar to UPS, MFS has shown responsiveness to T cell checkpoint blockade (42), suggesting that anti-tumor immune responses can also be mounted in these tumors. However, our findings do not support a strong modulatory effect of radiotherapy in the immune microenvironment of MFS, and pre-existing immunity appears to lack prognostic significance. This aligns with the findings of Yamashita *et al.* (24), who also demonstrated that T cell infiltration is not prognostic in MFS. The divergence between the roles of the immune microenvironment in UPS and MFS is striking. Despite similar overall immune cell densities, functional differences or distinct tumor-immune interactions likely drive these outcomes. For instance, Dancsok *et al.* identified $SIRP\alpha^+$ macrophages as negative prognostic markers specific to MFS and not in UPS (33). Furthermore, the lack of significant immune alterations in MFS post-radiotherapy underscores these differences. Future research could provide deeper insights into the functional heterogeneity and dynamics of the immune microenvironment of UPS and MFS.

Neoadjuvant radiotherapy together with surgical resection effectively controlled disease in both UPS and MFS, with only 4 out of 54 high-grade tumors experiencing local recurrence. However, metastasis remains a major challenge, occurring in approximately 50% of patients across both subtypes. This highlights the need for additional systemic therapies to target circulating or metastasizing tumor cells. Promisingly, Roland *et al.* (43) and Mowery *et al.* (44) demonstrated survival benefits with the combination of neoadjuvant checkpoint blockade and radiotherapy in UPS. For cases lacking a pre-existing immune response, converting the microenvironment from “cold” to “hot” might be necessary. Guegan *et al.* observed that immune “cold” UPS responded well to neoadjuvant chemotherapy (36), which subsequently enhanced immune cell infiltration.

Our study has several limitations, including a relatively small sample size and a single-institution design, with all patients receiving neoadjuvant radiotherapy. Most samples were diagnostic biopsies, which limited tissue availability. Furthermore, treatment approaches have only recently

become more standardized for UPS and MFS. As a result, we were unable to establish independent discovery and validation cohorts, Nevertheless, this study provides important insights into the immune landscape of these rare sarcomas and highlights key differences between these UPS and MFS, offering a foundation for future research.

In conclusion, this study underscores key differences in the immune microenvironments of UPS and MFS. While both subtypes exhibited high immune cell infiltration, only UPS showed improved metastasis-free survival associated with T cells and $CD68^{+}CD163^{+}$ macrophages. Radiotherapy appeared to reshape the immune response in UPS, increasing cytotoxic T cell infiltration and reducing myeloid cell populations, yet MFS remained largely resistant to such modulation. These results suggest that subtype-specific approaches may be required to improve outcomes from cancer immunotherapy in STS.

STATEMENTS & DECLARATIONS

Funding

This work was financially supported by an unrestricted research grant from Tracon Pharmaceuticals and the intramural Leiden Center for Computational Oncology strategic fund. N.F.C.C.d.M. is funded by the European Research Council (ERC) under the European Union's Horizon 2020 Research and Innovation Program (grant agreement no. 852832) and by the VIDI ZonMW (project number: 09150172110092).

Disclosure of interest

The authors declare no conflicts of interest.

Author contributions

S.v.O. contributed to the conceptualization, data curation, software, formal analysis, validation, investigation, visualization, methodology, writing-original draft, project administration and writing-review editing. **D.M.M.** contributed to the conceptualization, investigation and writing-review editing. **Z.B.E.** contributed to the investigation and writing-review editing. **M.E.IJ.** contributed to the methodology and writing-review editing. **J.R.** contributed to the methodology and writing-review editing. **S.L.** contributed to the investigation and writing-review editing. **M.S.B.** contributed to the investigation and writing-review editing. **B.v.d.A.** contributed to the investigation and writing-review editing. **R.v.d.B.** contributed to the investigation and writing-review editing.

I.H.B.d.B. contributed to the investigation and writing-review editing. **L.J.A.C.H.** contributed to the funding acquisition and writing-review editing. **A.A.K.** contributed to the resources and writing-review editing. **M.v.d.P.** contributed to the investigation and writing-review editing. **P.M.W.K.** contributed to the investigation and writing-review editing. **R.L.H.** contributed to the investigation and writing-review editing. **M.A.J.v.d.S.** contributed to the resources and writing-review editing. **N.F.C.C.d.M.** contributed to the conceptualization, supervision, funding acquisition, investigation, methodology, writing-original draft and writing-review editing. **J.V.M.G.B.** contributed to the conceptualization, supervision, funding acquisition, investigation, methodology, writing-original draft and writing-review editing. All authors have read and approved the final version of the manuscript.

Data availability

The RNAseq data generated in this study are publicly available in Gene Expression Omnibus GEO at GSE285944. The IMC data is available in BioStudies at S-BIAD1555. The QuPath script and the R code used to process the data are published on the LUMC Bone & Soft Tissue Pathology Group GitLab (**https://git.lumc.nl/bstp/papers/immunogenic-features-of-ups-and-mfs**) and the LUMC Cancer ImmunoGenomics Group GitHub (**https://github.com/demirandalab/immunogenic-features-of-ups-and-mfs**). All other data are available from the corresponding author upon reasonable request.

Ethics approval

All samples in this study were pseudo anonymized and handled according to the ethical guidelines outlined in 'Code for Proper Secondary Use of Human Tissue in The Netherlands' by the Dutch Federation of Medical Scientific Societies. A waiver of consent was obtained from the medical ethical evaluation committee (Medisch-Ethische Toetsingscommissie Leiden Den Haag Delft; protocol number: B17.036 and B20.067). As a result, this study adheres to the Declaration of Helsinki.

REFERENCES

1. WHO Classification of Tumours Editorial Board. Soft Tissue and Bone Tumours. WHO Classification of Tumours. 5 ed. Lyon, France: IARC Publications; 2020.
2. Gronchi A, Miah AB, Dei Tos AP, Abecassis N, Bajpai J, Bauer S, et al. Soft tissue and visceral sarcomas: ESMO-EURACAN-GENTURIS Clinical Practice Guidelines for diagnosis, treatment and follow-up. Ann Oncol. 2021;32(11):1348-65.
3. Yoshimoto M, Yamada Y, Ishihara S, Kohashi K, Toda Y, Ito Y, et al. Comparative Study of Myxofibrosarcoma With Undifferentiated Pleomorphic Sarcoma: Histopathologic and Clinicopathologic Review. Am J Surg Pathol. 2020;44(1):87-97.
4. van der Horst CAJ, Bongers SLM, Versleijen-Jonkers YMH, Ho VKY, Braam PM, Flucke UE, et al. Overall Survival of Patients with Myxofibrosarcomas: An Epidemiological Study. Cancers (Basel). 2022;14(5).
5. Gonzalez MR, Clunk MJ, Bedi ADS, Werenski JO, Lang JH, Karczewski D, et al. Prognostic and predictive factors in undifferentiated pleomorphic sarcoma: A long-term study from a large tertiary care urban center. J Surg Oncol. 2023;128(2):322-31.
6. Cancer Genome Atlas Research Network. Comprehensive and Integrated Genomic Characterization of Adult Soft Tissue Sarcomas. Cell. 2017;171(4):950-65 e28.
7. Mitra S, Farswan A, Piccinelli P, Sydow S, Hesla A, Tsagkozis P, et al. Transcriptomic profiles of myxofibrosarcoma and undifferentiated pleomorphic sarcoma correlate with clinical and genomic features. J Pathol. 2024;264(3):293-304.
8. Lyskjaer I, De Noon S, Tirabosco R, Rocha AM, Lindsay D, Amary F, et al. DNA methylation-based profiling of bone and soft tissue tumours: a validation study of the 'DKFZ Sarcoma Classifier'. J Pathol Clin Res. 2021;7(4):350-60.
9. Koelsche C, Schrimpf D, Stichel D, Sill M, Sahm F, Reuss DE, et al. Sarcoma classification by DNA methylation profiling. Nat Commun. 2021;12(1):498.
10. Allignet B, Meurgey A, Bouhamama A, Karanian M, Meeus P, Vaz G, et al. Impact of histological subtype on radiological and pathological response after neoadjuvant radiotherapy in soft tissue sarcoma. Eur J Surg Oncol. 2021;47(12):2995-3003.
11. Messiou C, Bonvalot S, Gronchi A, Vanel D, Meyer M, Robinson P, et al. Evaluation of response after pre-operative radiotherapy in soft tissue sarcomas; the European Organisation for Research and Treatment of Cancer-Soft Tissue and Bone Sarcoma Group (EORTC-STBSG) and Imaging Group recommendations for radiological examination and reporting with an emphasis on magnetic resonance imaging. Eur J Cancer. 2016;56:37-44.
12. Schaefer IM, Hornick JL, Barysauskas CM, Raut CP, Patel SA, Royce TJ, et al. Histologic Appearance After Preoperative Radiation Therapy for Soft Tissue Sarcoma: Assessment of the European Organization for Research and Treatment of Cancer-Soft Tissue and Bone Sarcoma Group Response Score. Int J Radiat Oncol Biol Phys. 2017;98(2):375-83.
13. van Oost S, Meijer DM, Ijsselsteijn ME, Roelands JP, van den Akker B, van der Breggen R, et al. Multimodal profiling of chordoma immunity reveals distinct immune contextures. J Immunother Cancer. 2024;12(1).
14. Anders S, Pyl PT, Huber W. HTSeq--a Python framework to work with high-throughput sequencing data. Bioinformatics. 2015;31(2):166-9.

15. Bertucci F, Finetti P, Simeone I, Hendrickx W, Wang E, Marincola FM, et al. The immunologic constant of rejection classification refines the prognostic value of conventional prognostic signatures in breast cancer. Br J Cancer. 2018;119(11):1383-91.

16. Bertucci F, Niziers V, de Nonneville A, Finetti P, Mescam L, Mir O, et al. Immunologic constant of rejection signature is prognostic in soft-tissue sarcoma and refines the CINSARC signature. J Immunother Cancer. 2022;10(1).

17. Petitprez F, de Reynies A, Keung EZ, Chen TW, Sun CM, Calderaro J, et al. B cells are associated with survival and immunotherapy response in sarcoma. Nature. 2020;577(7791):556-60.

18. Ijsselsteijn ME, van der Breggen R, Sarasqueta AF, Koning F, de Miranda NFCC. A 40-Marker Panel for High Dimensional Characterization of Cancer Immune Microenvironments by Imaging Mass Cytometry. Front Immunol. 2019;10.

19. Ijsselsteijn ME, Somarakis A, Lelieveldt BPF, Hollt T, de Miranda N. Semi-automated background removal limits data loss and normalizes imaging mass cytometry data. Cytometry A. 2021;99(12):1187-97.

20. Somarakis A, Van Unen V, Koning F, Lelieveldt B, Hollt T. ImaCytE: Visual Exploration of Cellular Micro-Environments for Imaging Mass Cytometry Data. IEEE Trans Vis Comput Graph. 2021;27(1):98-110.

21. Ijsselsteijn ME, Brouwer TP, Abdulrahman Z, Reidy E, Ramalheiro A, Heeren AM, et al. Cancer immunophenotyping by seven-colour multispectral imaging without tyramide signal amplification. J Pathol Clin Res. 2019;5(1):3-11.

22. van IJzendoorn DGP, Szuhai K, Briaire-de Bruijn IH, Kostine M, Kuijjer ML, Bovee JVMG. Machine learning analysis of gene expression data reveals novel diagnostic and prognostic biomarkers and identifies therapeutic targets for soft tissue sarcomas. PLoS Comput Biol. 2019;15(2):e1006826.

23. Roelands J, Hendrickx W, Zoppoli G, Mall R, Saad M, Halliwill K, et al. Oncogenic states dictate the prognostic and predictive connotations of intratumoral immune response. J Immunother Cancer. 2020;8(1).

24. Yamashita A, Suehara Y, Hayashi T, Takagi T, Kubota D, Sasa K, et al. Molecular and clinicopathological analysis revealed an immuno-checkpoint inhibitor as a potential therapeutic target in a subset of high-grade myxofibrosarcoma. Virchows Arch. 2022;481(4):1-17.

25. van Oost S, Meijer DM, Kuijjer ML, Bovee J, de Miranda N. Linking Immunity with Genomics in Sarcomas: Is Genomic Complexity an Immunogenic Trigger? Biomedicines. 2021;9(8).

26. Tawbi HA, Burgess M, Bolejack V, Van Tine BA, Schuetze SM, Hu J, et al. Pembrolizumab in advanced soft-tissue sarcoma and bone sarcoma (SARC028): a multicentre, two-cohort, single-arm, open-label, phase 2 trial. Lancet Oncol. 2017;18(11):1493-501.

27. Italiano A, Bessede A, Pulido M, Bompas E, Piperno-Neumann S, Chevreau C, et al. Pembrolizumab in soft-tissue sarcomas with tertiary lymphoid structures: a phase 2 PEMBROSARC trial cohort. Nat Med. 2022;28(6):1199-206.

28. Keung EZ, Burgess M, Salazar R, Parra ER, Rodrigues-Canales J, Bolejack V, et al. Correlative Analyses of the SARC028 Trial Reveal an Association Between Sarcoma-Associated Immune Infiltrate and Response to Pembrolizumab. Clin Cancer Res. 2020;26(6):1258-66.

29. Danieli M, Barretta F, Radaelli S, Fiore M, Sangalli C, Barisella M, et al. Pathological and radiological response following neoadjuvant treatments in primary localized resectable myxofibrosarcoma and undifferentiated pleomorphic sarcoma of the extremities and trunk wall. Cancer. 2023;129(21):3417-29.

30. Keung EZ, Tsai JW, Ali AM, Cormier JN, Bishop AJ, Guadagnolo BA, et al. Analysis of the immune infiltrate in undifferentiated pleomorphic sarcoma of the extremity and trunk in response to radiotherapy: Rationale for combination neoadjuvant immune checkpoint inhibition and radiotherapy. Oncoimmunology. 2018;7(2):e1385689.

31. Goff PH, Riolobos L, LaFleur BJ, Spraker MB, Seo YD, Smythe KS, et al. Neoadjuvant Therapy Induces a Potent Immune Response to Sarcoma, Dominated by Myeloid and B Cells. Clin Cancer Res. 2022;28(8):1701-11.

32. Mathiesen H, Juul-Madsen K, Tramm T, Vorup-Jensen T, Moller HJ, Etzerodt A, et al. Prognostic value of CD163(+) macrophages in solid tumor malignancies: A scoping review. Immunol Lett. 2025;272:106970.

33. Dancsok AR, Gao D, Lee AF, Steigen SE, Blay JY, Thomas DM, et al. Tumor-associated macrophages and macrophage-related immune checkpoint expression in sarcomas. Oncoimmunology. 2020;9(1):1747340.

34. Nystrom H, Jonsson M, Nilbert M, Carneiro A. Immune-cell infiltration in high-grade soft tissue sarcomas; prognostic implications of tumor-associated macrophages and B-cells. Acta Oncol. 2023;62(1):33-9.

35. Umakoshi M, Nakamura A, Tsuchie H, Li Z, Kudo-Asabe Y, Miyabe K, et al. Macrophage numbers in the marginal area of sarcomas predict clinical prognosis. Sci Rep. 2023;13(1):1290.

36. Guegan JP, El Ghazzi N, Vibert J, Rey C, Vanhersecke L, Coindre JM, et al. Predictive value of tumor microenvironment on pathologic response to neoadjuvant chemotherapy in patients with undifferentiated pleomorphic sarcomas. J Hematol Oncol. 2024;17(1):100.

37. Lazcano R, Barreto CM, Salazar R, Carapeto F, Traweek RS, Leung CH, et al. The immune landscape of undifferentiated pleomorphic sarcoma. Front Oncol. 2022;12:1008484.

38. Buddingh EP, Kuijjer ML, Duim RA, Burger H, Agelopoulos K, Myklebost O, et al. Tumor-infiltrating macrophages are associated with metastasis suppression in high-grade osteosarcoma: a rationale for treatment with macrophage activating agents. Clin Cancer Res. 2011;17(8):2110-9.

39. Gomez-Brouchet A, Illac C, Gilhodes J, Bouvier C, Aubert S, Guinebretiere JM, et al. CD163-positive tumor-associated macrophages and CD8-positive cytotoxic lymphocytes are powerful diagnostic markers for the therapeutic stratification of osteosarcoma patients: An immunohistochemical analysis of the biopsies fromthe French OS2006 phase 3 trial. Oncoimmunology. 2017;6(9):e1331193.

40. Ma RY, Black A, Qian BZ. Macrophage diversity in cancer revisited in the era of single-cell omics. Trends Immunol. 2022;43(7):546-63.

41. Toulmonde M, Lucchesi C, Verbeke S, Crombe A, Adam J, Geneste D, et al. High throughput profiling of undifferentiated pleomorphic sarcomas identifies two main subgroups with distinct immune profile, clinical outcome and sensitivity to targeted therapies. EBioMedicine. 2020;62:103131.

42. D'Angelo SP, Mahoney MR, Van Tine BA, Atkins J, Milhem MM, Jahagirdar BN, et al. Nivolumab with or without ipilimumab treatment for metastatic sarcoma (Alliance A091401): two open-label, non-comparative, randomised, phase 2 trials. Lancet Oncol. 2018;19(3):416-26.

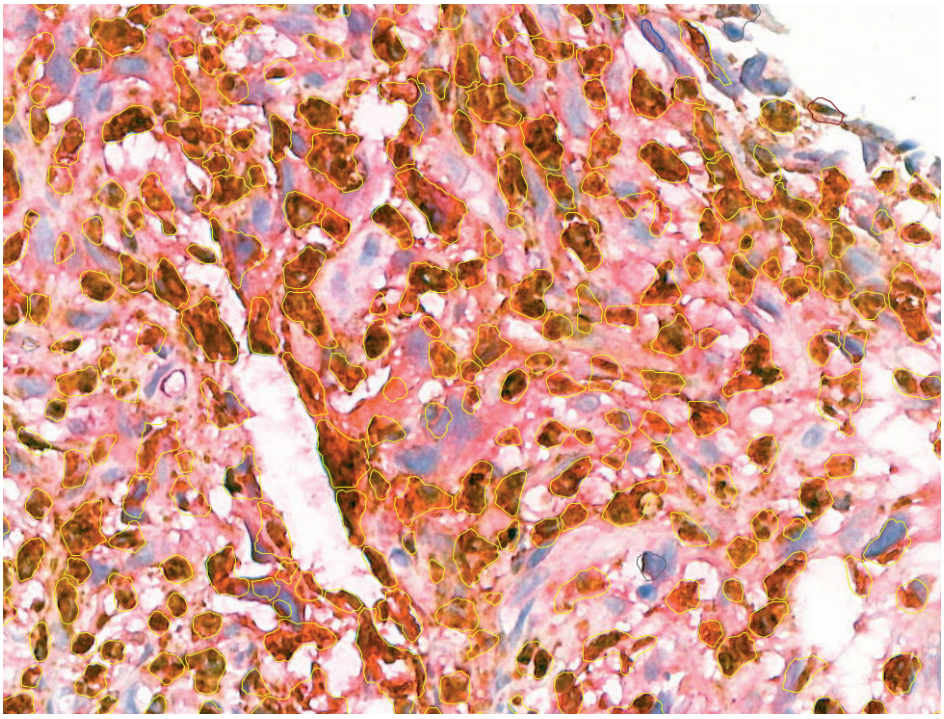
43. Roland CL, Nassif Haddad EF, Keung EZ, Wang WL, Lazar AJ, Lin H, et al. A randomized, non-comparative phase 2 study of neoadjuvant immune-checkpoint blockade in retroperitoneal dedifferentiated liposarcoma and extremity/truncal undifferentiated pleomorphic sarcoma. Nat Cancer. 2024.

44. Mowery YM, Ballman KV, Hong AM, Schuetze SM, Wagner AJ, Monga V, et al. Safety and efficacy of pembrolizumab, radiation therapy, and surgery versus radiation therapy and surgery for stage III soft tissue sarcoma of the extremity (SU2C-SARC032): an open-label, randomised clinical trial. Lancet. 2024;404(10467):2053-64.

SUPPLEMENTARY METHODS

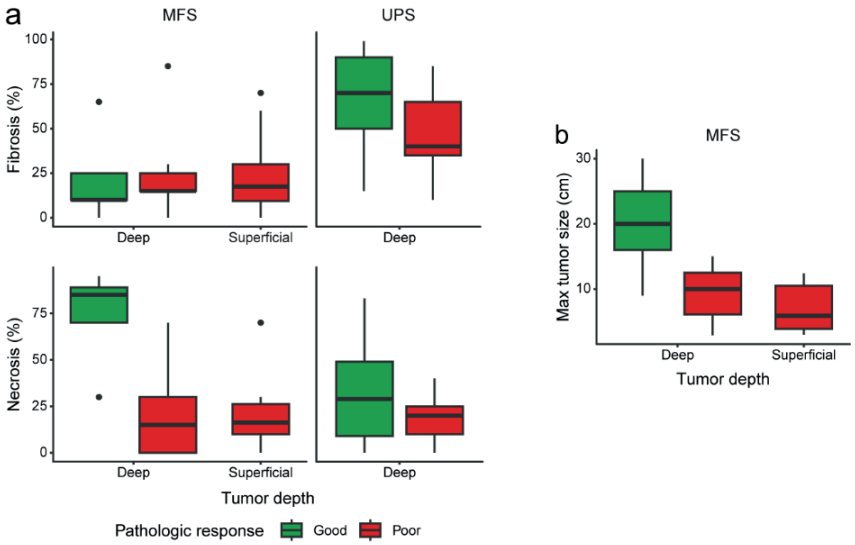
QuPath workflow to analyze double IHC images

- Load images as Brightfield (other).
- Single stains for CD68-DAB and CD163-AP were performed to identify the color values (estimate stain vectors in QuPath).
- Set deconvolution stain values manually based on the single stains.
- Create ROIs in each image (~ 1x1.3 mm rectangles).
- Detect (mostly) macrophages by using the optical density sum (instead of hematoxylin), this takes the intensity of the staining in consideration to detect cells rather than the hematoxylin. As depicted below, the result is that tumor cells (with the large nuclei) are often not even "detected" since the DAB staining is much stronger in macrophages. Moreover, this allows for a more proper identification of the macrophages their shape rather than taking the nucleus of a cell and then expanding with x µm. Using this cell segmentation method, you lose some accuracy in detecting the exact number of cells (some cells are oversegmented, others are undersegmented), but it allows for a more robust separation of tumor cells and macrophages and is consistent across the cohort.
- Train an object classifier to classify cells as either CD68+, CD163+, CD68+CD163+ or negative.
    - CD68+ cells and CD68+CD163+ cells were considered macrophages, while CD163+ cells were considered tumor cells and therefore excluded.
- Measure tissue area per ROI by training a pixel classifier (ANN_MLP or RTrees).
- Save detection measurements (cells / ROI) and annotation measurements (tissue area / ROI).
- In R -> count cells per ROI, then correct for tissue area, then average per sample.
- The used QuPath & R scripts are available on our GitLab (**https://git.lumc.nl/bstp/papers/immunogenic-features-of-ups-and-mfs**) or GitHub (**https://github.com/demirandalab/immunogenic-features-of-ups-and-mfs**).

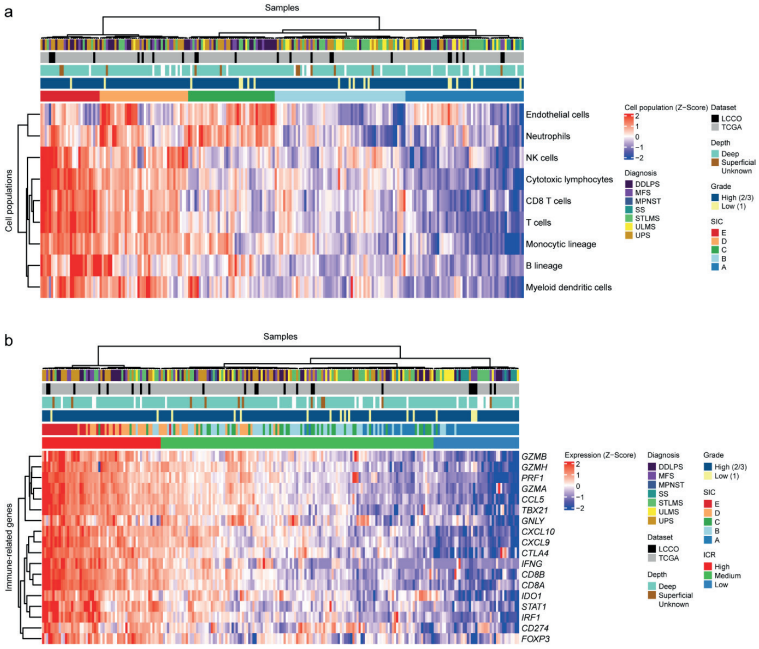


Snapshot of a double IHC image of an MFS. Macrophages were stained for CD68 (DAB-brown) and CD163 (AP-magenta). Cell detection is shown by the polygonal shapes. Yellow = $CD68^+CD163^+$, Blue = $CD163^+$, Brown = $CD68^+$. Black arrows indicate $CD68^+$ and/or $CD163^+$ tumor cells.

SUPPLEMENTARY FIGURES

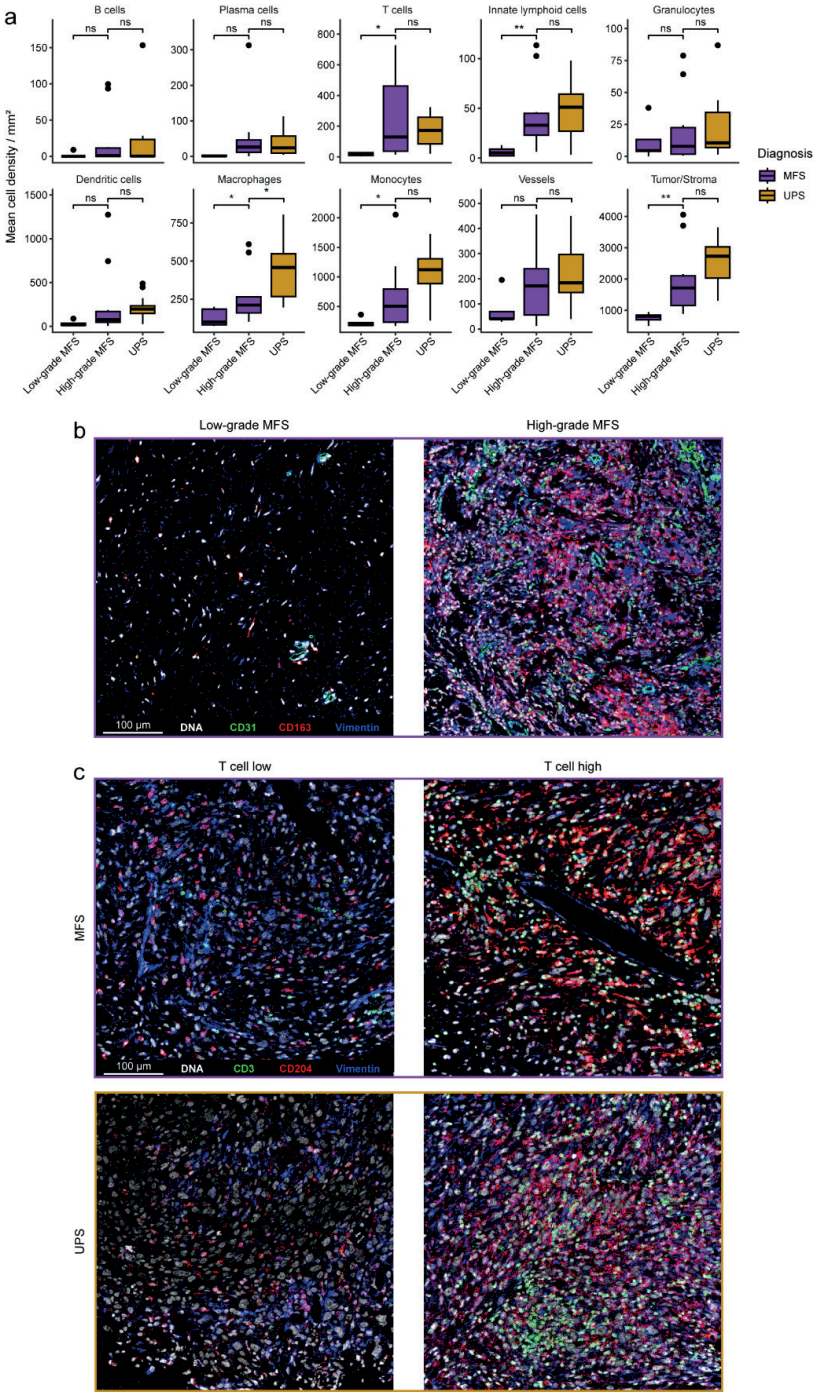


Supplementary Fig. 1 Association between tumor depth, tumor size and necrosis in MFS. **a)** Boxplots displaying the association between pathologic response (<%5 vital tumor), fibrosis, necrosis, tumor depth and diagnosis. **b)** Boxplots presenting the association between max tumor size (cm), pathologic response and tumor depth in MFS.

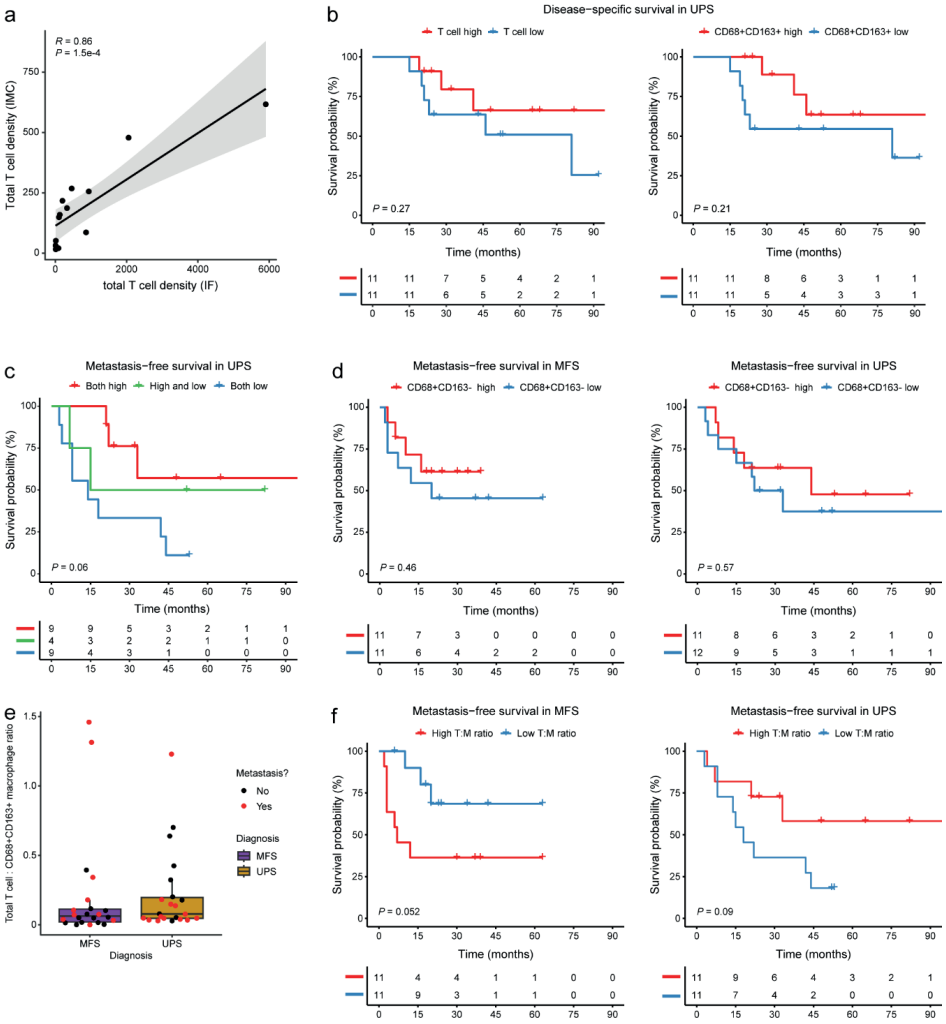


Supplementary Fig. 2 Clustering using the SIC and ICR signatures in UPS and MFS. a) Heatmap presenting the estimated cell population z-scores of the microenvironment cell population (MCP) counter in the LCCO and TCGA cohorts, resulting in five SIC phenotypes. Samples are annotated for diagnosis, dataset, tumor depth, tumor grade and SIC classification. **b)** Heatmap presenting the gene expression z-scores of 18 ICR-genes in the LCCO and TCGA cohorts, resulting in three ICR categories. Samples are annotated for diagnosis, dataset, tumor depth, tumor grade, SIC classification and ICR category. Abbreviations: DDLPS = dedifferentiated liposarcoma; MPNST = malignant peripheral nerve sheath tumor; SS = synovial sarcoma; STLMS = soft tissue leiomyosarcoma; ULMS = uterine leiomyosarcoma.

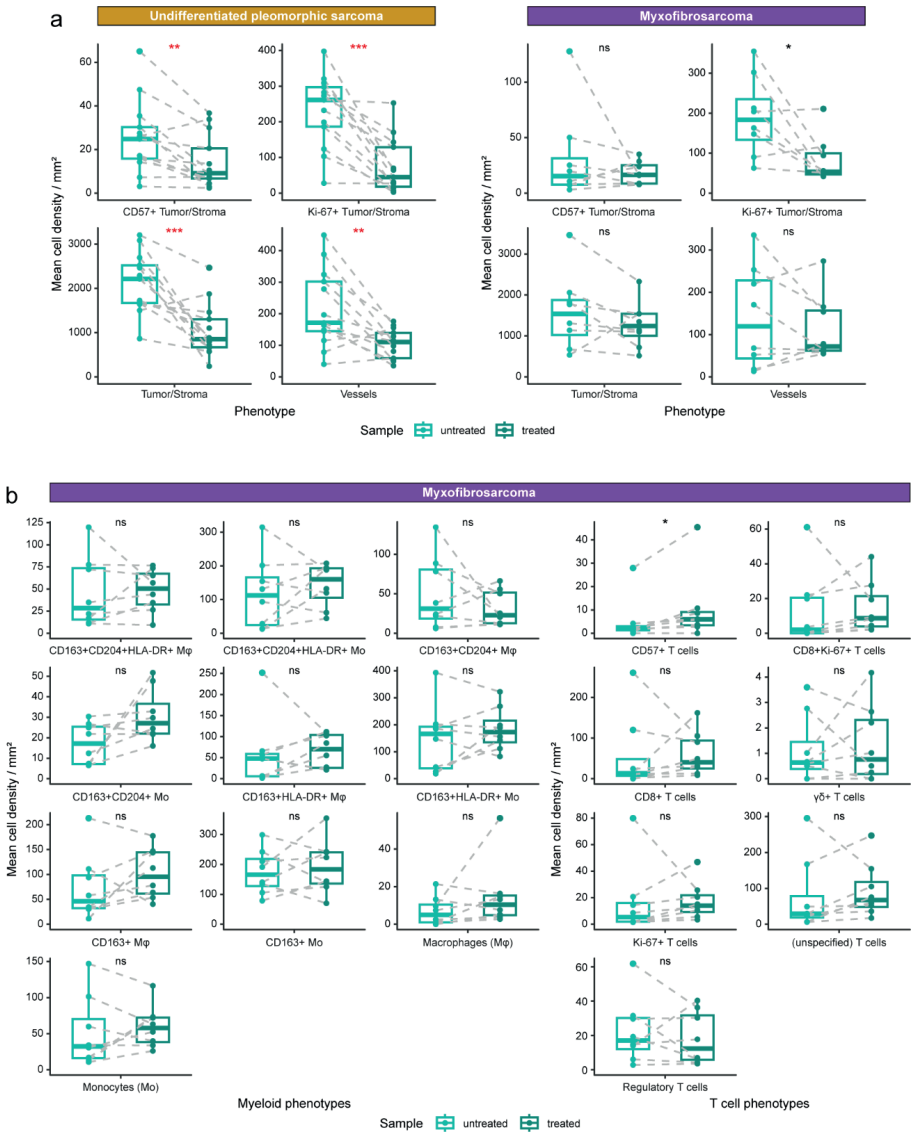
Supplementary Fig. 3 Overview of immune contextures in UPS and MFS. a) Boxplots presenting the mean cell density per mm^2 of major cell types for low-grade MFS, high-grade MFS and UPS. Differences between low-grade and high-grade MFS, as well as high-grade MFS and UPS were evaluated with a student's t-test. ns = not significant, * = P < 0.05, ** = P < 0.01. **b)** Example IMC images of a low-grade and a high-grade MFS, highlighting the difference in cellularity. The images display tumor/stromal cells (vimentin in blue), vessels (CD31 in green) and myeloid cells (CD163 in red). **c)** Example IMC images of a T cell low and a T cell high, high-grade MFS (top row) and UPS (bottom row). The images display T cells (CD3 in green), tumor/stromal cells (vimentin in blue) and myeloid cells (CD204 in red).



Supplementary Fig. 3 Overview of immune contextures in UPS and MFS.



Supplementary Fig. 4 Association between immune infiltration and survival in UPS and MFS. a) Correlation plot presenting the positive correlation between T cell densities as detected with IMC compared to IF. **b)** Survival analysis of the disease-specific survival in UPS, grouped based on the median total T cell and median $CD68^{+}CD163^{+}$ macrophage infiltration. **c)** Survival analysis of the metastasis-free survival in UPS, grouped based on the combined total T cell and $CD68^{+}CD163^{+}$ macrophage infiltration. **d)** Survival analysis of the metastasis-free survival in UPS and MFS, grouped based on the median $CD68^{+}CD163^{-}$ macrophage infiltration. **e)** Boxplots displaying the T cell-to-$CD68^{+}CD163^{+}$ macrophage ratio, separated per subtype. Samples are colored red when that patient has experienced metastatic disease. **f)** Survival analysis of the metastasis-free survival in UPS and MFS, grouped based on the median T cell-to-$CD68^{+}CD163^{+}$ macrophage (T:M) ratio. The significance of the Kaplan-Meier curves is presented by the log-rank P values.



Supplementary Fig. 5 The effect of radiotherapy on UPS and MFS. a) Paired boxplots presenting the other statistically significant alterations to the UPS immune microenvironment after radiotherapy. The same phenotypes are shown for MFS as a means of comparison. The significance level was evaluated with a student's t-test followed by a Benjamini-Hochberg false discovery rate (FDR) correction. The significance is indicated per phenotype and FDR-significant phenotypes are indicated in red. ns = not significant, * = P < 0.05, ** = P < 0.01, *** = P < 0.001. **b)** Comparison of pre- vs post-treatment immune cell phenotypes in MFS, presented in paired boxplots. The same phenotypes are presented in **Fig. 4** for UPS. The significance is indicated per phenotype and FDR-significant phenotypes are indicated in red. Abbreviations: Mφ = macrophages; Mo = monocytes.

SUPPLEMENTARY TABLES

Supplementary Table 1. IMC marker panel. Ab = antibody, ON = overnight, PDPN = podoplanin.

	Target	Clone	Metal	Incubation Time	Temp	Dilution (x)
Lymphoid	CD103	EPR4166(2)	168 Er	5h	RT	50
	CD19	D4V4B	172 Yb	5h	RT	100
	CD20	H1	142 Nd	Overnight	4C	100
	CD27	EPR8569	175 Lu	Overnight	4C	50
	CD3	EP449E	153 Eu	Overnight	4C	50
	CD38	EPR4106	169 Tm	Overnight	4C	100
	CD4 + 2nd AB	EPR6855	145 Nd	Indirect ON	4C	100
	CD7	EPR4242	174 Yb	5h	RT	100
	CD8a	D8A8Y	146 Nd	5h	RT	50
	FOXP3	D608R	159 Tb	Overnight	4C	50
	TCRγδ + 2nd Ab	H41	148 Nd	Indirect ON	4C	50
Myeloid	CD11b	D6X1N	144 Nd	5h	RT	100
	CD11c	EP1347Y	176 Yb	5h	RT	100
	CD14	D7A2T	163 Dy	5h	RT	100
	CD15	MC480	171 Yb	Overnight	4C	100
	CD163	D6U1J	173 Yb	5h	RT	50
	CD204	J5HTR3	164 Dy	5h	RT	50
	CD68	D4B9C	143 Nd	Overnight	4C	100
	HLA-DR	TAL 1B5	141 Pr	5h	RT	100
Tumor/ Stroma	CD31	89C2	147 Sm	Overnight	4C	100
	CD39	EPR20627	157 Gd	5h	RT	100
	CD45	D9M8I	149 Sm	Overnight	4C	50
	CD45RO	UCHL1	165 Ho	Overnight	4C	100
	CD56	E7X9M	167 Er	5h	RT	100
	CD57	HNK-1 / Leu-7	151 Eu	Overnight	4C	100
	D2-40 (PDPN)	D2-40	166 Er	Overnight	4C	100
	Keratin	C11 and AE1/ AE3	198 Pt	Overnight	4C	50
	TGF-β	TB21	115 In	5h	RT	100
	Vimentin	D21H3	194 Pt	Overnight	4C	50
	β-Catenin	D10A8	89 Y	Overnight	4C	100

Supplementary Table 1 *Continued*

	Target	Clone	Metal	Incubation Time	Temp	Dilution (x)
Activation	Granzyme B	D6E9W	150 Nd	5h	RT	100
	ICOS	D1K2T(TM)	161 Dy	5h	RT	50
	IDO	D5J4E(TM)	162 Dy	Overnight	4C	100
	Ki-67	8D5	152 Sm	Overnight	4C	100
	LAG-3	D2G40(TM)	155 Gd	5h	RT	50
	PD-1	D4W2J	160 Gd	5h	RT	50
	PD-L1	E1L3N(R)	156 Gd	Overnight	4C	50
	Tbet	4B10	170 Er	5h	RT	50
	TIM-3	D5D5R(TM)	154 Sm	5h	RT	100
	VISTA	D1L2G(TM)	158 Gd	5h	RT	100
DNA	Histone H3	D1H2	209 Bi	Overnight	4C	50

Supplementary Table 2. Cell types and used lineage markers for the IMC analysis.

Phenotype	Cell type	Lineage markers
B cells	B cells	CD20+
Plasma cells	Plasma cells/Plasmablasts	CD38+
HLA-DR+ CD11c+HLA-DR+	Dendritic cells	CD14-CD68-
Granulocytes	Granulocytes	CD15+
CD56+ CD57+ Innate lymphoid cells Ki-67+	Innate lymphoid cells	CD3-CD7+
CD163+CD204+ CD163+HLA-DR+ CD163+ CD163+CD204+HLA-DR+ Macrophages	Macrophages	CD68+
CD163+CD204+HLA-DR+ CD163+CD204+ CD163+HLA-DR+ CD163+ Monocytes	Monocytes	CD14+CD68-
CD57+ CD8+Ki-67+ CD8+ γδ+ Ki-67+ T cells Regulatory T cells	T cells	CD3+
CD56+ CD57+ PDPN+ Ki-67+ Tumor/Stroma	Tumor/Stroma	Vimentin+lineage markers-
Vessels	Vessels	CD31+

Supplementary Table 3. Univariate cox proportional hazard results for disease-specific and metastasis-free survival in UPS. The survival analysis includes 30 UPS patients who were neoadjuvantly treated with radiotherapy. Surgical margin was excluded because all UPS patients had R0 resection margins. Pathologic response was considered <5% vital tumor after treatment. Abbreviations: CI = confidence interval; HR = hazard ratio.

UPS		
Disease-specific survival	**Univariate**	
Variable	**HR (95% CI)**	**log-rank *P***
Age at diagnosis	1.01 (0.98 - 1.06)	0.7
Sex (Female)		
Male	0.62 (0.19 - 2.03)	0.4
Location (Lower extremities)		
Other[a]	1.3e-08 (0 - Inf)	0.3
Upper extremities	2.1 (0.43 - 10)	
Max tumor size (cm)[b]	1.05 (0.96 - 1.2)	0.3
Pathologic response (Good)		
Poor	0.46 (0.14 - 1.5)	0.2

a: Other includes tumors from the trunk and the head & neck area.
b: Tumor size was missing for one tumor from the head & neck area.

UPS		
Metastasis-free survival	**Univariate**	
Variable	**HR (95% CI)**	**log-rank *P***
Age at diagnosis	1.02 (0.98 - 1.06)	0.3
Sex (Female)		
Male	0.62 (0.24 - 1.6)	0.3
Location (Lower extremities)		
Other	1.3e-08 (0 - Inf)	0.06
Upper extremities	2.8 (0.88 - 8.7)	
Max tumor size (cm)	1.03 (0.95 - 1.1)	0.4
Pathologic response (Good)		
Poor	0.79 (0.31 - 2)	0.6

Supplementary table 4. Univariate and multivariate cox proportional hazard results for disease-specific and metastasis-free survival in MFS. The survival analysis includes 24 high-grade MFS patients who were neoadjuvantly treated with radiotherapy. Pathologic response was considered <5% vital tumor after treatment. Abbreviations: CI = confidence interval; HR = hazard ratio.

Myxofibrosarcoma				
Disease-specific survival	**Univariate**		**Multivariate**	
Variable	**HR (95% CI)**	**log-rank *P***	**HR (95% CI)**	**log-rank *P***
Age at diagnosis	1.1 (0.98 - 1.3)	0.1		
Sex (Female)				
Male	1.4 (0.26 - 7.7)	0.7		
Margin (R0)				
R1/R2	1.3 (0.15 - 12)	0.8		
Location (Lower extremities)				
Trunk	0.58 (0.066 - 5.1)	0.4		
Upper extremities	3.3 (0 - Inf)			
Tumor depth (Deep)				
Superficial	7.1e-10 (0 - Inf)	**0.03 ***	2.4e-09 (0 - Inf)	
Max tumor size	**1.3 (1.1 - 1.5) ****	**4e-04 *****	1.2 (0.97 - 1.4)	**0.002 ****
Pathologic response (Good)				
Poor	**0.096 (0.015 - 0.6) ***	**0.002 ****	0.57 (0.054 - 6)	

Myxofibrosarcoma				
Metastasis-free survival	**Univariate**		**Multivariate**	
Variable	**HR (95% CI)**	**log-rank *P***	**HR (95% CI)**	**log-rank *P***
Age at diagnosis	1 (0.96 - 1.1)	0.4		
Sex (Female)				
Male	1.8 (0.45 - 6.9)	0.4		
Location (Lower extremities)				
Trunk	0.45 (0.56 - 3.6)	0.6		
Upper extremities	0.45 (0.56 - 3.6)			
Margin (R0)				
R1/R2	0.79 (0.1 - 6.3)	0.8		
Tumor depth (Deep)				
Superficial	0.14 (0.17 - 1.08)	**0.03 ***	0.22 (0.026 - 1.9)	
Max tumor size (cm)	**1.2 (1.04 - 1.3) ****	**0.004 ****	1.1 (0.97 - 1.2)	**0.005 ****
Pathologic response (Good)				
Poor	**0.17 (0.044 - 0.66) ***	**0.004 ****	0.46 (0.087 - 2.4)	



4

Multimodal profiling of chordoma immunity reveals distinct immune contextures

S. van Oost, D.M. Meijer, M.E. IJsselsteijn, J. Roelands, B. van den Akker, R. van der Breggen, I.H. Briaire-de Bruijn, M. van der Ploeg, P.M. Wijers-Koster, S.B. Polak, W.C. Peul, R.J.P. van der Wal, N.F.C.C. de Miranda, and J.V.M.G. Bovée

Journal for ImmunoTherapy of Cancer **2024, 12(1).**

ABSTRACT

Chordomas are rare cancers from the axial skeleton which present a challenging clinical management with limited treatment options due to their anatomical location. In recent years, a few clinical trials demonstrated that chordomas can respond to immunotherapy. However, an in-depth portrayal of chordoma immunity and its association with clinical parameters is still lacking.

We present a comprehensive characterisation of immunological features of 76 chordomas through application of a multimodal approach. Transcriptomic profiling of 20 chordomas was performed to inform on the activity of immune-related genes through the immunologic constant of rejection (ICR) signature. Multidimensional immunophenotyping through imaging mass cytometry was applied to provide insights in the different immune contextures of 32 chordomas. T cell infiltration was further evaluated in all 76 patients by means of multispectral immunofluorescence and then associated with clinical parameters through univariate and multivariate cox proportional hazard models as well as Kaplan-Meier estimates. Moreover, distinct expression patterns of Human Leukocyte Antigen (HLA) class I were assessed by immunohistochemical staining in all 76 patients. Finally, clonal enrichment of the T cell receptor (TCR) was sought through profiling of the variable region of *TCRB* locus of 24 patients.

Chordomas generally presented an immune “hot” microenvironment in comparison to other sarcomas, as indicated by the ICR transcriptional signature. We identified two distinct groups of chordomas based on T cell infiltration which were independent from clinical parameters. The highly infiltrated group was further characterised by high dendritic cell infiltration and the presence of multicellular immune aggregates in tumours, whereas low T cell infiltration was associated with lower overall cell densities of immune and stromal cells. Interestingly, patients with higher T cell infiltration displayed a more pronounced clonal enrichment of the TCR repertoire compared to those with low T cell counts. Furthermore, we observed that the majority of chordomas maintained HLA class I expression.

Our findings shed light on the natural immunity against chordomas through the identification of distinct immune contextures. Understanding their immune landscape could guide the development and application of immunotherapies in a tailored manner, ultimately leading to an improved clinical outcome for chordoma patients.

INTRODUCTION

Chordomas are cancers displaying notochordal differentiation that arise predominantly in the axial skeleton at the skull base, the craniocervical and mobile spine, the sacrum, and, occasionally, at extra-axial areas (1). General treatment for chordomas consists of surgical resection and/or (neo-)adjuvant proton beam radiation. Since most chordomas are indolent tumours, chemotherapy is considered ineffective for the treatment of this disease (2). The clinical management of chordoma patients is complicated by the anatomical location of the tumours, their often late detection, as well as treatment-related morbidities (2, 3). Aiming at a gross total or en bloc resection involves sacrifice of neurovascular structures with permanent neurological disabilities. As such, disease recurrence is common after treatment and 30-40% of chordoma patients develop metastases (4). The overall 5-year survival following diagnosis is around 67% and there are currently no curative therapies for chordoma patients with advanced disease (1, 5). This reinforces the need for innovative treatments as local recurrences and distant metastases persist.

Recent findings have provided evidence for the presence of conspicuous immune cell infiltration in chordomas (6, 7) and, encouragingly, clinical responses of chordoma patients to checkpoint blockade immunotherapy targeting CTLA-4 and/or the PD-1/PD-L1 axis have been reported (8-12). This is an intriguing observation as chordomas display a low mutational burden and are, instead, affected by gross chromosomal alterations (13-15). Furthermore, PD-L1 expression is rarely encountered in sarcomas, including chordomas (16-18). Instead, the presence of pre-existing anti-tumour immune responses perceived by the infiltration of cytotoxic T cells in the tumour tissue or by the presence of tertiary lymphoid structures appear to inform on the sensitivity of soft tissue sarcomas to immune checkpoint blockade (19, 20). So far, whether tertiary lymphoid structures are predictive of responsiveness to immune checkpoint blockade has not been investigated in chordomas.

An in-depth immunological characterisation of chordomas and their association with clinical parameters is currently lacking. Here, we applied transcriptomic profiling and multidimensional immunophenotyping by imaging mass cytometry and multispectral immunofluorescence to resolve the immune landscape of chordomas. Chordomas presented hallmarks of anti-tumour immunity and were considered immune “hot” in comparison with other sarcomas. Within our cohort, we identified groups of chordomas with distinct immune contextures, independent from any clinical parameter. Our findings

support the rational utilisation of immunotherapeutic approaches, tailored to target these distinct microenvironments in chordoma.

METHODS

Patient samples

Formalin-fixed paraffin embedded (FFPE) and snap-frozen tissue material was initially collected for 43 and 24 chordomas respectively from 32 patients, followed by a second expansion cohort containing FFPE material of an additional 53 patients. Regions of interest (ROIs) representative for the tumour's immune microenvironment were selected on Haematoxylin & Eosin (H&E) sections of decalcified FFPE tissue by a bone and soft tissue tumour pathologist (JVMGB). These ROIs were then used to create tissue micro arrays (TMAs) using a TMA Master (3DHISTECH). These TMAs were holding 2-4 cores of 1.6 mm in diameter per tumour, dependent on the source of the material or the morphology of the tumour (two cores: biopsy; three cores: resection/excision etc; four cores: heterogeneous morphology, or separate areas of dedifferentiation). As controls and for orientation purposes, each TMA contained three cores tonsil and three cores placenta, either decalcified with EDTA or formic acid or non-decalcified.

RNA sequencing data

RNA was isolated from snap-frozen tissue from 20 primary tumours with TRIzol and Isopropanol/Ethanol. In addition, RNA sequencing data from primary tumours of osteosarcoma patients (n = 7; GSE237033), chondrosarcoma patients (n = 9), undifferentiated soft tissue sarcoma patients (n = 13), and myxofibrosarcoma patients (n = 10) was taken along as a means of comparison. RNA purification was performed with the RNeasy kit which included treatment with DNase. Paired-end 150 base pair (bp) reads were created on a NovaSeq6000 Illumina at GenomeScan (Leiden, The Netherlands). The sequencing data was processed with the RNA-seq BioWDL pipeline from the SASC with default settings (BioWDL Github, LUMC, The Netherlands). Alignment of the 150bp reads to hg38 was performed with STAR, after which the gene expression was quantified with HTSeq-count (21). The processed sequencing data was stored as a matrix containing the counts per gene per sample.

Gene expression analysis

Normalisation and exploratory analysis of the RNA sequencing data was performed in R (v.4.0.2) by using DESeq2 (v. 1.30.1). BiomaRt (R, v.2.46.3)

was used to translate the ensemble IDs to known protein coding genes. The most variably expressed genes were determined by calculating the variance per gene across all samples. The immunologic constant of rejection (ICR) gene signature was used to describe the activity state immune microenvironment and to identify distinct immune-related clusters (Th1-related markers: *IFNG*, *STAT1*, *IL12B*, *IRF1*, *TBX21*; CD8+ T cells: *CD8A*, *CD8B*; Immune effector molecules: *GZMA*, *GZMB*, *GZMH*, *PRF1*, *GNLY*; Chemokine ligands: *CXCL9*, *CXCL10*, *CCL5*; Immune suppressive molecules: *IDO1*, *PDCD1*, *CD274*, *CTLA4*, *FOXP3*) (22). The mean of the log2 normalised expression of these 20 genes was used to attribute an ICR "score" to each sample for comparison between the sarcoma subtypes, which was visualised with ggplot2 (R, v.3.3.6). For both the heatmaps in **figure 1**, a Z-Score was calculated per gene to visualise the transcriptional profile of the samples by using the Ward variance method with ComplexHeatmap (R, v.2.11.1). Differential gene expression analysis was performed with DESeq2 comparing chordomas to all other sarcomas. Genes were considered differentially expressed when the log2 fold change was above 2 and the adjusted *P* value was below 0.01. Immune-related genes were selected for visualisation in the enhanced volcano plot and additional boxplots. For visualisation purposes, the axes of the enhanced volcano plot were manually adjusted as follows: log2 fold change (x-axis) was set between -10 and 10, and the -log10 adjusted *P* (y-axis) was set to a maximum of 100.

Imaging mass cytometry

Conjugation of BSA-free antibodies and immunodetection with a 40-marker tumour immune microenvironment panel (**supplemental table 1**) was performed as previously described (23). In brief, four-µm sections of the created TMAs were deparaffinised and rehydrated, after which heat-induced antigen retrieval was performed in 1x low pH antigen retrieval solution (pH6, Thermo Fisher Scientific). Subsequently, the first batch of primary antibodies were incubated overnight at 4 °C. After washing in PBS supplemented with 1% BSA and 0.05% Tween, conjugated anti-mouse and anti-rabbit antibodies were incubated for one hour at room temperature. Next, the sections were incubated with the second batch of primary antibodies for five hours at room temperature, followed by an overnight incubation at 4 °C with the final batch of primary antibodies. To finish, 1.25 µM of the DNA intercalator Iridium (Fluidigm) was incubated for five minutes to stain DNA, after which the sections were washed, air-dried and stored at room temperature. ROIs of 1000x1000 µm were selected with consecutive H&E slides and ablated by using a Hyperion mass cytometry imaging system (Fluidigm) at the Flow Core Facility (LUMC,

Leiden) within a month after staining. The imaging data was acquired with CyTOF Software (v.7.0), visually inspected and then exported with MCD Viewer (v.1.0.5). In the end, 127 tumour ROIs were successfully ablated and analysed.

Imaging mass cytometry analysis

To correct for variability in signal-to-noise ratios between FFPE sections, the signal intensity of the generated images was normalised at pixel levels by using Matlab (v.R2021a), after which the images were binarised using semi-automated background removal in Ilastik (v.1.3.3) as described previously (23). Probability masks were generated in Ilastik by using a multicoloured image including the DNA channel, CD45 channel, Keratin channel and Vimentin channel to annotate nucleus, cytoplasm and background. Probability masks were loaded into CellProfiler (v.2.2.0) and used for creating cell segmentation masks. Next, the segmentation masks and binarised images were loaded into ImaCyte (24) to generate single cell-FCS files containing relative frequency of positive pixels for each marker, which were then used for phenotyping in CytoSplore (v.2.3.1) by sequentially utilizing Hierarchical Stochastic Neighbour Embedding (H-SNE) and t-distributed Stochastic Neighbour Embedding (t-SNE). Identified cell phenotypes were loaded into ImaCyte together with the segmentation masks and binarised images, which allows the mapping of the phenotypes back onto the images. Phenotypes per image were extracted to calculate the mean cell density per mm^2 for every sample (one image = one mm^2). An overview of the lineage markers used for phenotype identification is listed in **supplemental table 2**. Patients were clustered into two groups based on the Z-Score normalised mean cell densities per mm^2 of all five identified T cell phenotypes by using the Ward variance method with ComplexHeatmap. Ggplot2 was used to visualise the mean cell densities and to compare them between both T cell groups. For statistical testing, a two-sided student's t-test was performed followed by a Benjamini-Hochberg FDR correction. In addition, an overview heatmap containing all identified phenotypes in the microenvironment of chordomas was visualised with ComplexHeatmap.

Spatial interaction analysis

After phenotype calling, a spatial interaction analysis was performed with ImaCyte for all imaged samples, comparing T cell low with T cell high chordomas. ImaCyte utilises a 1000-iteration permutation test which calculates a Z-Score for the interaction between adjacent cells. However, permutation testing does not adjust for overabundant cell types, such as tumour cells, and is therefore not able to identify meaningful interactions for tumour cells. Because

of the range of the calculated Z-Scores, interactions with a Z-Score below 10 were considered not significant and therefore removed for visualisation only. If an interaction Z-Score was higher than 10 in one group and lower than 10 in the other group, this interaction was considered significant for one group. When both Z-Scores were higher than 10, this interaction would be considered significant in both groups. A comparative interaction heatmap between all phenotypes excluding tumour cells was visualised with ggplot2.

Multispectral immunofluorescent imaging of T cells

A T cell panel comprising five markers for five channels was generated for imaging with a Vectra (Akoya Biosciences) as previously described (25) for validation purposes. This panel included FoxP3 (236A/E7, 1:1000, Invitrogen, 14-4777-82), CD8α (D8A8Y, 1:100, Cell Signaling Technology, #85336), CD3ε (EP449E, 1:50, Abcam, ab52959), pan-cytokeratin (AE-1/AE-3 & C11, both 1:50, Novus & Santa Cruz, NBP2-33200AF647 & SC-8018) and Ki-67 (8D5, 1:200, Cell Signaling Technology, #9449) and DAPI as a nuclear staining. In short, slides were deparaffinised and incubated in 0.3% H_2O_2 in methanol for 20 minutes to block endogenous peroxidase. After antigen retrieval in citrate (pH 6.0), slides were incubated for 30 minutes with SuperBlock™ Blocking Buffer (ThermoFisher Scientific). Next, slides were incubated with primary antibody (FoxP3) for one hour at room temperature and subsequently with BrightVision DPVO-HRP (Immunologic) for 30 min at room temperature. Opal 520 reagent (Akoya Bioscience) was diluted in Opal amplification diluent and then added to the slides for one hour at room temperature, after which the slides were heated in citrate buffer (pH 6.0) for 15 min. The second round of primary antibodies (CD8α and Ki-67) were incubated overnight at room temperature and then stained with their respective fluorescent secondary antibodies (CF555, 1:400, Biotum and Alexa 680, 1:200, Invitrogen) for one hour at room temperature. Finally, the slides were stained with directly conjugated antibodies (CD3ε-Alexa 594 and pan-cytokeratins-Alexa 647) for 5 hours at room temperature and then mounted. All TMAs were imaged at 20x, after which the images were processed with inForm (v.2.4), which comprises background removal for each antibody by normalisation of the spectra, and analysed with QuPath (v.0.3.1). Object classification was performed by using the following classes: $CD3^+FOXP3^+$ = Regulatory T cells, $CD3^+CD8^+$ = $CD8^+$ T cells, $CD3^+$ = $CD4^+$ T cells, $CD3^+Ki\text{-}67^+$ = Proliferating T cells, CD3- = Rest. Counts per image (one image = 1 mm x 1.3 mm) were normalised per patient to counts per mm^2 tissue. Patients were divided into a T cell high and low cluster based on the unsupervised clustering of the Z-scores of all T cell phenotypes in R.

Survival analysis

For all chordoma patients, Kaplan-Meier curves for the disease-specific survival and recurrence-free survival were generated with the survminer and survival packages (R, v.0.4.9 and v.3.1-12 respectively). The disease-specific survival was considered the survival of a patient until death due to the disease, whereas the recurrence-free survival was considered the time until a patient was diagnosed with a recurrence, thereby excluding patients who did not receive surgery. Since the cohort included many censored cases, the log-rank *P* value was used to estimate the significance of the associations. Known prognostic factors such as the anatomical tumour location excluding the only extra-axial patient, age and type of treatment, surgical margin excluding patients who did not receive surgery and disease recurrence were investigated for their prognostic value, as well as the newly identified T cell infiltration groups. Univariate and multivariate analyses were performed in R according to the cox proportional hazard model. Only clinical parameters that were found significant in the univariate analysis were taken along in the multivariate analysis.

Immunohistochemical detection of HLA class I and β-2m

Immunohistochemistry was performed for the HLA class I heavy chain (HCA2, 1:1000, Nordic Bio, MUB2036P; HC10, 1:3200, Nordic Bio, MUB2037P) and β-2m (EPR21752-214, 1:4000, Abcam, ab218230) on all generated TMAs as described previously (26). Briefly, antigen retrieval was performed in citrate (pH 6.0), after which the TMA sections were pre-incubated with PBS-5% non-fat dry milk for 30 min at room temperature. Primary antibody dilutions were incubated overnight at 4 °C, after which the sections were incubated with BrightVision DPVO-HRP (Immunologic) for 30 min at room temperature. Finally, TMA sections were further developed with liquid DAB+ chromogen (Dako) for 10 min and subsequently counterstained with haematoxylin. Samples were classified as HLA class I positive, weak, or defective depending on the expression pattern of HC10 and HCA2 in the tissue and the contrast between the expression of the tumour cells and the immune cells. Tumours were classified as defective if one or more of the HLA class I antibodies were negative in the tumour cells. The distribution of the expression patterns among the identified T cell groups was visualised in R using ggplot2.

TCR β-chain sequencing

DNA was isolated from snap-frozen tissue from 27 chordomas from 23 patients for sequencing of the variable region of the *TCRB* locus. In brief, DNA libraries were generated with the AmpliSeq Library Kit Plus and the OncoMine TCRβ-

SR Assay following the manufacturer's instructions. Sample libraries were measured with the ION Library TaqMan Quantitation Kit and then pooled to a final concentration of 25 pM. Next, the pooled libraries were templated on ION 540 Chips with the Ion Chef System. The 80bp reads were created on an Ion GeneStudio S5 Prime Sequencing Technology at GenomeScan (Leiden). The number of clones and the Shannon diversity, a measure for clonal enrichment, were calculated in R by using productive counts only, meaning that a clone needed at least 10 plus and 10 minus counts. Because recurrences showed similar levels of TCR diversity as their respective primary tumour, we used the TCR repertoire of recurrences for three patients for which there was no frozen material of primary tumours available. Finally, the data was visualised in R using ggplot2.

RESULTS

Patient characteristics

In this study, two cohorts were established to investigate the immune microenvironment of chordomas. The first cohort included primary tumours of 32 patients and was explored using RNA sequencing (*n* = 20) and imaging mass cytometry (*n* = 32). The median age was 59 years (range 1 - 80 years) and the median follow-up time was 66 months (range 0 - 418 months). In total, the primary tumours in the cohort comprised eight skull base chordomas (25%), seven spinal chordomas (22%) and 17 sacrococcygeal chordomas (53%). The second cohort included primary tumours of an additional 53 patients. The median age of this cohort was 60 years (range 22 – 80) and the median follow-up time was 41 months (range 0 - 182). In total, this cohort comprised 17 skull base (32%), 15 spinal chordomas (28%), 20 sacrococcygeal chordomas (38%) and one extra-axial chordoma of the ribs (2%). The second cohort also comprised patients solely treated with radiotherapy, for which the treatment-naïve biopsies were used. All profiled primary tumour samples were annotated for their anatomical location as well as whether they underwent neoadjuvant radiotherapy. Further patient characteristics of both cohorts are listed in **table 1**.

Table 1. Patient characteristics of chordoma cohorts. This table contains an overview of each cohort separately as well as both cohorts combined.

Variable	First		Second		Combined	
Total patients, *n*	32		53		85	
Gender, *n* (%)						
Female	15	(46.9)	21	(39.6)	36	(42.4)
Male	17	(53.1)	32	(60.4)	49	(57.6)
Age (years), *median* (range)	59	(1-80)	60	(22-80)	60	(1-80)
Follow-up (months), *median* (range)	66	(0-418)	41	(0-182)	50	(0-418)
Anatomical location, *n* (%)[a]						
Skull base (Clivus)	8	(25.0)	17	(32.1)	25	(29.4)
Mobile spine (Craniocervical, Cervical, Thoracic, Lumbar)	7 (0, 1, 4, 2)	(21.9)	15 (3, 10, 1, 1)	(28.3)	22	(25.9)
Sacrococcygeal	17	(53.1)	20	(37.7)	27	(31.8)
Extra-axial (Costa)	-	-	1	(1.9)	1	(1.2)
Max tumour size (cm), *median* (IQR)[b]	7	(4.5)	6	(6.1)	6.1	(5.6)
Skull base (Clivus)	2.8	(0.88)	4.3	(1.5)	4	(2.5)
Mobile spine (Craniocervical, Cervical, Thoracic, Lumbar)	5.5	(3.4)	4.9	(1.4)	5	(1.7)
Sacrococcygeal	8	(4)	10.5	(3.6)	9	(3.9)
Extra-axial (Costa)	-	-	10	-	10	-
Treatment, *n* (%)						
Radiotherapy alone	-	-	11	(20.8)	11	(12.9)
Surgery alone	21	(65.6)	19	(35.8)	40	(47.1)
Surgery & radiotherapy	11	(34.4)	23	(43.4)	34	(40)
Other radiotherapy regimens, *n* (%)						
Monotherapy, conventional	-	-	1	(1.9)	1	(1.2)
Monotherapy, proton beam	-	-	9	(17)	9	(10.6)
Monotherapy, carbon ion	-	-	1	(1.9)	1	(1.2)
Sandwich, proton beam	-	-	2	(3.8)	2	(2.4)
Pre-operative radiotherapy, *n* (%)[c]						
Conventional	4	(12.5)	2	(3.8)	6	(7.1)
Proton beam	2	(6.3)	1	(1.9)	3	(3.5)
Post-operative radiotherapy, *n* (%)[c]						
Conventional	5	(15.6)	7	(13.2)	12	(14.1)
Proton beam	-	-	11	(20.8)	11	(12.9)
Patients with recurrent disease, *n* (%)[d]						
Local recurrence	16	(50)	29	(54.7)	45	(52.9)
Metastasis	6	(18.8)	14	(26.4)	20	(23.5)

[a]anatomical location of the primary tumours; [b]size was not available for 8 and 11 primary tumours in the initial and the additional cohort respectively (4 skull base and 2 mobile spine; 2 skull base, 2 mobile spine and 7 sacrococcygeal); [c]treatments regarding primary tumours; [d]Patients who experienced recurrent disease during follow-up. With the exception of 3 patients in the additional cohort, metastatic disease followed local recurrence.

Chordomas present transcriptional hallmarks of anti-cancer immunity

The transcriptomic profiles of the 20 chordomas were compared to those of osteosarcomas (*n* = 7), chondrosarcomas (*n* = 9), undifferentiated soft tissue sarcomas (USTS) (*n* = 13), and myxofibrosarcomas (*n* = 10). All chordoma samples clustered separately from the remaining sarcomas following unsupervised clustering based on the 200 genes with most variable expression among all samples (**figure 1A**). Sample clustering was largely driven by features related to the line of differentiation of the different sarcoma samples, with known chordoma-related genes such as *TBXT*, *CD24*, and several keratins enriched in the chordomas (27-29) (**figure 1A**, **supplemental table 3**). Moreover, genes associated with the extracellular matrix and adhesion related genes were enriched in chordomas and chondrosarcomas as compared to the other sarcomas (**figure 1A**, **supplemental table 3**). Interestingly, several immune-related genes, including Human Leukocyte Antigen (HLA) class I, HLA class II, *PLA2G2D* and immunoglobulin genes, were among the most variably expressed genes and were enriched in specific chordomas. Furthermore, differential gene expression analysis revealed enrichment for other immune-related genes in chordomas in comparison with the other sarcomas (**supplemental figure 1A-B**, **supplemental table 4**).

To substantiate that immune-related processes are enriched in chordomas, we evaluated the expression of genes included in the Immunologic Constant of Rejection (ICR) gene signature to compare between the distinct sarcoma subtypes (22). This 20 gene signature reflects the activation of type 1 T (Th1) cell signalling, expression of CXCR3/CCR5 chemokine ligands, cytotoxicity and counter-activation of immunoregulatory mechanisms and was previously shown to be an independent prognostic factor for metastasis-free survival in soft tissue sarcomas (30). Most chordomas are characterised by a high expression of ICR genes (ICR high) (**figure 1B**), particularly when comparing the ICR score (average of the 20 ICR genes) with samples from other sarcoma types (**figure 1C**). Furthermore, the ICR high immune subtype was associated with improved disease-specific survival in this cohort, albeit only three cases were classified as ICR low (Log rank *P* = 0.0055; **figure 1D**).

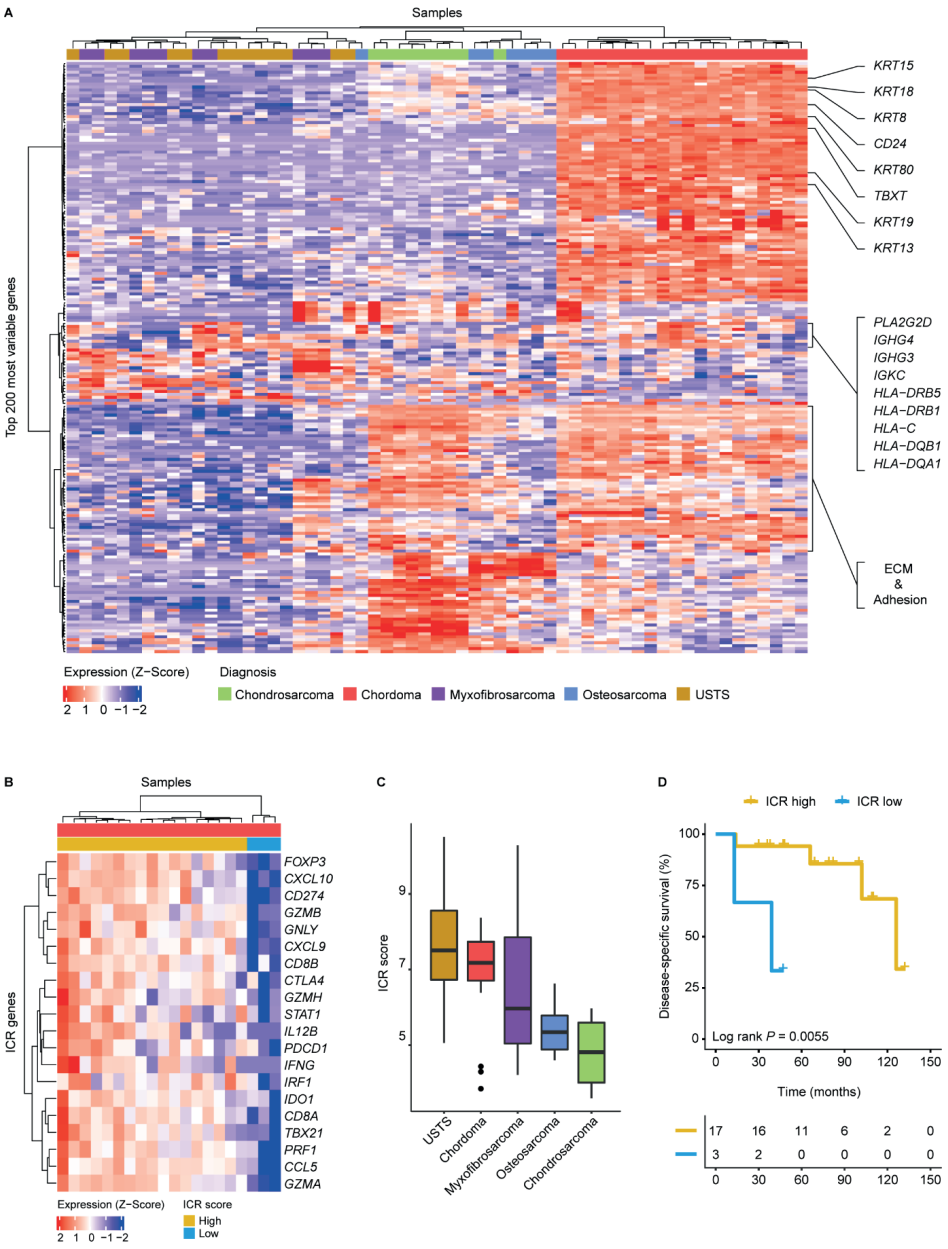


Figure 1 | Chordomas display hallmarks of anti-tumour immunity.

Figure 1 | Chordomas display hallmarks of anti-tumour immunity. A) Heatmap demonstrating the log2 normalised gene expression Z-Score of the top 200 most variably expressed genes in all sarcoma samples (n = 59). Samples are annotated according to their histotype. Genes associated with chordoma samples are highlighted on the right. These genes include chordoma-specific genes such as *TBXT, CD24* and several keratins. In addition, immune-related genes are highlighted, including Human Leukocyte Antigen (*HLA**) and immunoglobulin (*IG**) genes. **B)** Heatmap presenting the Z-Score for the log_2 normalised expression of the 20 ICR signature genes in 20 chordoma samples. Based on the expression Z-Score, the samples are classified into two groups through unsupervised hierarchical clustering: ICR high (n = 17) and ICR low (n = 3). **C)** Boxplots presenting the Immunologic Constant of Rejection (ICR) score per sarcoma subtype in descending order. **D)** Kaplan-Meier curves displaying disease-specific survival for the ICR high and ICR low chordomas. Two-sided log-rank tests were performed for the Kaplan Meier estimates. ECM = extracellular matrix; USTS = undifferentiated soft tissue sarcoma.

T cell infiltration in chordomas correlates with ICR score and separates patients into distinct groups

To confirm and expand our initial observations, we performed imaging mass cytometry to characterise the immune cell contexture of 32 primary tumours. Twenty-nine cell populations were identified including five T cell phenotypes comprising $CD4^+$ T cells, $CD8^+$ T cells, Ki-67^+ T cells, regulatory T cells and (unspecified) T cells including low numbers of $CD57^+$ and gamma delta T cells (**supplemental figure 2**). Since the ICR transcriptional signature is largely reminiscent of T cell-driven immune responses, we investigated the association between T cell infiltration and the ICR score. Indeed, T cell infiltration was more abundant in ICR high chordomas as compared to ICR low samples (**supplemental figure 3A**). Of note, T cells were detected in all chordomas although the levels of infiltration were highly variable, both within and between lesions, ranging from 6.5 to 284.6 cells / mm^2 (median = 51 cells / mm^2) between tumours (**figure 2A, B**). Although the vast majority of T cells was confined to the stromal compartment surrounding the tumour lobules, most tumours also show infiltration of a low number of T cells within the cancer cell compartment. Other commonly observed immune cell populations included various subsets of myeloid cells, such as monocytes, macrophages, dendritic cells, and granulocytes (**supplemental figure 2**).

Next, chordoma samples were clustered according to the extent of infiltration of the different T cell populations leading to the definition of two major groups (high vs. low T cell infiltration; **figure 2C-D**). Of note, infiltration by $CD4^+$ and $CD8^+$ T cells was highly correlated across the cohort (**supplemental figure 3B**). All three chordoma samples previously classified as ICR low clustered in the T cell low group but samples that were previously classified as ICR high were equally distributed between high and low T cell groups (**figure 2C**),

demonstrating the additional value of image-based evaluation of immune cell infiltration in solid tumours. Although it appeared that patients with higher T cell infiltration have an improved disease-specific survival, the observed association was not statistically significant (Log rank *P* = 0.11, **figure 2E**). There was no association between T cell infiltration and recurrence- or metastasis-free survival (**supplemental figure 4A-B**). Moreover, unsupervised clustering of sequential tumours of six patients revealed that the immune contexture of chordomas can change upon disease recurrence or metastasis (**supplemental figure 4C**).

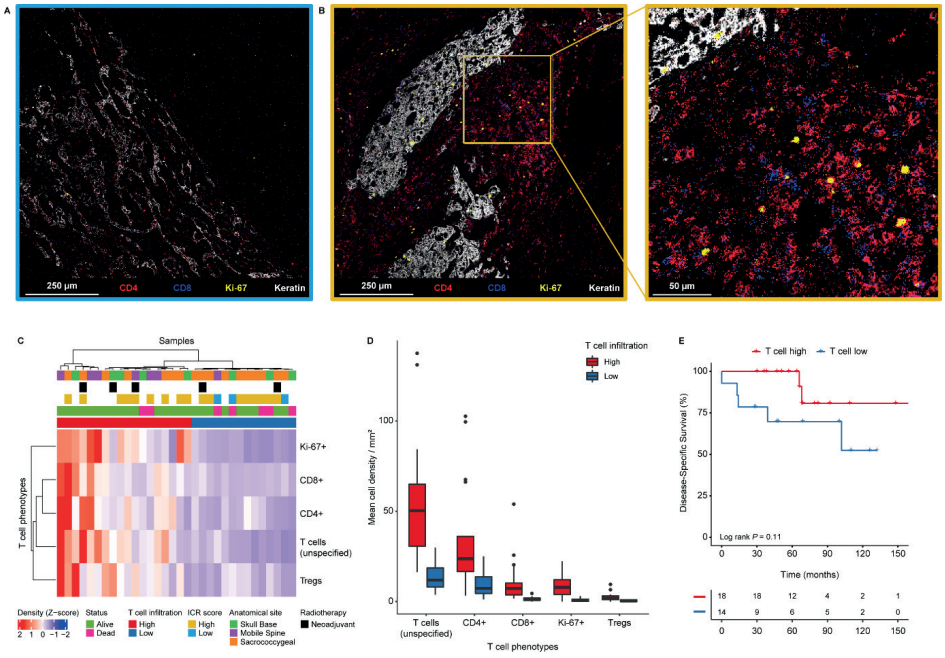


Figure 2 | Chordomas present distinct groups based on T cell infiltration. A-B) Heterogeneity in T cell infiltration in chordomas. The images show T cell-related markers (CD4 = red, CD8 = blue), a proliferation marker (Ki-67 = yellow) and a tumour marker (keratin = white) as detected by imaging mass cytometry. **A)** chordoma with low T cell infiltration (ICR low). **B)** chordoma with high T cell infiltration and a magnified image of the chordoma with high T cell infiltration (ICR high). **C)**, Heatmap showing the mean cell density Z-Score of all T cell phenotypes in all chordoma samples (n = 32), hierarchically clustered into a T cell high (n = 18) and T cell low (n = 14) group. Samples are annotated with their respective ICR score from the transcriptional analysis. In addition, the samples are annotated for their anatomical location, the follow-up status of the patients as well as whether the sample had received neoadjuvant radiotherapy. **D)** Boxplots presenting the mean cell densities per mm² per classified T cell group (T cell high: n = 18; T cell low: n = 14) for the identified T cell phenotypes. **E)** Kaplan-Meier curves interrogating the association between T cell infiltration and disease-specific survival. Two-sided log-rank tests were performed for the Kaplan Meier estimates. ICR = immunologic constant of rejection; Tregs = regulatory T cells.

Antigen-presenting myeloid cells are abundant in T cell high chordomas and co-localise with T cells

Further exploration of the imaging mass cytometry data revealed that high T cell infiltration was accompanied by the presence of dendritic cells (T cell high vs T cell low, $P < 0.001$, Benjamini-Hochberg corrected false discovery rate [FDR] = 0.0052, **figure 3A**). In addition, we found that T cell high chordomas were characterised by increased numbers of immune cell aggregates mainly composed of T cells and myeloid cells ($P < 0.001$, FDR = 0.0052, **figure 3A**). Other phenotypes that were significantly associated with T cell infiltration include CD11c$^+$HLA-DR$^+$ macrophages ($P = 0.014$, FDR = 0.048), CD163$^+$HLA-DR$^+$ macrophages ($P = 0.0079$, FDR = 0.035), granulocytes ($P = 0.0082$, FDR = 0.035), podoplanin$^+$ stromal cells ($P < 0.001$, FDR = 0.0052) and vessels ($P = 0.0088$, FDR = 0.035; **supplemental figure 5A-B**). No specific phenotypes were associated with low T cell infiltration. Instead, this group exhibited a significantly lower density of immune cells ($P < 0.001$) and stromal cells ($P < 0.01$), resulting in a higher relative proportion of tumour cells (**supplemental figure 5C**). HLA class II expression (HLA-DR) was only detected on immune cell populations and never on tumour cells.

A comparative neighbourhood analysis on the imaging mass cytometry data was conducted to reveal distinct interaction patterns between both T cell groups independent of their overall abundance (**figure 3C**). Naturally, most interactions involving T cells were enriched in the T cell high group, where most T cell phenotypes interacted with each other, with the exception of regulatory T cells which were only enriched in the neighbourhood of CD39$^+$ stromal cells (**figure 3C**) The pro-inflammatory nature of the microenvironment of T cell high chordomas was further reinforced by the observed interactions between dendritic cells and CD8$^+$ and Ki-67$^+$ T cells as well as CD38$^+$ plasma B cells and CD4$^+$ and unspecified T cells (**figure 3C**). Most notably, the co-localisation of Ki-67$^+$ T cells with CD4$^+$ T cells and dendritic cells suggests interaction between these anti-tumour immune cells in a coordinated manner. In contrast, the most dominant interactions in the microenvironment of T cell low chordomas involved macrophage and stromal cell subsets including CD163$^+$HLA-DR$^+$ macrophages, stromal cells, vessels and CD39$^+$ vessels (**figure 3C**). These observations suggest that the presence of T cells in T cell high chordomas accompanies a coordinated inflammatory response that also involves antigen-presenting myeloid cells such as dendritic cells, whereas the T cell low chordomas appear to be dominated with myeloid and stromal cell interactions.

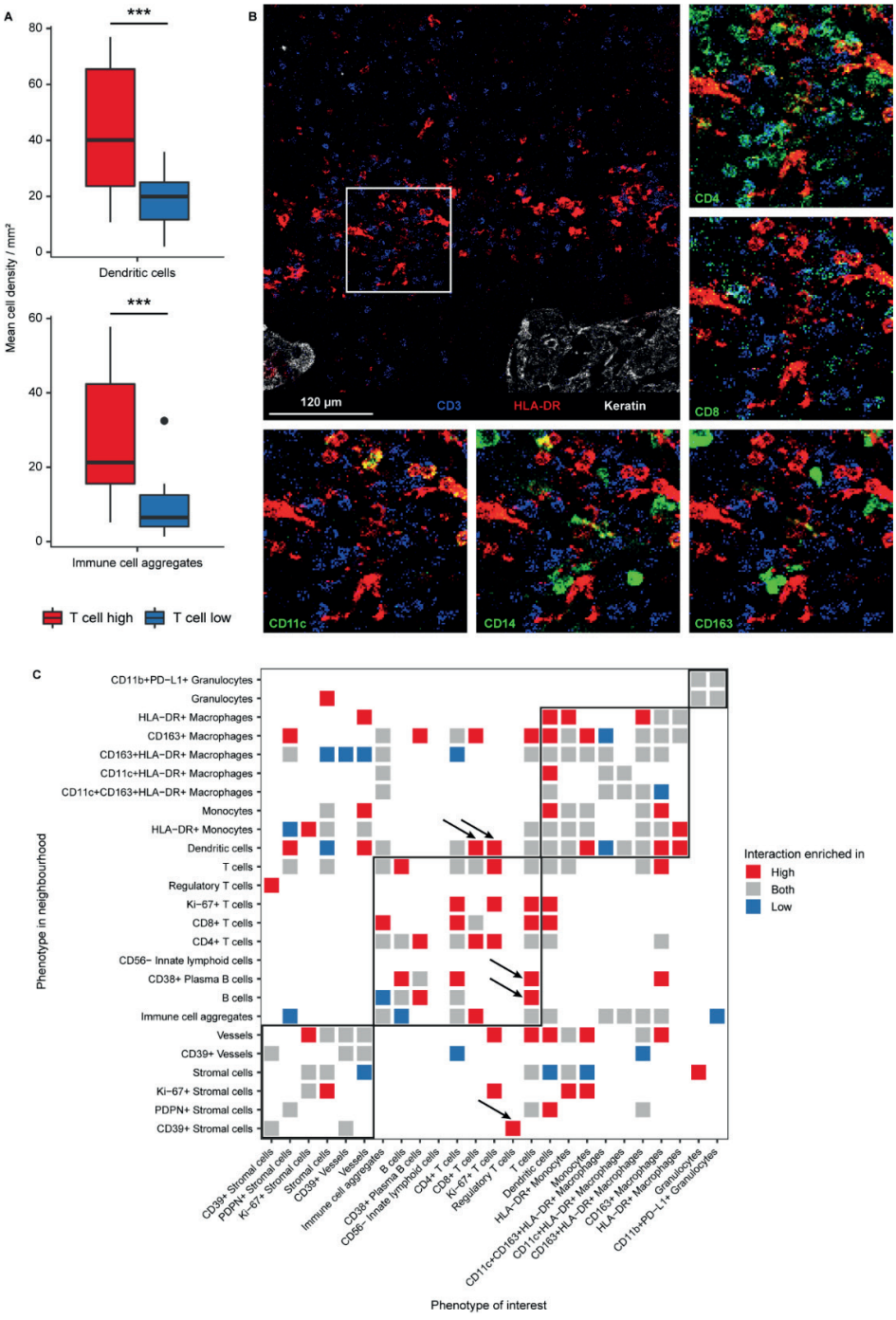


Figure 3 | Pro-inflammatory interactions shape the immune microenvironment of T cell high chordomas.

Figure 3 | Pro-inflammatory interactions shape the immune microenvironment of T cell high chordomas. A) Boxplots comparing cell densities between the T cell high (n = 18) and T cell low groups (n = 14). Dendritic cells ($CD11c^{+/-}HLA\text{-}DR^{+}CD68^{-}$) and immune cell aggregates ($CD45^{+}$ and multiple differentiation markers, e.g. $CD3^{+}CD68^{+}$) are significantly higher in the T cell high group as compared to the T cell low group. Two-sided t-test was performed in R and the P value was adjusted with the Benjamini-Hochberg false discovery rate (FDR). * = P < 0.05; ** = P < 0.01; *** P < 0.001. **B)**, An image generated with imaging mass cytometry displaying co-localisation of dendritic cells (HLA-DR = red) and T cells (CD3 = blue). Tumour cells are only shown in the overview image (top-left image, keratin = white). Other myeloid and T cell-related markers are presented in separate images around the overview image in green (CD4, CD8, CD11c, CD14 and CD163), to show co-localisation of different markers. **C)** Heatmap displaying the spatial interaction analysis results comparing the microenvironment of T cell high with T cell low chordomas. Only significant interactions are visualised and coloured for the subgroup(s) in which they are enriched. Permutation Z scores below 10 were considered not significant and thus removed for visualisation. Interactions of interest are indicated by black arrows. PDPN = podoplanin.

The extent of T cell infiltration in chordomas is independent of clinical parameters

To further explore the relation between the microenvironment of chordomas and the clinical behaviour of the disease, we performed multispectral immunofluorescence on the complete patient cohort (*n* = 76). A T cell-orientated antibody panel was designed to evaluate the expression of CD3, CD8, FoxP3, Ki-67 and pan-cytokeratin. Following cell phenotyping and automated counting, patients were clustered into T cell high and low groups (**figure 4A, B**). Also in this cohort, a positive correlation was observed between $CD4^{+}$ and $CD8^{+}$ T cell infiltration (**supplemental figure 6A**). No significant association was found between T cell infiltration and disease-specific survival (Log-rank *P* = 0.17, **figure 4C**). Further, we have investigated a potential effect of specific T cell phenotypes but not association with survival was found (supplemental table 5). Of note, a higher proportion of KI-67+ cells was found in the $CD8^{+}$ T cell population when compared to $CD4^{+}$ T cells (*P* = 0.006, **supplemental figure 6B**).

Clinical features, such as anatomical location of the tumour or neoadjuvant radiotherapy, were not associated with T cell infiltration, suggesting that the presence of a coordinated immune response is not dependent on neoadjuvant radiation or the tumour's location (**figure 4A**). Further associations between clinical parameters and prognosis were explored through cox proportional hazard models for the disease-specific, recurrence-free and metastasis-free survival, which are all presented in **supplemental table 6**. In short, previously established clinical parameters such as anatomical location of the primary tumour or the surgical resection margin were confirmed as prognostic factors.

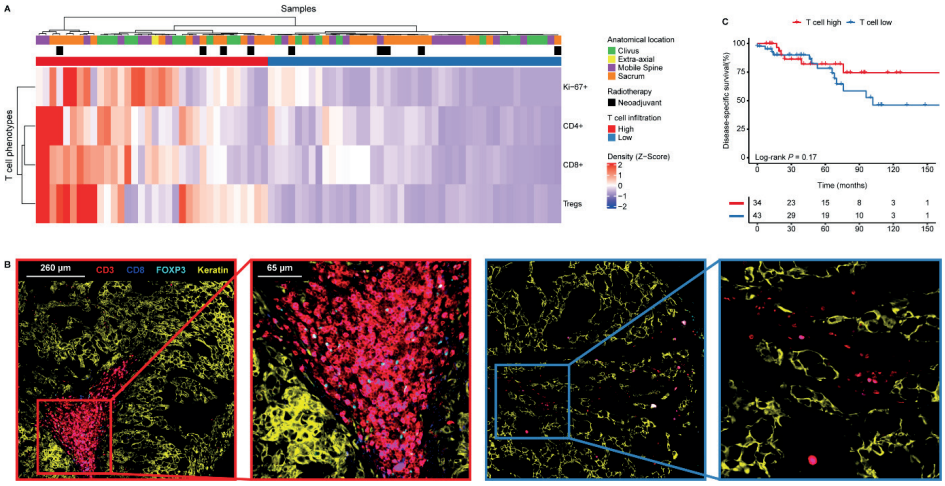


Figure 4 | T cell infiltration is independent from clinical parameters A), Heatmap displaying the mean cell density Z-Score per T cell phenotype as identified with multispectral immunofluorescence in the entire cohort (n = 76). The samples are clustered in an unsupervised manner and thereby marked as T cell high (n = 34) or T cell low (n = 42). The samples are annotated for their respective anatomical location and whether they had received radiotherapy prior. **B)** Images displaying different T cell infiltration patterns as generated by multispectral immunofluorescence. The original and magnified images show T cell-related markers (CD3 = red, CD8 = blue, FOXP3 = cyan) and a tumour marker (keratin = yellow) in two chordomas, each annotated for their respective T cell group (T cell high = red rectangles; T cell low = blue rectangles). **C)** Kaplan-Meier curves of the disease-specific survival comparing the T cell high an T cell low groups of the entire cohort. Two-sided log-rank tests were performed for the Kaplan Meier estimates. Tregs = regulatory T cells.

Figure 5 | Antigen presentation and T cell clonal enrichment are present in chordomas. A) Human Leukocyte Antigen (HLA) class I (HCA2 and HC10) and β-2m expression patterns as validated by immunohistochemistry presenting the distinct expression patterns. From top to bottom, these images display positive expression of HLA class I and thus also β-2m, weak expression of HLA class I and β-2m and defective expression of HLA class I accompanied by weak expression of β-2m. **B)** Stacked bar plots displaying the percentual distribution of the observed HLA class I (both HCA2 and HC10) expression patterns in the chordoma samples in both T cell groups (T cell high: n = 34; T cell low: n = 40) **C-D)** Boxplots displaying the Shannon diversity **C)** and the number of unique clones **D)** of the profiled T cell receptors (TCR) from the immune microenvironment of chordomas (n = 23). Both the Shannon diversity and the number of unique clones are compared between the T cell high (n = 10) and the T cell low (n = 13) groups. Two-sided t-tests were performed to compare the T cell high and the T cell low group. * = P < 0.05; ns = not significant (P > 0.05). **E)** Boxplots presenting the Shannon diversity in relation to the observed HLA class I expression patterns in the subset that underwent TCR profiling (n = 22).

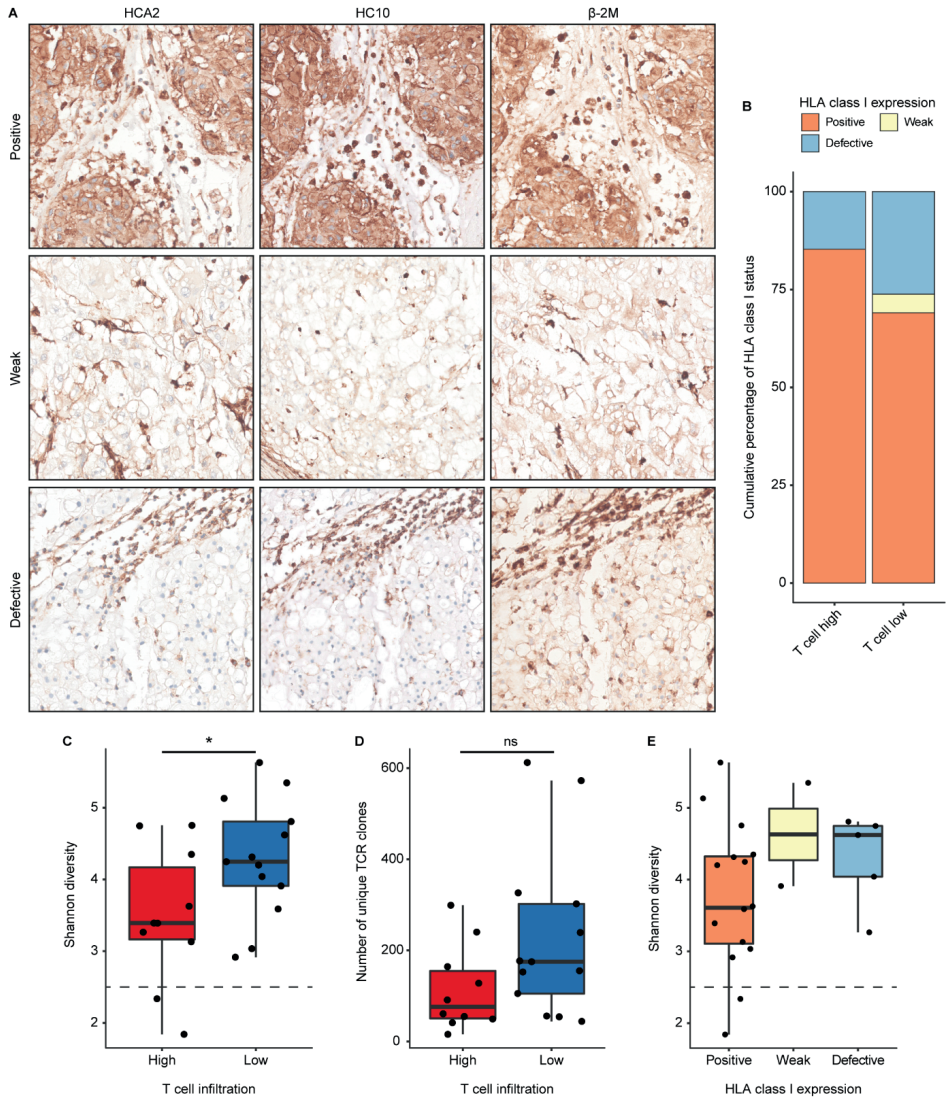


Figure 5 | Antigen presentation and T cell clonal enrichment are present in chordomas.

HLA class I expression is maintained in chordomas, but strong clonal expansion of T cells is rare

Strong immune selective pressure by T cells can lead to immune evasion by tumour cells, most notoriously through loss of HLA class I expression. Since high expression of HLA class I-related genes on RNA level does not preclude the loss of HLA class I expression due to, for instance, mutations in the *B2M* gene, we investigated the prevalence of HLA class I defects by immunodetection (**figure 5A**). In the complete cohort, HLA class I and β-2m membranous expression was observed in the majority of chordomas (73%). However, 22% of chordomas displayed defective HLA class I expression, which was accompanied by either loss or low expression of β-2m. The remaining 5% of the cases showed very weak expression of HLA class I and/or β-2m, which was identified by stronger stromal expression of HLA class I/β-2m but weak expression in the tumour cells. Thus, up to 27% of chordoma samples presented some form of impaired or altered antigen presentation. Interestingly, patients in the T cell low group more often had defective or weak HLA class I expression in comparison to T cell high patients (**figure 5B**). Positivity for HLA class I was relatively more frequent in T cell high patients (**figure 5B**). HLA class I expression was also examined specifically in the context of $CD8^+$ T cell infiltration but no association between HLA class I phenotypes and $CD8^+$ T cell infiltration was found (**supplemental figure 6C**). Intriguingly, we observed intratumoral γδ T cell infiltration in one T cell high chordoma lacking HLA class I expression (**supplemental figure 7A-B**). γδ T cells have recently been proposed as effectors of immunotherapy in HLA class I-defective cancers (31). These results indicate that HLA class I expression and, therefore, antigen presentation is maintained in the majority of chordomas.

Presentation of tumour antigens can lead to the specific enrichment of T cell clones with anti-tumour specificity in the tumour tissues. To investigate the clonality of T cell responses in chordomas, we sequenced the variable region of the *TCRB* locus in 27 chordoma samples from 23 patients. Intriguingly, T cell high chordomas presented a more focused TCR repertoire than T cell low chordomas, which was demonstrated by the lower number of unique clones ($P = 0.068$) and Shannon diversity ($P = 0.047$) in T cell high chordomas compared to T cell low chordomas (**figure 5C-D**). Additionally, tumours displaying a Shannon diversity below 2.5 were only contained within the T cell high group, suggesting the presence of strong clonal expansion in two T cell high chordomas (**figure 5C**). To substantiate the evidence for enriched TCR clonality, the Shannon diversity was compared to the HLA class I expression pattern of these 23 tumours, which revealed that patients with positive HLA class I expression,

presented a more enriched TCR repertoire than patients with either defective or weak HLA class I expression (**figure 5E**).

DISCUSSION

Through a multimodal approach comprising RNA sequencing, imaging mass cytometry, multispectral immunofluorescence and TCR profiling, we studied the immune microenvironment of in total 77 chordoma patients. We found that chordomas present many hallmarks of anti-tumour immunity. We observed the majority of chordomas to have an "immune hot" microenvironment based on their immune-related transcriptomic profile, especially compared to other bone sarcomas (e.g. chondrosarcoma and osteosarcoma). Spatial analysis of immune cell infiltration further defined groups of chordoma patients based on the prevalence of T cell phenotypes. Increased T cell infiltration was associated with an apparently coordinated anti-tumour immune response as indicated by the presence of dendritic cells and other immune cells in immune cell aggregates. In contrast, chordomas with lower T cell infiltration were characterised by a microenvironment dominated by interactions comprising stromal cells and myeloid cells. Neither group was associated with clinical outcome nor with any other clinical parameter.

Recently, several studies have contributed to the improved understanding of the chordoma microenvironment, based on approaches including immunohistochemistry, multispectral immunofluorescence or single cell-RNA sequencing (6, 7, 29, 32, 33). These studies identified myeloid cells and T cells as the most predominant immune cell populations in chordomas (7, 29, 32, 33). Similar to our findings, the majority of these immune cells was confined to the stroma, although both cell types could be found in the tumour nodules (6, 7, 33). Moreover, other lymphoid cells such as NK cells (or innate lymphoid cells) and B cells were considered rare in chordomas (7, 29, 33). Using imaging mass cytometry, we expanded on the previously identified immune cell populations and were able to establish immunologically relevant interactions within the chordoma microenvironment.

Studies focussed on methylation and RNA sequencing have identified groups of patients with either an inflamed or non-inflamed phenotype and associated these groups to clinical outcome, all with varying implications (34-36). For instance, Zuccato *et al.* found through methylation profiling that a group of patients presenting an inflamed phenotype had a worse prognosis than patients without these inflammatory features (35), whereas Huo *et al.*

observed that patients from the non-inflamed group had a worse clinical outcome (34). Furthermore, Baluszcek *et al.* described two similar groups based on methylation and transcriptomic profiling, without finding an association between these groups and survival (36). All these studies, however, either only include skull base chordomas or skull base chordomas combined with spinal chordomas. The variable composition of the cohorts based on institutional referral patterns complicates the identification of common prognostic markers across studies. Here we included tumours from all major anatomical locations as well as different treatment strategies, providing an extensive characterisation of a uniquely large series of chordomas as representative of the general patient population as possible. Presently, the cause of the apparent disconnect between the immune microenvironment and clinical outcomes in chordoma remains uncertain. It is conceivable that the extensive and intricate surgical interventions required for chordoma treatment exert a more significant influence on clinical outcomes than the natural immune response. Future investigations might delve into this by examining the prognostic significance of the immune microenvironment in patients exclusively undergoing radiotherapy. Alternatively, it is plausible that an inadequate cytotoxic T cell response stems from a lack of available CD8+ T cell epitopes due to the low mutation burden of chordomas, offering another potential explanation.

Nevertheless, most studies, including ours, support the separation of distinct groups of chordomas based on the abundance of pro-inflammatory immune cells in their microenvironment. Little is known, however, regarding potential drivers of these different immune contextures. In other tumour types (e.g., melanoma, carcinomas) spontaneous immune responses can often be explained by the mutation burden of a cancer where tumours with high mutation burden more often experience spontaneous anti-tumour immune responses as a consequence of high neoantigen abundance. In contrast, similar to most other sarcomas, the number of somatic, coding mutations in chordomas is generally low and stable between patients making it unlikely that distinct immune responses can be explained by the overall mutation burden of the tumours (13-15, 37). Although we only found evidence for strong clonal expansion in two T cell high chordomas, the TCR repertoire was less diverse in T cell high chordoma than T cell low chordomas, which would support that antigen recognition is a potential driver of immunity in chordomas. Naturally, this raises the question whether there is some specificity for the known chordoma-related transcription factor brachyury (*TBXT*) in these tumours, as it has increasingly been demonstrated that it can be recognised by T cells as

well as that it can be targeted by means of vaccination in chordomas (9, 38). Another possible underlying factor to these distinct groups could be the extent of immunosuppressive mechanisms in the chordoma microenvironment. For instance, we identified abundant CD39 expression on vessels and stromal cells, in the vicinity of immune cells in both T cell high and T cell low chordomas, suggesting that the adenosine pathway might be a potential mediator of immune suppression in chordomas. Although the immunosuppressive functionalities of this pathway have mainly been described in carcinomas (39, 40), expression of CD39 was recently found to associate with increased inflammation in primary tumours as well as with increased T cell densities and PD-1 expression in recurrent undifferentiated soft tissue sarcomas (41). Further research should determine the extent to which the adenosine pathway can modulate immune responses in this disease.

Going forward, it will be crucial to understand how the chordoma microenvironment impacts the outcomes of immunotherapy, in particular immune checkpoint blockade therapy. Intuitively, and as observed in other tumour types, responses should be more likely to occur in patients where spontaneous anti-tumour immune responses are observed. Encouragingly, our data also supports the notion that most chordoma patients may be eligible to immunotherapeutic approaches as: 1) despite differences in the extent of immune infiltration between tumours, the majority of chordomas display enhanced hallmarks of anti-tumour immunity as compared to other sarcoma types and 2) we determined that the majority of chordoma cases retain HLA class I expression and, therefore, antigen presentation. Therefore, other approaches including antigen vaccination or T cell based immunotherapies are, in theory, applicable for chordoma patients and may be particularly important in chordomas that do not present with a conspicuous anti-tumour immune response. We speculate that providing immunotherapy in the neoadjuvant setting (42) to chordoma patients, either with or without radiotherapy, might have a strong impact on the clinical management of these tumours as it might improve surgical outcomes through tumour shrinkage. This could contribute to less extensive and complicated surgical procedures which could either reduce the risk of surgery-related morbidities (e.g. by saving critical nerve structures in the axial skeleton) or possibly facilitate complete surgical resection.

In conclusion, through a multimodal approach we provided evidence that chordomas present multiple hallmarks of anti-tumour immunity. On a transcriptional level, chordomas appear more enriched for inflammatory signalling than other genetically complex sarcomas. Within our chordoma cohort, we identified distinct immune contextures, either defined by a

coordinated, possibly antigen-driven, immune response or a microenvironment dominated by stromal- and myeloid cell interactions. Furthermore, antigen presentation was maintained in the majority of chordomas. Our study provides a rationale for utilising immunotherapeutic strategies to aid in the clinical management of chordomas.

DATA AVAILABILITY STATEMENT

Code & data availability

The RNA sequencing data generated in this study are publicly available on GEO (GSE239531). The imaging mass cytometry data is available on BioImage Archive (S-BIAD830). The RNA sequencing data for the other studied sarcoma subtypes is unpublished and therefore not yet available, with the exception of the osteosarcomas (GSE237033). The used code and processed data are published on our group's GitLab (**https://git.lumc.nl/bstp/papers/multimodal-profiling-of-chordomas)** and GitHub (**https://github.com/demirandalab/multimodal-profiling-of-chordomas**) for reproducibility. All other data are available from the corresponding author on reasonable request.

ETHICS STATEMENT

Patient consent

A waiver of consent was obtained from the medical ethical evaluation committee (protocol number: B17.039 and B21.009).

Ethical approval

All specimens in this study were pseudo anonymised and handled according to the ethical guidelines described in 'Code for Proper Secondary Use of Human Tissue in The Netherlands' of the Dutch Federation of Medical Scientific Societies.

ACKNOWLEDGMENTS

The authors would like to thank the Flow Core Facility and the Information Technology & Digital Innovation department of the Leiden University Medical Center for their service.

REFERENCES

1. WHO Classification of Tumours Editorial Board. Soft Tissue and Bone Tumours. WHO Classification of Tumours. 5 ed. Lyon, France: IARC Publications; 2020.
2. Walcott BP, Nahed BV, Mohyeldin A, Coumans JV, Kahle KT, Ferreira MJ. Chordoma: current concepts, management, and future directions. Lancet Oncol. 2012;13(2):e69-76.
3. Stacchiotti S, Gronchi A, Fossati P, Akiyama T, Alapetite C, Baumann M, et al. Best practices for the management of local-regional recurrent chordoma: a position paper by the Chordoma Global Consensus Group. Ann Oncol. 2017;28(6):1230-42.
4. Smoll NR, Gautschi OP, Radovanovic I, Schaller K, Weber DC. Incidence and relative survival of chordomas: the standardized mortality ratio and the impact of chordomas on a population. Cancer. 2013;119(11):2029-37.
5. Colia V, Stacchiotti S. Medical treatment of advanced chordomas. Eur J Cancer. 2017;83:220-8.
6. Patel SS, Nota SP, Sabbatino F, Nielsen GP, Deshpande V, Wang X, et al. Defective HLA Class I Expression and Patterns of Lymphocyte Infiltration in Chordoma Tumors. Clin Orthop Relat Res. 2021;479(6):1373-82.
7. Dridi M, Krebs-Drouot L, Meyronet D, Dumollard JM, Vassal F, Jouanneau E, et al. The Immune Microenvironment of Chordomas: An Immunohistochemical Analysis. Cancers (Basel). 2021;13(13).
8. Wu X, Lin X, Chen Y, Kong W, Xu J, Yu Z. Response of Metastatic Chordoma to the Immune Checkpoint Inhibitor Pembrolizumab: A Case Report. Front Oncol. 2020;10:565945.
9. Williamson LM, Rive CM, Di Francesco D, Titmuss E, Chun HE, Brown SD, et al. Clinical response to nivolumab in an INI1-deficient pediatric chordoma correlates with immunogenic recognition of brachyury. NPJ Precis Oncol. 2021;5(1):103.
10. Somaiah N, Conley AP, Parra ER, Lin H, Amini B, Solis Soto L, et al. Durvalumab plus tremelimumab in advanced or metastatic soft tissue and bone sarcomas: a single-centre phase 2 trial. Lancet Oncol. 2022;23(9):1156-66.
11. Bishop AJ, Amini B, Lin H, Raza SM, Patel S, Grosshans DR, et al. Immune Checkpoint Inhibitors Have Clinical Activity in Patients With Recurrent Chordoma. J Immunother. 2022;45(8):374-8.
12. Blay JY, Chevret S, Le Cesne A, Brahmi M, Penel N, Cousin S, et al. Pembrolizumab in patients with rare and ultra-rare sarcomas (AcSe Pembrolizumab): analysis of a subgroup from a non-randomised, open-label, phase 2, basket trial. Lancet Oncol. 2023.
13. Tarpey PS, Behjati S, Young MD, Martincorena I, Alexandrov LB, Farndon SJ, et al. The driver landscape of sporadic chordoma. Nature Communications. 2017;8.
14. Bai J, Shi J, Li C, Wang S, Zhang T, Hua X, et al. Whole genome sequencing of skull-base chordoma reveals genomic alterations associated with recurrence and chordoma-specific survival. Nat Commun. 2021;12(1):757.
15. van Oost S, Meijer DM, Kuijjer ML, Bovee J, de Miranda N. Linking Immunity with Genomics in Sarcomas: Is Genomic Complexity an Immunogenic Trigger? Biomedicines. 2021;9(8).

16. D'Angelo SP, Shoushtari AN, Agaram NP, Kuk D, Qin LX, Carvajal RD, et al. Prevalence of tumor-infiltrating lymphocytes and PD-L1 expression in the soft tissue sarcoma microenvironment. Hum Pathol. 2015;46(3):357-65.

17. Chalmers ZR, Connelly CF, Fabrizio D, Gay L, Ali SM, Ennis R, et al. Analysis of 100,000 human cancer genomes reveals the landscape of tumor mutational burden. Genome Med. 2017;9(1):34.

18. Lam SW, Kostine M, de Miranda N, Schoffski P, Lee CJ, Morreau H, et al. Mismatch repair deficiency is rare in bone and soft tissue tumors. Histopathology. 2021.

19. Petitprez F, de Reynies A, Keung EZ, Chen TW, Sun CM, Calderaro J, et al. B cells are associated with survival and immunotherapy response in sarcoma. Nature. 2020;577(7791):556-60.

20. Italiano A, Bessede A, Pulido M, Bompas E, Piperno-Neumann S, Chevreau C, et al. Pembrolizumab in soft-tissue sarcomas with tertiary lymphoid structures: a phase 2 PEMBROSARC trial cohort. Nat Med. 2022;28(6):1199-206.

21. Anders S, Pyl PT, Huber W. HTSeq--a Python framework to work with high-throughput sequencing data. Bioinformatics. 2015;31(2):166-9.

22. Bertucci F, Finetti P, Simeone I, Hendrickx W, Wang E, Marincola FM, et al. The immunologic constant of rejection classification refines the prognostic value of conventional prognostic signatures in breast cancer. Br J Cancer. 2018;119(11):1383-91.

23. Ijsselsteijn ME, van der Breggen R, Sarasqueta AF, Koning F, de Miranda NFCC. A 40-Marker Panel for High Dimensional Characterization of Cancer Immune Microenvironments by Imaging Mass Cytometry. Front Immunol. 2019;10.

24. Somarakis A, Van Unen V, Koning F, Lelieveldt B, Hollt T. ImaCytE: Visual Exploration of Cellular Micro-Environments for Imaging Mass Cytometry Data. IEEE Trans Vis Comput Graph. 2021;27(1):98-110.

25. Ijsselsteijn ME, Brouwer TP, Abdulrahman Z, Reidy E, Ramalheiro A, Heeren AM, et al. Cancer immunophenotyping by seven-colour multispectral imaging without tyramide signal amplification. J Pathol Clin Res. 2019;5(1):3-11.

26. Ijsselsteijn ME, Petitprez F, Lacroix L, Ruano D, van der Breggen R, Julie C, et al. Revisiting immune escape in colorectal cancer in the era of immunotherapy. Br J Cancer. 2019;120(8):815-8.

27. Nelson AC, Pillay N, Henderson S, Presneau N, Tirabosco R, Halai D, et al. An integrated functional genomics approach identifies the regulatory network directed by brachyury (T) in chordoma. J Pathol. 2012;228(3):274-85.

28. Duan W, Zhang B, Li X, Chen W, Jia S, Xin Z, et al. Single-cell transcriptome profiling reveals intra-tumoral heterogeneity in human chordomas. Cancer Immunol Immunother. 2022;71(9):2185-95.

29. Zhang Q, Fei L, Han R, Huang R, Wang Y, Chen H, et al. Single-cell transcriptome reveals cellular hierarchies and guides p-EMT-targeted trial in skull base chordoma. Cell Discov. 2022;8(1):94.

30. Bertucci F, Niziers V, de Nonneville A, Finetti P, Mescam L, Mir O, et al. Immunologic constant of rejection signature is prognostic in soft-tissue sarcoma and refines the CINSARC signature. J Immunother Cancer. 2022;10(1).

31. de Vries NL, van de Haar J, Veninga V, Chalabi M, Ijsselsteijn ME, van der Ploeg M, et al. gammadelta T cells are effectors of immunotherapy in cancers with HLA class I defects. Nature. 2023;613(7945):743-50.

32. Dancsok AR, Gao D, Lee AF, Steigen SE, Blay JY, Thomas DM, et al. Tumor-associated macrophages and macrophage-related immune checkpoint expression in sarcomas. Oncoimmunology. 2020;9(1):1747340.

33. Lopez DC, Robbins YL, Kowalczyk JT, Lassoued W, Gulley JL, Miettinen MM, et al. Multispectral immunofluorescence evaluation of the myeloid, T cell, and natural killer cell tumor immune microenvironment in chordoma may guide immunotherapeutic strategies. Front Oncol. 2022;12:1012058.

34. Huo X, Guo T, Wang K, Yao B, Li D, Li H, et al. Methylation-based reclassification and risk stratification of skull-base chordomas. Front Oncol. 2022;12:960005.

35. Zuccato JA, Patil V, Mansouri S, Liu JC, Nassiri F, Mamatjan Y, et al. DNA methylation-based prognostic subtypes of chordoma tumors in tissue and plasma. Neuro Oncol. 2022;24(3):442-54.

36. Baluszek S, Kober P, Rusetska N, Wagrodzki M, Mandat T, Kunicki J, et al. DNA methylation, combined with RNA sequencing, provide novel insight into molecular classification of chordomas and their microenvironment. Acta Neuropathol Commun. 2023;11(1):113.

37. Bai J, Shi J, Zhang Y, Li C, Xiong Y, Koka H, et al. Gene Expression Profiling Identifies Two Chordoma Subtypes Associated with Distinct Molecular Mechanisms and Clinical Outcomes. Clin Cancer Res. 2023;29(1):261-70.

38. DeMaria PJ, Bilusic M, Park DM, Heery CR, Donahue RN, Madan RA, et al. Randomized, Double-Blind, Placebo-Controlled Phase II Study of Yeast-Brachyury Vaccine (GI-6301) in Combination with Standard-of-Care Radiotherapy in Locally Advanced, Unresectable Chordoma. Oncologist. 2021;26(5):e847-e58.

39. Allard B, Allard D, Buisseret L, Stagg J. The adenosine pathway in immuno-oncology. Nat Rev Clin Oncol. 2020;17(10):611-29.

40. Xia C, Yin S, To KKW, Fu L. CD39/CD73/A2AR pathway and cancer immunotherapy. Mol Cancer. 2023;22(1):44.

41. Lazcano R, Barreto CM, Salazar R, Carapeto F, Traweek RS, Leung CH, et al. The immune landscape of undifferentiated pleomorphic sarcoma. Front Oncol. 2022;12:1008484.

42. Patel SP, Othus M, Chen Y, Wright GP, Jr., Yost KJ, Hyngstrom JR, et al. Neoadjuvant-Adjuvant or Adjuvant-Only Pembrolizumab in Advanced Melanoma. N Engl J Med. 2023;388(9):813-23.

FOOTNOTES

Author contributions

S.v.O. contributed to the conceptualisation, methodology, investigation, data curation, data analysis, visualisation, writing-original draft and writing-review editing. **D.M.M.** contributed to the conceptualisation, investigation, data curation, data analysis and writing-review editing. **M.E.IJ.** contributed to the experiments, data analysis and writing-review editing. **J.R.** contributed to the data analysis and writing-review editing. **B.v.d.A.** contributed to the investigation and writing-review editing. **R.v.d.B.** contributed to the investigation and writing-review editing. **I.H.B.d.B.** contributed to the investigation and writing-review editing. **M.v.d.P.** contributed to the investigation and writing-review editing. **P.M.W.K.** contributed to the investigation and writing-review editing. **S.B.P.** contributed to the resources and writing-review editing. **W.C.P.** contributed to the resources and writing-review editing. **R.J.P.v.d.W.** contributed to the resources and writing-review editing. **N.F.C.C.d.M**. contributed to the conceptualisation, methodology, investigation, supervision, writing-original draft and writing-review editing. **J.V.M.G.B.** contributed to the conceptualisation, methodology, investigation, supervision, writing-original draft and writing-review editing.

Funding

This work was financially supported by the intramural Leiden Center for Computational Oncology strategic fund. N.F.C.C.d.M. is funded by the European Research Council (ERC) under the European Union's Horizon 2020 Research and Innovation Program (grant agreement no. 852832) and by the VIDI ZonMW (project number: 09150172110092).

Competing interests

The authors declare no competing interests.

SUPPLEMENTAL METHODS

Patient samples

These TMAs were holding 2-4 cores of 1.6 mm in diameter per tumour, dependent on the source of the material or the morphology of the tumour (two cores: biopsy; three cores: resection/excision etc; four cores: heterogeneous morphology, or separate areas of dedifferentiation). As controls and for orientation purposes, each TMA contained three cores tonsil and three cores placenta, either decalcified with EDTA or formic acid or non-decalcified.

Gene expression analysis

Normalisation and exploratory analysis of the RNA sequencing data was performed in R (v.4.0.2) by using DESeq2 (v. 1.30.1). BiomaRt (R, v.2.46.3) was used to translate the ensemble IDs to known protein coding genes. The most variably expressed genes were determined by calculating the variance per gene across all samples. The immunologic constant of rejection (ICR) gene signature was used to describe the activity state immune microenvironment and to identify distinct immune-related clusters (Th1-related markers: *IFNG*, *STAT1*, *IL12B*, *IRF1*, *TBX21*; CD8+ T cells: *CD8A*, *CD8B*; Immune effector molecules: *GZMA*, *GZMB*, *GZMH*, *PRF1*, *GNLY*; Chemokine ligands: *CXCL9*, *CXCL10*, *CCL5*; Immune suppressive molecules: *IDO1*, *PDCD1*, *CD274*, *CTLA4*, *FOXP3*) (1). The mean of the log2 normalised expression of these 20 genes was used to attribute an ICR "score" to each sample for comparison between the sarcoma subtypes, which was visualised with ggplot2 (R, v.3.3.6). For both the heatmaps in **figure 1**, a Z-Score was calculated per gene to visualise the transcriptional profile of the samples by using the Ward variance method with ComplexHeatmap (R, v.2.11.1). Differential gene expression analysis was performed with DESeq2 comparing chordomas to all other sarcomas. Genes were considered differentially expressed when the log2 fold change was above 2 and the adjusted *P* value was below 0.01. Immune-related genes were selected for visualisation in the enhanced volcano plot and additional boxplots. For visualisation purposes, the axes of the enhanced volcano plot were manually adjusted as follows: log2 fold change (x-axis) was set between -10 and 10, and the -log10 adjusted *P* (y-axis) was set to a maximum of 100.

Imaging mass cytometry analysis

To correct for variability in signal-to-noise ratios between FFPE sections, the signal intensity of the generated images was normalised at pixel levels by using Matlab (v.R2021a), after which the images were binarised using semi-

automated background removal in Ilastik (v.1.3.3) as described previously (2). Probability masks were generated in Ilastik by using a multicoloured image including the DNA channel, CD45 channel, Keratin channel and Vimentin channel to annotate nucleus, cytoplasm and background. Probability masks were loaded into CellProfiler (v.2.2.0) and used for creating cell segmentation masks. Next, the segmentation masks and binarised images were loaded into ImaCyte (3) to generate single cell-FCS files containing relative frequency of positive pixels for each marker, which were then used for phenotyping in CytoSplore (v.2.3.1) by sequentially utilizing Hierarchical Stochastic Neighbour Embedding (H-SNE) and t-distributed Stochastic Neighbour Embedding (t-SNE). Identified cell phenotypes were loaded into ImaCyte together with the segmentation masks and binarised images, which allows the mapping of the phenotypes back onto the images. Phenotypes per image were extracted to calculate the mean cell density per mm^2 for every sample (one image = one mm^2). An overview of the lineage markers used for phenotype identification is listed in **supplemental table 2**. Patients were clustered into two groups based on the Z-Score normalised mean cell densities per mm^2 of all five identified T cell phenotypes by using the Ward variance method with ComplexHeatmap. Ggplot2 was used to visualise the mean cell densities and to compare them between both T cell groups. For statistical testing, a two-sided student's t-test was performed followed by a Benjamini-Hochberg FDR correction. In addition, an overview heatmap containing all identified phenotypes in the microenvironment of chordomas was visualised with ComplexHeatmap.

Spatial interaction analysis

After phenotype calling, a spatial interaction analysis was performed with ImaCyte for all imaged samples, comparing T cell low with T cell high chordomas. ImaCyte utilises a 1000-iteration permutation test which calculates a Z-Score for the interaction between adjacent cells. However, permutation testing does not adjust for overabundant cell types, such as tumour cells, and is therefore not able to identify meaningful interactions for tumour cells. Because of the range of the calculated Z-Scores, interactions with a Z-Score below 10 were considered not significant and therefore removed for visualisation only. If an interaction Z-Score was higher than 10 in one group and lower than 10 in the other group, this interaction was considered significant for one group. When both Z-Scores were higher than 10, this interaction would be considered significant in both groups. A comparative interaction heatmap between all phenotypes excluding tumour cells was visualised with ggplot2.

Multispectral immunofluorescent imaging of T cells

All TMAs were imaged at 20x, after which the images were processed with inForm (v.2.4), which comprises background removal for each antibody by normalisation of the spectra, and analysed with QuPath (v.0.3.1). Object classification was performed by using the following classes: $CD3^+FOXP3^+$ = Regulatory T cells, $CD3^+CD8^+$ = $CD8^+$ T cells, $CD3^+$ = $CD4^+$ T cells, $CD3^+Ki\text{-}67^+$ = Proliferating T cells, $CD3^-$ = Rest. Counts per image (one image = 1 mm x 1.3 mm) were normalised per patient to counts per mm^2 tissue. Patients were divided into a T cell high and low cluster based on the unsupervised clustering of the Z-scores of all T cell phenotypes.

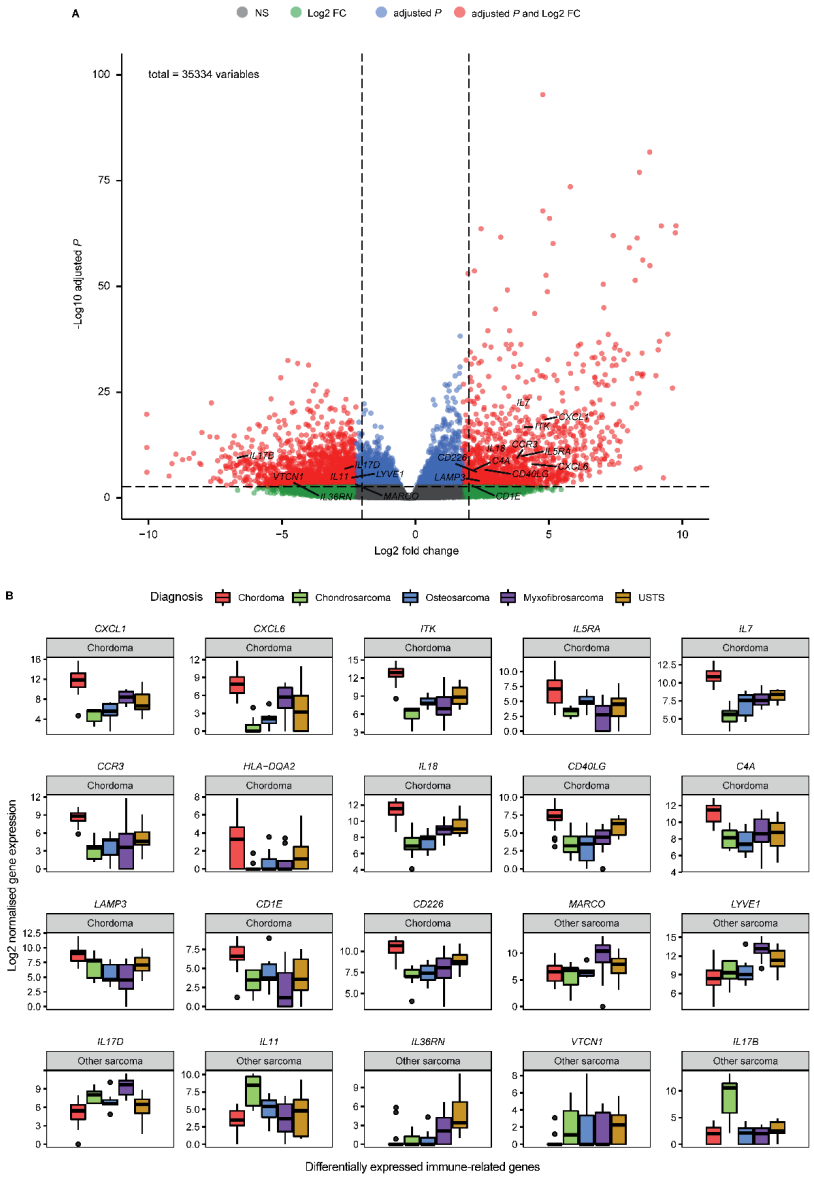
Survival analysis

For all chordoma patients, Kaplan-Meier curves for the disease-specific survival and recurrence-free survival were generated with the survminer and survival packages (R, v.0.4.9 and v.3.1-12 respectively). The disease-specific survival was considered the survival of a patient until death due to the disease, whereas the recurrence-free survival was considered the time until a patient was diagnosed with a recurrence, thereby excluding patients who did not receive surgery. Since the cohort included many censored cases, the log-rank *P* value was used to estimate the significance of the associations. Known prognostic factors such as the anatomical tumour location excluding the only extra-axial patient, age and type of treatment, surgical margin excluding patients who did not receive surgery and disease recurrence were investigated for their prognostic value, as well as the newly identified T cell infiltration groups. Univariate and multivariate analyses were performed in R according to the cox proportional hazard model. Only clinical parameters that were found significant in the univariate analysis were taken along in the multivariate analysis.

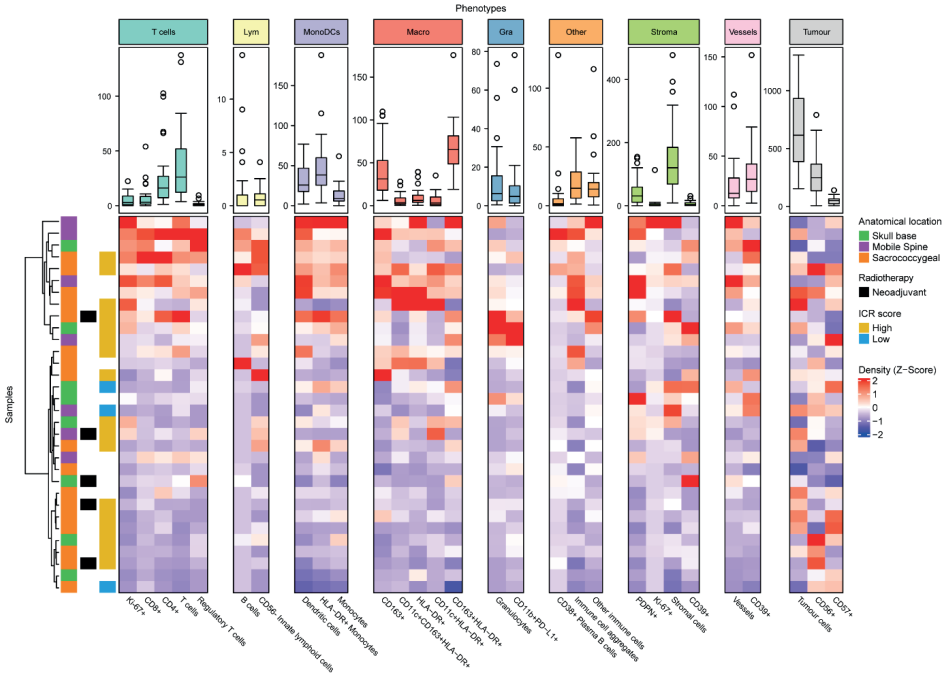
TCR β-chain sequencing

The number of clones and the Shannon diversity, a measure for clonal enrichment, were calculated in R by using productive counts only, meaning that a clone needed at least 10 plus and 10 minus counts. Because recurrences showed similar levels of TCR diversity as their respective primary tumour, we used the TCR repertoire of recurrences for three patients for which there was no frozen material of primary tumours available. Finally, the data was visualised in R using ggplot2.

SUPPLEMENTARY FIGURES

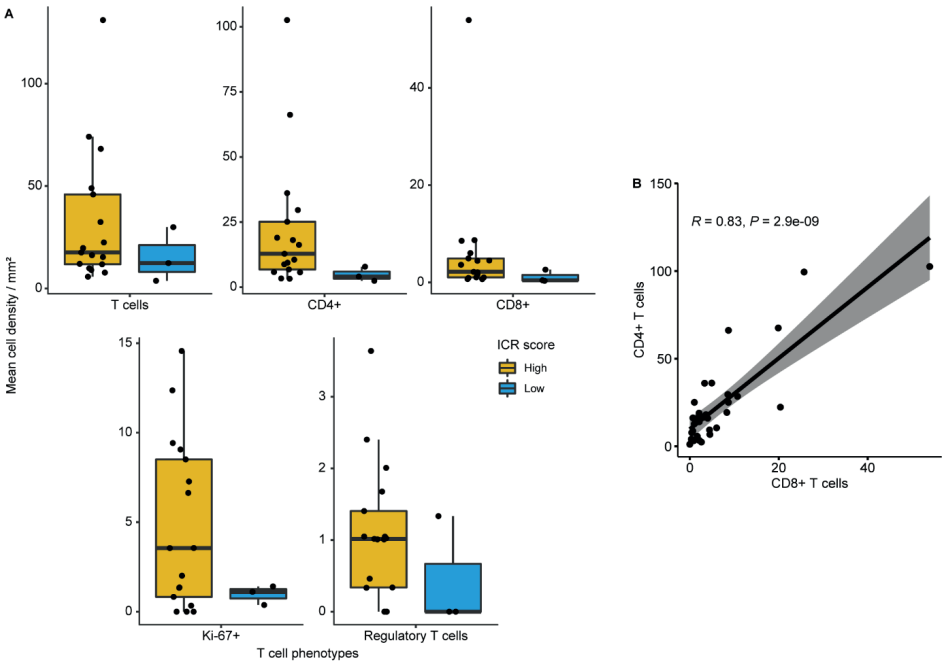


Supplemental figure 1 | Chordomas are enriched for immune-related gene signaling.



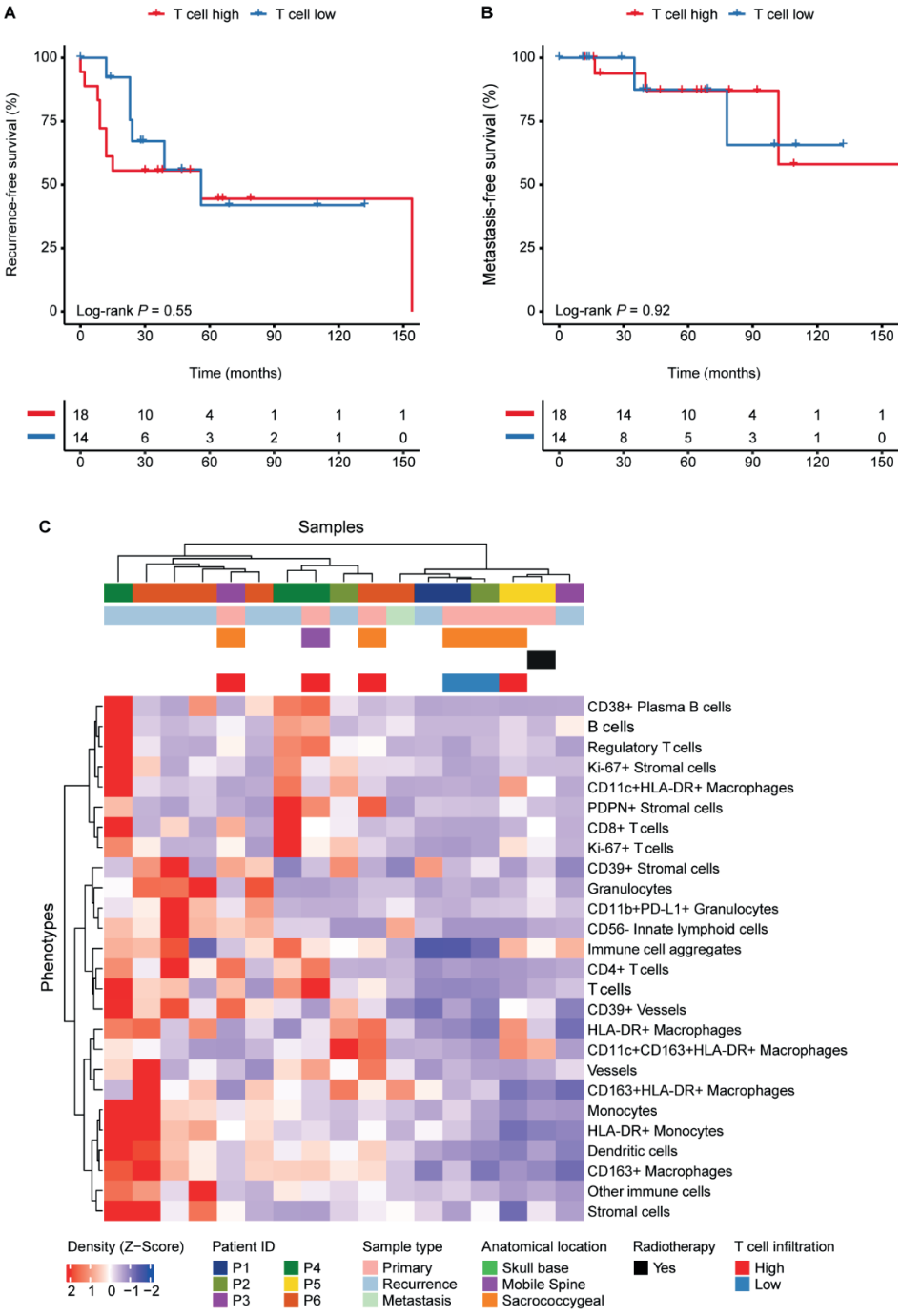
Supplemental figure 2 | Overview of the chordoma microenvironment. Overview heatmap of the mean cell density Z-Score of 29 identified cell phenotypes in all chordoma samples (n = 32). The samples that were used for transcriptome sequencing are annotated according to their ICR score. Samples are hierarchically clustered and annotated for their anatomical location and whether they had received neoadjuvant radiotherapy. Boxplots are presented per phenotype to display the general mean cell densities per mm^2 for each phenotype. ICR = immunologic constant of rejection; Lym = lymphoid; MonoDCs = monocytes and dendritic cells; Macro = macrophages; Gra = granulocytes; PDPN = podoplanin.

Supplemental figure 1 | Chordomas are enriched for immune-related gene signaling. **A)** Enhanced volcano plot presenting the differential gene expression analysis between chordomas (n = 20) and all other studied sarcomas (n = 39. Genes with a log_2 fold change above 2 and an adjusted P value below 0.01 were considered significantly differentially expressed. Immune-related genes were labelled for visualisation. **B)** Boxplots displaying the log_2 normalised expression of the differentially expressed immune related genes. The boxplots are ordered in descending order for the log_2 fold change and annotated for the respective group in which they are significanly enriched (chordoma vs other sarcoma). The boxplots are coloured for their respective histotype. NS = not significant; FC = fold change; USTS = undifferentiated soft tissue sarcoma.

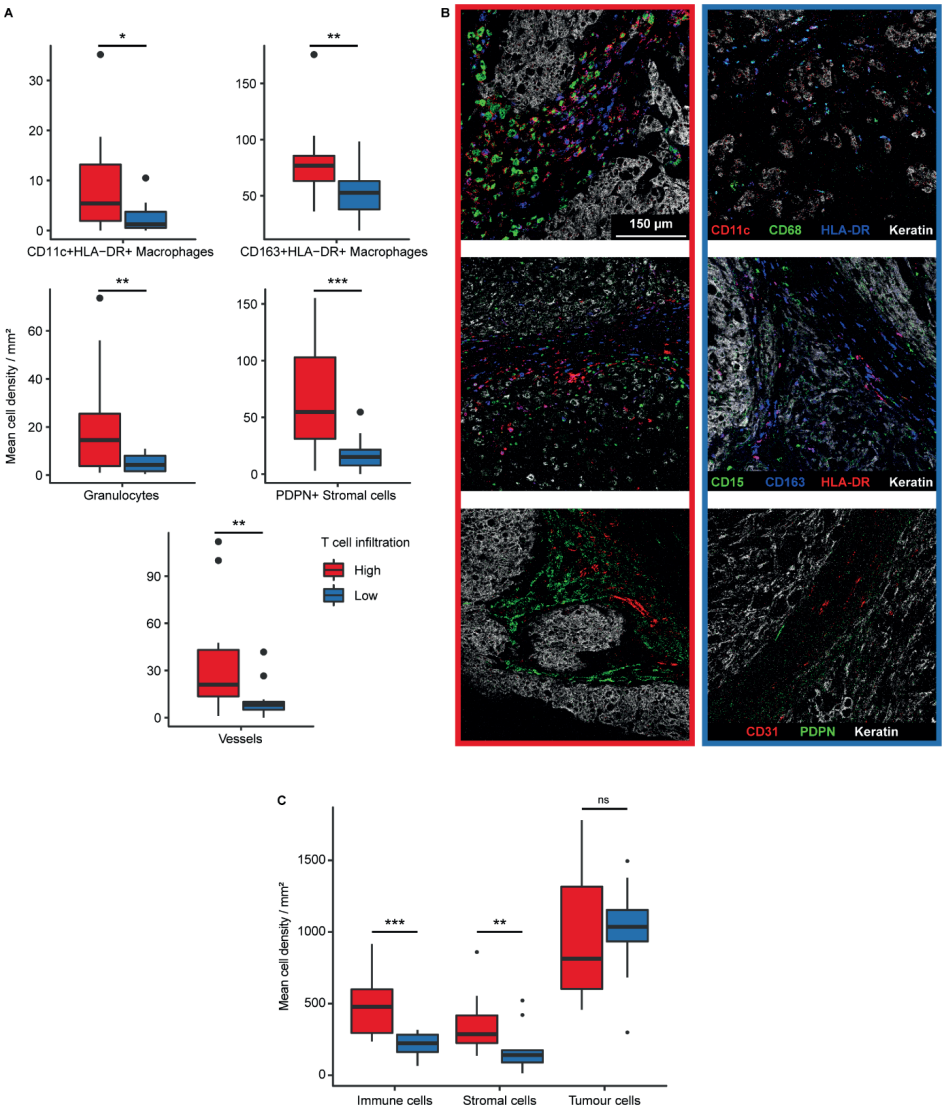


Supplemental figure 3 | ICR high chordomas are enriched with T cell phenotypes. A) Boxplots representing the different levels of infiltration of the identified T cell populations between ICR-high (n = 17) and ICR-low (n = 3) chordomas. No statistical tests were performed due to the small sample size. ICR = immunologic constant of rejection. **B)** Correlation plot presenting the Pearson correlation between $CD4^+$ T cell and $CD8^+$ T cell infiltration based on the imaging mass cytometry data.

Supplemental figure 4 | The immune contexture of chordomas varies over time. A-B) Kaplan-Meier curve indicating the association between T cell infiltration and recurrence-free survival **(A)** as well as metastasis-free survival **(B)**. Two-sided log-rank tests were performed for the Kaplan Meier estimates. **C)** Heatmap presenting the unsupervised clustering of untreated primary tumours (n = 6) and their respective treated primary tumour (n = 1), recurrences (n = 9) and metastases (n = 1). The heatmap displays the mean cell density Z-Score of the identified cell phenotypes, excluding tumour cells. The samples are annotated for patient ID, type of sample, anatomical location, whether the tumour was treated with neoadjuvant radiotherapy and T cell group of the primary tumour. PDPN = podoplanin. ▶



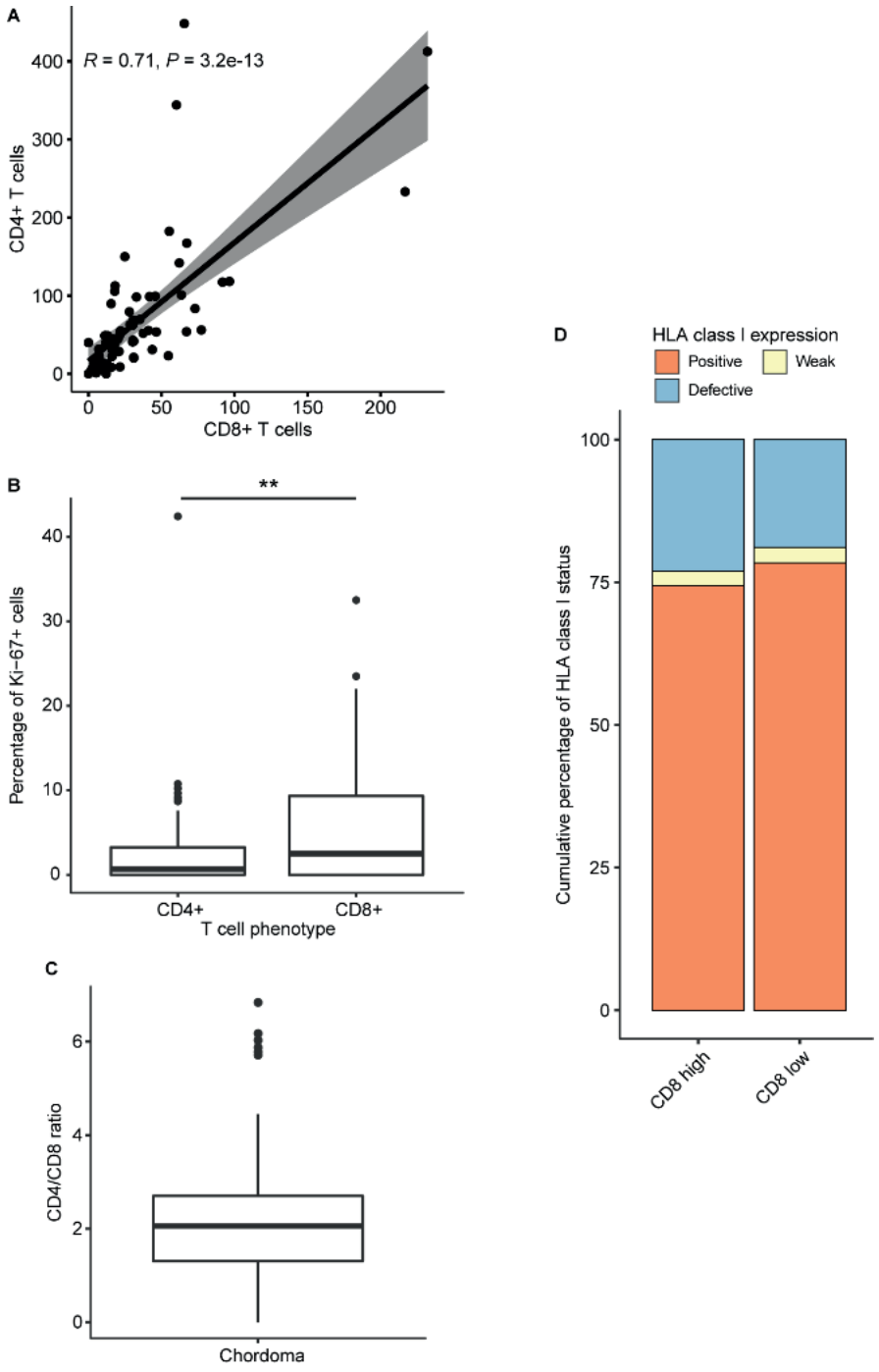
Supplemental figure 4 | The immune contexture of chordomas varies over time.



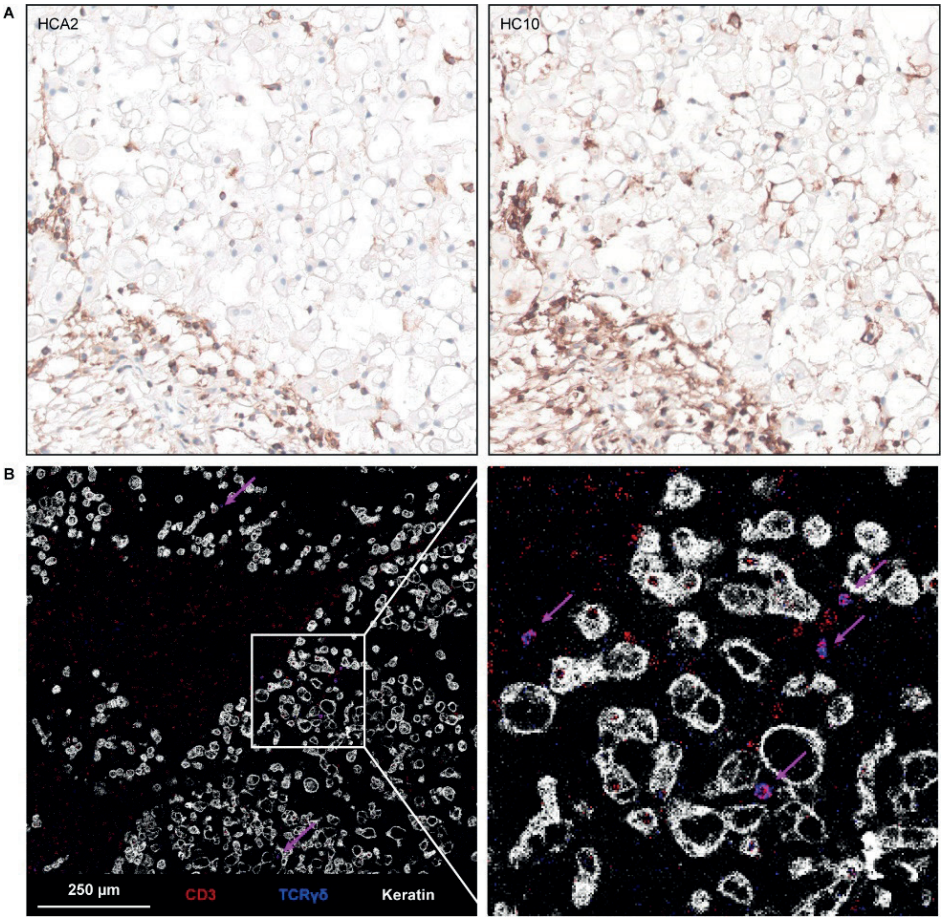
Supplemental figure 5 | Comparative overview of the chordoma immune microenvironment.

Supplemental figure 5 | Comparative overview of the chordoma immune microenvironment. A) Boxplots with the significantly different phenotypes between the T cell high and T cell low groups. Two-sided t-test was performed in R and the P value was adjusted with the Benjamini-Hochberg false discovery rate (FDR). All presented phenotypes were significantly different between the T cell high an T cell low group. * = P < 0.05; ** = P < 0.01; *** P < 0.001. **B)** Representative images generated with imaging mass cytometry displaying the differentially abundant cell phenotypes in both T cell low and T cell high samples. Images are grouped per row for the displayed cell markers and outlined with their respective T cell group (T cell high = red rectangle & left, T cell low = blue rectangle & right). The top row presents $CD11c^+$ macrophages (CD11c = red, CD68 = green, HLA-DR = blue, keratin = white), the middle row displays granulocytes and $CD163^+HLA\text{-}DR^+$ macrophages (CD15 = green, CD163 = blue, HLA-DR = red, keratin = white) and the bottom row shows vessels and $podoplanin^+$ stromal cells (CD31 = red, PDPN = green, keratin = white). **C)** Boxplots presenting the cumulative mean cell density per mm^2 of all immune cells, stromal cells and tumour cells in both T cell high and T cell low groups. Two-sided t-test was performed in R. ** = P < 0.01, *** = P < 0.001. PDPN = podoplanin.

◀



Supplemental figure 6 | CD4⁺ T cell infiltration and HLA class I expression in association with CD8⁺ T cell infiltration.



Supplemental figure 7 | γδ T cell infiltration in relation to HLA class I expression. A) Example images of Human Leukocyte Antigen (HLA) class I (HCA2 and HC10) expression in a T cell high chordoma as validated by immunohistochemistry. **B)** An example image and a corresponding magnification of the same tissue core as displayed in **(A)** as generated by imaging mass cytometry. The images present intratumoral γδ T cell infiltration as indicated by the magenta arrows (CD3 = red, TCRγδ = blue, keratin = white). TCR = T cell receptor.

Supplemental figure 6 | $CD4^+$ T cell infiltration and HLA class I expression in association with $CD8^+$ T cell infiltration. A) Correlation plot presenting the Pearson correlation between $CD4^+$ T cell and $CD8^+$ T cell infiltration based on the immunofluorescence data. **B)** Boxplots displaying the percentage of Ki-67+ cells for $CD4^+$ and $CD8^+$ T cells. A two-sided t-test was performed to compare Ki-67^+CD4^+ T cells with Ki-67^+CD8^+ T cells. ** = $P < 0.01$. **C)** Boxplot presenting the CD4/CD8 ratio in chordomas **D)** Stacked bar plots displaying the percentual distribution of the observed HLA class I (both HCA2 and HC10) expression patterns in the chordoma samples divided into $CD8^+$ T cell high and low with the median cell density as cut-off. ($CD8^+$ high: n = 37; $CD8^+$ low: n = 37).Supplemental table 1. Imaging mass cytometry marker panel. Ab = antibody, ON = overnight, PDPN = podoplanin.

Supplemental table 1. Imaging mass cytometry marker panel. Ab = antibody, ON = overnight, PDPN = podoplanin.

	Target	Clone	Metal	Incubation time	Temp	Dilution (x)
Lymphoid	CD103	EPR4166(2)	168 Er	5h	RT	50
	CD20	H1	142 Nd	Overnight	4C	100
	CD3	EP449E	153 Eu	Overnight	4C	50
	CD38	EPR4106	169 Tm	Overnight	4C	100
	CD4 + 2nd AB	EPR6855	145 Nd	Indirect ON	4C	100
	CD7	EPR4242	174 Yb	5h	RT	100
	CD8a	D8A8Y	146 Nd	5h	RT	50
	FOXP3	D608R	159 Tb	Overnight	4C	50
	TCRγδ + 2nd Ab	H41	148 Nd	Indirect ON	4C	50
Myeloid	CD11b	D6X1N	144 Nd	5h	RT	100
	CD11c	EP1347Y	176 Yb	5h	RT	100
	CD14	D7A2T	163 Dy	5h	RT	100
	CD15	MC480	171 Yb	Overnight	4C	100
	CD163	D6U1J	173 Yb	5h	RT	50
	CD204	J5HTR3	164 Dy	5h	RT	50
	CD68	D4B9C	143 Nd	Overnight	4C	100
	HLA-DR	TAL 1B5	141 Pr	5h	RT	100
Stroma	CD31	89C2	147 Sm	Overnight	4C	100
	CD39	EPR20627	157 Gd	5h	RT	100
	CD45	D9M8I	149 Sm	Overnight	4C	50
	CD45RO	UCHL1	165 Ho	Overnight	4C	100
	D2-40 (PDPN)	D2-40	166 Er	Overnight	4C	100
	TGF-β	TB21	115 In	5h	RT	100
	Vimentin	D21H3	194 Pt	Overnight	4C	50
Activation	Cleaved Caspase	5A1E	172 Yb	5h	RT	100
	Granzyme B	D6E9W	150 Nd	5h	RT	100
	ICOS	D1K2T(TM)	161 Dy	5h	RT	50
	IDO	D5J4E(TM)	162 Dy	Overnight	4C	100
	Ki-67	8D5	152 Sm	Overnight	4C	100
	LAG-3	D2G40(TM)	155 Gd	5h	RT	50
	PD-1	D4W2J	160 Gd	5h	RT	50
	PD-L1	E1L3N(R)	156 Gd	Overnight	4C	50
	Tbet	4B10	170 Er	5h	RT	50
	TIM-3	D5D5R(TM)	154 Sm	5h	RT	100
	VISTA	D1L2G(TM)	158 Gd	5h	RT	100

Supplemental table 1. *Continued*

	Target	Clone	Metal	Incubation time	Temp	Dilution (x)
Tumour	CD56	E7X9M	167 Er	5h	RT	100
	CD57	HNK-1 / Leu-7	151 Eu	Overnight	4C	100
	Keratin	C11 and AE1/AE3	198 Pt	Overnight	4C	50
	P16ink4a	D3W8G	175 Lu	Overnight	4C	100
	β-Catenin	D10A8	89 Y	Overnight	4C	100
DNA	Histone H3	D1H2	209 Bi	Overnight	4C	50

Supplemental table 2. Cell type lineage markers imaging mass cytometry. Colours are indicating cell types according to overview heatmap in **supplemental figure 2**. Lineage markers are describing the used markers for cell type identification as used in this study. Lin = lineage markers e.g. CD14 and CD68.

Cell type	Lineage markers
T cells	CD3+
B cells	CD20+
Innate lymphoid cells	CD3-CD7+
Dendritic cells	CD11c+CD68- | Lin-HLA-DR+
Monocytes	CD11c-CD14+CD68-
Immune cells	CD45+
Plasma B cells	CD38+
Macrophages	CD68+
Granulocytes	CD15+
Stromal cells	Vimentin+CD45-
Vessels	CD31+
Tumour cells	Keratin+

Supplemental table 3. Top 200 most variably expressed genes across sarcoma subtypes. Known chordoma-related genes are annotated in **bold** (4-6). Genes are ordered following the heatmap presented in **figure 1A**.

Gene ID	Cluster	Gene ID	Cluster
ENSG00000254626	1	***SHH***	1
HPCAL4	1	*IQCM*	1
CHST4	1	***KRT19***	1
SLC4A11	1	*ENSG00000232110*	1
PKP2	1	***HHLA2***	1
KRT15	1	***RAB3B***	1
NCMAP	1	***KRT13***	1
SALL3	1	*C3orf49*	1
KRT18	1	*CHRM2*	1
KRT8	1	***AKR1B10***	1
C1orf116	1	*LCN1*	1
MTMR7	1	*NPFFR2*	1
ANXA8	1	*GABRA2*	1
ANXA8L1	1	*GPM6A*	1
CD24	1	***NOL4***	1
LGR6	1	*LINC01293*	1
SCUBE1	1	*LINC01291*	1
RIPK4	1	*ALG1L7P*	1
KRT80	1	*ENSG00000290079*	1
CA3	1	*ENSG00000231918*	1
TRIM67	1	***SCEL***	1
AVPR1B	1	*ASTN1*	1
TBXT	1	***ADAMTS19***	1
LNCDAT	1	*LMX1A*	1
PPIAP46	1	*USH2A*	1
ENSG00000285933	1	*LINC00525*	1
GPR101	1	*RASEF*	1
ENSG00000285562	1	*TMPRSS3*	1
MRGPRX3	1	*DLGAP1−AS5*	1
LINC02065	1	*IP6K3*	1
PRSS51	1	*TMPRSS4*	1
ARHGAP40	1	***FAM135B***	1
KCNH6	1	***GDA***	1
ENSG00000280285	1	*LINC02351*	1
SLC15A5	1	*RORC*	1

Supplemental table 3. *Continued*

Gene ID	Cluster
CFAP46	1
POF1B	1
AP3B2	1
NPTX1	1
FAM153B	1
DNAH9	1
CACNA1I	1
MAN1A2P1	1
CNTN3	1
DPP6	1
COL4A6	1
XIRP2	2
ACTA1	2
MYH1	2
MYH2	2
MYH7	2
MYBPC1	2
MYL1	2
PLA2G2D	3
IGHG4	3
IGHG3	3
IGKC	3
HLA−DRB5	3
HLA−DRB1	3
HLA−C	3
HLA−DQB1	3
HLA−DQA1	3
CADM3	4
ADH1B	4
CYP4B1	4
CHRDL1	4
PRG4	4
PI16	4
THBS4	4
RSPO2	4
PLA2G2A	4
GFRA1	4
FEZF1−AS1	4
PAX3	4
EPHA6	4
GSTM1	4
ENSG00000277693	4
DKK1	4
LINC02154	4
XIST	4
PSPHP1	4
MYH14	5
HAPLN1	5
ACAN	5
COL11A1	5
S100A1	5
ITIH6	5
COL2A1	5
COL9A3	5
RFLNA	5
SOX9	5
POU3F3	5
PANTR1	5
FBN3	5
PRSS16	5
CDH19	5
PMP2	5
PCSK2	5
SDR16C5	5
DSP	5
CHST9	5
CNNM1	5
UNC80	5
PCLO	5
SORCS3	5
PWRN1	5
CRTAC1	5
COMP	5
CILP2	5
NGEF	5
KRT16	5

Supplemental table 3. *Continued*

Gene ID	Cluster
SFRP1	5
CXCL14	5
GDF10	5
SCRG1	5
PRELP	5
SEMA3E	5
GABRA1	5
CDH10	5
LGR5	5
SAA1	5
LRRN2	5
SUSD5	5
ECRG4	5
EGF	5
DSC3	5
MMP3	5
DNER	5
EMILIN3	5
ANGPTL7	5
SCN7A	5
MMP13	6
IBSP	6
DMP1	6
MEPE	6
IFITM5	6
PANX3	6
SP7	6
BMP3	6
IGF2BP1	7
FGFBP2	7
COL9A1	7
COL11A2	7
WIF1	7
CHAD	7
CLEC3A	7
COL10A1	7
EPYC	7
MATN3	7
SCUBE3	7

Gene ID	Cluster
CA9	7
MAGEL2	7
KIF1A	7
SLC38A3	7
SHISA9	7
MATN4	7
CNMD	7
PENK	7
DLK1	7
IGF2	7
CAPN6	7
NRK	7
MKX	7
PTPRZ1	7
SLITRK6	7

Supplemental table 4. Top differentially expressed genes comparing chordomas with other sarcomas. Contains the top results from the differential gene expression analysis with DESeq2. Due to the large number of DEGs (>3500), the original table is available as online supplement. Genes with a log2 fold change > 2 and an adjusted P < 0.01 were considered significantly differentially expressed. Known immune-related genes are annotated in the column "hgnc_symbol" with a yellow-filled cell. lfcSE = log fold change standard error; FDR = false discovery rate.

ensembl_gene_id	baseMean	log2FoldChange	lfcSE	pvalue	FDR	hgnc_symbol
ENSG00000179826	7965.996	13.652	0.525	3.56E-149	1.26E-144	*MRGPRX3*
ENSG00000163632	1630.580	13.624	0.600	3.64E-114	4.29E-110	*C3orf49*
ENSG00000260266	11851.775	11.826	0.758	8.39E-55	9.56E-52	*PPIAP46*
ENSG00000164690	1787.949	11.419	0.556	1.24E-93	6.25E-90	*SHH*
ENSG00000171401	2166.124	11.253	0.771	3.18E-48	2.88E-45	*KRT13*
ENSG00000164458	17720.383	11.250	0.904	1.40E-35	6.25E-33	*TBXT*
ENSG00000188991	437.437	10.888	0.510	3.36E-101	2.37E-97	*SLC15A5*
ENSG00000169676	132.857	10.409	0.854	3.75E-34	1.44E-31	*DRD5*
ENSG00000171345	65725.635	10.391	0.677	3.95E-53	4.23E-50	*KRT19*
ENSG00000124143	1036.153	10.221	0.437	6.43E-121	1.14E-116	*ARHGAP40*
ENSG00000181072	4607.207	10.086	0.788	1.75E-37	9.25E-35	*CHRM2*
ENSG00000179817	84.678	9.962	0.577	1.02E-66	2.11E-63	*MRGPRX4*
ENSG00000204121	60.801	9.856	0.880	4.09E-29	1.06E-26	*ECEL1P1*
ENSG00000173826	526.286	9.438	0.540	2.12E-68	5.00E-65	*KCNH6*
ENSG00000119125	4881.511	9.364	0.702	1.23E-40	9.44E-38	*GDA*
ENSG00000114455	466.314	9.320	0.718	1.59E-38	9.70E-36	*HHLA2*
ENSG00000198074	6231.892	9.010	0.557	8.58E-59	1.17E-55	*AKR1B10*
ENSG00000226780	45.299	8.755	0.737	1.43E-32	5.09E-30	*AVPR1B-DT*
ENSG00000234575	31.556	8.685	0.731	1.54E-32	5.42E-30	*CTSLP8*
ENSG00000249321	24.907	8.643	1.463	3.45E-09	7.12E-08	*OR5H5P*
ENSG00000136155	242.893	8.597	0.785	6.88E-28	1.68E-25	*SCEL*
ENSG00000165370	281.602	8.542	0.717	1.06E-32	3.82E-30	*GPR101*
ENSG00000232743	23.905	8.509	0.819	2.70E-25	5.42E-23	*ELF2P3*
ENSG00000234828	155.860	8.457	0.540	2.98E-55	3.51E-52	*IQCM*
ENSG00000198049	493.355	8.338	0.715	1.92E-31	5.91E-29	*AVPR1B*
ENSG00000163283	38.792	8.336	0.819	2.33E-24	4.36E-22	*ALPP*
ENSG00000169213	25483.930	8.241	0.492	4.61E-63	7.08E-60	*RAB3B*
ENSG00000160349	343.761	8.187	0.640	1.64E-37	8.84E-35	*LCN1*
ENSG00000086548	152.373	8.167	0.927	1.27E-18	1.25E-16	*CEACAM6*
ENSG00000170465	40.049	7.991	0.879	9.47E-20	1.05E-17	*KRT6C*
ENSG00000288638	4954.332	7.900	0.979	6.84E-16	4.68E-14	*LNCDAT*
ENSG00000253649	1988.727	7.888	0.609	2.07E-38	1.24E-35	*PRSS51*
ENSG00000022355	602.661	7.875	1.135	3.91E-12	1.48E-10	*GABRA1*
ENSG00000232803	58.235	7.869	0.838	5.91E-21	7.80E-19	*SLCO4A1-AS1*
ENSG00000183313	26.541	7.747	0.630	9.52E-35	3.90E-32	*OR52L1*
ENSG00000140835	786.989	7.746	0.845	4.89E-20	5.64E-18	*CHST4*
ENSG00000170421	50290.655	7.732	0.585	7.32E-40	5.07E-37	*KRT8*
ENSG00000250221	31.502	7.658	0.609	2.65E-36	1.30E-33	*KRT8P32*
ENSG00000267799	170.913	7.584	1.165	7.46E-11	2.19E-09	*MAN1A2P1*
ENSG00000239481	22.398	7.337	0.646	7.36E-30	2.00E-27	*RPS3AP41*

Supplemental table 4. *Continued*

ensembl_gene_id	baseMean	log2FoldChange	lfcSE	pvalue	FDR	hgnc_ symbol
ENSG00000134765	135.712	7.334	0.619	2.09E-32	7.32E-30	*DSC1*
ENSG00000100884	40.981	7.289	0.879	1.11E-16	8.29E-15	*CPNE6*
ENSG00000150625	1648.761	7.287	0.579	2.42E-36	1.21E-33	*GPM6A*
ENSG00000265190	738.169	7.286	0.497	1.09E-48	1.04E-45	*ANXA8*
ENSG00000088836	8496.681	7.263	0.468	2.66E-54	2.94E-51	*SLC4A11*
ENSG00000215372	58.235	7.230	0.968	8.15E-14	4.08E-12	*ZNF705G*
ENSG00000250821	124.316	7.208	0.825	2.41E-18	2.29E-16	*EXOC1L*
ENSG00000258628	34.327	7.110	0.740	6.97E-22	1.01E-19	*RHPN2P1*
ENSG00000116983	1096.094	7.058	0.571	4.29E-35	1.85E-32	*HPCAL4*
ENSG00000164007	125.465	7.017	1.036	1.28E-11	4.42E-10	*CLDN19*
ENSG00000149948	694.337	-5.613	0.616	8.29E-20	9.36E-18	*HMGA2*
ENSG00000112280	18140.111	-5.660	1.112	3.56E-07	4.61E-06	*COL9A1*
ENSG00000106278	486.527	-5.681	0.833	9.11E-12	3.25E-10	*PTPRZ1*
ENSG00000221867	137.788	-5.702	1.840	0.001946272	0.008201037	*MAGEA3*
ENSG00000214249	25.536	-5.705	0.911	3.76E-10	9.55E-09	*CTAGE11P*
ENSG00000228035	99.583	-5.830	1.016	9.71E-09	1.81E-07	*NGF-AS1*
ENSG00000130829	64.427	-5.866	1.090	7.31E-08	1.11E-06	*DUSP9*
ENSG00000163501	174.541	-5.912	0.765	1.12E-14	6.58E-13	*IHH*
ENSG00000204941	100.853	-5.947	1.623	0.000248902	0.001424626	*PSG5*
ENSG00000135903	334.212	-5.965	0.950	3.37E-10	8.67E-09	*PAX3*
ENSG00000047936	387.764	-6.007	0.896	1.99E-11	6.54E-10	*ROS1*
ENSG00000116690	7782.709	-6.017	0.824	2.90E-13	1.33E-11	*PRG4*
ENSG00000280650	20.970	-6.053	0.986	8.15E-10	1.93E-08	*KCNIP4-IT1*
ENSG00000147655	872.328	-6.078	0.931	6.60E-11	1.96E-09	*RSPO2*
ENSG00000228536	89.798	-6.085	0.727	5.93E-17	4.56E-15	*LYPLAL1-AS1*
ENSG00000206384	250.052	-6.127	1.054	6.11E-09	1.19E-07	*COL6A6*
ENSG00000187268	78.162	-6.201	0.925	2.03E-11	6.65E-10	*FAM9C*
ENSG00000185306	80.711	-6.292	0.824	2.31E-14	1.29E-12	*C12orf56*
ENSG00000002745	182.223	-6.318	0.984	1.35E-10	3.80E-09	*WNT16*
ENSG00000000005	181.441	-6.344	1.005	2.78E-10	7.31E-09	*TNMD*
ENSG00000223949	392.693	-6.419	0.818	4.09E-15	2.53E-13	*ROR1-AS1*
ENSG00000255399	137.995	-6.561	0.775	2.48E-17	2.05E-15	*TBX5-AS1*
ENSG00000128714	139.859	-6.612	0.828	1.35E-15	8.81E-14	*HOXD13*
ENSG00000224963	321.758	-6.694	0.874	1.91E-14	1.08E-12	*ECMXP*
ENSG00000019186	155.754	-6.710	1.129	2.79E-09	5.86E-08	*CYP24A1*
ENSG00000127743	328.669	-6.710	0.986	1.02E-11	3.59E-10	*IL17B*
ENSG00000197587	26.489	-6.711	1.050	1.67E-10	4.60E-09	*DMBX1*
ENSG00000237396	58.068	-6.854	1.820	0.000165895	0.001008677	*LNCNEF*
ENSG00000072041	328.019	-6.885	1.132	1.19E-09	2.73E-08	*SLC6A15*
ENSG00000016082	26.411	-6.893	0.988	3.07E-12	1.19E-10	*ISL1*
ENSG00000166509	2186.658	-7.063	1.645	1.75E-05	0.000143606	*CLEC3A*
ENSG00000162624	45.059	-7.081	1.291	4.17E-08	6.73E-07	*LHX8*
ENSG00000206013	448.828	-7.096	1.608	1.02E-05	8.94E-05	*IFITM5*
ENSG00000144191	36.932	-7.174	1.539	3.12E-06	3.15E-05	*CNGA3*
ENSG00000137745	8572.135	-7.207	0.861	5.60E-17	4.34E-15	*MMP13*
ENSG00000244681	97.039	-7.332	1.543	2.03E-06	2.15E-05	*MTHFD2P1*
ENSG00000107984	1704.251	-7.416	0.710	1.57E-25	3.24E-23	*DKK1*

Supplemental table 4. *Continued*

ensembl_gene_id	baseMean	log2FoldChange	lfcSE	pvalue	FDR	hgnc_ symbol
ENSG00000154143	459.193	-7.440	1.727	1.65E-05	0.000136125	*PANX3*
ENSG00000080224	566.494	-7.472	0.889	4.14E-17	3.26E-15	*EPHA6*
ENSG00000089225	114.537	-7.771	0.894	3.56E-18	3.30E-16	*TBX5*
ENSG00000164488	235.562	-7.804	1.256	5.28E-10	1.30E-08	*DACT2*
ENSG00000180318	88.989	-7.854	1.241	2.43E-10	6.47E-09	*ALX1*
ENSG00000254254	132.585	-8.081	1.123	6.20E-13	2.72E-11	*PENK-AS1*
ENSG00000164825	91.444	-8.248	1.219	1.31E-11	4.52E-10	*DEFB1*
ENSG00000185559	1362.438	-8.496	1.277	2.86E-11	9.05E-10	*DLK1*
ENSG00000136110	4485.869	-9.831	1.808	5.43E-08	8.51E-07	*CNMD*
ENSG00000182674	96.510	-9.833	1.286	2.08E-14	1.17E-12	*KCNB2*
ENSG00000181195	14343.109	-9.836	1.003	1.02E-22	1.61E-20	*PENK*
ENSG00000187689	31.002	-24.008	2.727	1.34E-18	1.31E-16	*AMTN*
ENSG00000185960	40.413	-24.343	1.455	8.36E-63	1.23E-59	*SHOX*

Supplemental table 5. Univariate cox proportional hazard results in the combined cohort. Table includes the results of the disease-specific survival in association with all identified T cell phenotypes. Log-rank P values < 0.05 were considered significant. * < 0 .05, ** < 0.01, *** < 0.001. HR = hazard ratio; CI = confidence interval.

	Disease-specific survival	
	Univariate	
Variable	**HR (95% CI)**	**log-rank P**
Ki-67$^+$CD4$^+$ T cells	0.93 (0.72-1.2)	0.6
Ki-67$^+$CD8$^+$ T cells	1 (0.9-1.1)	0.9
Ki-67$^+$ Regulatory T cells	0.8 (0.46-1.4)	0.4
CD4$^+$ T cells	1 (0.99-1)	0.5
CD8$^+$ T cells	1 (0.98-1.01)	0.8
Regulatory T cells	0.95 (0.88-1.02)	0.2

Supplemental table 6. Univariate and multivariate cox proportional hazard results in the combined cohort. Table includes the results of the disease-specific, recurrence-free and metastasis-free survival. Significant parameters from the univariate analysis were taken along for the multivariable analysis. Patients who were only treated with radiotherapy were excluded from the recurrence-free survival analysis. Log-rank P values < 0.05 were considered significant and are annotated in bold and by significance level; * < 0 .05, ** < 0.01, *** < 0.001. HR = hazard ratio; CI = confidence interval; RT = radiotherapy.

Disease-specific survival	Univariate	
Variable	**HR (95% CI)**	**log-rank *P***
Age at diagnosis	1 (0.98-0.99)	0.2
Max tumour size	1 (0.91-1.2)	0.7
Location (Skull base)[a]		
Mobile Spine	0.56 (0.2-1.6)	0.09
Sacrococcygeal	0.35 (0.13-0.92)	
Treatment (RT alone)		
Surgery	0.87 (0.24-3.1)	0.6
Surgery + RT	0.57 (0.15-2.2) *	
Timing of RT (Adjuvant)[b]		
Neoadjuvant	0.66 (0.076-5.8)	0.7
Surgical margin (R0)[c]		
R1	2.1 (0.23-19)	0.3
R2	2.3 (0.75-6.8)	
T cell infiltration (High)		
Low	2 (0.78-5.3)	0.1
Disease recurrence (No)[c]		
Yes	2 (0.78-5.3)	0.9

Metastasis-free survival	Univariate	
Variable	**HR (95% CI)**	**log-rank *P***
Age at diagnosis	1 (0.99-1)	0.3
Max tumour size	1.1 (0.95-1.2)	0.3
Location (Skull base)[a]		
Mobile Spine	0.84 (0.21-3.4)	0.8
Sacrococcygeal	1.2 (0.4-4)	
Treatment (RT alone)		
Surgery	1 (0.23-5.1)	1
Surgery + RT	0.95 (0.2-4.5)	

Supplemental table 6. *Continued*

Metastasis-free survival		Univariate
Timing of RT (Adjuvant)[b]		
Neoadjuvant	3.6e-9 (0-Inf)	0.2
Surgical margin (R0)		
R1	2.6 (0.29-23)	0.4
R2	0.68 (0.25-1.9)	
T cell infiltration (High)		
Low	1.5 (0.52-4)	0.5
Disease recurrence (No)[c]		
Yes	6.3 (0.83-48)	**0.04 ***

Recurrence-free survival[c]	Univariate		Multivariate	
Variable	**HR (95% CI)**	**log-rank *P***	**HR (95% CI)**	**log-rank *P***
Age at diagnosis	1 (0.98-1.02)	0.8		
Max tumour size	0.99 (0.9-1.1)	0.9		
Location (Skull base)[a]				
Mobile Spine	1.95 (0.94-4.02)	**0.003 ****	**2.2 (1-4.5) ***	
Sacrococcygeal	0.57 (0.26-1.2)		0.81 (0.32-2.1)	
Treatment (Surgery alone)				
Surgery + RT	0.82 (0.45-1.5)	0.5		0.01 *
Timing of RT (Adjuvant)[b]				
Neoadjuvant	0.29 (0.066-1.3)	0.08		
Surgical margin (R0)				
R1	1.6 (0.34-7.4)	0.07	1.2 (0.24-5.6)	
R2	**2.3 (1.1-4.8) ***		1.7 (0.7-4.2)	
T cell infiltration (High)				
Low	1.1 (0.6-2.1)	0.7		

[a]excluding the only patient with an extra-axial chordoma; [b]excluding patients who received a sandwich regimen of radiotherapy or radiotherapy alone; [c]excluding patients who were only treated with radiotherapy

SUPPLEMENTAL REFERENCES

1. Bertucci F, Finetti P, Simeone I, Hendrickx W, Wang E, Marincola FM, et al. The immunologic constant of rejection classification refines the prognostic value of conventional prognostic signatures in breast cancer. Br J Cancer. 2018;119(11):1383-91.
2. Ijsselsteijn ME, van der Breggen R, Sarasqueta AF, Koning F, de Miranda NFCC. A 40-Marker Panel for High Dimensional Characterization of Cancer Immune Microenvironments by Imaging Mass Cytometry. Front Immunol. 2019;10.
3. Somarakis A, Van Unen V, Koning F, Lelieveldt B, Hollt T. ImaCytE: Visual Exploration of Cellular Micro-Environments for Imaging Mass Cytometry Data. IEEE Trans Vis Comput Graph. 2021;27(1):98-110.
4. Nelson AC, Pillay N, Henderson S, Presneau N, Tirabosco R, Halai D, et al. An integrated functional genomics approach identifies the regulatory network directed by brachyury (T) in chordoma. J Pathol. 2012;228(3):274-85.
5. Duan W, Zhang B, Li X, Chen W, Jia S, Xin Z, et al. Single-cell transcriptome profiling reveals intra-tumoral heterogeneity in human chordomas. Cancer Immunol Immunother. 2022;71(9):2185-95.
6. Zhang Q, Fei L, Han R, Huang R, Wang Y, Chen H, et al. Single-cell transcriptome reveals cellular hierarchies and guides p-EMT-targeted trial in skull base chordoma. Cell Discov. 2022;8(1):94.



5

Immune infiltration is associated with distinct transcriptional states and metabolic profiles in chordomas

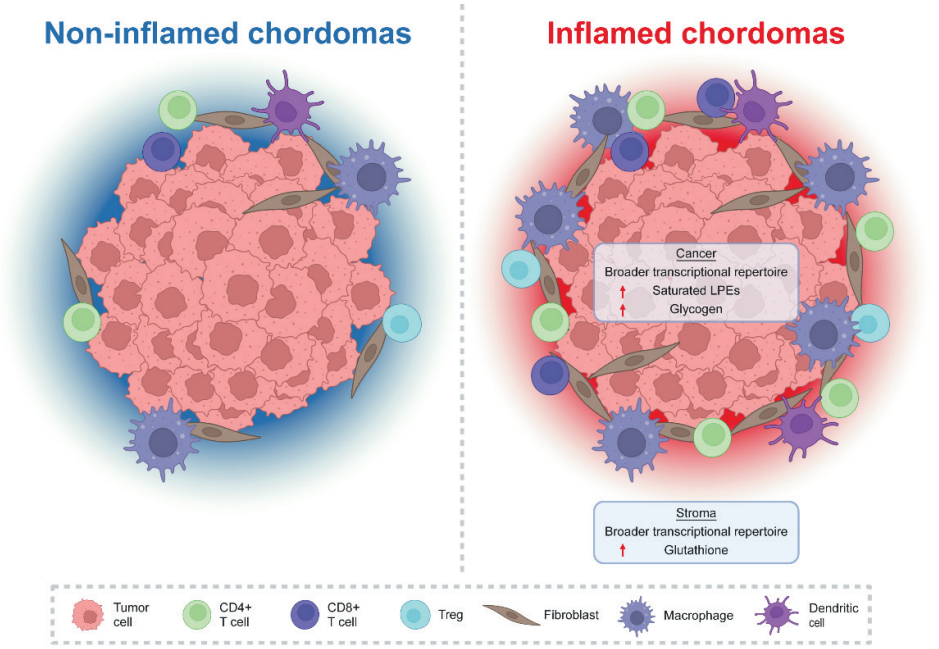
Siddh van Oost, Rick Ursem, Zeynep B. Erdem, Sara Cardoso, Sanne Venneker, Ruud van der Breggen, Inge H. Briaire-de Bruijn, Alwine B. Kruisselbrink, Wilco C. Peul, Karoly Szuhai, Robert J.P. van der Wal, Rene van Zeijl, Bram Heijs, Noel F.C.C. de Miranda, and Judith V.M.G. Bovée

iScience ***2026, 29(5)***

ABSTRACT

Chordomas are ultra-rare malignancies of the axial skeleton with limited treatment options. Some tumors exhibit immunogenic features and respond to checkpoint blockade, yet the biological determinants of these responses remain unclear. To investigate the basis of chordoma immunogenicity, we integrated spatial transcriptomic and metabolomic profiling. GeoMx digital spatial profiling was performed on 15 chordomas, analyzing tumor and stromal compartments and comparing inflamed versus non-inflamed tumors. Consecutive sections underwent MALDI mass spectrometry imaging (MSI) at 20 µm resolution, and key findings were validated by immunohistochemistry. To assess whether transcriptional states were linked to interferon-γ (IFN-γ) signaling, chordoma cell lines were treated with IFN-γ. Spatial profiling revealed transcriptomic differences between inflamed and non-inflamed tumors across both compartments. Immune infiltration correlated with a broader gene expression repertoire in cancer cells. MSI identified distinct metabolic signatures, including glycogen accumulation in inflamed tumors. However, IFN-γ did not induce *TBXT* (brachyury) expression in chordoma cells. Together, these data reveal strong associations between transcriptional states, metabolic profiles, and immune infiltration in chordomas.

Graphical abstract



INTRODUCTION

Chordomas are ultra-rare, malignant bone tumors demonstrating notochordal differentiation, arising almost exclusively in the axial skeleton, including the skull base, mobile spine and sacrum (1). The mainstay of treatment involves surgical resection and/or (proton beam) radiation (2, 3). While (proton beam) radiation can improve local control, *en bloc* resection remains the only curative option for localized disease. Clinical management is complicated by the proximity of tumors to critical neurovascular structures, often resulting in incomplete surgical margins, high rates of local recurrence, and high morbidity (2, 3). The lack of effective systemic therapies for advanced disease further emphasizes the urgent need for innovative and combinatory treatment strategies (4).

Intriguingly, T cell checkpoint blockade therapy has demonstrated promising results in a subset of patients, which suggests that chordomas harbor immunogenic features (5-7). However, biomarkers predicting responsiveness to T cell checkpoint blockade remain elusive. Previously, we shed light on natural immunity in chordomas through the identification of distinct immune contextures (8). Together with other studies (9-13), these findings suggest a dichotomy in chordoma inflammatory profiles, with some tumors showing pronounced immune infiltrate (inflamed), while others show little or no immune activity (non-inflamed). The mechanisms underlying this variability in immunogenic features remain unclear.

To investigate correlates of immunogenicity in chordomas, we applied an integrated spatial multimodal approach combining spatial transcriptomics with spatial metabolomics. Inflamed tumors showed higher expression of immune-related and chordoma-associated genes together with broader pathway engagement in both tumor and stromal compartments, consistent with coordinated biological states between tumor cells and the immune microenvironment. Furthermore, inflamed chordomas displayed distinct metabolic profiles. Collectively, these findings highlight distinct tumor cell states associated with immune infiltration in chordomas and could potentially inform patient stratification, particularly in the context of immunotherapy.

RESULTS

Inflammation is associated with distinct transcriptional states

To investigate transcriptional profiles of both tumor and stromal compartments that associate with immune infiltration in chordomas, GeoMx was performed on frozen sections from 15 conventional chordomas. For each sample, two to five regions of interest (ROIs) along the tumor-stroma interface were selected (**Figure S1**). Gene expression profiles were then delineated into tumor and stroma compartments based on pan-cytokeratin expression. Differential gene expression analysis was performed to compare tumor segments with stroma segments (**Figure 1A; Figure S2**). This analysis confirmed the enrichment of chordoma-associated genes in tumor segments, including *TBXT*, *KRT8,* and *KRT19*, and immune- and stroma-related genes in stroma segments, such as genes encoding collagens, Human Leukocyte Antigen (HLA) class II molecules, or immunoglobulins (**Figure 1A; Figure S2**). In line with the established transcriptional role of *TBXT*, several tumor-enriched genes correspond to known *TBXT* targets (14), including *ACAN* and *CCN2* (**Figure 1A**), with additional targets shown in **Figure S2**. Next, biological pathways were explored through a single-sample gene set enrichment analysis (ssGSEA) for all segments using an in-house curated WikiPathways list. Accordingly, differential pathway analysis comparing tumor with stroma segments confirmed that tumor segments were enriched for cancer-associated pathways, such as glycolysis, while stroma segments showed enrichment of immune- and stroma-related pathways like inflammatory signaling and neovascularization (**Figure 1B**).

Figure 1. Inflammation is associated with distinct transcriptional states. (A) Volcano plot presenting the differential gene expression between stroma (brown) and tumor (pink) segments. The top 10 differentially expressed genes (DEGs) per segment, ranked by fold change, are highlighted. Statistical significance was determined using a linear mixed model (LMM) correcting for sample ID. (B) Bar plot of the normalized enrichment score (NES) for the top 10 differentially enriched pathways per compartment, based on a curated WikiPathways list. Statistical significance was assessed using an LMM correcting for sample ID. (C) UMAP visualizations of stroma segments using the top 20% most variably expressed genes. Clusters were defined via graph-based clustering. Segments are colored by cluster (left) and sample ID (right). (D) Volcano plots comparing non-inflamed (blue) versus inflamed (red) stroma segments. The top 20 DEGs are highlighted per cluster. Statistical significance was determined using an LMM correcting for sample ID. (E) UMAP visualizations of tumor segments using the top 20% most variably expressed genes. Clusters were defined via graph-based clustering. Segments are colored by cluster (left) and sample ID (right). (F) Volcano plots comparing non-inflamed (blue) versus inflamed (red) tumor segments. The top 20 DEGs are highlighted per cluster. Statistical significance was determined using an LMM correcting for sample ID.

▶

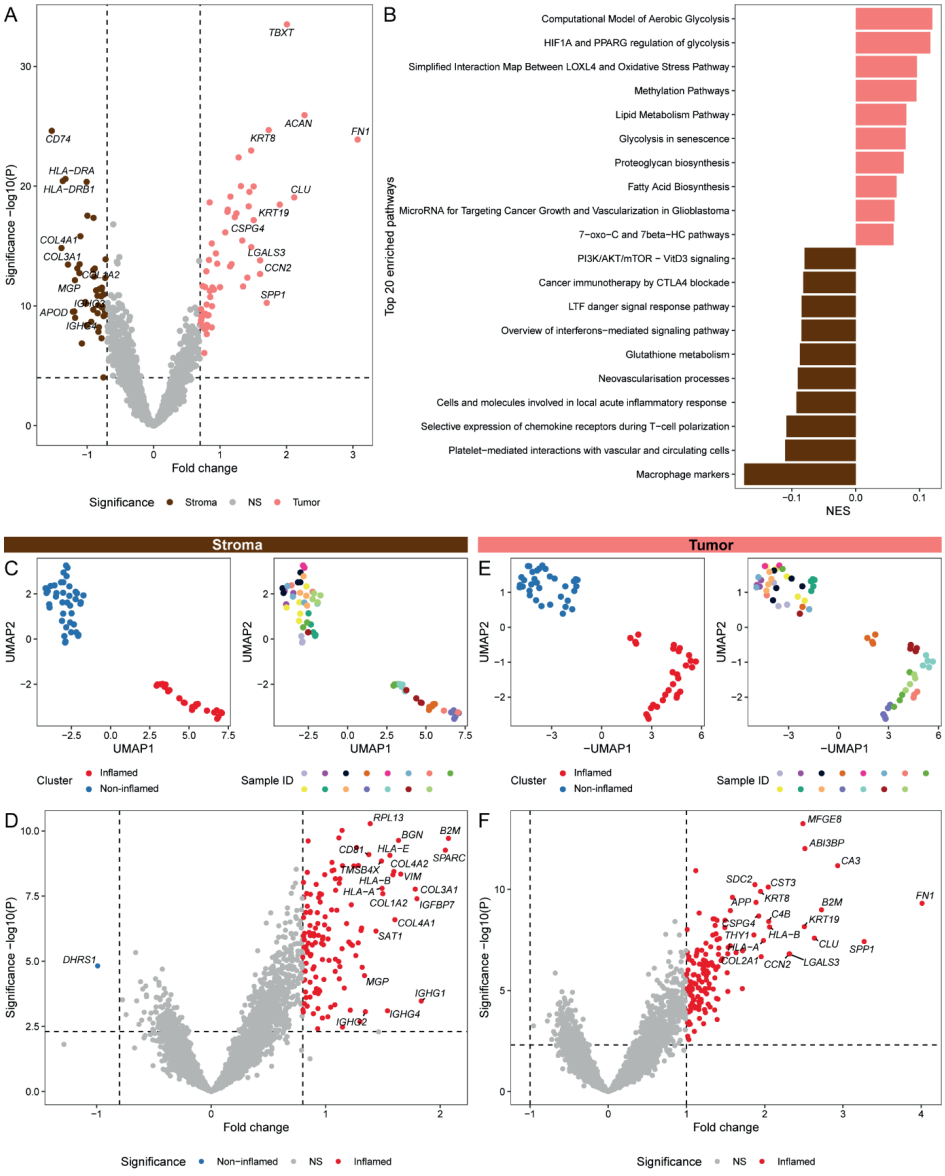


Figure 1. Inflammation is associated with distinct transcriptional states.

Following this general characterization, tumor and stroma segments were interrogated separately to investigate the association between cancer cell-specific gene expression and immune infiltration. Using the top 20% most variably expressed genes (1680 genes), graph-based clustering identified two distinct groups of stroma segments, which were visualized with Uniform Manifold Approximation and Projection (UMAP) (**Figure 1C**). Differential gene expression analysis indicated that these clusters reflected inflamed and non-inflamed stroma segments due to the enrichment of immune-related genes or the lack thereof (**Figure 1D; Figure S3**). These genes indicated enrichment of (plasma) B cells (*IGHG1*, *IGHG4*), antigen presenting cells (*HLA-DRA*, *HLA-DQB1*), macrophages (*CD68*, *LYZ*), fibroblasts (*COL1A2*, *COL3A1*), endothelial cells (*ACTA2*, *COL4A1*), complement (*C1R*, *C4B*), and T cells (*TRAC*). This pattern was accompanied by increased numbers of captured nuclei and detected genes in inflamed segments (**Figures S4A and S4B**), reflecting increased immune and stromal cell presence together with a broader detected gene repertoire.

Building on this clear dichotomy within the stroma segments, tumor segments were also clustered into two groups using graph-based clustering of the top 20% most variably expressed genes and visualized with UMAP (**Figure 1E**). Interestingly, these tumor clusters closely mirrored the inflammation-associated pattern observed in the stroma clusters, with 14 of the 15 samples grouping concordantly across both compartments. Because multiple ROIs were analyzed per sample, intratumoral heterogeneity was observed and both inflamed and non-inflamed segments could be present within a single tumor. For downstream analyses requiring a sample-level classification, tumors were therefore assigned an overall classification based on their predominant profile, defined as the cluster identity represented by the majority of segments within that sample. In rare cases, stromal and tumor compartments from the same sample displayed diverging profiles. This was observed for sample L6951 (light green), in which stromal segments clustered with the non-inflamed group whereas tumor segments clustered with the inflamed group. Histological evaluation revealed extensive radiotherapy-associated stromal fibrosis with limited immune infiltration, while viable tumor areas remained present. Supporting these observations, previously generated imaging mass cytometry data from the same tumors showed increased T cell infiltration in the inflamed tumor cluster compared with the non-inflamed cluster (**Figure S4C**). As expected, genes associated with immunity (*B2M*, *C1S*, *C4B*, *HLA-A*, *HLA-B, HLA-E, IFITM3*) showed higher expression in the inflamed tumor segments than in the non-inflamed segments (**Figure 1F; Figure S5**). More intriguingly, several chordoma-associated genes (*TBXT*, *CA3*, *CCN2, CD24*, *COL2A1*, *KRT19, SOX9*) also

exhibited higher expression in the inflamed tumor segments than in the non-inflamed segments (**Figure 1F; Figure S5**). Unlike the stromal compartment, the number of captured nuclei did not differ between inflamed and non-inflamed tumor segments (**Figure S4D**), whereas the number of detected genes was higher in the inflamed segments (**Figure S4E**). Together with the overall enrichment of differentially expressed genes (DEGs) in the inflamed segments, these results indicate that chordoma cells in inflamed segments exhibit a broader gene expression repertoire than those in non-inflamed segments, consistent with a distinct tumor cell state associated with immune infiltration.

To interrogate which biological pathways were associated with the observed inflamed phenotype, a differential ssGSEA was performed comparing inflamed with non-inflamed segments for both tumor and stromal compartments. To facilitate biological interpretation, the top 10% of differentially enriched pathways (22 pathways) based on adjusted *p*-values are shown for the stroma and tumor compartments (**Figures S6A and S6B**). Within the stroma compartment, inflamed segments exhibited enrichment of pathways related to immune activation and regulation, together with pathways involved in extracellular matrix organization, angiogenesis, and cellular stress responses (**Figure S6A**). In contrast, non-inflamed stroma segments showed few differentially enriched pathways. A similar pattern was observed within the tumor segments (**Figure S6B**). Inflamed tumor segments were enriched for a broad range of biological processes, including cellular metabolism, RNA processing and protein turnover, extracellular matrix production, and immune-related signaling. In contrast, non-inflamed tumor segments showed enrichment of only a limited number of pathways. Together, these pathway-level differences mirror the gene-level patterns observed between inflamed and non-inflamed segments, indicating broader pathway activity in inflamed segments across both tumor and stromal compartments.

Inflammation is associated with distinct lipid and metabolic profiles

In parallel with the spatial transcriptomic analyses, we explored the spatial metabolic and lipid profiles of chordomas in relation to immune infiltration using MALDI-MSI at 20 µm resolution on whole slides from consecutive frozen sections of the same samples analyzed by GeoMx. This analysis included sequential tissue sections from 13 of the 15 patients; for two patients, three recurrent tumor samples were additionally included to assess whether lipid profiles were preserved over the course of disease. For the data-driven annotation of the tissues, all measured lipid profiles were visualized using UMAP (**Figure 2A)** and, following clustering, were mapped back to their original

spatial coordinates. By aligning with histopathological images, the lipid clusters enabled differentiation between tumor and stromal regions (**Figure 2B)**. This facilitated comparative analyses both between tumor and stroma as well as between inflamed and non-inflamed regions within each compartment. Following classification of the lipid clusters as either tumor- (clusters 1-10) or stroma-associated (cluster 0), tumor regions exhibited strong patient-specific profiles, while stromal profiles were relatively similar across patients (**Figures 2A and 2B**). Notably, in patients for whom multiple tumor samples were available, tumor profiles clustered closely with those of previous tumors from the same patient, suggesting that these patient-specific lipid signatures appear largely preserved over time. Differential analysis showed that tumor areas were enriched for a diverse set of lipids, predominantly phosphatidylinositol (PI) species, along with some lysophosphatidylethanolamines (LPE), phosphatidic acid (PA), phosphatidylethanolamine (PE), and phosphatidylserine (PS) species, while stromal regions were enriched for only a single PS species (**Figure 2C**). Notably, tumors were enriched in polyunsaturated lipids (with more than two double bonds), suggesting more flexible and dynamic cell membranes. In contrast, the PS species enriched in stroma (PS(36:1)) is more saturated, containing only a single double bond, consistent with more rigid and stable membranes.

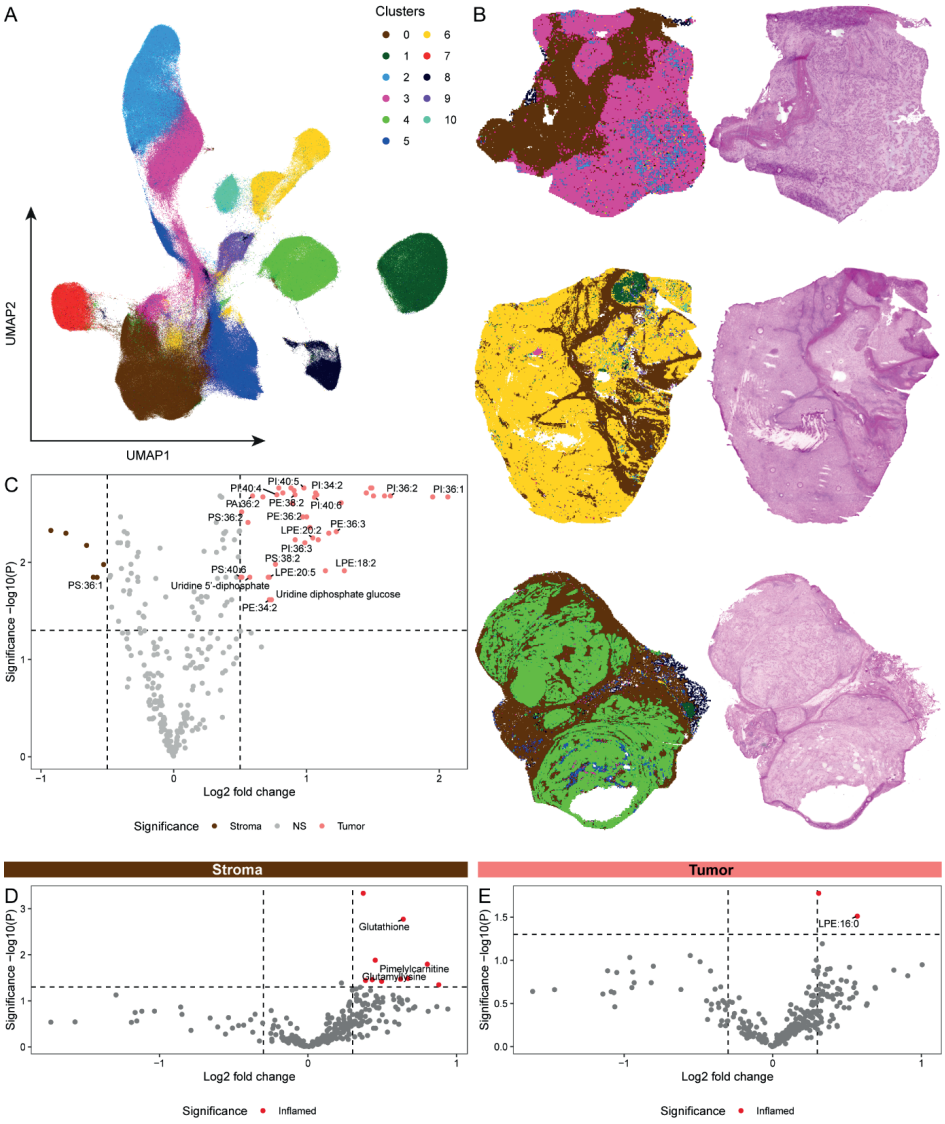


Figure 2. Spatial lipid and metabolite profiles in relation to inflammation. (A) UMAP visualization of all measured lipid profiles from the MALDI-MSI data. Clusters were identified through Louvain clustering. (B) Spatial visualization of the identified clusters (stroma = brown, tumor = pink, yellow, green) next to corresponding histopathological images for 3 samples. (C) Volcano plot presenting the differential lipid/metabolite abundance analysis comparing tumor with stroma regions. Significance was assessed by paired Student's t-tests, which were corrected for multiple testing with the Benjamini-Hochberg method. (D and E) Volcano plots presenting the differential lipid/metabolite abundance analysis comparing inflamed with non-inflamed samples, for tumor regions (D) and for stromal regions (E). Significance was determined by unpaired Student's t-tests.

Next, we compared inflamed and non-inflamed chordomas, as defined earlier by data-driven clustering of GeoMx segments, using differential abundance analysis within each compartment (**Figures 2D and 2E**). The resulting profiles mirrored the GeoMx findings, although differences were less pronounced: inflamed chordomas displayed a greater number of differentially abundant lipids and metabolites in both tumor and stromal regions than non-inflamed chordomas. In particular, glutathione was enriched in the inflamed stroma, while the saturated lipid species LPE(16:0) was elevated in inflamed tumor regions. Together, these findings indicate that inflamed chordomas are associated with distinct lipid and metabolic profiles compared with non-inflamed chordomas.

Inflammation is associated with increased glycogen accumulation and proliferation

The MSI analysis comparing tumor with stroma revealed that the metabolite uridine diphosphate (UDP)-glucose, the key substrate for glycogen synthase, was enriched in tumor regions compared to stroma (**Figure 2C**). Consistently, the GeoMx analysis showed increased expression of two glycogen synthesis–related genes, *PPP1R3C* and *UGP2*, in tumor segments from inflamed samples (as defined earlier by data-driven clustering of GeoMx segments; **Figure S5**). *PPP1R3C* encodes a subunit of the protein phosphatase 1 (PP1) complex, which activates glycogen synthase while inhibiting glycogen phosphorylase, thereby promoting glycogen storage. *UGP2* encodes UDP-Glucose Pyrophosphorylase 2, an enzyme that catalyzes the conversion of glucose-1-phosphate and uridine triphosphate (UTP) into UDP-glucose. Supporting these findings, Periodic acid-Schiff (PAS) and diastase-PAS (dPAS) staining demonstrated abundant glycogen accumulation in tumor cells of most chordomas, with inflamed tumors generally exhibiting stronger staining intensity and greater glycogen abundance than non-inflamed tumors (**Figures 3A-3C**). Collectively, these results indicate that glycogen synthesis pathways are active in chordomas, and that inflamed tumors exhibit higher glycogen accumulation than non-inflamed tumors.

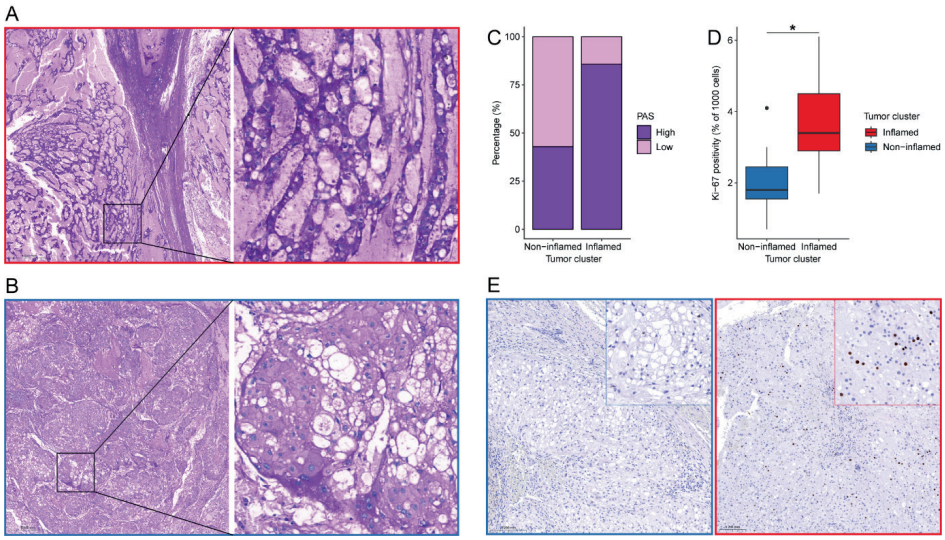


Figure 3. Glycogen accumulation and proliferation are increased in inflamed chordomas. (A and B) Example images of the PAS staining of an inflamed chordoma (A), classified as high PAS staining, and a non-inflamed chordoma (B), classified as low PAS staining. (C) Bar plots displaying the percentage of chordomas with high and low PAS staining, grouped per tumor cluster. (D) Boxplots presenting the percentage of Ki-67$^+$ tumor cells in proliferative hotspot areas, grouped per tumor cluster. Statistical significance was assessed through a Student's t-test: *p < 0.05. (E) Example of Ki-67 immunohistochemistry showing Ki-67 expression in a non-inflamed (left) and inflamed (right) chordoma.

Following this, we examined whether the distinct tumor cell state observed in inflamed chordomas, together with increased glycogen accumulation, was associated with differences in tumor cell proliferation. Although proliferation-associated genes were not detected in the GeoMx dataset, likely due to their low expression and the limitations of NanoString's Whole Transcriptome Atlas (WTA), immunohistochemistry for Ki-67 showed that inflamed tumors were more proliferative than the non-inflamed tumors (**Figures 3D and 3E**). Nonetheless, proliferation remained very low compared with that observed in carcinomas or high-grade sarcomas, with only two samples showing Ki-67 positivity above 5%.

Interferon-γ does not induce *TBXT* expression in chordoma cell lines

To determine whether the broader transcriptional repertoire observed in inflamed chordomas – including increased expression of *TBXT* and its target genes – could be driven by interferon-γ (IFN-γ) signaling, as suggested by the enrichment of IFN-γ-responsive genes (e.g., HLA class I) in inflamed tumor

regions and activation of type II interferon signaling in the stroma, we investigated whether IFN-γ modulates expression of *TBXT*, the master regulator of chordoma biology. Multiple chordoma cell lines were treated with IFN-γ, and expression of *B2M* (positive control for IFN-γ signaling) and *TBXT* was assessed by quantitative PCR (qPCR). Ct values were normalized to two established chordoma housekeeping genes, *HPRT1* and *TBP* (15, 16), which showed stable expression across all treatment conditions (**Figure S7**). As expected, IFN-γ treatment robustly increased *B2M* expression in all cell lines (**Figure 4**). In contrast, expression of *TBXT* isoforms remained unchanged across cell lines, indicating that *TBXT* expression is unlikely to be regulated by IFN-γ signaling.

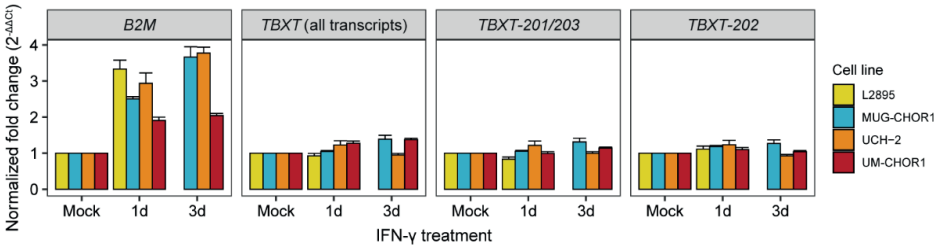


Figure 4. *TBXT* expression is not induced by IFN-γ. Normalized expression fold change for each chordoma cell line and treatment condition, for *B2M* and the *TBXT* isoforms. All values were normalized for both housekeeping genes, *HPRT1* and *TBP*. Data are represented as mean ± SD. Abbreviations: 1d = 1 day; 3d = 3days.

DISCUSSION

In this study, we applied an integrated spatial approach to explore correlates of immunogenicity in chordoma. Our findings revealed a clear dichotomy between inflamed and non-inflamed chordomas across both tumor and stromal compartments. Inflamed tumors exhibited higher expression of immune-related genes, such as those encoding HLA class I molecules and complement factors, as well as chordoma-associated genes, including *TBXT*, *SOX9*, and *COL2A1*, within the tumor cell compartment. These transcriptional differences were accompanied by distinct metabolic profiles and increased glycogen accumulation, indicating a distinct tumor cell state associated with, and potentially interacting with, immune infiltration. To examine whether inflammatory signaling could contribute to the broader transcriptional repertoire observed in inflamed tumors, we investigated whether IFN-γ modulates expression of *TBXT*, the master regulator of chordoma biology. While chordoma cells were responsive to IFN-γ, *TBXT* expression remained unchanged

following IFN-γ treatment, suggesting that IFN-γ signaling is unlikely to account for the higher *TBXT* expression observed in inflamed tumors. Nevertheless, other cytokines or mediators released by infiltrating immune or stromal cells may still contribute to the tumor cell states observed in inflamed chordomas.

These findings extend prior work, including our own, that identified distinct immune contextures in chordoma (8-13), and highlight a strong association between tumor cell gene expression patterns and immune infiltration. Although the causal link remains unresolved, differences in *TBXT* expression may contribute to the heterogeneity observed in tumor phenotypes and immune contextures. Such variability could be shaped by underlying genetic or epigenetic factors. For instance, duplications or amplifications of the *TBXT* locus have been reported in 15-30% of chordoma patients (17-19). In addition, chordomas are transcriptionally addicted to super-enhancer–driven *TBXT* expression (20-22), and variation in enhancer strength or chromatin state between tumors may contribute to differences in *TBXT* expression levels. Because *TBXT* regulates a broad range of transcriptional programs (14, 23), its differential activity may contribute to the broader transcriptional repertoire observed in inflamed chordomas. Of note, *TBXT* has also been linked to interferon-α response networks in chordomas (23), although this observation derives from a single study and its future implications for chordoma immunity remain to be established.

In addition to its role as a master regulator, *TBXT* has been identified as an immunogenic antigen in chordoma. Brachyury-derived peptides have been shown to expand T cells *in vitro* (24, 25), and vaccination strategies targeting brachyury have elicited *TBXT*-specific T cell responses in a subset of chordoma patients (26, 27). Furthermore, a recent conference abstract presented at the SITC 39th Annual Meeting (2024) reported naturally presented HLA peptides derived from brachyury across common alleles, covering 80% of their patient population (Pan K., Chiu Y., Patel H.A., Huang E., MacCoss M., Yee C. 387 Identification of novel T cell receptor (TCR) target to brachyury for the development of T cell-based immunotherapy of chordoma and other solid tumors. *Journal for ImmunoTherapy of Cancer*. 2024;12:. **https://doi.org/10.1136/jitc-2024-SITC2024.0387**). Together, these studies highlight the immunogenic potential of *TBXT* as an antigen and support further investigation into how *TBXT*-directed immune responses can be effectively leveraged in chordoma.

Our spatial metabolomics analysis revealed that tumor regions of chordoma were enriched in polyunsaturated lipids. Because these lipids contain multiple double bonds, they are particularly susceptible to lipid peroxidation – a process

in which reactive oxygen species attack fatty acids, generating toxic radicals that compromise membrane integrity and can trigger ferroptosis, a regulated form of cell death (28). Consistent with this vulnerability, the Chordoma Foundation recently reported preclinical evidence suggesting ferroptosis sensitivity in chordoma cell lines (Chordoma Foundation. (2024). Ferroptosis in chordoma. Figshare. **https://doi.org/10.6084/m9.figshare.26517532),** supporting the relevance of lipid peroxidation pathways in this disease. In parallel, inflamed tumors were enriched for a saturated LPE species (16:0) in tumor regions and glutathione in stromal regions. Glutathione, a key antioxidant, and saturated lipids, which are less prone to peroxidation, collectively point toward adaptive responses to oxidative stress. Together, these findings suggest that inflamed tumors may experience increased oxidative stress, potentially reflecting heightened tumor cell activity, immune infiltration, or both (29). Further studies will be required to clarify how oxidative stress relates to tumor cell states and immune infiltration in chordoma.

In addition to lipid and antioxidant adaptations, inflamed chordomas also exhibited increased glycogen accumulation, accompanied by higher expression of glycogen synthesis–related genes. Glycogen serves as a critical energy reserve that supports cell survival under hypoxic conditions (30), and its increased accumulation in inflamed tumors may therefore provide a metabolic advantage that sustains tumor cell activity and viability within an immune-infiltrated microenvironment. Glycogen storage is, however, a recognized feature of chordomas (31), likely associated with their notochordal differentiation (32). This notion is supported by the observation that *PPP1R3C* is a transcriptional target of *TBXT* (14). Accordingly, the increased glycogen accumulation observed in inflamed chordomas may reflect enhanced *TBXT*-associated transcriptional programs rather than representing solely a microenvironmental-driven metabolic adaptation.

Going forward, it will be important to identify proxies or biomarkers that reflect immunogenic potential, enabling broader clinical translation. Notably, recent work by Crombé *et al*. demonstrated that high ^{18}F-fluorodeoxyglucose (FDG) uptake correlates with increased immune cell densities in high-grade soft tissue sarcomas (33). Consistent with our findings, this suggests that metabolic imaging approaches such as FDG positron emission tomography could potentially serve as non-invasive tools to identify immunogenic chordoma subsets and guide patient stratification for immunotherapeutic strategies. This concept, however, will require validation in larger, ideally multi-institutional, cohorts to confirm its clinical utility.

This study has several limitations. First, the cohort predominantly comprises sacrococcygeal chordomas. This reflects the clinical reality that sacrococcygeal tumors are generally larger and more frequently resected *en bloc* than clival or spinal chordomas, resulting in greater amounts of frozen material suitable for spatial multi-omics analyses. Nevertheless, prior work (34), including our own (8), suggests that the immune microenvironment does not substantially differ across anatomical locations, which is supported here by the comparable distribution of clival and spinal samples across inflammatory clusters. Finally, functional experiments were limited to IFN-γ stimulation of chordoma cell lines. Although IFN-γ robustly induced *B2M*, *TBXT* expression remained stable across cell lines, indicating that *TBXT* is not regulated by IFN-γ under these conditions. This analysis was, however, restricted to a limited set of genes and a single cytokine. Expanding future studies to include broader panels of inflammatory mediators and downstream transcriptional programs will be important to determine whether the distinct tumor cell state observed in inflamed chordomas is driven by alternative microenvironmental cues or reflects intrinsic tumor biology.

In conclusion, our integrated spatial approach demonstrates that inflamed chordomas exhibit distinct transcriptional and metabolic features, marked by a broader transcriptional repertoire, adaptations to oxidative stress, and increased glycogen accumulation. These findings highlight a close association between tumor cell states, metabolic adaptations, and immune infiltration. While the causal relationships among these processes remain to be established, they point to metabolic and transcriptional states as potential indicators of tumor immunogenicity. Ultimately, such integrated molecular and spatial insights may guide the development of biomarkers and inform patient stratification for future immunotherapeutic strategies.

RESOURCE AVAILABILITY

Lead contact

Requests for further information and resources should be directed to and will be fulfilled by the lead contact, Judith V.M.G. Bovee (**j.v.m.g.bovee@lumc.nl**).

Materials availability

There are restrictions to the availability of the primary chordoma cell line L2895 because institutional and biobank approval for distribution outside our institute is currently pending.

Data and code availability

The utilized imaging mass cytometry data is available as raw data in BioStudies at S-BIAD830 or as processed data on our lab's GitHub (**https://github.com/deMirandaLab/multimodal-profiling-of-chordomas**). The raw and processed GeoMx digital spatial profiling data and the processed MALDI-MSI data generated in this study are publicly available on Figshare (**https://figshare.com/s/4d52d0129b9e0f9c7a8c**). The raw MALDI-MSI data are publicly available in MassIVE at MSV000100742. All other data are available from the corresponding author upon reasonable request.

The R code used to process the data from this study is also published on our group's GitLab (**https://github.com/deMirandaLab/spatial-profiling-of-chordomas**).

Acknowledgements

We acknowledge the Utrecht Sequencing Facility (USEQ) for providing sequencing service and data. USEQ is subsidized by the University Medical Center Utrecht and The Netherlands X-omics Initiative (NWO project 184.034.019). JVMGB is the recipient of a Cancer Research Institute/Chordoma Foundation CLIP Grant (CRI5106). This work was further funded by the intramural Leiden Center for Computational Oncology strategic fund. NFCCdM is funded by the European Research Council (ERC) under the European Union's Horizon 2020 Research and Innovation Program (grant agreement no. 852832) and by the VIDI ZonMW (project number: 09150172110092). The graphical abstract was created in **https://BioRender.com**.

Author contributions

SvO contributed to the conceptualization, funding acquisition, data curation, software, formal analysis, validation, investigation, visualization, methodology, writing-original draft, project administration, and writing-review editing. RU contributed to the data curation, software, formal analysis, validation, investigation, visualization, methodology, writing-original draft, and writing-review editing. ZBE contributed to the validation, investigation, and writing-review editing. SC contributed to the validation, methodology and writing-review editing. SV contributed to the validation, investigation, methodology, writing-original draft, and writing-review editing. RvdB contributed to the formal analysis, validation, investigation, methodology, and writing-review editing. IHBdB contributed to the investigation, methodology and writing-review editing. ABK contributed to the validation, investigation, methodology, writing-original draft, and writing-review editing. WCP contributed to the resources and writing-review editing. KS contributed to resources, writing-review editing. RJPvdW contributed to the resources and writing-review editing. RvZ contributed to the investigation and writing-review editing. BH contributed to the software, formal analysis, investigation, methodology, and writing-review editing. NFCCdM contributed to the conceptualization, supervision, funding acquisition, investigation, methodology, writing-original draft, and writing-review editing. JVMGB contributed to the conceptualization, supervision, funding acquisition, investigation, methodology, writing-original draft, and writing-review editing.

Declaration of interests

The authors declare no competing interests.

Declaration of generative AI and AI-assisted technologies

During the preparation of this work the author(s) used ChatGPT in order to improve the readability and language of the manuscript. After using this tool/service, the author(s) reviewed and edited the content as needed and take(s) full responsibility for the content of the published article.

STAR METHODS

Experimental model and study participant details

Patient samples

Snap-frozen tumor tissue was available for 18 samples from 15 patients with conventional chordoma (2 clival, 2 spinal and 11 sacrococcygeal), all of whom were part of a previously described cohort (8). An overview of the samples is provided in **Table S1**. All samples included in this study were derived from surgical resection specimens, including three from patients who had received neoadjuvant radiotherapy. Samples were pseudo anonymized and handled according to the ethical guidelines outlined in 'Code for Proper Secondary Use of Human Tissue in The Netherlands' by the Dutch Federation of Medical Scientific Societies. A waiver of consent was obtained from the medical ethical evaluation committee (Medisch-Ethische Toetsingscommissie Leiden Den Haag Delft; protocol number: B17.036 and B20.067). Therefore, this study adheres to the Declaration of Helsinki.

Cell lines

One chordoma cell line from a primary tumor was established in-house (L2895) and additional chordoma cell lines were acquired via the Chordoma Foundation, including MUG-CHOR1, UCH2, and UM-CHOR1. All chordoma cell lines were cultured in IMDM/RPMI 1640 (4:1, Gibco) supplemented with 10% non-inactivated FBS (F7524, Sigma-Aldrich) and 1% Insulin-Transferrin-Selenium (ITS-G, Gibco).

Method details

GeoMx digital spatial profiling

Slides were prepared in a cryostat and kept on dry-ice. Tissue sections of 5 µm were thaw-mounted onto pre-cooled slides to prevent RNA degradation and then stored at -80°C until use. Slide preparation was performed by the Utrecht Sequencing Facility (Utrecht, The Netherlands) according to NanoString's protocol. In brief, slides were fixed using 10% neutral-buffered formalin, followed by overnight *in situ* hybridization using the Human NGS WTA RNA (v1.0) probe set (NanoString Technologies). Slides were concurrently incubated with immunofluorescent antibodies, including pan-cytokeratin (AE-1/AE-3, Novus Biologicals, NBP2-33200AF532) to identify tumor cells and CD45 (2B11 + PD7/26, Novus Biologicals, NBP2-34528AF594) to detect immune cells. Next, slides were stained with the GeoMx Nuclear Stain (Syto13, Thermo Fisher Scientific,

S7575), after which slides were loaded into the GeoMx Digital Spatial Profiler instrument (NanoString Technologies) and scanned. For each sample, two to five ROIs were selected at the tumor-stroma interface to represent the overall tumor microenvironment. ROI selection was reviewed and confirmed by a bone tumor pathologist (JVMGB). ROI areas were variable (0.145-0.481 mm^2), with the aim of capturing at least 200 cells per segment to ensure representative gene expression data. A total of 63 ROIs were UV-illuminated twice to capture the pan-cytokeratin-positive tumor segment separately from all other cells, which were classified as stroma. CD45 staining was used to visualize immune cells and guide ROI selection but was not used for segment capture.

T cell infiltration from imaging mass cytometry data

We previously analyzed samples from the current cohort by means of imaging mass cytometry (8). T cell counts from that analysis were extracted to validate the GeoMx classification of the samples into inflamed and non-inflamed categories. One sample (L5436) was excluded due to the imaging mass cytometry data including both conventional and dedifferentiated tumor components, while the frozen sample analyzed by GeoMx comprised only of conventional chordoma.

MALDI-TOF-MSI

Concurrently with the preparation of the GeoMx slides, consecutive 5 µm tissue sections were cut from the frozen tissue samples, thaw-mounted onto conductive indium-tin-oxide (ITO)-coated glass slides (VisionTek Systems) and stored at -80°C until use. Before use, slides were placed in a vacuum freeze-drier for a minimum of 15 minutes. In total, samples from 13 of the 15 patients analyzed by GeoMx were available, and three recurrent tumor samples from two patients were additionally included to evaluate the preservation of lipid profiles over the course of disease.

Spatial metabolomics data was obtained using matrix-assisted laser desorption/ionization (MALDI)-MSI, using *N*-(1-naphthyl) ethylenediamine dihydrochloride (NEDC) (Sigma-Aldrich) as the matrix. A solution of 7 mg/mL NEDC in 70% MeOH (Actu-All Chemicals), 20% acetonitrile (Actu-All Chemicals) and 5% deionized water (MQ) was prepared. The tissue sections were coated with the matrix solution using a HTX M3+ sprayer (HTX Technologies). Detailed information about the matrix deposition step is available in **Table S2**.

Spatial metabolomics data was acquired at a spatial resolution of 20 µm using a rapifleX MALDI-TOF/TOF system (Bruker Daltonics) operating in reflectron

mode, negative polarity, and set to detect a mass range of 60 to 1200 *m/z*. Each pixel was acquired with 50 shots at a laser repetition rate of 10 kHz.

High-resolution accurate-mass profiling acquisition

After spatial metabolomics data acquisition using the rapifleX MALDI-TOF/TOF, each tissue section was also subjected to high-resolution, accurate-mass (HRAM) profiling using a 15T solariX MALDI-FTICR mass spectrometer (Bruker Daltonics). The MALDI-FTICR was operated in negative-ion mode, using a 2M transient length, and set to detect a mass range of 400 to 1000 *m/z*. Each HRAM lipid/metabolite profile was collected from 25 laser shots, using a laser repetition rate of 120 Hz and with the laser focus set to 'minimum'. After visual inspection of the spatial metabolomics results, HRAM profiles were acquired from regions that exhibited distinct lipid and metabolite signatures. After completing the spatial metabolomics and HRAM profiling, residual MALDI matrix was removed from the slides by ethanol washing and rehydration, followed by hematoxylin and eosin (H&E) staining according to standard diagnostic procedures. Finally, high resolution optical images of the H&E-stained tissue sections were recorded using a ZEISS Axio Scan.Z1 slide scanner (ZEISS).

PAS staining

Formalin-fixed paraffin-embedded (FFPE) tissue sections from corresponding tumors were stained using PAS and dPAS. PAS staining was performed using the Artisan PAS Stain Kit (AR165, Artisan, Agilent), while dPAS staining was carried out using the same kit in combination with alpha-amylase digestion using the Artisan Alpha-Amylase reagent (AR171, Artisan, Agilent). All staining procedures were executed on the Artisan Link Pro Special Staining System (Dako, Agilent) according to the manufacturer's protocols. Comparison of PAS and dPAS staining demonstrated that the majority of the PAS signal in tumor cells was attributable to glycogen, as diastase digestion abolished most of the staining (**Figure S8**). Samples were subsequently classified as high or low based on the relative PAS staining intensity within the tumor cell compartment, as assessed by one observer (ZBE). The resulting groups were visualized in cumulative bar plots per identified GeoMx cluster using ggplot2 (R, v.3.5.1).

Immunohistochemistry

Immunohistochemical detection for Ki-67 (MIB-1, FLEX RTU, 1:1, Dako, GA626) was performed as described previously (8). FFPE tissue blocks corresponding to the same tumors used for the GeoMx/MALDI analyses were assessed. Given

its overall low expression, Ki-67$^+$ histological tumor regions were selected in QuPath (v.0.3.1) to quantify the percentage of Ki-67$^+$ tumor cells per 1000 tumor cells.

IFN-γ treatment of chordoma cell lines

All chordoma cell lines were seeded in 50 µg/mL Collagen Type I (50202, Ibidi) coated 6-well plates at a cell density of 50.000 cells/well. After 11 days, cells were either not treated (mock) or treated with 100 U/mL IFN-γ (11343536, Immunotools). After one or three days of treatment, cells were harvested and pellets were stored at -80°C until RNA isolation was performed.

qPCR

Total RNA was isolated from the cell pellets using the NucleoSpin RNA Mini kit (Macherey-Nagel), and cDNA synthesis was performed using the Transcriptor First Strand cDNA Synthesis Kit (Roche). QPCR was performed to quantify four genes: *TBP* and *HPRT1* as housekeeping genes (15, 16), *B2M* as positive control and *TBXT* as gene of interest. Transcript structure data from Ensembl indicates that *TBXT* (ENSG00000164458) encodes three protein-coding isoforms: *TBXT-201* (ENST00000296946) and *TBXT-203* (ENST00000366876) both include exon 6, while *TBXT-202* (ENST00000366871) excludes exon 6 (35). Isoform-specific primers were therefore designed to distinguish between the "long" isoforms (*TBXT-201/203*) and the "short" isoform (*TBXT-202*), as well as primers targeting a region common to all *TBXT* transcripts (*TBXT* (all transcripts)). Primer sequences are provided in **Table 1**. The qPCR reactions were performed using iQ SYBR Green Supermix (Bio-Rad) and run on a C1000 Touch Thermal Cycler equipped with the CFX384 Touch Real-Time PCR Detection System (Bio-Rad). A standard PCR protocol was followed by annealing/extension at 59.2 °C for 45 seconds. All reactions were carried out in triplicate. Reactions were performed in 384-well Hard-Shell thin-wall PCR plates (Bio-Rad, HSP3805) sealed with Microseal 'B' adhesive film (Bio-Rad, MSB1001). Data were analyzed using CFX Maestro software (v.5.3.022.1030, Bio-Rad).

Table 1. Primer sequences. Fwseq = forward primer sequence; Revseq = reverse primer sequence; bp = base pairs.

		('5-'3)	
Gene / Transcript	**Amplicon length (bp)**	**Fwseq**	**Revseq**
B2M	69	CTCCGTGGCCTTAGCTGTG	TTTGGAGTACGCTGGATAGCCT
HPRT1	94	TGACACTGGCAAAACAATGCA	GGTCCTTTTCACCAGCAAGCT
TBP	117	GAGCTGTGATGTGAAGTTTCC	TCTGGGTTTGATCATTCTGTAG
TBXT-202	94	CCTTGATGCAAAGGAAAGAAGTGA	GTTGTCAGAATAGGATTGGGAGT
TBXT-201/203	107	CCTTGATGCAAAGGAAAGAAGTGA	TGGTTCCAGGAAGAAGCCAC
TBXT (all transcripts)	93	CTCACCAACAAGCTCAACGG	TGGACCCCCAACTCTCACT

Quantification and statistical analysis

GeoMx data processing

All data processing and downstream analyses were performed in R (v.4.4.0) using the GeomxTools package (v.3.8.0). Quality control of the segments and the WTA probes was performed following NanoString's analysis guideline. The used parameters and code are available on our lab's GitHub at **https://github.com/deMirandaLab/spatial-profiling-of-chordomas**. In short, no segments were excluded after quality control, but 21 probes were excluded after performing the Grubb's test. A limit of quantification was calculated for the detected genes in each segment, after which genes were excluded that were detected in less than 5% (n=6) of all segments. This resulted in a final set of 8401 genes in 126 segments, with a minimum of 100 captured nuclei. The data was further processed with a Q3 quantile normalization and log2 transformation.

GeoMx data analysis

Tumor segments were compared with stroma segments through a differential gene expression analysis. A linear mixed model (LMM) was used to correct for varying number of segments per sample, as described by NanoString's analysis guideline. The results were visualized in a volcano plot with ggplot2 (R, v.3.5.1) and the top 20 DEGs ranked by $\log_2$ fold change were selected for visualization. All DEGs were visualized in a heatmap using ComplexHeatmap (R, v.2.20.0). ssGSEA was performed using GSVA (R, v.1.52.3), which utilized an in-house curated WikiPathways gene list. The top differentially enriched biological pathways were identified comparing tumor and stroma segments through a similar LMM.

Next, segments were analyzed within their respective compartments. Both tumor and stroma segments were clustered into two groups through graph-based clustering (Louvain algorithm) using bluster (R, v.1.14.0), which were then visualized using UMAP. Differential gene expression analysis was again performed using an LMM, now comparing the identified clusters within their respective compartments. Again, the top 20 DEGs per cluster ranked by $\log_2$ fold change were selected for visualization in a volcano plot. All DEGs were visualized per compartment in heatmaps. The number of captured nuclei and detected genes per segment were compared between the identified clusters using unpaired Student's t-tests.

ssGSEA was subsequently performed for each compartment to compare pathway enrichment between the identified clusters. Differentially enriched pathways were identified using an LMM applied to ssGSEA scores, and the top 10% of pathways ranked by normalized enrichment score were visualized in heatmaps to guide biological interpretation. For all differential analyses, *p*-values were adjusted for multiple testing using the Benjamini–Hochberg method.

MALDI-TOF-MSI data processing

All spatial metabolomics data were imported into SCiLS Lab (v.2023b 11.01.14623, Bruker Daltonics) and subjected to baseline correction using the TopHat algorithm (width 200). The average spectrum of all tissues was exported from SCiLS Lab and used for peak picking in mMass (v.5.5.0) with a Signal-to-Noise Ratio (SNR) > 9, followed by removal of matrix derived peaks by image correlation to the principal matrix peak ($[NEDC+Cl]^-$). Bisecting *k*-means clustering was employed in SCiLS Lab to differentiate on-tissue pixels from off-tissue pixels and areas without signal. Total Ion Count (TIC) normalized peak intensities and masses were exported as .csv files and processed further. Masses were internally calibrated to a list of abundant lipids and molecules commonly detected as negative ions when using NEDC as the matrix (**Table S3**). Spectra were normalized to the total ion count before further analysis. For small metabolite assignment, MALDI-TOF-MSI peaks were matched to the HMDB database (accessed 10/07/2024) with a mass error tolerance of ± 30 ppm allowing for $[M-H]^-$ and $[M+Cl]^-$ adducts.

Lipid/metabolite assignment based on high-resolution accurate-mass profiling

The HRAM profiles obtained from the MALDI-FTICR mass spectrometer were imported and processed in R (v.4.1) with MALDIquantForeign (v.0.13)

and MALDIquant (v.1.20). Spectra were aligned, peak picked, and internally calibrated similarly to the MSI data (**Table S4**).

Resulting peaks were matched to the LIPIDMAPS LMSD database (accessed 14/01/2021) for phosphatidic acid (PA), phosphatidylethanolamine (PE), phosphatidylinositol (PI), phosphatidylserine (PS), and phosphatidylglycerol (PG), using a mass tolerance of ± 3 ppm and allowing for $[M-H]^-$ and $[M+Cl]^-$ adducts. This list was transferred to the lower mass resolution spatial metabolomics MALDI-TOF-MSI data, matching every MALDI-TOF-MSI peak with its analogous peak in the HRAM MALDI-FTICR spectra, using a tolerance of ± 40 ppm. Finally, all lipid assignments were manually curated to remove false positives and to ensure that all mass spectral peaks, which were used for the subsequent data analysis steps, corresponded to a single lipid species in the HRAM lipid profiles.

MALDI-TOF-MSI data analysis

Downstream analysis of the curated spatial metabolomics data was performed using Seurat (R, v.4.2). Per sample, data points (pixels) corresponding to holes in the tissue or necrotic tissue were removed after *k*-means clustering and subsequent clustering with Seurat. The lipid/metabolite abundance data of all samples was transformed into a single Seurat object followed by log normalization, after which a total of 1,223,810 pixels were clustered (Louvain algorithm) and visualized by a dimensionality reduction using UMAP. For differential analyses, clusters were classified as tumor or stroma by comparing their spatial localization with corresponding histopathological images, after which the mean lipid/metabolite intensity per region was calculated per sample.

qPCR data analysis

Average Ct values were calculated from technical triplicates. For each condition, ΔCt values were determined by subtracting the Ct of the housekeeping gene from that of the gene or transcript of interest. ΔΔCt values were then calculated by subtracting the ΔCt of the control condition (mock) from the ΔCt of the condition of interest. Fold changes in expression were computed using the $2^{-\Delta\Delta Ct}$ method. These calculations were performed separately using *HPRT1* and *TBP*, after which the average and standard deviation were calculated across both housekeeping genes. Boxplots were generated using ggplot2 (R, v.3.5.1) to visualize the normalized fold change in expression of the target genes and transcripts.

REFERENCES

1. WHO Classification of Tumours Editorial Board. Soft Tissue and Bone Tumours. WHO Classification of Tumours. 5 ed. Lyon, France: IARC Publications; 2020.
2. Stacchiotti S, Gronchi A, Fossati P, Akiyama T, Alapetite C, Baumann M, et al. Best practices for the management of local-regional recurrent chordoma: a position paper by the Chordoma Global Consensus Group. Ann Oncol. 2017;28(6):1230-42.
3. Wedekind MF, Widemann BC, Cote G. Chordoma: Current status, problems, and future directions. Curr Probl Cancer. 2021;45(4):100771.
4. Colia V, Stacchiotti S. Medical treatment of advanced chordomas. Eur J Cancer. 2017;83:220-8.
5. Somaiah N, Conley AP, Parra ER, Lin H, Amini B, Solis Soto L, et al. Durvalumab plus tremelimumab in advanced or metastatic soft tissue and bone sarcomas: a single-centre phase 2 trial. Lancet Oncol. 2022;23(9):1156-66.
6. Bishop AJ, Amini B, Lin H, Raza SM, Patel S, Grosshans DR, et al. Immune Checkpoint Inhibitors Have Clinical Activity in Patients With Recurrent Chordoma. J Immunother. 2022;45(8):374-8.
7. Blay JY, Chevret S, Le Cesne A, Brahmi M, Penel N, Cousin S, et al. Pembrolizumab in patients with rare and ultra-rare sarcomas (AcSe Pembrolizumab): analysis of a subgroup from a non-randomised, open-label, phase 2, basket trial. Lancet Oncol. 2023.
8. van Oost S, Meijer DM, Ijsselsteijn ME, Roelands JP, van den Akker B, van der Breggen R, et al. Multimodal profiling of chordoma immunity reveals distinct immune contextures. J Immunother Cancer. 2024;12(1).
9. Huo X, Guo T, Wang K, Yao B, Li D, Li H, et al. Methylation-based reclassification and risk stratification of skull-base chordomas. Front Oncol. 2022;12:960005.
10. Zuccato JA, Patil V, Mansouri S, Liu JC, Nassiri F, Mamatjan Y, et al. DNA methylation-based prognostic subtypes of chordoma tumors in tissue and plasma. Neuro Oncol. 2022;24(3):442-54.
11. Baluszek S, Kober P, Rusetska N, Wagrodzki M, Mandat T, Kunicki J, et al. DNA methylation, combined with RNA sequencing, provide novel insight into molecular classification of chordomas and their microenvironment. Acta Neuropathol Commun. 2023;11(1):113.
12. Bai J, Shi J, Zhang Y, Li C, Xiong Y, Koka H, et al. Gene Expression Profiling Identifies Two Chordoma Subtypes Associated with Distinct Molecular Mechanisms and Clinical Outcomes. Clin Cancer Res. 2023;29(1):261-70.
13. Xiong Y, Li M, Niu G, Xu T, Li C, Ma T, et al. Identification of immune subtypes associated with the prognosis in skull base chordoma. Acta Neuropathol Commun. 2025;13(1):130.
14. Nelson AC, Pillay N, Henderson S, Presneau N, Tirabosco R, Halai D, et al. An integrated functional genomics approach identifies the regulatory network directed by brachyury (T) in chordoma. J Pathol. 2012;228(3):274-85.
15. Santegoeds RGC, Yakkioui Y, Jahanshahi A, Hoogland G, Temel Y, van Overbeeke JJ. Validation of reference genes in human chordoma. Surg Neurol Int. 2017;8:100.

16. Seven D, Kizililsoley N, Nikerel E, Bayrak OF, Ture U. Identification of Reference Genes in Chordoma Cells Allows Cross-Comparison of Expression Studies Across Subtypes. Turk Neurosurg. 2024;34(1):121-7.

17. Tarpey PS, Behjati S, Young MD, Martincorena I, Alexandrov LB, Farndon SJ, et al. The driver landscape of sporadic chordoma. Nature Communications. 2017;8.

18. Bai J, Shi J, Li C, Wang S, Zhang T, Hua X, et al. Whole genome sequencing of skull-base chordoma reveals genomic alterations associated with recurrence and chordoma-specific survival. Nat Commun. 2021;12(1):757.

19. Kelley MJ, Shi J, Ballew B, Hyland PL, Li WQ, Rotunno M, et al. Characterization of T gene sequence variants and germline duplications in familial and sporadic chordoma. Hum Genet. 2014;133(10):1289-97.

20. Sharifnia T, Wawer MJ, Chen T, Huang QY, Weir BA, Sizemore A, et al. Small-molecule targeting of brachyury transcription factor addiction in chordoma. Nat Med. 2019;25(2):292-300.

21. Sheppard HE, Dall'Agnese A, Park WD, Shamim MH, Dubrulle J, Johnson HL, et al. Targeted brachyury degradation disrupts a highly specific autoregulatory program controlling chordoma cell identity. Cell Rep Med. 2021;2(1):100188.

22. Cottone L, Cribbs AP, Khandelwal G, Wells G, Ligammari L, Philpott M, et al. Inhibition of Histone H3K27 Demethylases Inactivates Brachyury (TBXT) and Promotes Chordoma Cell Death. Cancer Res. 2020;80(20):4540-51.

23. Umbaugh CS, Groth M, Erkut C, Lee KS, Marinho J, Linder S, et al. Selective targeting of TBXT with DARPins identifies regulatory networks and therapeutic vulnerabilities in chordoma. Sci Adv. 2025;11(36):eadu2796.

24. Palena C, Polev DE, Tsang KY, Fernando RI, Litzinger M, Krukovskaya LL, et al. The human T-box mesodermal transcription factor Brachyury is a candidate target for T-cell-mediated cancer immunotherapy. Clin Cancer Res. 2007;13(8):2471-8.

25. Tucker JA, Jochems C, Boyerinas B, Fallon J, Greiner JW, Palena C, et al. Identification and characterization of a cytotoxic T-lymphocyte agonist epitope of brachyury, a transcription factor involved in epithelial to mesenchymal transition and metastasis. Cancer Immunol Immunother. 2014;63(12):1307-17.

26. DeMaria PJ, Lee-Wisdom K, Donahue RN, Madan RA, Karzai F, Schwab A, et al. Phase 1 open-label trial of intravenous administration of MVA-BN-brachyury-TRICOM vaccine in patients with advanced cancer. J Immunother Cancer. 2021;9(9).

27. DeMaria PJ, Bilusic M, Park DM, Heery CR, Donahue RN, Madan RA, et al. Randomized, Double-Blind, Placebo-Controlled Phase II Study of Yeast-Brachyury Vaccine (GI-6301) in Combination with Standard-of-Care Radiotherapy in Locally Advanced, Unresectable Chordoma. Oncologist. 2021;26(5):e847-e58.

28. Bano I, Horky P, Abbas SQ, Majid M, Bilal AHM, Ali F, et al. Ferroptosis: A New Road towards Cancer Management. Molecules. 2022;27(7).

29. Glorieux C, Liu S, Trachootham D, Huang P. Targeting ROS in cancer: rationale and strategies. Nat Rev Drug Discov. 2024;23(8):583-606.

30. Zois CE, Harris AL. Glycogen metabolism has a key role in the cancer microenvironment and provides new targets for cancer therapy. J Mol Med (Berl). 2016;94(2):137-54.

31. Hirosawa RM, Santos AB, Franca MM, Fabris VE, Castro AV, Zanini MA, et al. Intrasellar chondroid chordoma: a case report. ISRN Endocrinol. 2011;2011:259392.

32. Kolb-Lenz D, Fuchs R, Lohberger B, Heitzer E, Meditz K, Pernitsch D, et al. Characterization of the endolysosomal system in human chordoma cell lines: is there a role of lysosomes in chemoresistance of this rare bone tumor? Histochem Cell Biol. 2018;150(1):83-92.

33. Crombe A, Bertolo F, Vanhersecke L, Guegan JP, Bessede A, Perret R, et al. Deciphering the correlation between metabolic activity through 18F-FDG-PET/CT and immune landscape in soft-tissue sarcomas: an insight from the NEOSARCOMICS study. Biomark Res. 2024;12(1):3.

34. Arrieta VA, Benotmane JK, Du R, Habashy KJ, Zhao J, Najem H, et al. Integrated Immune Profiling of Chordomas Reveals Spatially Organized Niches and Functional Heterogeneity. Neuro-Oncology. 2025.

35. Ma J, Chen W, Wang K, Tian K, Li Q, Zhao T, et al. Identification of the Different Roles and Potential Mechanisms of T Isoforms in the Tumor Recurrence and Cell Cycle of Chordomas. Onco Targets Ther. 2019;12:11777-91.

SUPPLEMENTARY FIGURES

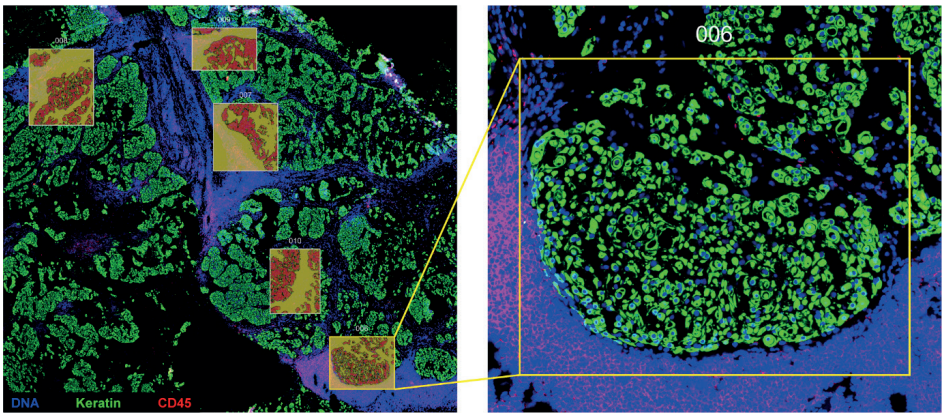
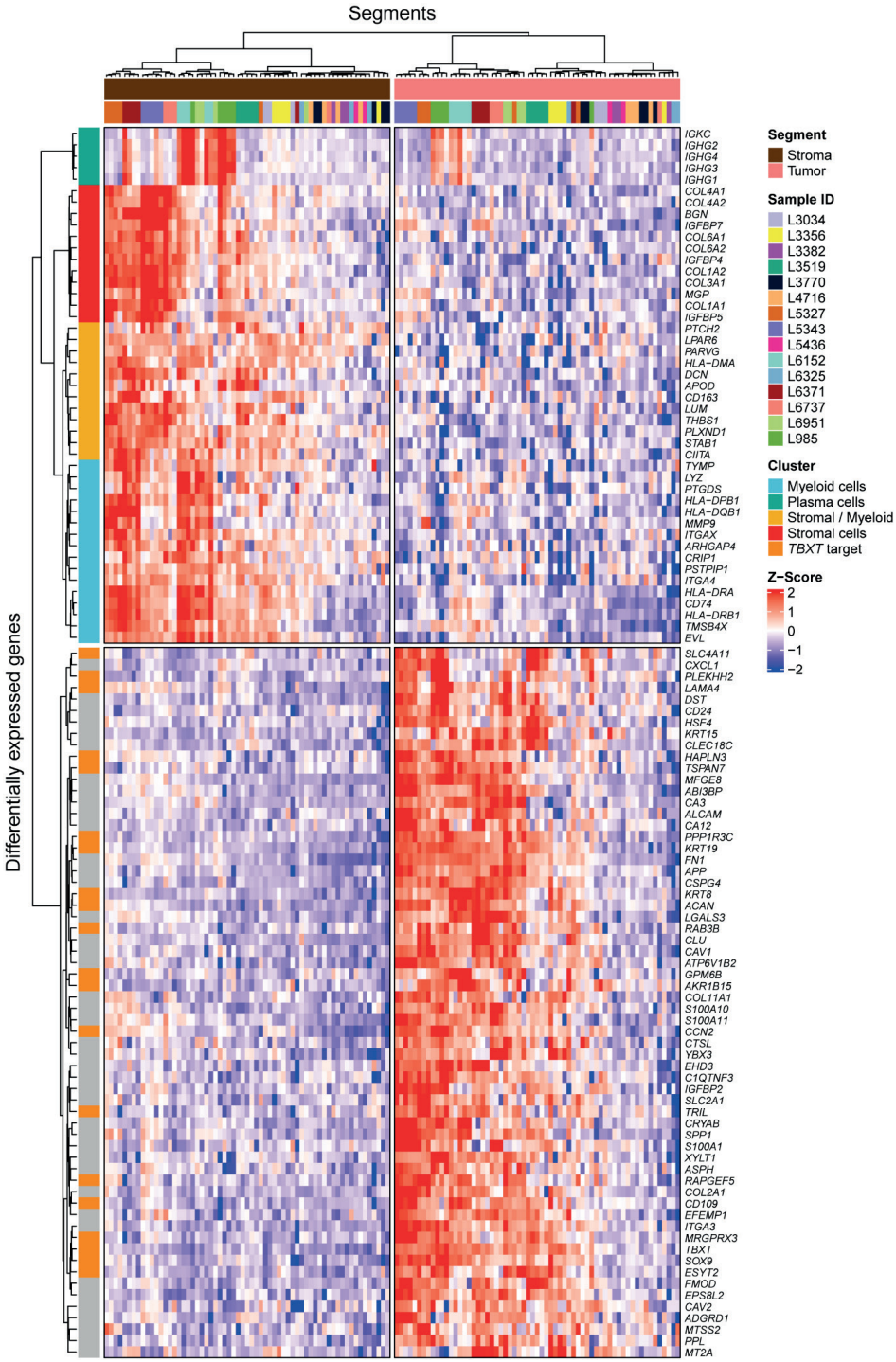


Figure S1. GeoMx digital spatial profiling ROI selection. Representative immunofluorescence image of a chordoma, annotated with the selected ROIs for the GeoMx experiment. The ROIs were segmented based on keratin (green), thereby generating tumor and stroma segments. Stroma segments contained all other captured cells (DNA in blue), including immune cells (CD45 in red).

Figure S2. Differentially expressed genes in tumor and stroma segments, related to Figure 1A. Heatmap displaying the differentially expressed genes (DEGs) comparing tumor with stroma segments. Segments are annotated for their tissue compartment and sample ID. Genes are separated by their enriched compartment. In addition, stroma DEGs are annotated for cell type clusters and tumor DEGs are annotated if they are a target of *TBXT* [S1]. Differential gene expression analysis was performed as described in the **Figure 1** legend.

▶


Segments
Differentially expressed genes
IGKC
IGHG2
IGHG4
IGHG3
IGHG1
COL4A1
COL4A2
BGN
IGFBP7
COL6A1
COL6A2
IGFBP4
COL1A2
COL3A1
MGP
COL1A1
IGFBP5
PTCH2
LPAR6
PARVG
HLA−DMA
DCN
APOD
CD163
LUM
THBS1
PLXND1
STAB1
CIITA
TYMP
LYZ
PTGDS
HLA−DPB1
HLA−DQB1
MMP9
ITGAX
ARHGAP4
CRIP1
PSTPIP1
ITGA4
HLA−DRA
CD74
HLA−DRB1
TMSB4X
EVL
SLC4A11
CXCL1
PLEKHH2
LAMA4
DST
CD24
HSF4
KRT15
CLEC18C
HAPLN3
TSPAN7
MFGE8
ABI3BP
CA3
ALCAM
CA12
PPP1R3C
KRT19
FN1
APP
CSPG4
KRT8
ACAN
LGALS3
RAB3B
CLU
CAV1
ATP6V1B2
GPM6B
AKR1B15
COL11A1
S100A10
S100A11
CCN2
CTSL
YBX3
EHD3
C1QTNF3
IGFBP2
SLC2A1
TRIL
CRYAB
SPP1
S100A1
XYLT1
ASPH
RAPGEF5
COL2A1
CD109
EFEMP1
ITGA3
MRGPRX3
TBXT
SOX9
ESYT2
FMOD
EPS8L2
CAV2
ADGRD1
MTSS2
PPL
MT2A
Segment
Stroma
Tumor
Sample ID
L3034
L3356
L3382
L3519
L3770
L4716
L5327
L5343
L5436
L6152
L6325
L6371
L6737
L6951
L985
Cluster
Myeloid cells
Plasma cells
Stromal / Myeloid
Stromal cells
TBXT target
Z−Score
2
1
0
−1
−2

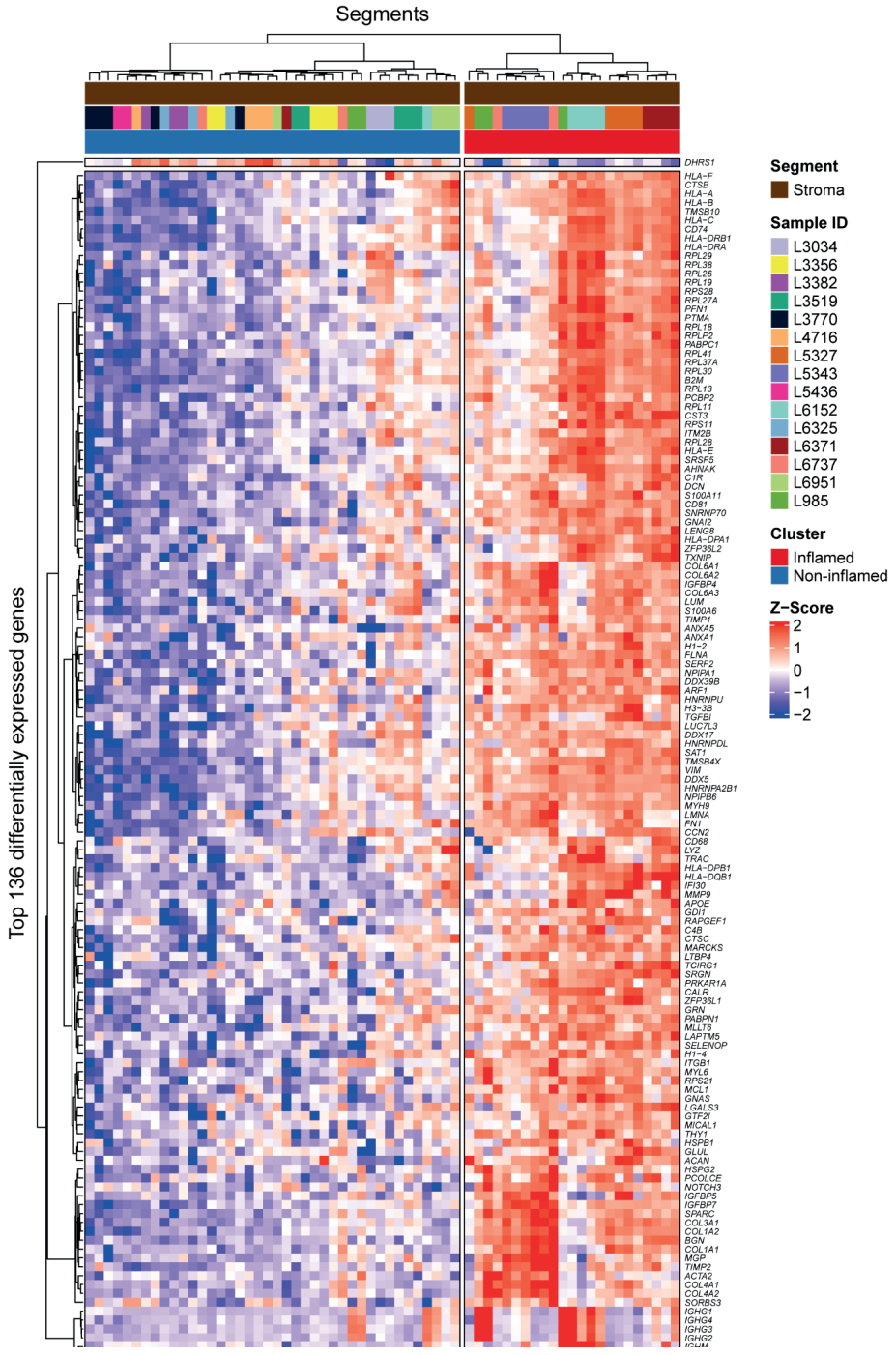


Figure S3. Differentially expressed genes in inflamed and non-inflamed stroma segments, related to Figure 1D.

Figure S3. Differentially expressed genes in inflamed and non-inflamed stroma segments, related to Figure 1D. Heatmap displaying the DEGs comparing inflamed with non-inflamed stroma segments. Segments are annotated for their tissue compartment, sample ID and cluster. Genes are separated by their enriched cluster. Differential gene expression analysis was performed as described in the **Figure 1** legend.

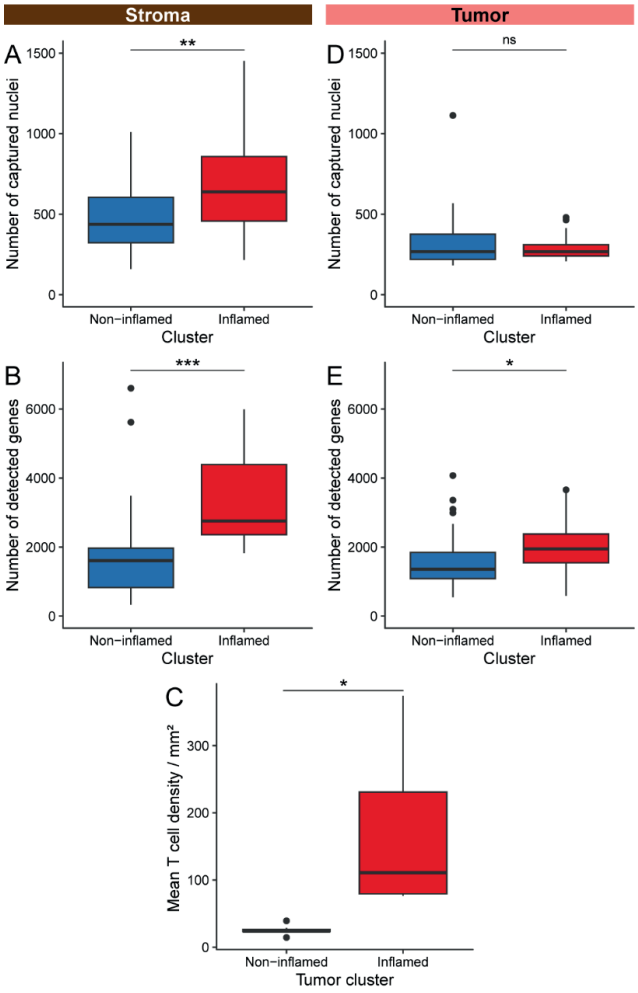


Figure S4. Feature comparisons between inflamed and non-inflamed segments, related to Figures 1C-1F. (A and B) Boxplots presenting the number of captured nuclei (A) and the number of detected genes (B) per stroma segment, separated by the assigned clusters. Statistical significance was assessed by unpaired Student's t-tests. *$p < 0.05$; **$p < 0.01$; ***$p < 0.001$; ns = not significant. (C) Boxplots presenting the mean T cell density / mm^2, as previously determined by imaging mass cytometry [S2], for the assigned tumor clusters. Statistical significance was assessed by performing an unpaired Student's t-test. (D and E) Boxplots presenting the number of captured nuclei (D) and the number of detected genes (E) per tumor segment, separated by the assigned clusters. Statistical significance was determined by unpaired Student's t-tests.

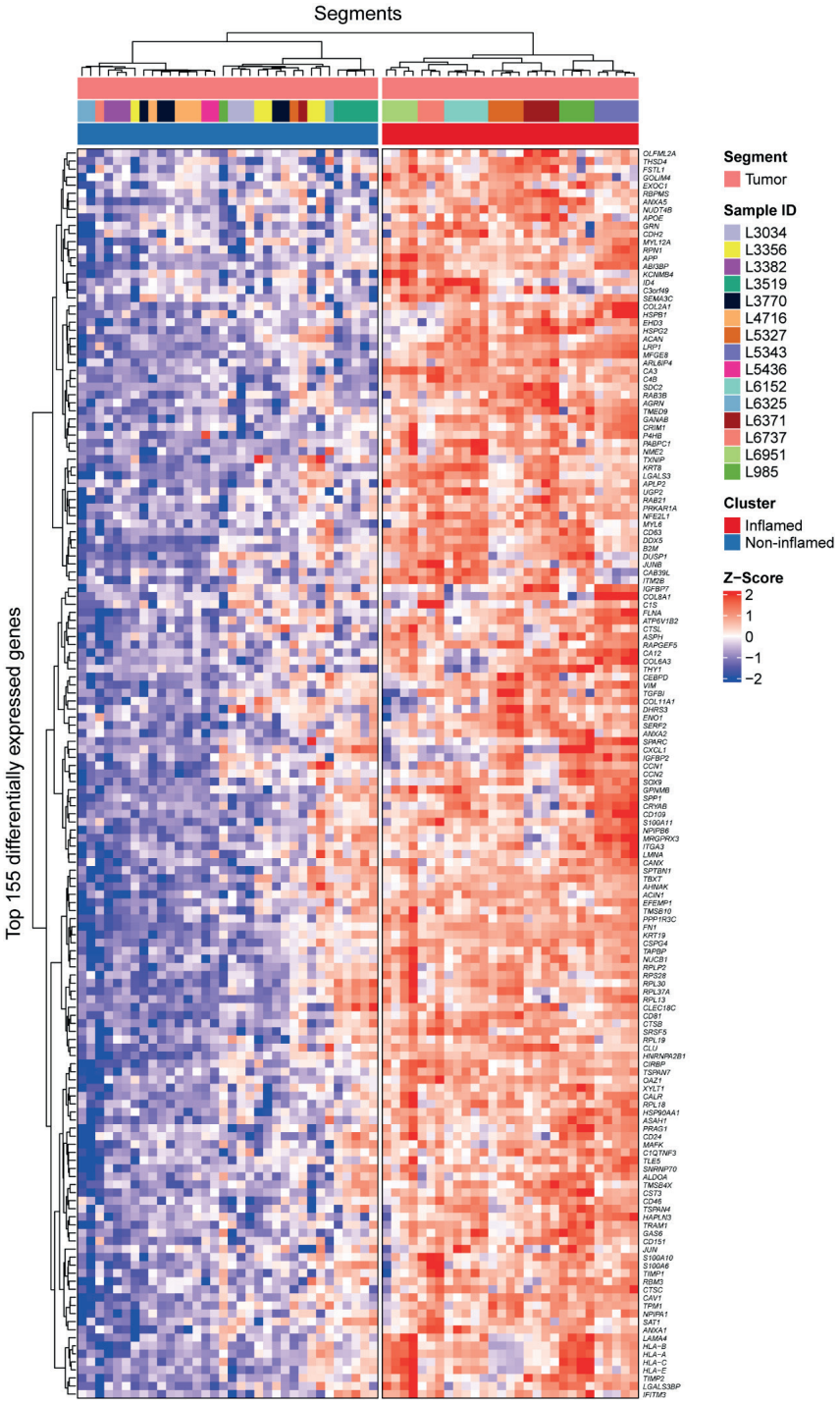

Segments
Top 155 differentially expressed genes
Segment
Tumor
Sample ID
L3034
L3356
L3382
L3519
L3770
L4716
L5327
L5343
L5436
L6152
L6325
L6371
L6737
L6951
L985
Cluster
Inflamed
Non-inflamed
Z−Score
2
1
0
−1
−2

Figure S5. Differentially expressed genes in inflamed and non-inflamed tumor segments, related to Figure 1F. Heatmap displaying the DEGs comparing inflamed with non-inflamed tumor segments. Segments are annotated for their tissue compartment, sample ID and cluster. Differential gene expression analysis was performed as described in the **Figure 1** legend.

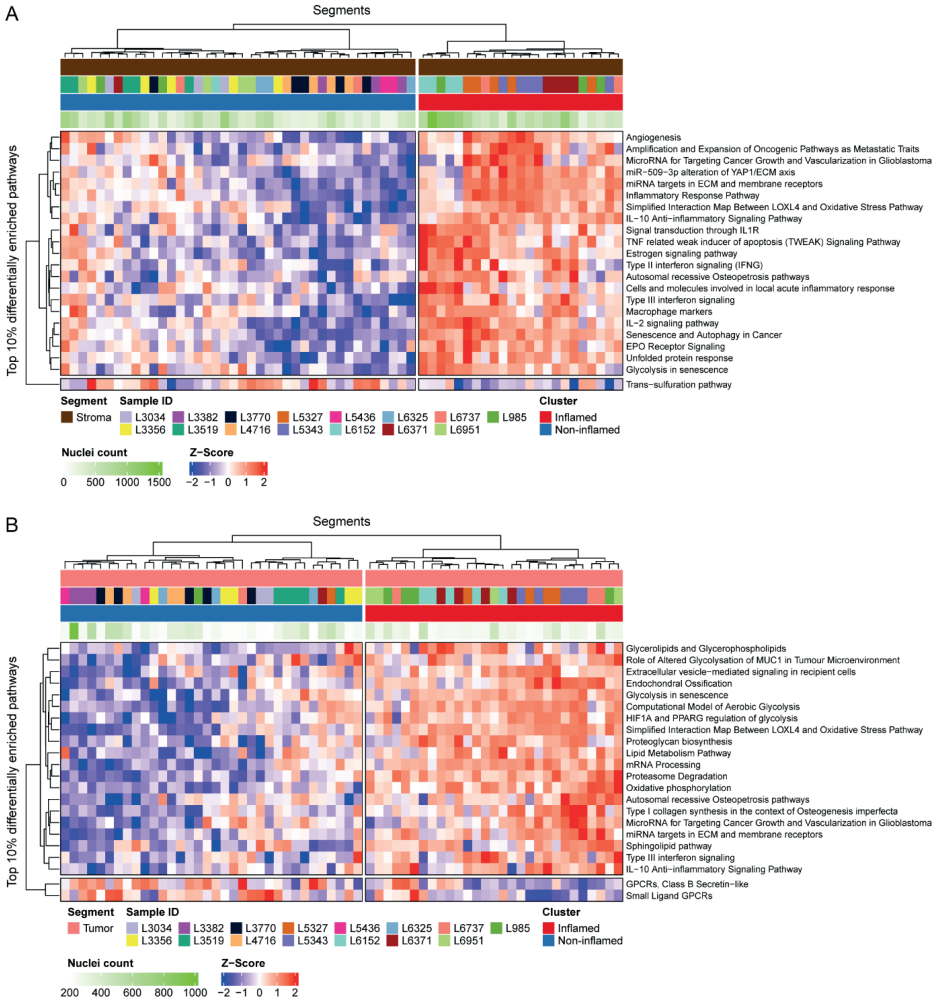


Figure S6. Differentially enriched pathways in inflamed and non-inflamed segments, related to Figures 1C-1F. (A and B) Heatmaps displaying the top differentially enriched pathways in stroma (A) and tumor (B) segments. Pathways are separated by their enriched cluster. In addition, segments are annotated for their tissue compartment, sample ID, cluster, and nuclei count. Statistical significance was determined using a linear mixed model correcting for sample ID and the top 10% of pathways ranked by normalized enrichment score were selected for visualization.

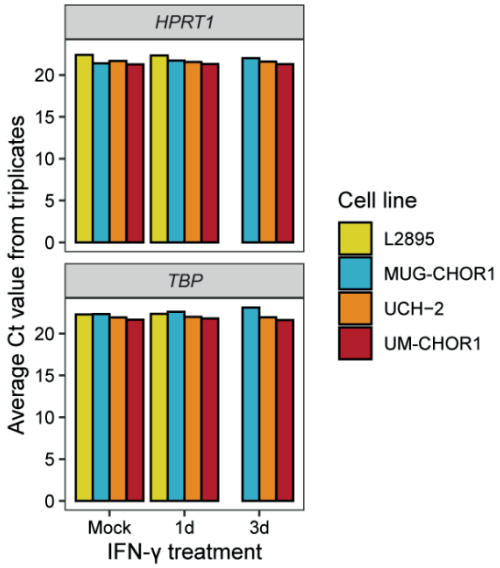


Figure S7. Housekeeping genes remain stable after IFN-γ treatment, related to Figure 4. Average Ct values for *HPRT1* and *TBP* from technical triplicates for each chordoma cell line and treatment condition.

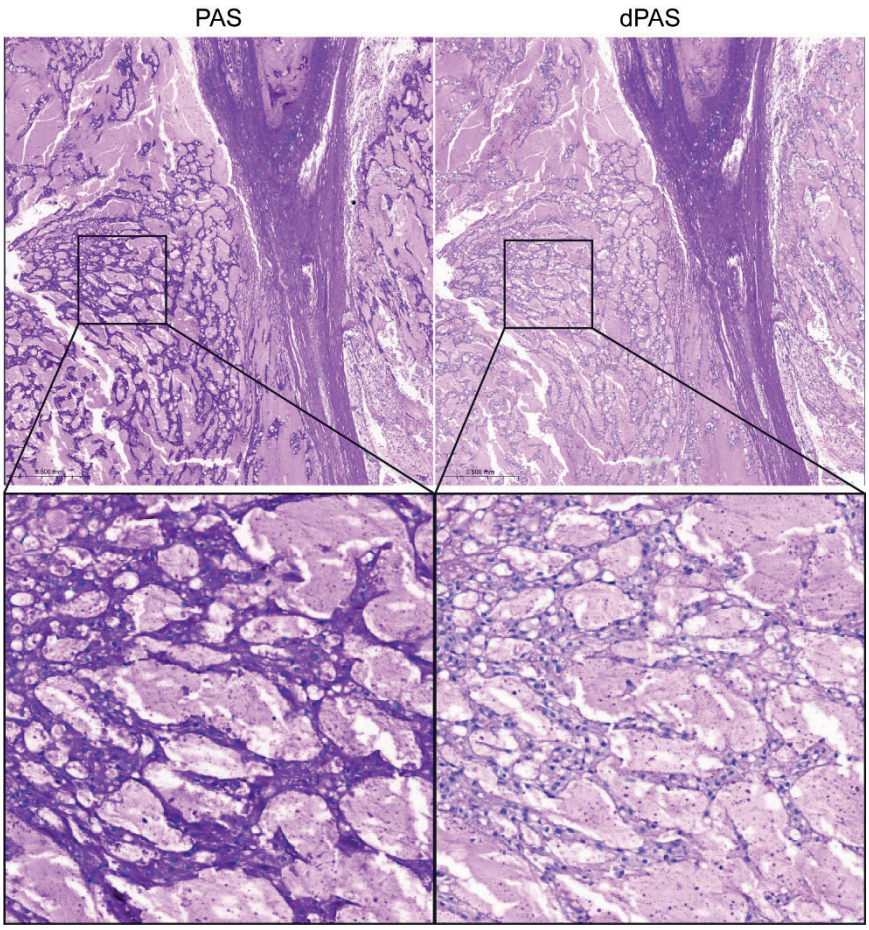


Figure S8. PAS/dPAS staining shows cytoplasmic glycogen, related to STAR Methods. PAS and dPAS staining from corresponding areas in the same sample on consecutive FFPE slides, showing the loss of glycogen after digestion with diastase.

Table S1. Overview of the studied samples. RT = radiotherapy, ST = soft tissue.

Sample ID	Patient ID	Anatomical location	Sample type	Neoadjuvant RT	GeoMx	MALDI
L985	P1	Sacrum	Recurrence		Yes	Yes
L2038	P1		Recurrence			Yes
L4336	P1		Recurrence			Yes
L3034		Sacrum	Primary		Yes	Yes
L3356		Sacrum	Primary		Yes	
L3382		Clivus	Primary		Yes	Yes
L3519		Sacrum	Primary		Yes	Yes
L3770		Sacrum	Primary		Yes	Yes
L4716		Sacrum	Primary		Yes	Yes
L5327		Sacrum	Primary	Yes	Yes	Yes
L5343	P2	Sacrum	Primary		Yes	Yes
L6448	P2		Recurrence			Yes
L5436		Mobile Spine (Lumbar)	Primary		Yes	Yes
L6152		Mobile Spine (Left Flank ST)	Recurrence		Yes	Yes
L6325		Sacrum	Primary	Yes	Yes	Yes
L6371		Sacrum	Primary		Yes	Yes
L6737		Clivus	Primary		Yes	Yes
L6951		Sacrum (Coccyx)	Primary	Yes	Yes	

Table S2. Matrix deposition details.

Parameter	Setting
Nozzle temperature (C)	60
Passes	20
Flowrate (µL / min)	80
Velocity (mm / min)	2000
Track spacing (mm)	3
Pattern	CC
Nitrogen pressure (psi)	10
Drying time between passes (s)	30

Table S3. Molecular ions detected by FTICR used for calibration of the HRAM profiling data.

Compound	Accurate mass
LPE(18:1)	478.2939
LPE(22:6)	524.2783
GSSG	611.1452
Heme	615.1700
PE(36:2)	742.5392
PE(38:4)	766.5392
PS(38:4)	810.5290
PI(38:4)	885.5498

Table S4. Molecular ions commonly detected by MALDI-MSI when using NEDC as matrix, used here for internal mass calibration.

Compound	Accurate mass
Taurine	124.006841
Phosphoethanolamine	140.01187
L-Glutamic acid	146.045334
F6P	259.022446
Inosine	267.073494
Linoleic acid	279.232953
Oleic acid	281.248603
Stearic acid	283.264253
Arachidonic acid	303.232953
Glutathione	306.076532
AMP	346.055811
ADP	426.022144
LPE(18:1)	478.293915
LPE(22:6)	524.2783
GSSG	611.145272
Heme	615.170018
PE(36:2)	742.53923
PE(38:4)	766.53923
PS(38:4)	810.52906
PI(38:4)	885.549856

SUPPLEMENTAL REFERENCE LIST

S1. Nelson, A.C., et al., *An integrated functional genomics approach identifies the regulatory network directed by brachyury (T) in chordoma.* J Pathol, 2012. **228**(3): p. 274-85.

S2. van Oost, S., et al., *Multimodal profiling of chordoma immunity reveals distinct immune contextures.* J Immunother Cancer, 2024. **12**(1).



6

General discussion & future perspectives

GENERAL DISCUSSION

Sarcomas comprise a diverse group of mesenchymal malignancies in which genomic complexity, immune contexture, and therapeutic responsiveness vary substantially across subtypes. The aim of this thesis was to gain insight into the sarcoma immune landscape to help guide patient stratification for immunotherapeutic or combination treatment strategies. A central observation emerging from this thesis is that the clinical relevance of immune infiltration differs markedly between sarcoma histologies. Across sarcoma subtypes with reported but heterogeneous sensitivity to checkpoint blockade — undifferentiated pleomorphic sarcoma (UPS), myxofibrosarcoma (MFS), and chordoma — this thesis demonstrates that similar degrees of immune infiltration can have divergent implications for prognosis and treatment responsiveness. These findings point to the need for subtype-specific and context-dependent frameworks that integrate immune features with genomic complexity, microenvironmental organization, and treatment-induced remodeling. **Chapter 2** establishes this foundation by linking patterns of immune infiltration to genomic complexity across sarcomas, providing the rationale for the subsequent subtype-specific and translational discussions.

Undifferentiated pleomorphic sarcoma and myxofibrosarcoma

A 2017 study from The Cancer Genome Atlas (TCGA) proposed that UPS and MFS may represent a biological continuum rather than distinct entities (1). In that analysis, no consistent subtype-specific differences were identified at the genomic, epigenetic, or transcriptional level, apart from the expression of myxoid matrix–associated genes in MFS with a more pronounced myxoid component. This molecular overlap, together with their shared historical classification under malignant fibrous histiocytoma (MFH), has led UPS and MFS to be frequently studied together. However, accumulating evidence indicates that they are biologically and clinically distinct (2-4), differing in histology, clinical presentation, recurrence patterns, and response to radiotherapy. **Chapter 3** adds to this evidence by demonstrating divergent associations between immune infiltration and clinical outcome, as well as subtype-specific microenvironmental responses to radiotherapy.

One key finding in Chapter 3 is that a pre-existing immune response in UPS, characterized by T cells and macrophages, is associated with improved metastasis-free survival. In contrast, despite a comparable degree of immune infiltration in MFS, this beneficial association is absent. This discrepancy suggests differences in immune infiltrate functionality (4), tumor specificity,

or spatial organization. Alternatively, the biology driving tumor aggressiveness in MFS may dominate metastatic progression, thereby offsetting any protective effect of the immune system. Consistent with this, the MFS microenvironment appears less responsive to radiotherapy than that of UPS, both histologically and immunologically. Following radiotherapy, UPS specimens exhibited extensive fibrosis/hyalinization, with clear reductions in myeloid cells, tumor and stromal cells, and vascular structures; these changes were accompanied by an increase in cytotoxic T cells, collectively indicating a coordinated, tissue-wide response. By comparison, MFS specimens post-radiotherapy remained largely viable with no significant changes in cellular composition, irrespective of tumor depth. These observations underscore differences in their immunobiology and radiotherapy response, likely reflecting distinct tumor-stroma-immune interactions.

Resistance to radiotherapy in MFS: beyond the myxoid extracellular matrix

The limited radiotherapy response of MFS raises questions about underlying microenvironmental features. One defining histological feature of MFS is its myxoid extracellular matrix — a structural component that differs substantially from UPS and may influence microenvironmental organization. TCGA analyses indicate that myxoid matrix–related gene signatures are enriched mainly in tumors with extensive myxoid areas (1). However, high-grade MFS typically displays a heterogeneous architecture, with intermixed myxoid and more cellular regions, such that matrix-rich areas do not dominate the tumor as a whole. For comparison, myxoid liposarcoma — another sarcoma subtype characterized by a prominent myxoid matrix — exhibits a strikingly different radiotherapy response (5): it is highly radiosensitive and typically demonstrates pronounced post-radiation changes, including hyalinization and, to a lesser extent, adipocytic maturation (6). Unlike the curvilinear and irregular vascular pattern characteristic of MFS, myxoid liposarcoma also features a distinctive branching capillary network. Together, these observations underscore that the presence of a myxoid matrix alone is insufficient to explain radioresistance and that vascular architecture and tumor-stroma interactions likely play an important role. Further work is needed to examine how stromal composition, vascular organization, and immune cell distribution together shape these distinct radiobiological behaviors. Recent efforts to map extracellular matrix signatures across soft tissue sarcoma (STS) subtypes provide a useful starting point for such analyses (7, 8).

Reconsidering treatment response assessment in the context of immunotherapy

As discussed previously, the clinical efficacy of immunotherapy in MFS remains less well defined, largely because most clinical trials to date have included fewer than five MFS patients. Encouragingly, several ongoing trials now include larger cohorts of both MFS and UPS, which will help clarify subtype-specific responses to checkpoint blockade (NCT04332874; NCT04480502; NCT06128863). The findings presented in Chapter 3 may therefore inform translational analyses within such studies, particularly those seeking to link immune features with treatment response. In this context, the concept of treatment responsiveness in STS warrants careful reconsideration. Tissue responses to therapy vary substantially between subtypes and treatment modalities (9, 10), and the histopathological criteria used to define response can strongly influence prognostic interpretation. For instance, in both UPS and MFS treated with neoadjuvant radiotherapy or combined regimens, response assessment based on viable tumor percentage has shown limited prognostic value (11)**.** In contrast, hyalinization has emerged as a more informative marker of treatment effect (12, 13)**.** More recently, a hyalinization-based threshold of 30% has been proposed as a potential marker of response in trials combining radiotherapy with checkpoint blockade (14, 15), although this approach remains preliminary and requires validation in independent cohorts.

The need for biomarkers of immunotherapy response

A natural follow-up question concerns which immune features are relevant for response to immune checkpoint blockade. Accordingly, increasing attention has focused on tertiary lymphoid structures (TLS) as a potential biomarker of response. Accumulating evidence indicates that TLS represent a context-dependent manifestation of anti-tumor immunity rather than a standalone predictive marker for checkpoint blockade (16, 17). Consistent with this view, TLS are generally associated with a favorable prognosis across STS (14, 18-20), reflecting coordinated and chronic immune activation; however, they frequently coexist with other immune features. Notably, intratumoral $CD8^+$ T cell infiltration often accompanies TLS in immunologically active subtypes such as UPS and dedifferentiated liposarcoma (DDLPS), whereas other subtypes like rhabdomyosarcoma may lack broader immune activation despite the occasional presence of TLS (21). Consequently, the predictive value of TLS varies according to histology, immune composition, and treatment context.

Importantly, TLS are dynamic structures whose presence and functionality can be altered by therapy. For example, recent data show that DDLPS may develop TLS during checkpoint blockade, whereas UPS tends to lose them over the

course of treatment (14) — likely reflecting tissue remodeling in responding tumors, as also observed in Chapter 3. These findings highlight that TLS scoring is not static and may be influenced by therapy-induced changes in the tumor microenvironment. Moreover, the relationship between anti-tumor immunity and therapeutic outcomes extends beyond TLS alone: patterns of intratumoral T cell infiltration correlate with prognosis in both UPS and DDLPS treated with checkpoint blockade, even in the absence of well-defined TLS.

Frameworks that integrate immune organization with underlying tumor biology help reconcile these observations (17). In UPS, for instance, immune infiltration inversely correlates with genomic complexity, as tumors with a higher burden of copy-number alterations exhibit reduced immune infiltration (22). Sarcoma ecotypes further contextualize this relationship by distinguishing an inflamed ecotype with fewer genomic alterations from an intermediate-inflamed ecotype with greater genomic instability. Notably, tumors in the latter ecotype show a distinct association with response to checkpoint blockade despite comparable TLS prevalence to inflamed ecotype tumors. Collectively, these insights demonstrate that ecotypes capture functionally relevant immune states not fully reflected by TLS presence alone, offering a more nuanced framework for predicting immunotherapy response in STS.

From a translational perspective, digital pathology applied to H&E-stained resections enables scalable TLS detection and phenotypic characterization (23, 24), contributing to a refined understanding of TLS biology. However, since TLS are frequently underdetected in biopsies and may be modulated by treatment, surrogate markers of functional TLS and local immune activation are needed — particularly those assessable in pre-treatment biopsies or via non-invasive approaches. For instance, intratumoral plasma cells may serve as a proxy for active TLS (16, 20), while MRI-based radiomic signatures offer a promising non-invasive method to infer TLS presence (25). Together, these strategies support integrated biomarker frameworks in which TLS are interpreted alongside histology, immune organization, and genomic context to guide patient stratification and therapeutic decision-making in STS.

Chordoma

Since it has become apparent that chordomas can respond to checkpoint blockade, interest in the immunogenomic characterization of this ultra-rare bone sarcoma has surged. Unlike genomically complex STS such as UPS and MFS, chordomas exhibit relative genomic stability, despite occasional chromosomal alterations. This genomic profile raises an intriguing question:

why do approximately 16% of chordomas respond to checkpoint blockade (26, 27)? **Chapter 4** addressed this by providing the first large-scale characterization of the chordoma immune microenvironment. This analysis revealed that, compared to other sarcomas, chordomas proved relatively immunologically active, with a subset displaying coordinated immune responses — marked by T cells co-localizing with antigen-presenting cells in the stromal compartment. These inflamed tumors also showed T cell receptor (TCR) clonal enrichment; however, levels indicative of antigen-driven responses were uncommon. This aligns with chordomas' low mutational burden and consequent scarcity of T cell-recognizable neoantigens, which may explain why most tumors retain intact antigen-presentation machinery, reflecting limited selective pressure from cytotoxic T cells. Collectively, these findings reveal a paradox: low genomic complexity alongside discernible immune responses, highlighting the need to uncover mechanisms driving chordoma immunogenicity.

Building on these insights, **Chapter 5** applied integrated spatial transcriptomic and metabolomic profiling to a subset of chordomas from Chapter 4, reinforcing the inflamed/non-inflamed dichotomy. As anticipated, inflamed tumors had higher densities of immune and stromal cells, with comparable tumor cell densities across groups. Notably, tumor cells in inflamed cases showed broader transcriptional repertoires — including higher expression of chordoma-associated and immune-related genes — alongside increased glycogen accumulation. These tumors also exhibited distinct metabolic and lipid adaptations consistent with oxidative stress, suggesting transcriptional and metabolic remodeling as hallmarks of chordoma immunogenicity. This prompts the question: do such adaptations reflect intrinsic tumor cell properties, microenvironmental induction, or reciprocal tumor-immune feedback? To probe this, we investigated whether interferon-γ (IFN-γ) — a key immunomodulatory cytokine — could be a driver of this transcriptional state in inflamed tumors. However, IFN-γ did not regulate *TBXT* (brachyury) expression, implicating alternative mechanisms like other cytokine signals, genomic alterations, or epigenetic regulation in the upregulation of *TBXT* and its transcriptional programs.

TBXT as a determinant of immunogenicity

In light of the association between immune responses and *TBXT*-associated transcriptional programs observed in Chapter 5, the potential contribution of *TBXT* to tumor immunogenicity warrants closer investigation. Two key questions arise: first, whether *TBXT* itself functions as an antigenic target; and second, whether its transcriptional programs actively shape the broader immune

landscape of chordomas. Addressing the first, a recent immunopeptidomic study demonstrated that *TBXT*-derived peptides are naturally presented on HLA class I molecules in most chordoma patients (28), rendering *TBXT* accessible to immune recognition. However, functional reactivity assays would be needed to confirm whether these peptides elicit robust, patient-specific T cell responses; such assays could employ *TBXT* peptides presented by autologous antigen-presenting cells to stimulate tumor-infiltrating lymphocytes.

Turning to the second question, prior work has shown that *TBXT* regulates interferon-α response networks in chordoma cells (29). Given that interferon signaling modulates antigen presentation and cytokine production, these *TBXT*-associated programs may actively shape the tumor-immune interface. Whether *TBXT* further influences immunogenicity through mechanisms such as chemokine secretion or cellular stress responses remains unclear. Elucidating these pathways will be essential to defining *TBXT*'s precise role in chordoma immunogenicity.

Associations between immunity and clinical outcome

The clinical significance of the immune microenvironment in chordoma remains unresolved. In the extended cohort analyzed in Chapter 4, T cell infiltration showed no association with disease-specific survival or recurrence-free survival. This finding aligns with other published studies (30, 31), which similarly reported no prognostic effect of immune infiltration. Interestingly, both studies observed that chromosomal instability or a higher burden of copy-number alterations correlated with worse prognosis and lower immune infiltration. These patterns suggest an indirect relationship whereby genomic complexity — rather than immune infiltration itself — may drive adverse outcomes. A potential mechanistic explanation emerged from a recent proteogenomic study (31), which showed that loss of 9p and 10q may reduce immune infiltration by decreasing expression of immune-related genes encoded on these chromosomal arms. Specifically, 9p loss was associated with reduced IL-6/JAK/STAT signaling, whereas 10q loss was linked to decreased NF-κB signaling and diminished interferon-α responses.

However, other reports have described negative associations between immune activity and clinical outcome (32-34), highlighting substantial heterogeneity across studies and underscoring the complexity of interpreting the prognostic relevance of immunity in chordoma. This heterogeneity may stem from differences in immunobiology, the extent and nature of genomic instability, clinical management, or a combination of these factors. Anatomical location

represents another potential source of variability, as cohorts are often restricted to chordomas from a single anatomical site. Yet, results from Chapter 4 — together with a recent multimodal study that included chordomas from multiple anatomical locations (35) — suggest that anatomical site alone is unlikely to explain the inconsistent prognostic effects.

In this context, the complexity and heterogeneity of chordoma treatment, together with patient comorbidities and anatomical constraints that complicate surgery and radiotherapy, may obscure any contribution of natural anti-tumor immunity. Moreover, immune responses in chordoma may lack the robustness needed for effective tumor control, owing to limited antigenicity, immunosuppressive mechanisms within the tumor microenvironment, restricted intratumoral infiltration, or infiltration that reflects local inflammation rather than coordinated anti-tumor activity. Despite these challenges, the identification of shared and expanded TCR clonotypes between tumor tissue and peripheral blood supports systemic, antigen-driven T cell responses in a subset of patients (35), indicating that clinically meaningful immunity may occur even without broad prognostic value. Overall, the limited prognostic value of immune infiltration in chordoma likely reflects biologically modest immune responses combined with clinical factors that mask their effects, rather than a true absence of immunogenic potential.

Several strategies could help disentangle these clinical and biological factors. For instance, analyzing pre-treatment biopsies from patients receiving exclusively proton beam radiotherapy — an increasingly common definitive treatment for clival chordomas and a standard local-control option for sacrococcygeal tumors in older patients (36-38) — would minimize treatment-related confounders and enable a cleaner assessment of baseline immunity and its association with clinical outcome. Pairing such analyses with prospective FDG-PET imaging could further clarify whether metabolic features correlate with immune activity, building on the metabolic adaptations observed in Chapter 5.

FUTURE PERSPECTIVES

Building on the findings presented in this thesis, future research in sarcoma immunobiology should focus on identifying immune features that are functionally relevant and therapeutically actionable. In particular, the divergent prognostic implications of immune infiltration across UPS, MFS, and

chordoma underscore the need to define how immune functionality and spatial organization interact with genomic complexity to influence clinical relevance.

Over the past decade, bulk, single-cell, and spatial profiling have mapped the immunogenomic landscape of sarcomas with increasing resolution. These efforts have defined baseline immune features and identified immunologically active subgroups. However, without well-annotated treatment cohorts, clinical validation of these immune states remains limited. Integrative analyses of samples from patients in immunotherapy trials — directly linking immune features to treatment response and clinical outcomes — will therefore be crucial. Embedding high-resolution multi-omic profiling into ongoing and future clinical studies will help determine which immune features or integrative frameworks, such as Sarcoma Immune Classes (18), TLS, intratumoral $CD8^+$ T cell infiltration, the Immunologic Constant of Rejection signature (39), and sarcoma ecotypes (17), can serve as robust, clinically actionable biomarkers for patient stratification across sarcoma subtypes.

A related opportunity involves characterizing antigenicity in both genomically simple and complex sarcomas. Although recurrent, mutation-driven neoantigens are rare, alternative sources — including fusion-derived peptides (40) and aberrant RNA processing (41) — may drive immune recognition. Combining immunopeptidomics with emerging technologies like long-read sequencing and single-cell genomics will define sarcoma antigen landscapes and reveal how T cells recognize noncanonical tumor-associated antigens. These methods will also deepen insights into innate immune recognition, which may be particularly relevant in sarcomas with limited classical antigenicity. NK cells, gd-T cells, and innate lymphoid cells respond to stress signals, cytokines, and nonclassical ligands rather than MHC-restricted peptides (42, 43). Elucidating how genomic instability and stress responses shape these innate pathways could unlock therapies beyond conventional checkpoint blockade.

The development of single-cell spatial profiling enables subtype-specific interrogation of the sarcoma immune landscape. In UPS and MFS, this tool can dissect their divergent immunobiology by resolving differences in tumor-intrinsic programs, stromal organization, immune functionality, and spatial arrangement. In chordoma, where immune infiltration shows limited, context-dependent prognostic associations, this approach may uncover cellular neighborhoods or functional states that better predict immunogenicity, prognosis, or treatment sensitivity than bulk measures. Hypotheses from these descriptive studies can then be tested in selected functional model systems to probe specific tumor–immune interactions under controlled conditions.

Collectively, these approaches provide a framework for connecting tumor biology to immune organization and function across sarcoma subtypes, refining interpretations of patient-derived immune phenotypes.

For chordoma specifically, this thesis highlights key areas for investigation. Although *TBXT* drives chordoma biology, its role in immunogenicity remains unclear. Beyond confirming the consistent presentation and immunogenicity of *TBXT*-derived peptides, studies must explore whether *TBXT*'s transcriptional program influences broader immunogenicity. Clarifying these mechanisms will help inform *TBXT*-targeted therapies, including peptide vaccines, adoptive TCR approaches, and checkpoint blockade combinations.

Taken together, the future of sarcoma immunobiology lies in leveraging high-resolution multi-omic profiling, with particular emphasis on embedding these efforts within translational work in clinical trials, and validating those findings with mechanistic studies. This will elucidate how genomic aberrations generate antigenicity; how tumor, stromal, and immune cells orchestrate anti-tumor responses; and how to refine patient selection and therapeutic strategies. As molecular profiling advances and sarcoma trials expand, these efforts promise to translate immunogenomic insights into meaningful improvements in patient care.

REFERENCES

1. Cancer Genome Atlas Research Network. Comprehensive and Integrated Genomic Characterization of Adult Soft Tissue Sarcomas. Cell. 2017;171(4):950-65 e28.
2. Yoshimoto M, Yamada Y, Ishihara S, Kohashi K, Toda Y, Ito Y, et al. Comparative Study of Myxofibrosarcoma With Undifferentiated Pleomorphic Sarcoma: Histopathologic and Clinicopathologic Review. Am J Surg Pathol. 2020;44(1):87-97.
3. Mitra S, Farswan A, Piccinelli P, Sydow S, Hesla A, Tsagkozis P, et al. Transcriptomic profiles of myxofibrosarcoma and undifferentiated pleomorphic sarcoma correlate with clinical and genomic features. J Pathol. 2024;264(3):293-304.
4. Melake MJ, Smith HG, Mansfield D, Davies E, Dillon MT, Wilkins AC, et al. OX40 and 4-1BB delineate distinct immune profiles in sarcoma. Oncoimmunology. 2022;11(1):2066050.
5. Stergioula A, Kormas T, Kokkali S, Memos N, Pantelis E, Pouloudi D, et al. What Is the Prognostic Value of the Pathologic Response after Neoadjuvant Radiotherapy in Soft Tissue Sarcoma? An Institutional Study Using the EORTC-STBSG Response Score. Cancers (Basel). 2024;16(20).
6. Lam SW, Silva TM, Traast-Kooistra J, Bruijn IB, van den Akker B, Bakker PAC, et al. Histological response to radiotherapy is an early event in myxoid liposarcoma. Virchows Arch. 2023;483(4):487-95.
7. Burns J, Wilding CP, Krasny L, Zhu X, Chadha M, Tam YB, et al. The proteomic landscape of soft tissue sarcomas. Nat Commun. 2023;14(1):3834.
8. Pankova V, Krasny L, Kerrison W, Tam YB, Chadha M, Burns J, et al. Clinical Implications and Molecular Features of Extracellular Matrix Networks in Soft Tissue Sarcomas. Clin Cancer Res. 2024;30(15):3229-42.
9. Callegaro D, Miceli R, Bonvalot S, Ferguson P, Strauss DC, Levy A, et al. Impact of perioperative chemotherapy and radiotherapy in patients with primary extremity soft tissue sarcoma: retrospective analysis across major histological subtypes and major reference centres. Eur J Cancer. 2018;105:19-27.
10. Allignet B, Meurgey A, Bouhamama A, Karanian M, Meeus P, Vaz G, et al. Impact of histological subtype on radiological and pathological response after neoadjuvant radiotherapy in soft tissue sarcoma. Eur J Surg Oncol. 2021;47(12):2995-3003.
11. Danieli M, Barretta F, Radaelli S, Fiore M, Sangalli C, Barisella M, et al. Pathological and radiological response following neoadjuvant treatments in primary localized resectable myxofibrosarcoma and undifferentiated pleomorphic sarcoma of the extremities and trunk wall. Cancer. 2023;129(21):3417-29.
12. Schaefer IM, Hornick JL, Barysauskas CM, Raut CP, Patel SA, Royce TJ, et al. Histologic Appearance After Preoperative Radiation Therapy for Soft Tissue Sarcoma: Assessment of the European Organization for Research and Treatment of Cancer-Soft Tissue and Bone Sarcoma Group Response Score. Int J Radiat Oncol Biol Phys. 2017;98(2):375-83.
13. Boxberg M, Langer R, Woertler K, Knebel C, Rechl H, von Eisenhart-Rothe R, et al. Neoadjuvant Radiation in High-Grade Soft-Tissue Sarcomas: Histopathologic Features and Response Evaluation. Am J Surg Pathol. 2022;46(8):1060-70.

14. Roland CL, Nassif Haddad EF, Keung EZ, Wang WL, Lazar AJ, Lin H, et al. A randomized, non-comparative phase 2 study of neoadjuvant immune-checkpoint blockade in retroperitoneal dedifferentiated liposarcoma and extremity/truncal undifferentiated pleomorphic sarcoma. Nat Cancer. 2024.

15. Traweek RS, Zoghbi M, Lazcano R, Cope BM, Bishop AJ, Farooqi A, et al. Hyalinization-based pathologic response and immune infiltration following neoadjuvant radiotherapy with or without immune-checkpoint blockade in localized undifferentiated pleomorphic sarcoma. ESMO Open. 2025;10(7):105493.

16. Italiano A, Bessede A, Pulido M, Bompas E, Piperno-Neumann S, Chevreau C, et al. Pembrolizumab in soft-tissue sarcomas with tertiary lymphoid structures: a phase 2 PEMBROSARC trial cohort. Nat Med. 2022;28(6):1199-206.

17. Subramanian A, Nemat-Gorgani N, Ellis-Caleo TJ, van IDGP, Sears TJ, Somani A, et al. Sarcoma microenvironment cell states and ecosystems are associated with prognosis and predict response to immunotherapy. Nat Cancer. 2024;5(4):642-58.

18. Petitprez F, de Reynies A, Keung EZ, Chen TW, Sun CM, Calderaro J, et al. B cells are associated with survival and immunotherapy response in sarcoma. Nature. 2020;577(7791):556-60.

19. Kijima T, Takada-Owada A, Kokubun H, Uematsu T, Takei K, Betsunoh H, et al. Tertiary Lymphoid Structures Correlate With Better Prognosis in Patients With Retroperitoneal Sarcoma: A Retrospective Study. Int J Urol. 2025;32(7):859-67.

20. Sonoda H, Iwasaki T, Ishihara S, Mori T, Nakashima Y, Oda Y. Impact of Tertiary Lymphoid Structure on Prognosis and Tumor Microenvironment in Undifferentiated Pleomorphic Sarcoma. Cancer Sci. 2025.

21. Chen L, Oke T, Siegel N, Cojocaru G, Tam AJ, Blosser RL, et al. The Immunosuppressive Niche of Soft-Tissue Sarcomas is Sustained by Tumor-Associated Macrophages and Characterized by Intratumoral Tertiary Lymphoid Structures. Clin Cancer Res. 2020;26(15):4018-30.

22. Toulmonde M, Lucchesi C, Verbeke S, Crombe A, Adam J, Geneste D, et al. High throughput profiling of undifferentiated pleomorphic sarcomas identifies two main subgroups with distinct immune profile, clinical outcome and sensitivity to targeted therapies. EBioMedicine. 2020;62:103131.

23. Vanhersecke L, Bougouin A, Crombe A, Brunet M, Sofeu C, Parrens M, et al. Standardized Pathology Screening of Mature Tertiary Lymphoid Structures in Cancers. Lab Invest. 2023;103(5):100063.

24. Michot A, Le VL, Coindre JM, Velasco V, Soussi M, Mesli N, et al. Prognostic prediction in soft-tissue sarcomas using deep learning and digital pathology of tumor and margin areas. Sci Rep. 2025;15(1):38534.

25. Wang T, Wang L, Zhong H, Zong Y, Hou F, Wang H, et al. MRI-derived radiomics model for predicting intratumoral tertiary lymphoid structures in soft tissue sarcoma. Insights Imaging. 2025;16(1):201.

26. Somaiah N, Conley AP, Parra ER, Lin H, Amini B, Solis Soto L, et al. Durvalumab plus tremelimumab in advanced or metastatic soft tissue and bone sarcomas: a single-centre phase 2 trial. Lancet Oncol. 2022;23(9):1156-66.

27. Blay JY, Chevret S, Le Cesne A, Brahmi M, Penel N, Cousin S, et al. Pembrolizumab in patients with rare and ultra-rare sarcomas (AcSe Pembrolizumab): analysis of a subgroup from a non-randomised, open-label, phase 2, basket trial. Lancet Oncol. 2023.

28. Pan K, Chiu Y, Patel HA, Huang E, MacCoss M, Yee C. 387 Identification of novel T cell receptor (TCR) target to brachyury for the development of T cell-based immunotherapy of chordoma and other solid tumors. Journal for ImmunoTherapy of Cancer. 2024;12(Suppl 2).

29. Umbaugh CS, Groth M, Erkut C, Lee KS, Marinho J, Linder S, et al. Selective targeting of TBXT with DARPins identifies regulatory networks and therapeutic vulnerabilities in chordoma. Sci Adv. 2025;11(36):eadu2796.

30. Baluszek S, Kober P, Rusetska N, Wagrodzki M, Mandat T, Kunicki J, et al. DNA methylation, combined with RNA sequencing, provide novel insight into molecular classification of chordomas and their microenvironment. Acta Neuropathol Commun. 2023;11(1):113.

31. Zhang Q, Xu Z, Han R, Wang Y, Ye Z, Zhu J, et al. Proteogenomic characterization of skull-base chordoma. Nat Commun. 2024;15(1):8338.

32. Zuccato JA, Patil V, Mansouri S, Liu JC, Nassiri F, Mamatjan Y, et al. DNA methylation-based prognostic subtypes of chordoma tumors in tissue and plasma. Neuro Oncol. 2022;24(3):442-54.

33. Huo X, Guo T, Wang K, Yao B, Li D, Li H, et al. Methylation-based reclassification and risk stratification of skull-base chordomas. Front Oncol. 2022;12:960005.

34. Xiong Y, Li M, Niu G, Xu T, Li C, Ma T, et al. Identification of immune subtypes associated with the prognosis in skull base chordoma. Acta Neuropathol Commun. 2025;13(1):130.

35. Arrieta VA, Benotmane JK, Du R, Habashy KJ, Zhao J, Najem H, et al. Integrated Immune Profiling of Chordomas Reveals Spatially Organized Niches and Functional Heterogeneity. Neuro-Oncology. 2025.

36. Pennicooke B, Laufer I, Sahgal A, Varga PP, Gokaslan ZL, Bilsky MH, et al. Safety and Local Control of Radiation Therapy for Chordoma of the Spine and Sacrum: A Systematic Review. Spine (Phila Pa 1976). 2016;41 Suppl 20(Suppl 20):S186-S92.

37. Miladinovic V, Klaver YLB, Krol ADG, Kroesen M, Verbist BM, Habraken SJM, et al. Robust IMPT and follow-up toxicity in skull base chordoma and chondrosarcoma-a single-institution clinical experience. Strahlenther Onkol. 2024;200(12):1066-73.

38. Saito T, Mizumoto M, Oshiro Y, Shimizu S, Li Y, Nakamura M, et al. Systematic Review and Meta-Analysis of Particle Beam Therapy versus Photon Radiotherapy for Skull Base Chordoma: TRP-Chordoma 2024. Cancers (Basel). 2024;16(14).

39. Bertucci F, Niziers V, de Nonneville A, Finetti P, Mescam L, Mir O, et al. Immunologic constant of rejection signature is prognostic in soft-tissue sarcoma and refines the CINSARC signature. J Immunother Cancer. 2022;10(1).

40. Bei Y, Huang Y, Wu N, Li Y, Xu R, Liu B, et al. A therapeutic regimen using neoantigen-specific TCR-T cells for HLA-A*2402-positive solid tumors. EMBO Mol Med. 2025;17(2):365-83.

41. Tretter C, de Andrade Kratzig N, Pecoraro M, Lange S, Seifert P, von Frankenberg C, et al. Proteogenomic analysis reveals RNA as a source for tumor-agnostic neoantigen identification. Nat Commun. 2023;14(1):4632.

42. Chiossone L, Dumas PY, Vienne M, Vivier E. Natural killer cells and other innate lymphoid cells in cancer. Nat Rev Immunol. 2018;18(11):671-88.

43. Silva-Santos B, Mensurado S, Coffelt SB. gammadelta T cells: pleiotropic immune effectors with therapeutic potential in cancer. Nat Rev Cancer. 2019;19(7):392-404.



Appendices

PhD Portfolio

Nederlandse samenvatting

Curriculum Vitae

List of publications

Dankwoord

PHD PORTFOLIO

The PhD trajectory – an overview

I started my PhD in 2020 at the Department of Pathology at Leiden University Medical Center, where I joined a project within the Leiden Center for Computational Oncology under the supervision of Judith Bovée and Noel de Miranda. My research focused on characterizing the immune landscape of bone and soft tissue sarcomas, with the aim of identifying opportunities for immunotherapy in these rare malignancies.

At the beginning of my PhD, I established a strong methodological and computational foundation by completing courses in genomics and transcriptomics, biostatistics, and Linux programming. These courses enabled me to work with high-dimensional datasets and apply bioinformatic approaches in translational oncology. In parallel, I familiarized myself with the broader field by conducting a comprehensive review on immunity and genomics in sarcomas together with Debora Meijer, which resulted in our first peer-reviewed (**Chapter 2**). This work helped define key challenges and opportunities in the field and guided the direction of my subsequent research.

Building on this foundation, I investigated chordoma, a rare bone tumor with limited treatment options. Using multimodal and spatial profiling approaches, I characterized the tumor microenvironment and investigated immune cell interactions within these tumors. These studies required the integration of multiple data types and close collaboration with clinicians, pathologists, cancer biologists, and computational scientists. During the final stages of this first chordoma project, I was co-applicant on a grant awarded by the Cancer Research Institute and the Chordoma Foundation in 2023, which enabled us to further expand this research line. This ultimately resulted in two peer-reviewed publications (**Chapters 4** and **5**) and marked an important step in establishing a dedicated research line on chordoma immunology within our group. Through this work, I also developed close interactions with patient organizations, which strengthened my awareness of the direct clinical relevance of translational research for patients with rare cancers. Alongside this work, I studied the immunogenic features of undifferentiated pleomorphic sarcoma and myxofibrosarcoma using a similar approach to our first chordoma study. This project also resulted in a peer-reviewed publication (**Chapter 3**).

Beyond the projects included in this thesis, I contributed to additional studies on chordoma and other bone tumors, including high-grade osteosarcoma and osteofibrous dysplasia/OFD-like adamantinoma/adamantinoma. In these

projects, I applied similar spatial technologies to further characterize tumor microenvironments, broadening my expertise in sarcoma biology and strengthening my technical and analytical skills.

To support my scientific development, I actively participated in national and international conferences. I presented my work at meetings of CTOS, FORTRESS, CIMT, and specialized chordoma workshops. Over time, my role evolved from attendee to oral presenter and organizer of scientific events, particularly local symposia at Leiden University Medical Center. These experiences strengthened my ability to communicate complex findings to diverse audiences and engage with the international research community.

Collaboration was a central component of my PhD trajectory. My projects involved close interaction between multiple disciplines, including cancer biology, computational biology, pathology, radiotherapy, neurosurgery, and orthopedic surgery. These collaborations were essential for integrating diverse methodologies, collecting patient material and clinical data, and translating molecular findings into clinically meaningful insights.

My work was recognized through several awards and grants. I received the award for most relevant abstract for patients at the Dutch Sarcoma Group PhD Symposium in 2022 and the award for best presentation at the chordoma research symposium organized by the Bone Cancer Research Trust in 2024. In addition, I received a personal Skills Development Grant from the Bone Cancer Research Trust in 2024.

In addition to research, I contributed to education and supervision by mentoring bachelor's and master's students and participating in teaching activities within the Biomedical Sciences curriculum. These experiences further strengthened my ability to mentor junior researchers, communicate scientific concepts effectively, and foster enthusiasm for research.

Overall, my PhD trajectory reflects a progression from building a strong methodological foundation to leading complex, collaborative research projects in translational oncology, with a particular focus on improving our understanding of the immune landscape of rare cancers and identifying potential therapeutic opportunities.

CRediT statement for the Chapters in this thesis

CRediT table for the thesis of Siddh van Oost

Ch.	Type*	Short Title	Conceptualization	Data Curation	Formal Analysis	Funding Acquisition	Investigation	Methodology	Project Administration	Resources	Software	Supervision	Validation	Visualization	Writing – Original Draft	Writing – Review & Editing	Preregistered	Preprinted	Published with Peer Review
1	Introduction	General Introduction	■											■	■	■	☐	☐	☐
2	PhD project chapter	Review on immunity and genomics	■											■	■	■	☐	☐	☑
3	PhD project chapter	Immunogenic features of UPS and MFS	■	■	■		■	■	■		■	■	■	■	■	■	☐	☑	☑
4	PhD project chapter	Multimodal profiling of chordomas	■	■	■		■	■	■		■		■	■	■	■	☐	☑	☑
5	PhD project chapter	Spatial profiling of chordomas	■	■	■	■	■	■	■		■		■	■	■	■	☐	☑	☑
6	Discussion	Discussion and future perspectives	■												■	■	☐	☐	☐

**PhD project chapters are the direct result of the PhD project of the PhD candidate.*
Some theses also include Collaboration Chapters, to which the PhD candidate has contributed but fall outside the PhD project.

Dissemination table

1.	***van Oost S, Meijer DM, Kuijjer ML, Bovee J, de Miranda N. Linking Immunity with Genomics in Sarcomas: Is Genomic Complexity an Immunogenic Trigger?***	
	Chapter in this thesis	*2*
	Publication in peer-reviewed journal	*https://doi.org/10.3390/biomedicines9081048*
2.	***van Oost S, Meijer DM, Erdem ZB, IJsselsteijn ME, Roelands J, Lam SW, et al. Divergent therapeutic and prognostic impacts of immunogenic features in undifferentiated pleomorphic sarcoma and myxofibrosarcoma***	
	Chapter in this thesis	*3*
	Preprint	*https://doi.org/10.1101/2025.03.27.645727*
	Publication in peer-reviewed journal	*https://doi.org/10.1007/s00262-025-04123-y*
	Open access data	*RNA sequencing: GEO at GSE285944* *Imaging Mass Cytometry: BioStudies at S-BIAD1555* *GitLab: https://git.lumc.nl/bstp/papers/immunogenic-features-of-ups-and-mfs*
	Open access code	*GitHub: https://github.com/deMirandaLab/immunogenic-features-of-ups-and-mfs*
3.	***van Oost S, Meijer DM, IJsselsteijn ME, Roelands JP, van den Akker B, van der Breggen R, et al. Multimodal profiling of chordoma immunity reveals distinct immune contextures***	
	Chapter in this thesis	*4*
	Preprint	*https://doi.org/10.1101/2023.09.14.557579*
	Publication in peer-reviewed journal	*https://doi.org/10.1136/jitc-2023-008138*
	Open access data	*RNA sequencing: GEO at GSE239531* *Imaging Mass Cytometry: BioStudies at S-BIAD830* *GitLab: https://git.lumc.nl/bstp/papers/multimodal-profiling-of-chordomas*
	Open access code	*GitHub: https://github.com/deMirandaLab/multimodal-profiling-of-chordomas*
4.	***van Oost S, Ursem R, Erdem ZB, Cardoso S, Venneker S, van der Breggen R, et al. Immune infiltration is associated with distinct transcriptional states and metabolic profiles in chordomas***	
	Chapter in this thesis	*5*
	Preprint	*https://doi.org/10.1101/2025.11.04.686078*
	Publication in peer-reviewed journal	*https://doi.org/10.1016/j.isci.2026.115668*
	Open access data	*GeoMx DSP & MALDI-MSI (processed): https://figshare.com/s/4d52d0129b9e0f9c7a8c* *MALDI-MSI (raw): MassIVe at MSV000100742* *GitLab: https://git.lumc.nl/bstp/papers/spatial-profiling-of-chordomas*
	Open access code	*GitHub: https://github.com/deMirandaLab/spatial-profiling-of-chordomas*

Overview of completed courses and other training

Completed courses and other training		
Mandatory activities		
Year	**Description**	**Hours**
2021	*Leiden University Onboarding Program Inform & Connect*	*5*
2021	*Basic Methods and Reasoning in Biostatistics*	*42*
2024	*Responsible Research – eBROK*	*42*
Scientific courses, workshops, and other training activities		
Year	**Description**	**Hours**
2021	*MGC - Genomics & Transcriptomics*	*7*
2022	*Organization of the post-CTOS recap for LUMC Sarcoma Researchers*	*2*
2023	*Organization of the LUMC Sarcoma Research Night*	*5*
2023	*Supervision MSc student Biomedical Sciences*	*130*
2023	*CPM – A hitchhiker's guide to GALAXY*	*5*
2023	*CPM – MALDI-TOF-MSI Imaging Analysis*	*5*
2024	*Organization of the LUMC Chordoma Research Workshop*	*3*
2025	*Co-supervision BSc student Biomedical Sciences*	*24*
Transferable skills courses, workshops, and other training activities		
Year	**Description**	**Hours**
2021	*Practical Linux*	*4*

Dissemination, acknowledgement, esteem, and other relevant scientific activities

Other scientific activities related to this thesis		
Year	**Description**	**Linked to**
2022	*Oral presentation, Dutch Sarcoma Group (DSG) PhD Symposium, Utrecht*	*Chapter 4*
2022	*Most relevant abstract for patients award, DSG PhD Symposium, Utrecht*	*Chapter 4*
2022	*Oral presentation, Dutch Tumor Immunology Meeting (DTIM), Breukelen*	*Chapter 4*
2022	*Oral presentation, Connective Tissue Oncology Society, Vancouver, Canada*	*Chapter 4*
2023	*Poster presentation, FORTRESS Research Meeting, Essen, Germany*	*Chapter 4*
2023	*Oral presentation, DSG PhD Symposium, Utrecht*	*Chapter 3*
2023	*Oral presentation, LUMC Cancer Research Day, Leiden*	*Chapter 3*
2023	*Clinic and Laboratory Integration Program Grant, "Leveraging Natural Immunity in Chordomas for Tailored Immunotherapy", Cancer Research Institute & Chordoma Foundation, co-applicant*	*Chapter 4+5*
2023	*Oral presentation, Chordoma Foundation Research Workshop, Boston, US*	*Chapter 4*
2023	*Poster presentation, Cancer Immunotherapy (CIMT), Mainz, Germany*	*Chapter 3*
2023	*Oral presentation, CONDOR Symposium Microenvironment and Immunotherapy of Sarcomas, Bordeaux, France*	*Chapter 3*
2024	*Oral presentation, FORTRESS Research Meeting, Leuven, Belgium*	*Chapter 5*
2024	*Oral presentation, LUMC Cancer Research Day, Leiden*	*Chapter 5*
2024	*Skills Development Grant, Bone Cancer Research Trust (BCRT), personal grant*	*Chapter 5*
2024	*Oral presentation, BCRT Chordoma Research Symposium, London, UK*	*Chapter 5*
2024	*Best presentation award, BCRT Chordoma Research Meeting, London, UK*	*Chapter 5*
2025	*Oral presentation, FORTRESS Research Meeting, Essen, Germany*	*Chapter 3*

NEDERLANDSE SAMENVATTING

Introductie

Sarcomen vormen een heterogene groep zeldzame tumoren die ontstaan in steunweefsels van het lichaam, zoals bindweefsel, spieren, vetweefsel en bot. Er bestaan meer dan honderd verschillende subtypen, die sterk kunnen verschillen in biologische eigenschappen en klinisch gedrag. Op genetisch niveau worden sarcomen vaak onderverdeeld in tumoren met een relatief eenvoudige genetische opbouw (met weinig veranderingen in hun DNA) en tumoren met een complexe genetische structuur (met veel veranderingen in hun DNA). Deze verschillen beïnvloeden hoe tumoren zich gedragen en hoe patiënten reageren op behandelingen, wat de klinische behandeling uitdagend maakt. Ondanks verbeteringen in chirurgie, radiotherapie en systemische behandelingen is de prognose van patiënten met sarcomen de afgelopen jaren slechts beperkt verbeterd. Dit komt onder andere doordat de ziekte regelmatig terugkeert of ongevoelig wordt voor standaardbehandelingen.

Het immuunsysteem speelt een belangrijke rol bij het herkennen en bestrijden van kankercellen. Tumorcellen kunnen worden onderscheiden van gezonde cellen doordat zij afwijkende stukjes eiwit (antigenen) presenteren op hun celoppervlak. Deze antigenen kunnen worden herkend door immuuncellen, met name T-cellen, die vervolgens een afweerreactie (ook wel immuunreactie genoemd) tegen de tumor kunnen opwekken. Tumoren kunnen deze immuunreactie echter ontwijken. Zij kunnen bijvoorbeeld de presentatie van antigenen verminderen, immuunremmende cellen aantrekken of remmende signalen activeren, ook wel immuuncheckpoints genoemd.

De ontwikkeling van immuuntherapie, en in het bijzonder immuuncheckpointremmers, heeft de behandeling van verschillende kankersoorten ingrijpend veranderd. Deze therapieën herstellen de activiteit van T-cellen en kunnen leiden tot langdurige responsen, vooral bij tumoren die sterk immunogeen zijn. Dit betekent dat deze tumoren goed herkenbaar zijn voor het immuunsysteem, bijvoorbeeld doordat zij veel mutaties in hun DNA bevatten. Voorbeelden hiervan zijn huidkanker en longkanker. De effectiviteit van immuuntherapie verschilt echter sterk tussen tumortypen en patiënten.

Bij sarcomen is het effect van immuuntherapie over het algemeen beperkt. Dit wordt vaak toegeschreven aan het relatief lage aantal mutaties, waardoor deze tumoren minder goed herkenbaar zijn voor het immuunsysteem, en aan een minder actieve immuunomgeving. Toch worden bij bepaalde sarcoomsubtypen wel klinische responsen gezien. Dit suggereert dat een

deel van de sarcomen gevoelig kan zijn voor immuuntherapie. Daarnaast lijken combinaties met behandelingen zoals radiotherapie of chemotherapie de effectiviteit van immuuntherapie mogelijk te vergroten.

Steeds duidelijker wordt dat niet alleen de tumorcellen zelf, maar ook de tumoromgeving een belangrijke rol speelt bij behandelrespons. De tumoromgeving bestaat uit alle cellen en structuren rondom de tumor, zoals bloedvaten, bindweefsel en verschillende soorten immuuncellen. De samenstelling en ruimtelijke organisatie van deze omgeving kunnen bepalen of immuuncellen de tumor effectief kunnen bereiken en aanvallen.

Binnen de wekedelensarcomen zijn ongedifferentieerd pleiomorf sarcoom (UPS) en myxofibrosarcoom (MFS) twee subtypen met een complexe genetische opbouw en weinig specifieke differentiatie. Dit betekent dat het onduidelijk is van welk oorspronkelijk celtype deze tumoren precies afkomstig zijn. Hoewel beide subtypen enige gevoeligheid voor immuuntherapie laten zien, is nog onduidelijk in hoeverre hun immuunomgevingen op elkaar lijken.

Chordomen daarentegen zijn zeer zeldzame bottumoren met een relatief stabiel genoom. Opvallend is dat deze tumoren, ondanks kenmerken die normaal gesproken wijzen op lage immunogeniciteit, in sommige gevallen toch reageren op immuuntherapie. Dit benadrukt dat er nog belangrijke kennis ontbreekt over de rol van het immuunsysteem bij sarcomen.

In dit proefschrift werd daarom onderzocht hoe het immuunsysteem en de tumoromgeving verschillen tussen verschillende sarcoomsubtypen, met als doel beter te begrijpen welke patiënten mogelijk baat kunnen hebben bij immuuntherapie.

Discussie

In dit proefschrift laten we zien dat de rol van immuuncellen binnen tumoren sterk verschilt tussen sarcoomsubtypen. Het doel van dit onderzoek was om meer inzicht te krijgen in de immuunomgeving van sarcomen, zodat patiënten in de toekomst mogelijk beter geselecteerd kunnen worden voor immuuntherapie of combinaties van behandelingen. Onze resultaten laten zien dat vergelijkbare hoeveelheden immuuncellen in verschillende sarcoomsubtypen heel verschillende gevolgen kunnen hebben voor prognose en behandelrespons. Dit benadrukt dat immuunkenmerken altijd moeten worden geïnterpreteerd in samenhang met genetische eigenschappen, de structuur van de tumor en de invloed van behandeling.

Hoewel UPS en MFS vaak samen worden bestudeerd vanwege hun vergelijkbare genetische complexiteit, laten onze resultaten zien dat deze tumoren biologisch en klinisch van elkaar verschillen. Bij UPS hangt de aanwezigheid van immuuncellen samen met een betere uitkomst, wat wijst op een effectieve immuunrespons tegen de tumor. Bij MFS werd deze relatie niet gevonden, ondanks een vergelijkbare mate van immuuncellen in de tumoromgeving. Dit suggereert dat niet alleen de aanwezigheid van immuuncellen belangrijk is, maar ook hun activiteit en ruimtelijke organisatie binnen de tumor. Deze verschillen kwamen ook naar voren in de respons op radiotherapie. Bij UPS zagen we duidelijke veranderingen na behandeling, zoals littekenvorming en een toename van cytotoxische T-cellen (celdodende T-cellen), wat wijst op zowel weefselverandering als activatie van het immuunsysteem. MFS bleek daarentegen relatief ongevoelig voor radiotherapie, met weinig veranderingen in de samenstelling van de tumor. Dit wijst op verschillen in de interactie tussen tumorcellen, steunweefsel en immuuncellen.

Deze bevindingen hebben ook gevolgen voor de ontwikkeling van biomarkers: meetbare kenmerken die iets kunnen zeggen over ziekteverloop of behandelrespons. Tertiaire lymfoïde structuren (TLS)—georganiseerde verzamelingen van immuuncellen, vaak aan de rand van de tumor—worden gezien als een teken van een actieve immuunrespons en zijn in sommige sarcomen geassocieerd met een betere prognose. Onze resultaten laten echter zien dat TLS niet op zichzelf beoordeeld moeten worden. Hun betekenis hangt af van de bredere immuuncontext en kan bovendien veranderen onder invloed van behandeling. Dit pleit voor een meer geïntegreerde benadering, waarbij meerdere kenmerken van de tumor en de immuunomgeving samen worden meegenomen.

Chordomen vormen een interessant contrast. Ondanks hun relatief eenvoudige genetische profiel laten zij wel tekenen van immuunactiviteit zien en kunnen zij in sommige gevallen reageren op immuuntherapie. We laten zien dat een deel van de chordomen een georganiseerde immuunrespons vertoont, met interacties tussen T-cellen en antigeenpresenterende cellen (cellen die tumorantigenen tonen aan andere immuuncellen). Tegelijkertijd werden deze immuunreacties slechts bij een subgroep van patiënten gevonden en waren ze niet duidelijk gekoppeld aan een betere klinische uitkomst. Mogelijk spelen de lage herkenbaarheid van tumorcellen, bijvoorbeeld door een lage mutatielast, en een remmende tumoromgeving hierbij een rol. Daarnaast vonden we dat immuuncelrijke chordomen specifieke veranderingen vertonen in hun genexpressie (het “gedrag” van cellen) en hun stofwisseling. Dit suggereert dat eigenschappen van de tumor zelf mogelijk bijdragen aan het vormgeven van de immuunomgeving.

Samenvattend laten onze resultaten zien dat de relatie tussen het immuunsysteem en klinische uitkomst bij sarcomen complex is en sterk afhankelijk van de context. In plaats van te vertrouwen op één enkele biomarker is een geïntegreerde benadering nodig, waarbij immuunkenmerken, genetische eigenschappen en de tumoromgeving gezamenlijk worden meegenomen om behandelingen in de toekomst beter af te stemmen op individuele patiënten.

Toekomstperspectief

Op basis van de bevindingen in dit proefschrift is het belangrijk dat toekomstig onderzoek zich richt op immuunkenmerken die niet alleen beschrijvend zijn, maar ook daadwerkelijk relevant zijn voor behandeling en klinische besluitvorming. Daarvoor is een beter begrip nodig van hoe de activiteit en organisatie van het immuunsysteem samenhangen met genetische eigenschappen van de tumor.

Een belangrijke volgende stap is het combineren van gedetailleerde moleculaire analyses met goed beschreven patiëntengroepen. Hoewel de immuunomgeving van sarcomen steeds beter in kaart wordt gebracht, is nog onvoldoende bekend hoe deze inzichten zich vertalen naar behandelrespons. Door geavanceerde analysetechnieken te integreren in klinische studies kan beter worden vastgesteld welke kenmerken bruikbaar zijn om behandelingen te voorspellen en uiteindelijk gerichter in te zetten.

Daarnaast is meer onderzoek nodig naar de manier waarop sarcomen door het immuunsysteem worden herkend. Omdat klassieke tumorantigenen bij sarcomen vaak schaars zijn, kunnen alternatieve vormen van herkenning een belangrijke rol spelen. Ook het aangeboren immuunsysteem—het deel van het afweersysteem dat snel maar minder specifiek reageert—kan hierbij relevant zijn, vooral in tumoren waarin de klassieke T-celrespons beperkt is.

Tot slot is meer onderzoek nodig naar tumorspecifieke factoren die zowel tumorgroei als de immuunomgeving beïnvloeden. In chordomen lijkt de transcriptiefactor *TBXT*—een eiwit dat bepaalt welke genen in een cel actief zijn en daarmee het gedrag van tumorcellen beïnvloedt—hierin een belangrijke rol te spelen. *TBXT* kan mogelijk zowel een aangrijpingspunt voor nieuwe therapieën zijn als een factor die de immuunomgeving van chordomen mede vormgeeft. Meer inzicht in deze processen kan bijdragen aan de ontwikkeling van nieuwe behandelstrategieën.

Samen kunnen deze ontwikkelingen bijdragen aan een beter begrip van sarcomen en uiteindelijk aan meer gerichte en effectieve behandelingen voor patiënten.

CURRICULUM VITAE

Siddh van Oost is geboren op 3 september 1995 te Rotterdam. In 2014 behaalde hij zijn middelbareschooldiploma aan het Johan van Oldenbarnevelt Stedelijk Gymnasium in Amersfoort, waarna Siddh begon aan de bacheloropleiding Bio-Farmaceutische Wetenschappen aan de Universiteit Leiden. Na het behalen van zijn bachelorsdiploma in 2018 vervolgde hij zijn studie met de masteropleiding Bio-Pharmaceutical Sciences in Leiden. Tijdens zijn wetenschapsstage op de afdeling Drug Discovery & Safety bij het Leiden Academic Center for Drug Research kwam Siddh in aanraking met computationeel onderzoek, waarbij hij met behulp van microscopiebeelden stressreacties van cellen analyseerde na blootstelling aan kankermedicatie, zoals kinaseremmers. Vervolgens voerde hij, in samenwerking met de afdeling Imaging & Bioinformatics van het Leiden Institute of Advanced Computer Science, zijn literatuuronderzoek uit naar het gebruik van openbare data van verschillende vormen van kanker en hoe inzichten verkregen kunnen worden door het combineren van verschillende lagen van biologische informatie. Siddh rondde zijn master in 2020 af met een wetenschapsstage op de afdeling Medical Oncology van het Erasmus Medisch Centrum in Rotterdam, waar hij onderzoek deed naar neurofibromatose type 1 en het karakteriseren van cellijnen van (plexiforme) neurofibromen en maligne perifere zenuwschedetumoren, een vorm van wekedelensarcoom.

Aansluitend begon Siddh aan zijn promotieonderzoek naar het immuunlandschap van sarcomen aan het Leids Universitair Medisch Centrum (LUMC) in Leiden. Dit onderzoek vond plaats binnen het Leiden Center for Computational Oncology, onder begeleiding van Prof.dr. Judith Bovée en Prof. dr. Noel de Miranda. Tijdens zijn promotie deed Siddh onderzoek naar het immuunsysteem in verschillende vormen van bot- en wekedelensarcomen, waarbij hij gebruikmaakte van diverse (ruimtelijke) technologieën. Hij kreeg regelmatig de gelegenheid om zijn werk te presenteren op conferenties en ontving tweemaal een prijs: voor het meest relevante onderzoek voor patiënten (Dutch Sarcoma Group PhD Symposium, 2022) en voor beste presentatie (Bone Cancer Research Trust Chordoma Research Symposium, 2024). Daarnaast ontving hij samen met zijn promotores in 2023 een subsidie van de Chordoma Foundation om hun onderzoek naar immuniteit in chordomen voort te zetten.

Sinds 1 april 2026 is Siddh werkzaam als postdoctoraal onderzoeker in de onderzoeksgroep van Dr. Joost Vermaat op de afdeling Hematologie van het LUMC. Hier werkt hij mee aan het in kaart brengen van het immuunlandschap van verschillende vormen van lymfeklierkanker, met name B-cellymfomen.

LIST OF PUBLICATIONS

van Oost S*, Meijer DM*, Kuijjer ML, Bovée JVMG, de Miranda NFCC. Linking Immunity with Genomics in Sarcomas: Is Genomic Complexity an Immunogenic Trigger? *Biomedicines*. 2021 Aug 19;9(8):1048.

van Oost S, Meijer DM, IJsselsteijn ME, Roelands JP, van den Akker BEMW, van der Breggen R, Briaire-de Bruijn IH, van der Ploeg M, Wijers-Koster PM, Polak SB, Peul WC, van der Wal RJP, de Miranda NFCC*, Bovée JVMG*. Multimodal profiling of chordoma immunity reveals distinct immune contextures. *J Immunother Cancer*. 2024 Jan 25;12(1):e008138.

Vlasveld M, Callegaro G, Fisher C, Eakins J, Walker P, Lok S, **van Oost S**, de Jong B, Pellegrino-Coppola D, Burger G, Wink S, van de Water B. The integrated stress response-related expression of CHOP due to mitochondrial toxicity is a warning sign for DILI liability. *Liver Int*. 2024 Mar;44(3):760-775.

Meijer DM, **van Oost S**, Roelands JP, Ruano D, Briaire-de Bruijn IH, van den Akker BE, Kruisselbrink AB, Wijers-Koster PM, van der Ploeg M, IJsselsteijn M, Lam SW, de Ru AH, Tjokrodirijo RTN, van de Sande MAJ, Gelderblom H, Van Veelen PA, Kuijjer ML, de Miranda N*, Bovée JVMG*. Enhanced immune responses are accompanied by increased MAGEA expression in osteosarcoma metastases. *BMJ Oncol*. 2024 Nov 13;3(1):e000472.

van Oost S, Meijer DM, Erdem ZB, IJsselsteijn ME, Roelands J, Lam SW, Boejharat MS, van den Akker BEWM, van der Breggen R, Briaire-de Bruijn IH, Hawinkels LJAC, Kruiswijk AA, van der Ploeg M, Wijers-Koster PM, Haas RL, van den Sande MAJ, de Miranda NFCC*, Bovée JVMG*. Divergent therapeutic and prognostic impacts of immunogenic features in undifferentiated pleomorphic sarcoma and myxofibrosarcoma. *Cancer Immunol Immunother*. 2025 Jul 2;74(8):258.

Kaya M, Post CCB, de Gruil N, **van Oost S**, Tromp J, Boere IA, Witteveen PO, Sonke GS, Lalisang RI, Putter H, Meershoek-Klein Kranenbarg E, Braak J, Creutzberg CL, Bosse T, Welters MJP, van der Burg S, Kroep JR. 1156P Transcriptomic analysis in p53-abnormal endometrial cancer and final overall survival analyses from the DOMEC phase II trial. *Annals of Oncology*. 2025 Sep;36:S716

van Oost S, Ursem R, Erdem ZB, Cardoso S, Venneker S, van der Breggen R, Briaire-de Bruijn IH, Kruisselbrink AB, van Zeijl R, Heijs B, Szuhai K, de Miranda NFCC*, Bovée JVMG*. Immune infiltration is associated with distinct transcriptional states and metabolic profiles in chordomas. *iScience.* 2026 Apr 9.

*These authors contributed equally to this work

DANKWOORD

Samen sta je sterker. Dat is mij de afgelopen jaren nog duidelijker geworden. Daarom wil ik graag iedereen bedanken die heeft bijgedragen aan deze prachtige reis en het tot stand komen van dit proefschrift.

Of course, first to my promotors, Judith and Noel. Thank you both for your guidance and for believing in me. I am very grateful to have had both of you as mentors; it has been a privilege to learn from you and grow with you. From Queen in Vancouver to techno in Leuven, I appreciate all the opportunities you have given me. You were the perfect tag team.

Debora, mijn PhD- en LCCO-buddy vanaf mijn eerste dag, echt enorm bedankt voor de geweldige tijd, voor je behulpzaamheid en ondersteuning, maar bovenal al het gelach. Ik had me geen betere partner-in-crime kunnen wensen.

Lieve analisten, dank jullie wel voor alle fijne en gezellige momenten op het lab en daarbuiten. Bedankt voor al jullie harde werk en ondersteuning; zonder jullie was dit proefschrift er niet geweest. Inge, bedankt voor die veel te vroege kopjes koffie op het lab in de eerste jaren en voor alle support die je bent blijven geven, zowel op werk als op persoonlijk vlak. Alwine, Brendy, Pauline en Ruud, dank jullie wel voor het altijd klaarstaan; en voor het helpen met opruimen, opzoeken, overnemen, wegbrengen en ophalen van materiaal. Manon, ook jij bedankt voor het altijd klaarstaan op het lab, maar vooral voor alle lol die we hebben gehad door de jaren heen.

To all PhDs, postdocs, and students from the cancer immunogenomics and bone groups, dear colleagues, thank you all so much for this amazing time and for your contributions to the work in this thesis. We've had excellent scientific discussions as well as amazingly fun conversations and activities. I will never be able to choose a color palette for a figure without smirking again. A special thank you to Zeynep, Ricki, Marieke, Jitske, Joana, Sanne, Sheena, Rick, Debora, Jessica, Zheng, Marta, Paul, Suraya, Danielle & Chris Frips Soundsystem (Marie & Scott, & Manon).

Beste maten, dank jullie voor alle steun, alle gezelligheid en alle gekkigheid. In het bijzonder Marijn, Ivar, Rogier, Matthijs, Thomas, Jasper, Arjan & Sam, door jullie is mijn leven een stuk rijker.

Mam, dankjewel dat je er altijd bent geweest. Pap, dankjewel voor je uitgebreide interesse in mijn werk. Sylke, dankjewel voor je enthousiasme en je warmte. Mauce, dankjewel voor je liefde en je trots, voor mij maar ook zeker voor Lanette. Ik ben je heel dankbaar. Lieve familie, bedankt voor jullie luisterend oor en jullie steun.

Last but definitely not least, dear-est Lanette, dankjewel dat je er bent; zonder jou was ik nooit tot hier gekomen. Ik geniet ervan dat we samen de wereld ontdekken, ons fijne thuis hebben met die gestoorde Nova, en dat we elkaar altijd steunen. This is only the beginning.